PREPARATION OF BIOCOMPATIBLE COMPOSITE 3D ARCHITECTURES BASED ON GRAPHENE OXIDE (GO) AND CHITOSAN FOR FLEXIBLE ALL SOLID STATE SUPERCAPACITORS

ESNEK TÜM KATI HAL SÜPER KAPASİTÖRLER İÇİN GRAFEN OKSİT (GO) VE KİTOSAN BAZLI BİYOUYUMLU KOMPOZİT 3D MİMARİLERİN HAZIRLANMASI

SAEIDEH ALIPOORILEMEESLAM

PROF. DR MURAT BARSBAY

Supervisor

Submitted to

Graduated School of Science and Engineering of Hacettepe University

As a Partial Fulfillment to Requirements

For the Award of PhD Degree in Polymer Science and Technology

2024

ABSTRACT

Preparation of Biocompatible Composite 3D Architectures Based on Graphene Oxide (GO) and Chitosan for Flexible All Solid State Supercapacitors

SAEIDEH ALIPOORILEMEESLAM

Doctor of Philosophy, Department of CHEMISTRY

Prof. Dr. MURAT BARSBAY

April 2024, 281 pages

Today, an increasing number of elderly people or patients with chronic diseases need new generation flexible, implantable, and biocompatible devices to monitor their health conditions moment by moment. Although many people currently use implantable medical devices (IMDs), they require power from an external source or an internal battery. Flexible and biocompatible implantable electronic devices provide an effective strategy to monitor health conditions within the biological body and provide information flow when necessary. In this way, monitoring of patients' current health status, continuity of routine monitoring processes and emergency interventions when necessary can be carried out effectively. It is critical that the power systems of the electronic devices used for this purpose are flexible and high-performance, as well as biocompatible and implantable. Unfortunately, traditional

energy sources can cause biocompatibility issues such as immunological rejection, inflammatory reactions and secondary biological toxicity due to corrosion and leakage of battery packs. Additionally, existing energy storage devices require surgical replacement every 6-10 years, posing additional risk to the user. Therefore, alternative energy storage devices that do not have such disadvantages are needed. Supercapacitors are proposed as promising candidates for powering implantable electronic devices, thanks to their high power density, long cycle life, and ability to charge-discharge quickly within seconds.

For this purpose, the aim of the current PhD thesis is to design a solid-state supercapacitor with high electrochemical performance, based on graphene oxide/chitosan (GO/CS) as electrode materials and poly(vinyl alcohol) (PVA)/potassium chloride (KCl) as gel polymer electrolyte (GPE). In this thesis, PVA a hydrophilic and biocompatible polymer, is utilized as the matrix and KCl is used as the ion generator. This thesis focuses on optimizing the key properties of the gel electrolytes, including ionic conductivity, film formation, mechanical-thermal properties, and biocompatibility. Since the ionic conductivity of an electrolyte depends on the charge carrier concentration and mobility, in the first part of this thesis, the effect of KCl amount and polymer molecular weight (M_w) on ionic conductivity of PVA/KCl/H_2O-based gel polymer electrolytes were systematically investigated for the first time. The result of characterization tests confirms the combination of PVA and KCl. Finally, by considering the electrochemical impedance spectroscopy (EIS) test and mechanical-thermal properties results, GPE with M_w=195000 g mol^{-1} and PVA/KCl (w/w:1/2) was found to have the greatest ionic conductivity (3.48 ±0.25 mS cm^{-1}). Even after 5000 cycles, it retained 88% of the initial specific capacitance. Our findings reveal that GPEs exhibit exceptional mechanical strength as well as unique ionic conductivity characterized by minimal interfacial resistance. Moreover, the gel electrolyte exhibited exceptional biocompatibility, evident in a cell viability test where 72.3% of cells remained unaffected after 72 h of exposure to PVA/KCl gel.

For the first time, symmetric solid-state supercapacitor based on GO/CS composite fiber was developed by wet-spinning method for different weight ratios of GO/CS. In this way, at an optimum concentration of chitosan, the supercapacitor containing RGO/CS (w/w: 90/10) showed the highest specific capacitance of 523.06± 53.57 F g^{-1} at scan rate of 5 mV s^{-1}. Chitosan effectively prevents re-stacking of GO nanosheets and provides high specific

surface area and high conductivity, thus leading to excellent energy storage performance. Additionally, film-based GO/CS electrodes were prepared using the solution mixing method for various GO/CS weight ratios. The supercapacitor containing RGO/CS (w/w: 90/10) showed the highest specific capacitance of 872.75 ± 68.35 F g^{-1} at scan rate of 5 mV s^{-1}. The highest specific capacitance of the film-based supercapacitor can be attributed to variations in the material's surface area, porosity, and accessibility of active sites in the film morphology. Film generally provides a larger surface area, more active sites for electrochemical reactions, and better accessibility of electrolyte ions to the electrode surface compared to fibers, leading to higher specific capacitance. Additionally, the film structure may contribute to improved electrochemical performance by providing improved electron and ion transport within the electrode, better porous structure, and potentially flexibility. Therefore, the results of characterization and microscopic tests of GO/CS film confirm the combination of GO and chitosan. Moreover, the film composite electrode retained 87.31% of its initial capacitance even after 10,000 cycles. The symmetric solid-state supercapacitor exhibits excellent energy and power densities of 234.97 W h kg^{-1} and 1499.98 kW kg^{-1}, respectively. Beyond its electrochemical benefits, the integration of CS improved biocompatibility and mechanical strength, making it a suitable candidate for implantation. In evaluating the cell viability of the RGO/CS composite, the results showed a viability rate of 76.4% after 72 hours. The recorded cell viability of 76.4% indicates that a significant proportion of cells maintained their viability and well-being after exposure to the RGO/CS electrode.

Following the optimization studies conducted on the structures of electrolyte and electrode materials, in the third stage of the thesis, a flexible solid-state supercapacitor based on RGO/CS (w/w: 90/10) and PVA/KCl gel electrolyte (M_w=195000 g mol^{-1}, PVA/KCl (w/w:1/2)) was fabricated using PET as a flexible current collector substrate, instead of stainless-steel substrate. The specific capacitance value was found as 191.07 ± 19.24 F g^{-1} at 5 mVs^{-1} (186.64 ± 21.69 F g^{-1} at 1 A g^{-1}), and this value was lower than that of the stainless-steel substrate. This may be due to the stable platform for uniform adhesion of the electrode material and good electricity conductor of stainless steel which is beneficial for efficient charge transfer and overall excellent durability and electrochemical performance.

Furthermore, a flexible solid-state supercapacitor based on RGO/CS (w/w: 90/10) and PVA/KCl gel electrolyte (M_w=195000 g mol^{-1}, PVA/KCl (w/w:1/2)) was fabricated using laser 3D-printing technology on polyimide (PI) film. The interdigital RGO/CS electrodes displayed a hair comb formation and showed an outstanding adhesive properties and durability. In this stage of the thesis, the adaptability of the obtained supercapacitors to 3D printing technology was demonstrated.

These findings offer a promising route towards the fabrication of stable and high-performance biocompatible electrode material and gel polymer electrolytes that can be used in solid-state supercapacitors, thus laying the foundation for their integration into flexible, safer, and wearable bioelectronics. Developed with environmentally friendly materials, the electrode paves the way for the production of solid-state supercapacitors with advanced electrochemical and biocompatibility properties, making them suitable for integration into sustainable next-generation biomedical devices.

Keywords: Solid-state supercapacitors, Biocompatible, Poly(vinyl alcohol), Chitosan, Graphene Oxide.

ÖZET

Esnek Tüm Katı Hal Süper Kapasitörler İçin Grafen Oksit (GO) ve Kitosan Bazlı Biyouyumlu Kompozit 3D Mimarilerin Hazırlanması

SAEIDEH ALIPOORILEMEESLAM

Doktora, Polimer Bilim ve Teknoloji Bölümü

Prof. Dr. MURAT BARSBAY

April 2024, 281 Sayfa

Günümüzde giderek artan sayıda yaşlı insan, ya da kronik hastalar, sağlık durumlarının an ve an izlenmesi için, yeni nesil esnek, implante edilebilir, biyouyumlu cihazlara ihtiyaç duymaktadır. Pek çok kişi halihazırda implante edilebilir tıbbi cihazları (Implantable Medical Devices-IMD'ler) kullanıyor olsa da, bunların harici bir kaynaktan veya dahili bir bataryadan güç alması gerekmektedir. Vücuda yerleştirilebilir esnek ve biyouyumlu elektronik cihazlar, biyolojik vücut içindeki sağlık koşullarını an ve an ve gerekli durumlarda bilgi akışını sağlamak için etkin bir strateji sağlar. Böylece hastaların anlık sağlık durumlarının monitörizasyonu, rutin izleme süreçlerinin devamlılığı ve gerekli durumlarda acil müdahaleler etkin bir şekilde yürütülebilir. Bu amaca yönelik kullanılacak elektronik cihazların güç sistemlerinin esnek ve üstün performanslı olmalarının yanı sıra, biyouyumlu ve implante edilebilir olmaları kritik önem taşımaktadır. Ne yazık ki geleneksel enerji kaynakları, pil paketlerinin korozyonu ve sızıntısı nedeniyle immünolojik red, inflamatuar reaksiyonlar ve ikincil biyolojik toksisite gibi biyouyumluluk sorunlarına neden

olabilmektedir. Ayrıca mevcut enerji depolama cihazlarının her 6-10 yılda bir ameliyat yoluyla değiştirilmesi gerekir ve bu da kullanıcı için ek risk oluşturur. Dolayısıyla bu gibi dezavantajları olmayan alternatif enerji depolama cihazlarına ihtiyaç duyulmaktadır. Süperkapasitörler, yüksek güç yoğunlukları, uzun çevrim ömrleri ve saniyeler içinde hızlı şarj-deşarj olabilmeleri sayesinde, implante edilebilir elektronik cihazlara güç vermek için umut verici adaylar olarak önerilmektedir.

Bu amaçla, mevcut doktora tezinin amacı, elektrot malzemesi olarak grafen oksit/kitosan (GO/CS) kompozit yapıları ve elektrolit olarak ise poli(vinil alkol) (PVA)/potasyum klorür (KCl) bazlı bir katı jel polimer yapısını kullanarak, yüksek elektrokimyasal performansa sahip, tam katı hal bir süperkapasitör tasarlamaktır. Bu tez çalışmasında, suda çözünebilen biyouyumlu bir polimer olan PVA matris olarak, KCl ise iyon üretici tuz olarak kullanılmıştır. Tez çalışmasının elektrolit üretim aşaması; iyonik iletkenlik, film oluşumu, termal özellikler ve biyouyumluluk da dahil olmak üzere, geliştirilen jel elektrolitlerin temel özelliklerinin optimize edilmesine odaklanmaktadır. Bir elektrolitin iyonik iletkenliği yük taşıyıcı konsantrasyonuna ve hareketliliğine bağlı olduğundan, tez çalışmasının ilk kısmında, KCl miktarının ve polimer molekül ağırlığının (M_w) PVA/KCl/H_2O bazlı jel polimer elektrolitlerin (Gel Polymer Electrolyte-GPE) iyonik iletkenliğine olan etkisi ilk kez sistematik olarak araştırıldı. Gerçekleştirilen yapısal karakterizasyonların, özellikle de elektrokimyasal empedans spektroskopisi (EIS) testi sonuçları ve termomekanik özellikler dikkate alındığında, M_w=195000 g mol^{-1} ve PVA/KCl (w/w:1/2) değerine sahip GPE'nin, hem uygun termal ve mekanik özelliklere hem de en yüksek iyonik iletkenliğe (3.48 ±0.25 mS cm^{-1}) sahip olduğu bulunmuştur. Bu GPE formülasyonu, 5000 döngüden sonra bile başlangıçtaki özgül kapasitansının %88'ini korudu. Optimum jel elektrolit yapısının, 72 saatlik maruziyetten sonra hücrelerin %72.3'ünün etkilenmeden kaldığının görüldüğü hücre canlılığı test sonuçlarına göre, yüksek düzeyde biyouyumluluk sergilediği tespit edildi.

GPE geliştirilmesine yönelik çalışmalar sonrasında tezin odağı, biyouyumlu ve esnek bir elektrot malzeme geliştirilmesine yönlendirilmiştir. Bu amaçla, fiber ve film halinde iki farklı kompozit elektrot mazleme, grafen oksit (GO) ve kitosan (CS) kullanılarak optimize edilmiştir. Optimum kitosan konsantrasyonu olarak tespit edilen RGO/CS (w/w: 90/10) ağırlık oranında, fiber halinde hazırlanan kompozit elektot kullanılarak geliştirilen süperkapasitörün, 5 mV s^{-1} tarama hızında 523.06± 53.57 F g^{-1} ile en yüksek spesifik

kapasitans değerini verdiği bulunmuştur. Kitosan, GO nano tabakalarının agregasyonunu etkili bir şekilde önleyerek, yüksek spesifik yüzey alanı ve yüksek iletkenlik sağlanmasında ve böylece mükemmel bir enerji depolama performansının elde edilmesinde rol almıştır. Film bazlı GO/CS elektrotları da çeşitli GO/CS ağırlık oranlarında hazırlanmış, RGO/CS (w/w: 90/10) oranındaki kompozit film elektrot ile geliştirilen süper kapasitörün, 5 mV s^{-1} tarama hızında 872.75± 68.35 F g^{-1} ile en yüksek spesifik kapasitans değerini verdiği görülmüştür. Film bazlı elektrot ile hazırlanan süper kapasitörün, fibere kıyasla daha yüksek spesifik kapasitans vermesi, malzemenin yüzey alanındaki, gözenekliliğindeki ve morfolojisindeki farklılıklara bağlı olarak aktif bölgelerin erişilebilirliğinin artmasına bağlanabilir. Filmler fibere kıyasla, genellikle daha geniş bir yüzey alanı, elektrokimyasal reaksiyonlar için daha fazla aktif bölge ve elektrolit iyonlarının elektrot yüzeyine daha kolay erişilebilirliği gibi avantajlar sağlar. Bu avantajlar ise elde edilen yüksek spesifik kapasitansın temel sebebini oluşturur. Ek olarak film yapısı, elektrot yapısında daha yüksek elektron ve iyon taşınması, daha iyi gözenekli yapı ve potansiyel olarak yüksek esneklik sunarak elektrokimyasal performansın artmasına katkıda bulunabilir. Optimum formülasyondaki (RGO/CS=90/10, w/w) film kompozit elektrot, 10,000 döngüden sonra bile başlangıç kapasitansının %87.31'ini korudu. Bu kompozit elektrot ile geliştirilen simetrik katı hal süper kapasitör, sırasıyla 234.97 W h kg^{-1} ve 1499.98 kW kg^{-1} değerlerine ulaşan mükemmel düzeyde enerji ve güç yoğunluğu sergiledi. Elde edilen bu üstün elektrokimyasal kazanımın ötesinde, kitosanın yapıdaki varlığı, biyouyumluluğu ve mekanik sağlamlığı geliştirerek, elektrot malzemeyi implantasyon için uygun bir aday haline getirmiştir. RGO/CS kompozitin biyouyumluluğunun değerlendirildiği test neticesinde, 72 saat sonunda %76.4'lük bir hücre canlılığı tespit edilmiştir. Kaydedilen bu oran, hücrelerin kayda değer bir kısmının RGO/CS elektroduna maruz kaldıktan sonra canlılıklarını koruduğunu göstermektedir.

Elektrolit ve elektrot malzemelerin yapısına yönelik yürütülen optimizasyon çalışmalarının ardından tezin üçüncü adımında, RGO/CS (w/w: 90/10) elektrot ve PVA/KCl jel elektrolit (M_w=195000 g mol^{-1}, PVA/KCl (w/w:1/2)) bazlı esnek katı hal süper kapasitör, esnek bir akım toplayıcı alt tabaka olarak çelik yerine PET kullanılarak üretildi ve elektrokimyasal performansı incelendi. Bu tam esnek süper kapasitörün spesifik kapasitans değeri 5 mVs^{-1}'de 191.07±19.24 F g^{-1} (1 A g^{-1}'de 186.64±21.69 F g^{-1}) olarak tespit edildi. Bu değer, paslanmaz çelik alt tabakanın kullanıldığı süper kapasitöre kıyasla daha düşüktür. Bunun

nedeni paslanmaz çeliğin, elektrot malzemesinin daha düzgün bir şekilde yüzeye yapışmasını sağlayan kararlı bir platform ve verimli bir yük aktarımı için gerekli mükemmel dayanıklılık ve yüksek elektrik iletkenliği kriterlerini sağlanması olabilir.

Tezin son aşamasında, RGO/CS (w/w: 90/10) ve PVA/KCl jel elektrolit (M_w=195000 g mol^{-1}, PVA/KCl (w/w:1/2)) bazlı esnek bir katı hal süper kapasitör, poliimid (PI) film üzerine lazer 3D baskı teknolojisi kullanılarak basıldı. Interdigital RGO/CS elektrotları, PI yüzeyde saç tarağı oluşumu sergiledi ve olağanüstü yapışma özellikleri ve dayanıklılık gösterdi. Tezin bu aşamasında, elde edilen süper kapasitörlerin 3D lazer baskılama teknolojisine uyarlanabilirlikleri gösterildi.

Tez çalışmamız, katı hal süper kapasitörlerinde kullanılabilecek kararlı, yüksek performanslı ve biyouyumlu jel polimer elektrolitlerin imalatına yönelik etkin bir yol sunmakta ve elde edilen malzemelerin esnek, daha güvenli ve giyilebilir biyo-elektroniklere entegrasyonunun temeline yönelik ışık tutmaktadır. Çevre dostu malzemelerle geliştirilen jel elektrolit ve elektrot malzemeler, üstün elektrokimyasal performansları ve biyouyumluluklarıyla katı hal süper kapasitörlerinin üretiminde alternatif bir malzeme olarak, sürdürülebilir yeni nesil biyomedikal cihazların geliştirilmesine katkıda bulunabilir.

Anahtar Kelimeler: Katı hal süper kapasitörleri, Biyouyumluluk, Poli(vinil alkol), Kitosan, Grapehen Oksit.

ACKNOWLEGMENT

CONTENTS

IMAGES

SCHEMATICS

TABLES

ICONS AND ABBREVATIONS

Icons

C   Capacitance ($F\ g^{-1}$, $F\ cm^{-3}$, $F\ cm^{-2}$)

Q   Charge

V   Voltage (V)

A   Surface area

ε_0 Dielectric constant of the vacuum

ε_r Material dielectric constant

E   Energy density ($Wh\ kg^{-1}$)

P   Power density ($W\ kg^{-1}$)

ESR   Equivalent resistance of the circuit (ohm)

χ Crystallinity degree

n   Integer of reflection order

λ Wavelength (nm)

d   Spacing of the crystal layers (nm/ Å)

Θ Incident angle

β   Full-width at half maximum (FWHM)

L   Crystallite size

K   Shape factor

V_0 Voltage amplitude (V)

I_0 Current amplitude (A)

φ   Phase angle

ω   Angular frequency

Z   Impedance (ohm)

σ   Ionic conductivity (mS cm^{-1})

t   Thickness

ρ   Specific electrical resistivity

R   Resistance (ohm)

R_s Ionic resistance of electrolyte (ohm)

R_{ct} Charge transfer resistance (ohm)

ν   Scan rate (mV s^{-1})

m   Mass (g)

M_w Molecular weight (g mol^{-1})

μ   Carrier mobility

n   Charge carrier concentration

E' Storage modulus

E'' Loss modulus

$\tan\delta$ Damping factor

L   Crystallite size

χ^2 Chi-square statistic

Abbreviations

AC   Activated carbon

AFM   Atomic force microscopy

BET   Brunauer-Emmet-Teller

CS   Chitosan

CV   Cyclic voltammetry

CNTs   Carbon nanotubes

DSC   Differential scanning calorimetry

DMA   Dynamic Mechanical Analysis

EDAX   Energy dispersive X-ray analysis

EDLC	Electric double layer capacitor
EIS	Electrochemical impedance spectroscopy
FTIR	Fourier-transform infrared spectroscopy
FE-SEM	Field emission scanning electron microscopy
GCD	Galvanostatic charge- discharge
GO	Graphene Oxide
GPEs	Gel polymer electrolytes
T_g	Glass transition temperature
IMDs	Implantable medical devices
MWCNTs	Multi-wall carbon nanotubes
T_m	Melting temperature
PVA	Poly(vinyl alcohol)
PVDF	Poly(vinylidene fluoride)
PAN	Poly(acrylonitrile)
PMMA	Poly(methyl methacrylate)
PEO	Poly(ethylene oxide)
KCl	Potassium chloride

PVAc   Poly(vinyl acetate)

PANI   Poly aniline

POM   Polarized optical microscopy

RGO   Reduced graphene oxide

SWCNTs   Single-wall carbon nanotubes

SEM   Scanning electron microscope

TEM   Transmission electron microscopy

2D   Two-dimensional

3D   Three-dimensional

UV-Vis   Ultraviolet visible spectroscopy

XRD   X-ray diffraction analysis

XPS   X-ray photoelectron spectroscopy

1. TÜRKÇE ÖZET

Günümüzde üstün enerji yoğunluğu, kısa şarj süresi ve uzun devre ömrüne sahip katı hal süperkapasitörlerin yeni nesil elektronik cihazlardaki uygulamaları, esnek ve giyilebilir elektronik ekipman ve ekranlar gibi alanlarda büyük ilgi görmektedir [1]. Üstün özellikli bu enerji depolama ekipmanları sayesinde, biyomedikal implantlar ya da esnek elektronikler gibi yeni nesil cihazların hazırlanmasında ihtiyaç duyulan tüm nano ve makro ölçekli hiyerarşik hibrit mimarilerin hassaslıkla tasarlanması, mühendisliği ve üretilmesi mümkün olabilmektedir [2]. Esnek ve üstün performanslı ekranlar ve taşınabilir elektroniklerin ihtiyaç duyduğu, yüksek performans, kısa yükleme süreleri, hafiflik ve ultra ince tasarımlara ek olarak biyouyumluluk, çevresel uyumluluk ve esneklik gibi ihtiyaçlar, geleneksel pil teknolojileri ile karşılanamaz [3]. Esnek tüm katı hal elektrokimyasal süperkapasitörler, geleneksel pillere kıyasla, bu gereksinimleri daha fazla güç yoğunlukları, tasarım alternatiflerinin zenginliği, saniyeler içinde hızlı şarj-deşarj edilebilirlikleri ve uzun ömürleri ile karşılayabildiklerinden, hem akademik camiada hem de endüstride büyük ilgi görmektedir [5 ,4].

Giderek artan sayıda yaşlı insan ya da kronik hastalıkları olan hastalar, sağlık durumlarının an ve an izlenmesi için, yeni nesil esnek, implante edilebilir, biyouyumlu cihazlara ihtiyaç duymaktadır. Her ne kadar pek çok kişi halihazırda kalp pili gibi vücuda yerleştirilebilir tıbbi cihazları (Implantable Medical Devices - IMD'ler) kullanıyor olsa da, bunların ya harici bir kaynaktan ya da dahili bir bataryadan güç alması gerekmektedir [6, 7]. Esnek elektroniklerin hızlı gelişimi bilhassa biyomedikal alanda, termal, mekanik veya elektrofizyolojik bilgileri içeren çeşitli biyolojik sinyallerin izlenmesini mümkün kılarak, teknolojik ve bilimsel gelişime öncülük etmektedir [8, 9]. Vücuda yerleştirilebilir esnek ve biyouyumlu elektronik cihazlar, biyolojik vücut içindeki sağlık koşullarını an ve an izlemek ve gerekli durumlarda bilgi akışını sağlamak için etkin bir strateji sağlar. Böylece, hastaların anlık sağlık durumlarının monitörizasyonu, rutin izleme süreçlerinin devamlılığı ve gerekli durumlarda acil müdahaleler etkin bir şekilde yürütülebilir [10, 11].

Bu amaca yönelik kullanılacak elektronik cihazların güç sistemlerinin esnek ve üstün performanslı olmalarının yanı sıra, biyouyumlu ve implante edilebilir olması da kritik önem taşımaktadır. Ne yazık ki geleneksel enerji kaynakları, pil paketlerinin korozyonu ve sızıntısı nedeniyle immünolojik red, inflamatuar reaksiyonlar ve ikincil biyolojik toksisite gibi biyouyumluluk sorunlarına neden olabilmektedir. Bu sorunlar bazen kullanıcının hayatını tehdit edecek boyutlara ulaşabilir [9, 11]. Ayrıca, mevcut enerji depolama cihazlarının her 6-10 yılda bir ameliyat yoluyla değiştirilmesi gerekir ve bu da kullanıcı için ek risk oluşturur. Bu nedenle, IMD'leri çalıştırmak için kullanılan mevcut implante edilebilir enerji depolama cihazları, sağlık otoritelerinin gerektirdiği katı standartları, bilhassa boyut ve biyouyumluluk açısından, karşılamakta ciddi engellere sahiptir. Bu nedenle, biyomedikal alanda alternatif enerji depolama cihazlarına ihtiyaç duyulmaktadır. Bu enerji depolama cihazları, sadece biyomedikal alanda değil, esnek tüm elektroniklerde yüksek kullanım potansiyeli sergiler [10, 12].

Süper kapasitörler, yüksek güç yoğunlukları, uzun çevrim ömürleri ve saniyeler içinde hızlı şarj-deşarj olabilmeleri sayesinde, implante edilebilir elektronik cihazlara güç sağlamak için umut verici adaylar olarak önerilmektedirler [13, 14]. Bununla birlikte, süper kapasitörlerin karşılaştığı temel engel, yüksek enerji yoğunluğunun gerekli olduğu uygulamalarda bir sorun olarak karşımıza çıkan düşük düzeydeki enerji yoğunluklarıdır. Bu sorunu çözmek için, süper kapasitörlerin enerji yoğunluğunun arttırılmasına yönelik yoğun araştırma mevcuttur [15, 16]. Bahsedilmesi gereken bir diğer bir zorluk, geleneksel süper kapasitörlerin imalatında sıvı elektrolitlerin kullanılmasıdır [17]. Sıvı elektrolitler genellikle toksik ve aşındırıcıdır. Bu nedenle imalat sürecine önemli bir paketleme maliyeti getirir. Daha önemlisi, bu paketleme ihtiyacı tasarımsal engellere ve arzu edilen esneklik kriterinin karşılanamamasına sebep olur. Dolayısıyla sıvı elektrolitlerin kullanılmadığı tüm katı hal süper kapasitörler, bilhassa daha fazla biyouyumluluk, tasarım özgürlüğü ve esnekliğin istendiği uygulamlarda ön plana çıkmaktadır [14, 18].

Jel polimer elektrolitler (Gel Polymer Electrolytes-GPE'ler), esnek katı hal süper kapasitörlerin geliştirilmesinde polimer temelli benzersiz bir elektrolit türü olarak dikkat çekmektedir. Kolay uyarlanabilirlikleri, hafif yapıları, basit üretim süreçleri, güçlü yapışkan nitelikleri ve geniş elektrokimyasal potansiyel pencereleri nedeniyle, GPE'ler, akademik ve endüstriyel anlamda yoğun çalışılmaktadır [14, 19]. GPE'ler arasında fiziksel jeller,

ayarlanabilir kristallenme oranları ve fiziksel etkileşimler (hidrojen bağları ya da iyonik bağlar gibi) sayesinde kontrol edilebilir mekanik özellikler sergilemeleri, küçük moleküllerin (tuz gibi) yapılarına özyerleşim (self-assembly) yoluyla entegre edilebilir olması, basit üretim teknikleri ve kimyasal çapraz bağlayıcılar gerektirmemeleri gibi nedenlerle avantajlıdırlar. Bu jel malzemeler ayrıca, sıcaklık, pH veya çözücü bileşimindeki değişiklikler gibi çevresel koşullara bağlı olarak, polimer zincirleri arasındaki geçici etkileşimlerle, tersinir özellikler de sergileyebilir [15]. Poli(vinil alkol) (PVA), poli(viniliden florür) (PVDF), poli(akrilonitril) (PAN), poli(metil metakrilat) (PMMA) ve poli(etilen oksit) (PEO) gibi bir dizi polimer, yüksek performanslı GPE'lerde potansiyel kullanımları açısından kapsamlı bir şekilde araştırılmıştır [14, 20].

GPE yapısında kullanılacak polimelerin genel olarak, hızlı segmental hareketliliğe, tuz iyonları ile yüksek etkileşim kapasitesine, düşük camsı geçiş sıcaklığına (glass transition temperature-T_g) ve iyi elektrokimyasal ve termal kararlılığa sahip olması beklenir. Ancak yukarıda bahsi geçen polimerlerin her biri, gerçek uygulamalarda kullanımlarını sınırlayan belirli dezavantajlara sahiptir [14, 21]. Örneğin, PEO bazlı jel elektrolitler, polimerin yüksek kristalliği ve polimer zincirlerinin kısıtlı hareketinin bir sonucu olarak sınırlı iyonik iletkenlik sergiler. Benzer şekilde, PMMA bazlı jel elektrolitler iyi elektrokimyasal stabilite göstermelerine rağmen, düşük iyonik iletkenlik gösterir. PAN ve PVDF matrisleri homojen jel film oluşumunu kolaylaştırırken, iyonik taşıma mekanizmalarında kullanımlarını sınırlayan parametrelere sahiptir. PVDF yüksek bir dielektrik sabiti sergilemesine rağmen, iyonik iletkenliği, kristal doğası ve ortalamanın altındaki arayüzey kimyasal kararlılığı nedeniyle sınırlıdır [14, 22-24]. Bu polimerler arasında, PVA, biyolojik olarak parçalanabilirliği, biyouyumluluğu, düşük maliyeti ve toksik olmaması gibi nedenlere bağlı olarak, GPE üretiminde öne çıkan adaylardan biri olarak gösterilmektedir [14, 25]. Bununla birlikte, PVA bazlı mevcut katı hal elektrolitlerinin hem mekanik özelliklerinin, hem de elektrokimyasal performanslarının daha da geliştirilmesine ihtiyaç vardır. Bu tür yeni katı hal elektrolitleri, mekanik dayanıklılık, mükemmel iyonik iletkenlik, minimum arayüzey direnci ve gelişmiş iyon aktarım verimliliği dahil olmak üzere pek çok gereksinimi aynı anda karşılamalıdır [26, 27].

Esneklik, üstün performans ve biyouyumluluk gibi kriterleri eşzamanlı karşılayacak süper kapasitör teknolojileri, yukarıdaki polimerler ya da başkalarına dayanan üstün elektrolit

malzemelerin yanı sıra, yüksek performanslı elektrot malzemelere de ihtiyaç duymaktadır [13, 15]. İhtiyaç duyulan tüm gereksinimleri tek bir pakette karşılayan tek bir elektrot malzeme mevcut değildir. Süperkapasitörlerin tasarımında kullanılan elektrot malzemeler arasında grafen içerikli kompozitlerin önemli bir konumu vardır [14]. Grafen, tek bir atom kalınlığındaki karbon tabakalardan oluşan yapısıyla benzersiz özellikler sergiler. Grafen içeren elektrotlar, yüksek yüzey alanına, mükemmel elektriksel iletkenliğe ve mekanik dayanıklılığa sahiptir. Bu özellikler, süper kapasitörlerin enerji depolama kapasitesini artırmak için idealdir. Ayrıca grafen içerikli elektrotlar, düşük iç dirençleri sayesinde hızlı şarj-deşarj özellikleri sunar, bu da süper kapasitörlerin verimliliğini artırır. Ayrıca, grafenin esnekliği, özellikle giyilebilir teknolojiler ve esnek elektronik cihaz uygulamaları gibi alanlarda kullanıma uyumludur [28, 29]. Grafen içerikli elektrotlar, enerji depolama teknolojilerindeki gelişmelerde önemli bir rol oynamakta olup, yüksek performans, dayanıklılık ve esneklik gibi avantajlarıyla süper kapasitör teknolojilerinin ilerlemesine katkıda bulunmaktadır [30]. Grafen bazlı polimerik kompozitlerin, diğer nanokarbon yapılarını içeren alternatif kompozitlere kıyasla, mekanik mukavemet ve elektriksel özelliklerde belirgin bir iyileşme sağladığı gösterilmiştir [31]. Kısacası grafen, yüksek spesifik yüzey alanı (2630 m^2 g^{-1}), yüksek iletkenlik, mekanik esneklik ve kimyasal kararlılık gibi özelliklerine bağlı olarak süper kapasitör imalatında geniş bir uygulama alanı bulmuştur [16, 32].

Yukarıda sayılan avantajlarına rağmen, nano ölçekli etkileşimler nedeniyle grafen nano tabakalarının istiflenmeye yönelik doğal eğilimleri, yüzey alanının azalmasına yol açarak süper kapasitörlerin performansını sınırlayabilir [33]. Bir grafen türevi olan grafen oksit (graphene oxide-GO), yüzeyinde ve kenarlarında epoksi, hidroksil ve karboksil gibi oksijen içerikli fonksiyonel gruplar içeren önemli miktarda spesifik yüzey alanına sahip, hidrofilikliği grafene kıyasla yüksek bir nanomalzemedir [34, 35]. Bu, özellikle hidrofilik malzemelerle birlikte kullanımda, GO'yu süper kapasitörlerde uygun bir elektrot ve elektrolit malzeme haline getirir [36]. Grafenin performansının arttırılması amacıyla, grafen tabakaları içerisine aralayıcı olarak ek malzemelerin kullanımı araştırılmıştır. Polimerler gibi aralayıcılar, grafen tabakaları arasındaki van der Waals kuvvetlerini azaltmaya, istiflemeyi-agregasyonu engellemeye, iyon difüzyonunu kolaylaştırmaya ve difüzyon direncini azaltmaya yardımcı olur [1, 37].

4

Kitin polimerinin N-deasetillenmiş bir türevi olan kitosan, deasetillenmiş ünite olan β-(1-4)-bağlı D-glukozamin ve asetillenmiş ünite olan N-asetil-D-glukozaminin doğrusal olarak bir arada olduğu doğal bir polisakarittir [38, 39]. Kitosan yapısındaki bu gruplar toksik değildirler ve yüksek su tutma ve mükemmel iyon adsorpsiyon kapasitesi taşımaya sebep olurlar. Buna bağlı olarak, ktison mükemmel bir elektrot malzemesi olmaya adaydır [40, 41]. Bununla birlikte kitosan, amorf nano-gözenekli yapısı ve sp^3 hibrid karbon-karbon bağlarının varlığına atfedilen düşük bir iletkenlik ve optimal olmayan bir enerji yoğunluğu sergiler. Bu kısıtlamalar, kitosan ve grafen içerikli kompozit malzemelerin hazırlanması ile potansiyel bir çözüme kavuşabilir [42, 43].

Bu tez çalışmasında, hidrofilik ve biyouyumlu bir polimer olan poli(vinil alkol) (poly(vinyl alcohol)-PVA) matris, potasyum klorür (potassium chloride-KCl) ise iyon sağlayıcı olarak kullanılmıştır. Çalışmamızın ilk kısmı, iyonik iletkenlik, film oluşumu, mekanik-termal özellikler ve biyouyumluluk dahil olmak üzere bu jel elektrolitlerin temel özelliklerini optimize etmeye odaklanmaktadır.

KCl, vücut sıvılarında doğal olarak bulunan bir tuzdur ve fizyolojik sıvılarda önemli bir elektrolittir. Biyouyumlu bir tuz olarak jel elektrolit içinde KCl'nin kullanılması, elektrolitin fizyolojik uygunluğu için önemlidir. Ayrıca, KCl'nin en küçük hidrat-iyon boyutuna sahip olması, yüksek iyonik iletkenlik ve biyolojik süreçlere minimum müdahale sağlar. Suda yüksek oranda çözünür bir tuz olan KCl, PVA ile yüksek stabiliteye sahip homojen bir jel oluşturabilmektedir. KCl gıda ve farmasötik ürünlerde kullanım için güvenli bir malzeme olarak kabul edilmektedir [27, 44]. Bir elektrolitin iyonik iletkenliği, yük taşıyıcı konsantrasyonuna ve hareketliliğine bağlı olduğundan, bu tezde ilk kez farklı PVA molekül ağırlıkları ve farklı PVA/tuz ağırlık oranlarının jelin iyonik iletkenliğine ve termal-mekanik özelliklerine etkisi sistematik olarak incelenmiştir.

KCl tuzunun eklenmesi, polimer zincirleri arasındaki bağları moleküler düzeyde zayıflatır. Bunun nedeni, polimer zincirleri arasındaki hidrojen bağını bozan KCl'nin iyonik doğasından kaynaklanmaktadır. Bu bağlar zayıfladıkça polimer zincirleri arasındaki serbest hacim artar ve bu da polimer zincirlerinde daha fazla esnekliğe neden olur [45]. KCl, PVA yapısındaki amorf içeriği arttırırken, kristalliği azaltır. Bunun nedeni, tuzun kristal bölgelerin düzenli yapısını bozarak onları daha düzensiz, amorf bölgelere dönüştürmesidir.

Amorf içerikteki artış ve kristallikteki azalma, elektrolitin esnekliğinin ve iyonik iletkenliğinin genel olarak artmasına katkıda bulunur [46, 47].

Jel elektrolitlerin iyonik iletkenliğini incelemek için elektrokimyasal empedans spektroskopisi (Electrochemical Impedance Spectroscopy-EIS) kullanılır. GPE'nin iyonik iletkenliği aşağıdaki denklem temel alınarak değerlendirilir [48, 49]:

$$\sigma = t/RA \tag{1}$$

Burada, "t" filmin 400-500 μm arasındaki kalınlığıdır, "R" ohm cinsinden elektrolitin ohmik direncidir ve "A" ise test sırasında elektrolit filmin paslanmaz çelik elektrotlarla temas yüzey alanıdır (cm^2).

Jel elektrolitin iyonik iletkenliği, yük taşıyıcı konsantrasyonuna (n) ve taşıyıcı hareketliliğine (μ) de bağlıdır [50]. Sabit bir PVA/KCl ağırlık oranında, PVA molekül ağırlığının arttırılmasıyla, jel elektrolitin yığın direnci ve polimer zincirleri arasındaki fiziksel etkileşim artar. Polimerin molekül ağırlığı arttıkça, polimer omurgasının en hareketli bölgeleri olan zincir uçlarının bağıl miktarı ve polimer zincirleri arasındaki serbest hacim azalır, dolayısıyla zincir hareketleri kısıtlanır, bu da yüksek viskoziteye, düşük iyonik hareket ve dolayısıyla daha düşük iyonik iletkenliye neden olur [51]. Düşük molekül ağırlığı durumunda, iyon hareketliliğini artıran daha fazla segmental hareket mevcuttur [48]. Bununla birlikte düşük molekül ağırlığı, mekanik özelliklerde azalışa neden olduğundan, dayanım ve iyon taşıma kapasitesi arasındaki hassas dengenin optimize edilmesi gereklidir. Yüksek molekül ağırlığı mekanik dayanımı arttırırken, azalan zincir hareketliliklerine bağlı olarak iyonik iletkenliği azaltıcı bir etkiye sebep olsa da, öte taraftan su tutma kapasitesnin artmasına sebep olur. PVA'nın fiziksel çapraz bağlı jelleri, molekül ağırlığı arttıkça daha fazla zincir dolaşması içerir ki bu da yapıda daha fazla su molekülü tutunabilmesini sağlar. Artan miktarda su molekülü ise iyon sağlayıcı tuz miktarın artmasına, dolayısıyla da daha yüksek iyonik iletkenliğe yol açar [15]. Bu nedenle molekül ağırlığındaki değişimler, mekanik özellikler ve iyonik iletkenlikte olumlu ve olumsuz addedilebilecek bir dizi değişikliğe sebep olup, önemli bir parametre olarak öne çıkmaktadır. Bu tez çalışmasının ilk kısmında, farklı molekül kütlesine sahip PVA örnekleri ile hazırlanan, değişen oranlarda KCl içeren, fiziksel çapraz bağlı jel elektrolitlerin mekanik özellikleri ve iyonik iletkenlikleri

incelenmiş ve 195000 g mol^{-1} mol kütlesi ile PVA/KCl (w/w: 1/2) kütle kesri, en yüksek iyonik iletkenliğe (3.48 ±0.25 mS cm^{-1}) olanak tanıyan optimum jel elektroliti bileşimi olarak tespit edilmiştir. Tez çalışmamızın ilerleyen kısımlarında bu bileşimdeki örnekler, katı hal süperkapasitör üretimi için optimum jel elektrolit olarak seçilmiştir.

Optimum jel elektrolit filmin (Mw=195000 g mol^{-1}, PVA/KCl (w/w: 1/2)) belirlenmesinde, XRD, ATR-FTIR, UV-Vis, çekme testi ve dinamik mekanik analiz (DMA) yöntemlerinden yararlanılmıştır. Jel elektrolit, hem kristalin hem de amorf bölgeleri olan yarı kristalin bir yapıya sahiptir. Tezin 122 sayfası itibarı ile başlayan Sonuçlar ve Tartışma (Results and Discussions) kısmında detaylıca sunulan verilerden görülebileceği gibi, saf PVA'nın XRD modelinde iki farklı kırınım zirvesi dikkat çekmektedir. Bu tepe noktaları PVA'de yarı kristal bir yapının varlığını gösterir. (110) kırınım zirvesi, PVA yan gruplarındaki -OH gruplarının güçlü hidrojen bağlanmasına işaret eder [51]. XRD sonuçlarından, KCl ilavesi üzerine PVA kristalliğinin azaldığı, ancak PVA/KCl jel filminde kristalit boyutunun arttığı görülmüştür. Bu, bir plastikleştirici gibi davranan KCl'nin, polimer kırılganlığının azalmasına ve esnekliği ile işlenebilirliğin artmasına yol açan tipik faydalı etkileri ile ilişkilendirilebilir [47]. Kristalit boyutlarındaki değişiklikler aynı zamanda plastikleştiricilerin eklenmesiyle ortaya çıkan moleküler hareketlilikteki değişikliklere de atfedilebilir. KCl'nin varlığı serbest hacimdeki genişlemeye katkıda bulunarak kristal boyutunda hafif bir artışa sebep olmuştur [50]. KCl varlığında gözlenen yüzde kristallikteki azalma ve kristalit boyutundaki artış, PVA kristal yapısındaki düzensizliklerin ve dolayısıyla amorf karakterin artışı ile ilişkilidir. Amorf yapıda artan polimer zinciri segmental hareketleri iyon hareketini destekler ve yüksek iyonik iletkenlik seviyelerine ulaşmaya pozitif katkıda bulunur. Elde edilen XRD sonuçları, önceki literatür bilgisi ile uyumludur [52, 53].

XRD ile gözlemlenen etkiler, UV-Vis sonuçlarıyla da desteklenmiştir. Saf PVA çözeltisinde, görünür bölgede bir omuzun eşlik ettiği, UV bölgesinde belirgin bir absorpsiyon zirvesi gözlemlenir. Bu zirveler, -(CH=CH)$_2$CO- gruplarındaki etilen (C=C) ile bağlı karbonil (C=O) gruplarının n→π* ve π→π* hidroksil geçişlerine karşılık gelir [51]. Bu tür geçişler, paylaşılmayan elektron çiftlerinin π* yörüngesine hareket etmesiyle, elektronların temel durumdan daha yüksek enerji durumlarına uyarılmasını içerir. PVA/KCl jel elektrolit çözeltisinde, 194 nm'deki absorpsiyon zirvesinde düşük dalga boylarına doğru bir kayma meydana gelir [53]. Bu kayma, muhtemelen K$^+$/Cl$^-$ iyonları ile PVA içindeki polar

gruplar arasındaki etkileşimlere bağlı olarak, PVA zincirleri arasındaki hidrojen bağlarında bir azalma olduğunu göstermektedir. Bu gözlemler literatür verileri ve FTIR analizinden elde edilen bulgularla da doğrulanan, PVA ve KCl arasında bir kompleks oluşumuna işaret etmektedir [54].

Saf PVA filmin ATR-FTIR spektrumunda görülen tepe noktaları, yapıda bulunan karakteristik O–H gerilme, C–H gerilme, C=O gerilme, C–H salınım ve C–O gerilme piklerine atanır [54]. Kuru PVA/KCl jel filminde, bu tepe noktaları hafif kaymalara uğrar ve bu da polimer ile tuz arasındaki potansiyel etkileşimleri gösterir. Özellikle, -OH ve -CO gruplarının esneme titreşimleri, saf PVA'ya kıyasla tepe yoğunluğunda bir azalma ve kırmızıya kayma ile önemli değişiklikler sergilemiştir. Bu değişiklikler, KCl ile PVA'daki polar gruplar (-OH ve –CO) arasında komplekslerin veya etkileşimlerin oluşumunu kuvvetle önerir [51]. Uygun elektrostatik çekimler ve sulu bir ortamda PVA içindeki oksijen atomları ile KCl iyonları arasındaki koordinasyon, potansiyel olarak bir iyonik atlama mekanizmasını harekete geçirebilir ve böylece iyonik iletkenliği artırabilir [55]. Amorf faz içindeki polimer zincirlerinin artan segmental hareketliliği iyon hareketliliğini arttırır, böylece daha yüksek iyonik iletkenliği destekler. Sonuç olarak KCl'nin jel yapısındaki varlığı, jel içindeki iyonik iletkenliği büyük ölçüde artırarak iyonların hareketini kolaylaştırır [56].

Polimer jeller, sıvılar ve katılar arasında çeşitli özelliklere sahip, çok yönlü bir malzeme grubudur. Hazırlanan kuru jel filmlerin viskoelastik özelliklerini değerlendirmek için Dinamik Mekanik Analiz (Dynamic Mechanical Analysis-DMA) kullanılmıştır [57, 58]. Viskoelastik bir polimer, elastik ve viskoz bileşenlerin bir kombinasyonu olarak tanımlanabilir [59, 60]. DMA sonucu, az miktarda KCl tuzun eklenmesinin (M_w=195000 g mol^{-1}, PVA/KCl (w/w: 1/0.1)) saf PVA filme kıyasla, elastiklik veya depolama modülünde (E') bir artışa yol açtığını gösterdi. Bu sonuç, fiziksel çapraz bağlı PVA/KCl jelin, yüksek deformasyon direncine sahip olduğunu, ve jel yapısının mekanik mukavemetinde bir iyileşme gerçekleştiğini gösterir [57]. Ancak, KCl miktarı PVA'ya göre daha da arttığında (PVA/KCl (w/w: 1/0.5, 1/1, 1/2)), polimer zincirleri arasındaki etkişimler bozulabilir ve fiziksel çapraz bağlı yapının mukavemeti azalbilir. Bu, jelin daha yumuşak hale gelmesi nedeniyle E' değerinde bir azalmaya yol açabilir [59]. Yüksek KCl oranlarında, T_g azaltır ve tanδ (Damping factor) zirvesinde daha düşük sıcaklığa bir kaymaya tespit edilir. Çünkü yapıda bulunan yüksek miktardaki KCl, plastikleştirici görevi görerek polimer zincir

8

etkileşimlerini bozar ve zincir hareketliliğini arttırır. K^+ ve Cl^- iyonlarının varlığı, polimer zincirleri arasındaki hidrojen bağlarını azaltır, zincir hareketliliğini kolaylaştırır, bu da mekanik meukavemette azalışa neden olur. Düşük T_g, jelin daha esnek hale geldiğini, polimer segmentlerinin artan hareketlilik sergilediğini gösterir ve bu sonuçlar başka benzer çalışmalarda da görünmüştür [57, 60-63]. KCl'nin yüksek miktarda oluşu mekanik mukavemette bir azalışa sebep oluyorsa da, öte yandan iyonik iletkenlik üzerindeki olumlu etkisi ve esnekliği arttırması dikkate alındığında, miktarının optimize edilmesindeki önem anlaşılacaktır.

Kuru haldeki saf PVA ve PVA/KCl jel filmlerin mekanik özellikleri de tez kapsamında incelenmiştir. PVA, kristal katmanlar içeren yarı kristalin bir polimerdir. Saf PVA filmin, PVA/KCl (w/w: 1/2) oranındaki jel film numunesine (15.88±0.25 MPa) kıyasla daha yüksek gerilme mukavemetine (68.5±5.35 MPa) sahip olduğu tespit edilmiştir. Jel filmin PVA'ya kıyasla sergilediği daha düşük Young modülü ve elastik mukavemeti, daha esnek ve deforme edilebilir bir yapıya sahip olduğuna işaret etmektedir [48, 49]. KCl tuzu plastikleştirici görevi görür ve polimer zincirleri arasındaki bağları moleküler düzeyde zayıflatır. Ayrıca, PVA zincirleri arasındaki serbest hacim veya zincirler arası boşlukları artırılarak polimer zincirlerinin daha esnek hale gelmesine yardımcı olur [45, 64]. Mekanik analiz neticesinde de KCl tuzunun, önceki karakterizasyon testlerinin sonuçlarıyla tutarlı olarak PVA'nın amorf içeriğini arttırdığı ve kristalinitesini azalttığı sonucuna ulaşılmıştır. PVA/KCl jel film numunesinin saf PVA'ya kıyasla sergilediği daha yüksek esneklik, gerilebilir esnek katı hal süper kapasitör uygulamalarında bir avantaj olabilir [65, 66].

Saf PVA ve PVA/KCl içeren kuru jel filmin yüzey morfolojisi ve mikro yapısı, alan emisyon taramalı elektron mikroskobu (Field Emission-Scanning Electron Microscopy-FE-SEM) ile incelendi. Saf PVA görüntüsü, minimum düzeyde pürüzlülük sergileyen düzgün bir yüzey sergiledi [67-69]. Kuru haldeki PVA/KCl numunesinin yüzeyi ise, PVA matrisi içinde dağılmış potasyum klorür parçacıklarının varlığını düşündüren dokulu bir görünüm sergiledi [70, 71]. KCl'nin PVA matrisi ile birleştirilmesi üzerine, hidrojen bağlarının azalması ve PVA ve KCl iyon-dipol etkileşimlerinin oluşması sonucunda filmin yüzeyi nispeten pürüzlü hale gelmiştir. KCl içeren jellerin kurutulması ile alınan SEM görüntülerinde, yüksek KCl miktarında (PVA/KCl (w/w: 1/2)), PVA filmin yüzeyinde öbekleşen KCl parçacıklarının homojen bir dağılım sergilediği görüldü. Genel olarak, KCl parçacıklarının tüm hacim

boyunca homojen ve tekdüze dağılım sergilemesi, jel halinde iyi dağılmış PVA/KCl yapısının oluşumunu doğrular [45, 70]. PVA/KCl jel filminin EDAX ve haritalama sonuçları, PVA zincirlerinden kaynaklanan karbon (C), oksijen (O) ve KCl'nın varlığı nedeniyle tespit edilen potasyum (K) ve klor (Cl) elementlerini göstermiştir. Bu sonuç, hazırlanan numunenin yüksek saflıkta olduğunu ve beklenen yapıların varlığını doğrulamıştır [72].

Esnek jel elektrolitin döngüsel stabilitesi, 5000 döngü için 200 mVs^{-1}'de değerlendirildi. Spesifik kapasitans, 5000 döngüden sonra 5'ten yaklaşık 4.4 mF g^{-1}'e düşmüştür. Böylece 5000 döngüden sonra jel başlangıç kapasitansının %88'ini korur. Yapılan ölçümler neticesinde, molekül ağırlığı 195000 g mol^{-1} olan PVA ile hazırlanmış PVA/KCl (w/w: 1/2) jel elektrolitin, en yüksek iyonik iletkenliği ve daha iyi döngüsel stabiliteyi gösterdiği tespit edildi. Tez kapsamında hazırlanan jel elektrolitin iyonik iletkenliğinin, PVA/KCl'ye dayanan daha önce rapor edilmiş jel elektrolitlerinkinden [73-75] önemli ölçüde daha yüksek (3.48±0.25 mS cm^{-1}) olduğu tespit edildi. Bu yüksek iyonik iletkenlik, jeldeki yüksek tuz konsantrasyonuna ve su miktarına bağlanabilir. Numunelerin biyouyumluluklarına yönelik gerçekleştirdiğimiz çalışmada, 72 saatlik bir maruziyet sonrasında, hücrelerin %72.3'ünün etkilenmeden kaldığı tespit edildi. Bu, elektrolitin dikkate değer bir biyouyumluluk sergilediği anlamına gelmektedir.

Polimer bazlı katı elektrolit geliştirmeye yönelik yaptığımız çalışmalar sonrasında, tez kapsamındaki odağımız esnek ve yüksek performanslı elektrot geliştirmeye yönlendirilmiştir. Yüksek enerji yoğunluğuna sahip katı hal süper kapasitör yapılarında karbon bazlı malzemeler, yüksek elektrik iletkenliğine ve mükemmel mekanik stabiliteye sahip olduklarından en iyi seçimdir [1, 13]. Grafen, yüksek spesifik yüzey alanı, yüksek iletkenlik, mekanik esneklik ve kimyasal stabilite gibi seçkin özelliklerinden yararlanarak süper kapasitör malzemeler olarak geniş bir uygulama alanı bulmuştur. Bununla birlikte, grafen nanotabakaları, nano ölçekli etkileşimler nedeniyle yeniden istiflenme eğilimindedir, bu da yüzey alanının azalmasına yol açabilir, dolayısıyla süper kapasitörlerin performansını sınırlayabilir [76, 77]. Bir grafen türevi olan grafen oksit (GO), yüzeyinde ve kenarlarında oksijen fonksiyonel grupları (epoksi, hidroksil, karbonil ve karboksil) içeren, önemli düzeyde spesifik yüzey alanına sahip bir nanomalzemedir [78, 79]. Kitin polimerinin bir türevi olan kitosan, yüksek su tutma kapasitesine sahiptir, toksik değildir ve mükemmel iyon

adsorpsiyon yeterliliği sergiler. Bu özellikleri kitosanı, elektrot malzemesi olarak umut verici bir aday haline getirir [80].

Tez kapsamında fiber ve film halinde iki farklı elektrot malzeme geliştirilip, süper kapasitör uygulamalarındaki performansları araştırılmıştır. Fiber halindeki ve film yapısındaki GO/CS bazlı kompozit fiberlerin katı hal süper kapasitörler uygulamalarındaki performansları, bu elektrotların, optimum PVA/KCl jel elektroliti ile (M_w=195000 g mol^{-1}, PVA/KCl (w/w: 1/2)) birleştirilmelerini takiben, dönüşümlü voltametri (Cyclic Voltammetry-CV), elektrokimyasal empedans spektroskopisi (Electrochemical impedance spectroscopy-EIS) ve galvanostatik şarj/deşarj (Glavanostatic charge.discharge-GCD) testleri ile değerlendirilmiştir.

Fiber halinde, farklı ağırlık oranlarına sahip indirgenmiş grafen oksit (RGO) ve kitosan (CS) içeren RGO/CS kompozit malzemelerin dönüşümlü voltametri (CV) testleri sonucunda, RGO ile karşılaştırıldığında, RGO/CS fiber kompozitlerin daha geniş bir kapalı alan sergiledikleri tespit edildi. Bu durum, hem elektrik çift tabaka kapasitör (Electric double layer capacitor-EDLC) hem de psödokapasitif davranışın sinerjistik etkileşiminden ortaya çıkan oldukça yüksek spesifik kapasitansa işaret etmektedir [3, 5]. Çalışılan kompozit bileşimleri arasında RGO/CS (w/w: 90/10) en büyük CV alanını sergiledi. Bu malzemenin, en yüksek spesifik kapasitansa (5 mV s^{-1}'de 523.06±53.57 Fg^{-1}) sahip olduğu görüldü. Optimumun altındaki kitosan seviyelerinde, RGO tabakaları arasındaki boşluk yetersiz hale geldiğinden, iyon değişimi ve elektriksel çift tabaka oluşumu için erişilebilir yüzey alanında azalma yaşanmış, bu da iletkenliği olumsuz yönde etkileyip daha düşük kapasitansa yol açmıştır [81, 82]. Kitosan miktarının arttırılmasıyla kapasitans artmış, böylece kitosanın optimum konsantrasyonda, RGO levhaları arasında bir aralayıcı görevi görerek tabakaların mesafesini etkili bir şekilde arttırdığı yorumuna ulaşılmıştır [83]. Bu mekansal düzenleme, yük depolama için mevcut etkili yüzey alanını genişleterek ve iyon değişimi için kanalları teşvik ederek kapasitansın artmasına katkıda bulunur. Kitosanın yapısında –NH$_2$ ve –OH gruplarının varlığı, elektrot-elektrolit arayüzündeki iyon geçirgen direncin en aza indirilmesine önemli ölçüde katkıda bulunur [84]. Ancak, kitosan içeriği %10'u aştığında, daha yüksek kitosan konsantrasyonlarında iletkenlikte azalma gözlenmiştir. Bunun nedeni literatürde, optimum polimer matrisi miktarının ötesinde spesifik yüzey alanında ve elektriksel iletkenlikte azalma ve etkin iyon taşıma ağının oluşamaması olarak rapor

edilmiştir [85-87]. Tez kapsamında fiber bazlı elektrotlar ile gerçekleştirilen elektrokimyasal analizler neticesinde tespit edilen kapasitans ve yük depolama kapasitesi değerleri istenen düzeye ulaşamamıştır. Düşük seviyedeki bu performans, tez kapsamında geliştirilmesi gereken bir husus olarak vurgulanmış ve fiber formunda arayüzey etkileşimlerindeki doğal sınırlamalara atfedilmiştir. Ayrıca, filmle kıyaslandığında, fiberin zayıf yapısal bütünlüğü ve mekanik stabilitesi, elektrokimyasal aktivitenin ve performansın düşük kalmasında etkili olmuş olabilir. Bu nedenle elektrot malzemesi geliştirmeye yönelik tez kapsamında gerçekleştirilen çalışmalar, tezin ilerleyen kısmında fiber yerine film halindeki RGO/CS kompozit malzemelere kaydırılmıştır.

Farklı ağırlık oranlarına sahip RGO/CS film kompozit yapıları için gerçekleştirilen CV analizleri sonucunda, w/w: 90/10 oranındaki RGO/CS kompozit elektrot içeren süper kapasitörün, en büyük CV alanını sergilediği görüldü. Bu numune, en yüksek spesifik kapasitans (5 mV s^{-1}'de 872.74±68.35 Fg^{-1}) değerini verdi. Bu kompozit kullanılarak geliştirilen süper kapasitörün galvanostatik şarj-deşarj (Galvanostatic Charge-discharge-GCD) testinin sonucu, deşarj eğrisinin neredeyse düz bir çizgi olduğu, süper kapasitörün hızlı ve kısa akım yanıt süreleri sergilediğini gösterdi. Bu sonuç, daha önceki benzer çalışmalar göz önüne alındığında, iyi bir elektrik çift katman (electric double layer-EDL) oluşumu ile ilişkilendirilebilir [37].

Fiber ve film bazlı katı hal süper kapasitörlerinin spesifik kapasitansı karşılaştırıldığında, filmin daha yüksek spesifik kapasitansa sahip olduğunu görülmüştür. Bu durum, film malzemenin yüzey alanı, gözenekliliği ve aktif bölgelerin erişilebilirliğindeki olumlu değişikliklere bağlanabilir. Filmler genellikle daha geniş bir yüzey alanı, elektrokimyasal reaksiyonlar için daha ulaşılabilir aktif bölgeler ve fiberlere kıyasla elektrolit iyonlarının elektrot yüzeyine daha iyi erişilebilirliğini sağlar ve bu da daha yüksek spesifik kapasitansa yol açar. Ek olarak film yapısı, elektrot içinde daha yüksek elektron ve iyon taşınması ve daha iyi gözenekli yapı sunarak elektrokimyasal performansın artmasına katkıda bulunabilir [88, 89].

Film formundaki kompozitlerin fiberlere kıyasla daha üstün elektrokimyasal performans sergilediği tespit edildiğinden, RGO/CS film numunelerin, elektrokimyasal empedans spektroskopisi (Electrochemical Impedance Spectroscopy-EIS) azalizleri, çevrim ömürleri

ve yapısal özellikleri de araştırıldı. RGO/CS (w/w: 90/10) numunesinin Nyquist grafiği, karşılık gelen eşdeğer devreyle birlikte elektrokimyasal empedans spektroskopisi verilerinin kapsamlı bir şekilde analiz edilmesine olanak sağladı. RGO/CS kompozit elektrotunun yük transfer direncinin (charge transfer resistance-R_{ct}) ve elektrolit iyonik direncinin (electrolyte resistance-R_s), RGO film elektroda kıyasla, çok daha düşük olduğu tespit edildi. Bunun nedeni sistemdeki yüksek iyonik iletkenlik ve hızlı elektron transferleridir. Tezin ilerleyen kısımlarında tartışılan sonuçlar, kitosan ve RGO arasındakietkileşimlerin, elektrolit iyonları için gelişmiş bir elektriksel iletkenlik veya kolayca erişilebilen iyon difüzyon yolları sağladığını düşündürmektedir. Bu gözlem başka çalışmalarca da desteklenmektedir [90, 91].

GO/CS film kompozitlerin yapısal özellikleri ATR-FTIR, UV-Vis, XRD, XPS, AFM, BET, POM (Polarized Optical Microscopy), TEM, FE-SEM, elektriksel iletkenlik ve çekme testleri ile de incelendi. Bu test sonuçları neticesinde, yapıların kimyasal, fiziksel, morfolojik ve mekanik özellikleri tezin ilerleyen kısımlarında detaylıca tartışıldığı gibi açıklandı. Özetle, GO/CS ve RGO/CS'nın FTIR spektrumları, GO ve kitosanın karakteristik piklerinin varlığını sergiledi. Ayrıca, piklerde ortaya çıkan kayma ve şiddet değişiklikleri bileşenler arasındaki hidrojen bağları gibi etkileşimlere atfedildi [48, 50].

UV-Vis test sonuçları, GO'nun kitosan yapısına eklenmesi ardından, GO ile ilişkili piklerin yüksek dalga boyuna doğru bir kayma sergilediğini ortaya koydu. Bu değişim, GO üzerindeki epoksi grupları ile kitosan üzerindeki amino grupları (NH_2) arasındaki etkileşime işaret eder [92]. Bu tür etkileşimler, GO/CS kompozitinin oluşumunda etkilidir. XRD sonuçlarında, kristal kafes düzlemleri arasındaki aralıkların (d), kitosan varlığında, saf RGO ve GO'ya kıyasla, değişimlere uğradığı tespit edilmiştir. Bu durum, kitosanın RGO ve GO katmanlarının istiflenmesinde ve düzenlenmesinde değişikliklere yol açabilecek etkileşimlere sebep olduğuna işaret eder. Ayroca, kitosana ek olarak RGO veya GO içeren kompozitlerin XRD desenleri, her iki bileşen materyalinin karakteristik özelliklerini yansıtmıştır. XPS ile gerçeklştirilen yüzey analizleri, karbon (C) ve oksijen (O) gibi elementelerin varlığının yanı sıra, malzemelerin kimyasal yapılarıyla uyumlu bir bileşimin varlığına işaret etmiştir [93, 94].

Ölçülen gerilim-gerinim eğrilerinden, GO, RGO, CS, GO/CS ve RGO/CS filmlerinin nihai gerilme mukavemeti, tokluğu ve Young modülü değerleri elde edilmiştir. GO'nun

indirgenmesiyle elde edilen RGO'nun, sünekliğinin, mukavemetinin ve tokluğunun geliştiği tespit edilmiştir ki bu, önceki literatür sonuçları ile uyumludur [95, 96]. GO ve RGO filmleri ile karşılaştırıldığında, GO/CS ve RGO/CS kompozitleri Young modülünde sırasıyla %46 ve %36'lık, çekme mukavemetinde ise sırasıyla %61 ve %64'lük bir artış sergilemiştir.

CS, RGO, ve RGO/CS malzemelerin spesifik yüzey alanlarının, toplam gözenek hacimlerinin ve gözenek çaplarının belirlenmesi amacıyla, Brunauer-Emmett-Teller (BET) analizi yapıldı. Brunei-Deming-Teller (BDDT) IUPAC sınıflandırmasına göre, RGO/CS nanokompozitinin adsorpsiyon-desorpsiyon izoterm grafiklerinin, mezogözenekli malzeme için histerezis döngüsünün spesifik akışıyla tip IV'ü takip etme eğiliminde olduğu gözlendi. Bu özellik, yapıda bulunan mezo ve makro gözenekleri ve rastgele gözenek dağılımını ifade etmektedir [97, 98]. RGO/CS nanokompozitinin BET özellikleri, RGO için gözlemlenen değerler ile uyumludur. Bu, yapıya kitosan ilavesinin yüksek yüzey alanını (13.672 $m^2\,g^{-1}$), adsorpsiyon kapasitesini ve gözenekli yapıyı önemli ölçüde değiştirmediğini göstermektedir. BET sonuçları, genel olarak benzer yapılar için literatürde daha önce sunulan verilerle uyumludur [99, 100].

GO'nun AFM görüntülerinde yüzeyde karakteristik morfolojik özellikler tespit edildi. GO/CS kompozit malzemede ise, literatürle uyumlu olarak, daha heterojen yüzey özellikleri dikkat çekti [97, 101]. GO tabakaları, sıvı bir ortamda sıralı yapılar halinde kendiliğinden bir araya gelme yeteneklerini ifade eden, sıvı kristal özellikler sergileyebilir. Polarize optik mikroskopisi (Polarized Optical Microscopy-POM), GO'nun organizasyonu ve davranışı hakkında bilgi sağlayarak polarize ışığın etkisi altındaki bu yapıların görselleştirilmesine ve analiz edilmesine yardımcı olur [102]. GO ve GO/CS (w/w: 90/10) dispersiyonunun polarize optik mikrografları incelendiğinde, GO'nun tipik liyotropik nematik LC'leri, GO tabakalarının sulu ortamdaki geniş Schlieren dokusu (Schlieren texture) tespit edildi. GO/CS kompozitlerinde LC dokularının oluşumu, oksijen ve amit fonksiyonel grupları arasındaki etkileşimler yoluyla, supramoleküler kendi kendine sıralanma neticesinde oluşan, katmanlı kitosan kümelerinin varlığını göstermektedir [103, 104].

GO, RGO, GO/CS ve RGO/CS'nin morfolojileri ve mikro yapıları TEM analizi ile incelendi. Oksitlenmiş pul pul dökülmüş GO tabakalarının varlığı, birkaç mikrometre boyutunda ve oldukça pürüzsüz yüzeye sahip tek katmanlar şeklinde TEM analizlerinde tespit edildi [105,

106]. Buna karşılık, RGO nano tabakalarının, oksijen içerikli fonksiyonel grupların yapıdan çıkarılması nedeniyle agregasyon eğiliminde oldukları görüldü [106, 107]. GO/CS'nin TEM görüntüleri, GO tabakalarının yüzeyinde kitosan varlığı nedeniyle ortaya çıkan, çok daha pürüzlü ve yüksek yoğunluklu bir yüzey sergilemiştir. Bu, GO tabakalarının kitosan ile etkileşerek, GO/CS kompozitini oluşturduğunu göstermektedir [93, 108]. İndirgenmeden sonra, RGO/CS yapısının artan miktarda pürüzlülük ve agregasyon sergilediği görülmüştür. Bu, indirgenmenin gerçekleştiğine işaret eden bir kanıttır [109, 110].

GO, RGO, CS, GO/CS, RGO/CS için alan emisyon taramalı elektron mikroskobu (FE-SEM) görüntüleri, GO tabakaları, pul pul dökülmüş nano tabakalara atfedilen dalgalı desenler şeklinde gösterdi [111, 112]. RGO görüntüsünde ise, rastgele toplanmış ince tabakalardan oluşan desenler izlendi. Görüntülerde, GO/CS filmi kendine özgü bir "sandviç" konfigürasyonu sergilerken, GO nano tabakalarının önemli bir kısmının tamamen pul pul döküldüğü ve kitosan matrisi içinde tek tip bir dağılım sergilediği tespit edildi. Kitosan matrisi, GO tabakaları çevreleyip kapsülleyerek üç boyutlu bir çerçeve oluşumuna yol açmıştır [9, 113]. RGO/CS kompozit görüntüleri ise, daha düzensiz, kırışık ve yüksek pürüzlü yapılar sergileyerek, kitosan içinde dağılmış grafen tabakalarının varlığına işaret etmiştir. RGO tabakaları, literatürle de uyumlu bir şekilde, buruşma veya katlanma ile karakterize edilen bir morfolojide, birbirine bağlı katmanlar veya pullar halinde görünmektedir [114, 115].

Elektriksel iletkenlik, EIS, testi neticesinde, RGO'nun (1.10×10^{-4} S cm^{-1}) GO'ya (6.89×10^{-5} S cm^{-1}) kıyasla daha yüksek elektrik iletkenliğine sahip olduğu görüldü. Bu durum, daha iyi tabakalar arası bağlantı ve daha yüksek yük taşıyıcı hareketliliğine işaret etmektedir [97]. Son olarak, RGO/CS kompoziti (2.62×10^{-3} S cm^{-1}), RGO ve CS'nin sinerjistik etkisinden dolayı RGO'dan daha yüksek elektrik iletkenliği gösterdi. RGO'nun iletken doğası, CS'nin yalıtkan doğasını tamamlar ve neticede genel iletkenliği iyileştirilmiş bir kompozit elde edilir [116, 117]. RGO ve CS'nin kombinasyonu muhtemelen kompozit içindeki grafen tabakalarının birbirine bağlanmasını geliştirir. Bu gelişmiş bağlantı, yük taşıyıcılarının daha yüksek elektrik iletkenliğine sebep olacak şekilde hareketini kolaylaştırır. Ayrıca, kitosanın RGO dahil edilmesi, daha istikrarlı ve iyi bağlanmış bir yapıya katkıda bulunarak elektriksel iletkenliği daha da geliştirebilir [118].

Tez kapsamında hazırlanan RGO/CS (w/w:90/10) filmin elektrot olarak kullanıldığı katı hal süper kapasitörün, 10,000 döngü ömrü testinin sonucunda, spesifik kapasitans değerlerinde 64.24'ten yaklaşık 56.09 Fg^{-1}'e hafif bir düşüş sergilediği tespit edildi. Etkileyici bir şekilde, bu kapsamlı döngü sayımından sonra bile elektrot, başlangıç kapasitansının %87.31'ini korumaktadır. Simetrik katı hal süper kapasitör, sırasıyla 234.97 Wh kg^{-1} ve 1499.98 kW kg^{-1} değerinde sahip mükemmel düzeyde enerji ve güç yoğunlukları sergiledi. RGO/CS kompozitin hücre canlılığının değerlendirilmesi neticesinde, 72 saatlik maruziyet sonrasında %76,4'lük bir canlılık oranı tespit edilmiştir. Kaydedilen bu hücre canlılığı, hücrelerin kayda değer bir kısmının RGO/CS elektroduna maruz kaldıktan sonra canlılıklarını koruduğunu gösterir. Bu değer ideal %100 canlılığın gerisinde kalsa da yine de önemli derecede biyouyumluluğa işaret eder.

Tez çalışmasının takip eden aşamasında, standart olarak uygulanan çelik alt tabaka yerine, esneklik kriterini karşılayan PET yüzeye dökülerek elde edilen filmlerle esnek tam katı hal süper kapasitörlerin hazırlanması ve bu yapıların elektrokimyasal performans çalışmaları gerçekleştirildi. Bu üretimde, PET üzerine dökülen RGO/CS (w/w: 90/10) filmi elektrot, PVA/KCl jeli (M$_w$=195000 g mol^{-1}, PVA/KCl (w/w:1/2)) ise elektrolit olarak kullanıldı. Üretilen esnek süper kapasitörün spesifik kapasitans değeri 5 mVs^{-1}'de 191.07±19.24 F g^{-1} (1 A g^{-1}'de 186.64±21.69 F g^{-1}) olarak bulundu. Bu değer paslanmaz çelik alt tabaka kullanılarak elde edilen değerden (5 mV s^{-1}'de 872.74±68.35 Fg^{-1}) oldukça düşüktür. Paslanmaz çelik, PET'e kıyasla çok daha iyi elektrik iletkenliği ve daha düşük direnç sağlayan iletken bir malzemedir [119]. Ayrıca, RGO/CS elektrotunun akım toplayıcıya yapışması çok önemlidir ve sert bir yüzey olan paslanmaz çelik, esnek olan ve daha az pürüzsüz bir yüzeye sahip olabilen PET ile karşılaştırıldığında elektrotun daha iyi ve homojen yapışmasını sağlayabilir [120]. Ayrıca paslanmaz çelik, elektrot için daha iyi mekanik stabilite ve destek sunarak şarj-deşarj döngüleri sırasında yapısal bütünlüğü korur, ancak PET daha esnek olduğundan performansı etkileyebilecek deformasyona veya yapısal değişikliklere maruz kalabilir. Bu nedenle, RGO/CS kompozit malzemenin paslanmaz çelik yüzeyde gerçekleştirlen ölçümleri daha iyi sonuç vermiştir. Ancak yine de PET ile elde edilen sonuçlar da oldukça umut verici düzeydedir. Mevcut tez çalışmasında esnek katı hal süper kapasitör üretimi amacıyla PET yüzeyinde gerçekleştirilen çalışma neticesinde, literatürde mevcut diğer ilgili araştırma çalışmalarına kıyasla daha yüksek bir spesifik kapasitans değeri elde edilmiştir [121-124].

Tez çalışmamızın son kısmında, hazırlanan elektrolit ve elektrot yapıların lazer 3D-baskı teknolojisinde kullanım potansiyelini irdelemek amacıyla, RGO/CS (w/w: 90/10) elektrodu ve PVA/KCl (M_w=195000 g mol^{-1}, PVA/KCl (w/w:1/2)) jel elektroliti, esnek bir katı hal süper kapasitör verecek şekilde, poliimid (PI) film üzerine basıldı. Interdigital RGO/CS elektrotları saç tarağı oluşumu sergiledi ve olağanüstü yapışma özellikleri ve dayanıklılık gösterdi. Ancak, PI yüzeyinde kalan desensiz RGO/CS film elektrot kısımlar, asetik asit, aseton, etanol ve 2-propanol gibi çözücüler denense de, yapıdan uzaklaştırılamadı. Bu durum, lazer 3D-baskı teknolojisinin tez kapsamında hazırlanan elektrot ve elektrolit malzemelere uyarlanmasında aşılması gereken bir zorluk olarak tespit edilip, tezin ilerleyen ksıımlarında tartışılmıştır.

Katı hal süper kapasitörlerde kullanılabilecek kararlı ve yüksek performanslı biyouyumlu elektrot ve jel polimer elektrolitlerin üretimine yönelik yürütülen tez çalışmasına dair elde edilen umut verici sonuçlar, tezin ilerleyen ksıımlarında detaylı bir şekilde sunulmaktadır. Çevre dostu malzemelerle geliştirilen esnek elektrot ve elektroilit malzemelerin, üst düzey fizikokimyasal ve elektrokimyasal performanslarına ek olarak sergiledikleri yüksek düzeydeki biyouyumluluklarının, yeni nesil katı hal süperkapasitörlerinin üretimine ve biyomedikal cihazlara entegrasyona yönelik sürdürülebilir bir yol sunduğu düşünülmektedir.

2. INTRODUCTION

The main objective of this PhD thesis is to develop a biocompatible and solid-state supercapacitor with high electrochemical performance for wearable and implantable biomedical devices. For this purpose, gel polymer electrolyte containing PVA/KCl and electrode materials based on Graphene oxide (GO) and chitosan (CS) were prepared.

Graphene contains a single layer of carbon atoms arranged in a hexagonal lattice. Pristine graphene sheets have a hydrophobic nature and tend to aggregate, which can impact their interactions with biological entities and this may lead to concerns about biocompatibility [125]. Graphene oxide, a derivative of graphene, often exhibits enhanced biocompatibility due to the introduction of oxygen-containing functional groups on its surface and edges. These groups improve water dispensability and interactions with biological molecules. In vivo studies have shown that graphene can accumulate in organs and raising potential toxicity [31, 33]. GO can be engineered to have a controllable surface charge which may affect its interactions with cell membranes and proteins. Surface functionalization of GO with biocompatible polymers or molecules can enhance water dispensability and reduce potential cytotoxic effects [34, 126]. Due to the fact that graphene is a hydrophobic material and the incompatibility of its interfacial interactions with a hydrophilic polymer such as chitosan, thus composite electrodes were first prepared with GO, which has less aggregation in the hydrophilic environment and is more compatible with chitosan.

When GO combined with chitosan, chitosan contributes its inherent biocompatible properties to the composite. Both of them have hydrophilic characteristics that facilitates better dispersion in biological fluids, promoting interactions with cells [127]. The functional groups present on the surface of GO, and chitosan's amino and hydroxyl groups create multiple sites for potential interactions with biological molecules and can enhance the overall biocompatibility and dispensability of GO [91]. Thus, GO found in the structure of these electrodes was then thermally reduced to RGO to obtain a graphene structure with superior electrochemical properties.

The solid-state supercapacitor design in this thesis includes PVA/KCl as the gel electrolyte and chitosan/reduced graphene as the electrode structure which was first prepared in the form of fibers. However, when the supercapacitors obtained in fiber form did not exhibit the desired level of electrochemical performance, fiber design was abandoned and the preparation of film-shaped supercapacitors was attempted. Moreover, a flexible solid-state supercapacitor based on PET as a flexible current collector was also developed. In the final part of this PhD thesis work, RGO/CS (w/w: 90/10) electrode and PVA/KCl (Mw=195000 g mol^{-1}, PVA/KCl (w/w:1/2)) gel electrolyte were printed onto a polyimide (PI) film to provide a flexible solid-state supercapacitor, aiming to examine the potential use of prepared electrolyte and electrode structures in laser 3D-printing technology. Interdigital RGO/CS electrodes exhibited comb-like formations and demonstrated exceptional adhesion properties and durability. However, the desensitized RGO/CS film electrode portions remaining on the PI surface could not be removed despite testing with solvents such as acetic acid, acetone, ethanol, and 2-propanol. This situation was identified as a challenge to be overcome in adapting laser 3D-printing technology to the electrode and electrolyte materials prepared within the scope of the thesis, and it is discussed in the subsequent sections of the thesis.

Electrolyte is one of the key component of a supercapacitor which affects the overall electrochemical performance. Therefore, the electrochemical performance of gel polymer electrolytes (GPEs) were first examined by electrochemical impedance spectroscopy (EIS) and Cyclic voltammetry (CV) tests. The ionic conductivity was evaluated for each molecular weight (M_w) of PVA and different PVA/KCl weight ratios. At a constant weight ratio of PVA/KCl, by increasing the PVA molecular weight, the bulk resistance of the gel electrolyte and the physical interaction between the polymer chains are increased [128]. As the molecular weight of polymer increases, the relative amount of chain-ends, which are the most mobile regions of a polymer backbone, and the free-volume between the polymer chains decrease, thus the chain movements are restricted, resulting in high viscosity, low ionic motion and hence lower ionic conductivity [129]. On the other hand, the ionic conductivity increases as the amount of KCl (charge carriers) increases because the bulk resistance reduces. This can be attributed to the increased number of charge carrier ions produced by KCl [130]. Low-molecular-weight has more segmental motions, increasing ion

mobility. However, high molecular weight is desirable for obtaining more mechanically durable films as it enhances the interactions between polymer chains. Furthermore, high-molecular-weight PVA contains more chain entanglements, holding more water molecules. Consequently, an increased amount of water molecules and salt amount leads to higher ionic conductivity, resulting in a greater quantity of dissociated free ions [131, 132]. Thus, the gel electrolyte with M_w=195000 g mol^{-1}and PVA/KCl (w/w: 1/2) with the highest ionic conductivity (3.48 ±0.25 mS cm^{-1}) was selected as the best gel electrolyte for the fabrication of solid-state supercapacitor.

For the evaluation of the structural properties of the optimum gel, XRD, ATR-FTIR, UV-Vis, Tensile mechanical, DMA, and FE-SEM tests were done. The gel electrolyte possesses a semi-crystalline structure with both crystalline and amorphous regions. The XRD result showed that the presence of KCl may contribute to an expansion in free volume, allowing for a slight enhancements in crystal growth [133, 134]. This reduction in crystallinity and increase in crystallite size due to KCl suggest a disorganization of the PVA crystalline structure, resulting in a more amorphous nature [135]. Enhanced polymer chain segmental motions within the amorphous structure promotes ion movement and contributes to elevated ionic conductivity levels [136].

This mechanism is further supported by UV-Vis results. In the gel electrolyte, a blue shift occurs in the absorption peak, along with a shift towards lower wavelengths in the absorption spectrum [137]. This shift suggests a reduction in hydrogen bonding among PVA chains, likely resulting from interactions between K$^+$/Cl$^-$ ions and the polar groups within PVA [5]. These observations suggest the formation of complexes between PVA and KCl, that consistent with the FTIR analysis.

In the ATR-FTIR spectrum of gel film, there are slight shifts in peaks of PVA, indicating potential interactions between the polymer and salt. Notably, the stretching vibrations of -OH and -CO groups experience significant modifications, with a decrease in peak intensity and a red-shift compared to pure PVA [51]. These alterations strongly suggest the formation of complexes or interactions between the KCl and the polar groups in PVA (-OH and –CO) [137]. These interactions likely facilitated by favorable electrostatic attractions and coordination effects between the ions of KCl and the oxygen groups within PVA in an

aqueous environment, may potentially drive a hopping mechanism, thus bolstering ionic conductivity [138].

The Dynamic mechanical analysis (DMA) result showed that the introduction of a small amount of salt (M_w=195000 g mol^{-1}, PVA/KCl (w/w: 1/0.1)) to PVA leads to an increase in the elastic or storage modulus (E') compared to pure PVA, indicating the formation of a more interconnected physical gel network structure with greater resistance to deformation, which suggesting an improvement in mechanical strength and stability of the gel structure [57]. On the other hand, as the concentration of KCl increases relative to PVA (PVA/KCl (w/w: 1/0.5, 1/1, 1/2)), it can disrupt the polymer network and reduce the overall physical crosslinking between PVA and KCl within the gel structure allows for greater relaxation of polymer chains. This can lead to a decrease in the E', as the gel becomes less rigid and more fluid-like [59]. Moreover, the addition of KCl salt decreases T_g and causes a shift to lower temperature in the tanδ (Damping factor) peak because it acts as a plasticizer, disrupting the polymer chain interactions and increasing chain mobility. The presence of KCl ions reduces the hydorgen bonds between polymer chains, making it easier for the chain to move past each other, indicating that the polymer chains transition to the rubbery state. The lower T_g suggests that the gel becomes more flexible and exhibits increased mobility of polymer segments, which is characterized of a plasticized polymer system [57, 60-63].

PVA is a semi-crystalline polymer containing crystalline layers and amorphous folded chains with a higher tensile strength (68.5±5.35 MPa) compared to the PVA/KCl gel film (15.88±0.25 MPa). PVA demonstrates a relatively high strength in its elastic region, representing its ability to resist deformation under load without permanent damage. The lower Young's modulus and elastic strength of the gel film suggest a more flexible and deformable nature compared to pure PVA [48, 49]. However, the highest elongation at break for the gel film signifying enhanced flexibility and stretchability because KCl salt acts as a plasticizer and weakens the bonds between polymer chains at the molecular level [45, 64]. Although the pure PVA demonstrates higher stiffness and elastic strength compared to the gel sample exhibiting superior flexibility and stretchability which could be the advantageous in solid-state supercapacitor applications requiring conformability and deformability [65, 66].

The surface morphology and microstructure of the PVA/KCl sample exhibited a textured appearance, suggesting the presence of dispersed potassium chloride particles within the PVA matrix. These particles contribute to the overall roughness and texture of the sample surface [67]. Additionally, the FE-SEM image highlights the uniform distribution of potassium chloride particles throughout the PVA matrix, indicating good compatibility and interaction between PVA and KCl [70]. For the sample with the highest KCl amount, the image reveals a homogeneous distribution of KCl clustered particles on the surface of the PVA film, characterized by white dots and relatively larger spots, indicating the presence of individual KCl particles and their aggregates [45, 72]. The EDAX-Mapping results of PVA/KCl gel film indicated four elements which were denoted as carbon (C), oxygen (O) that arose from the carbon chains of PVA, and potassium (K), chlorine (Cl) that arose from the KCl salt. This result suggests that the as-prepared sample is in high-purity condition and good spatial distributions of C, O, K ,Cl elements in pure polymer sample [72].

Cyclic stability of the flexible gel electrolyte was evaluated at 200 mVs^{-1}. The specific capacitance reduces from 5 to about 4.4 mF g^{-1} after 5000 cycles. Thus, the gel maintains %88 of initial capacitance. Moreover, the gel electrolyte exhibited remarkable biocompatibility, evident in a cell viability test where 72.3% of cells remained unaffected after a 72-hour exposure to PVA/KCl. Therefore, the gel electrolyte containing PVA with M_w of 195000 g mol^{-1} and PVA/KCl (w/w: 1/2) shows the greatest ionic conductivity and better cyclic stability which is a promising candidate for making the flexible and wearable energy storage devices.

The electrochemical properties of GO/CS-based fiber and film electrodes for solid-state supercapacitors assembled with the PVA/KCl gel electrolyte (M_w=195000 g mol^{-1}, PVA/KCl (w/w: 1/2)) were evaluated by CV, EIS, and GCD tests. The result of CV test for RGO/CS fiber composite with different GO/CS weight ratios exhibited a larger enclosed area within the CV curve compared to RGO, demonstrating its remarkably high specific capacitance that arises from the synergistic interplay of both electric double layer (EDL) and pseudocapacitive behavior [3]. The supercapacitor contains RGO/CS (w/w: 90/10) exhibits the largest CV area, indicating that it has the largest specific capacitance (523.06±53.57 Fg^{-1} at 5 mVs^{-1}) of all the symmetrical solid-state supercapacitors. At chitosan levels below the optimum, the spacing between GO sheets becomes insufficient, leads to a reduction in the

accessible surface area for ion exchange and electrical double-layer formation, adversely affecting conductivity and give lower capacitance [139]. By increasing the CS amount, the capacitance increases, so at an optimal concentration of chitosan, acted as a spacer between RGO sheets, effectively increasing the distance between them. This spatial arrangement contributed to enhanced capacitance by expanding the effective surface area available for charge storage and facilitating channels for ion exchange. The presence of $-NH_2$ and $-OH$ groups in the chitosan structure contributes significantly to minimizing ion permeable resistance at the electrode-electrolyte interface [140]. However, when the chitosan content surpasses 10%, at higher chitosan concentrations, a reduction in conductivity was observed. Beyond this ratio, there is a reduction in specific surface area and electrical conductivity, and no efficient ion transport network which is consistent with the literatures [85-87].The electrochemical performance of fiber-based electrodes indicates low capacitance and poor charge storage capability which may be attributed to inherent limitations in the fiber morphology and interface interactions, which hinder efficient charge transfer and ion diffusion processes. Furthermore, the fiber's structural integrity and mechanical stability may have been compromised during fabrication, resulting in reduced electrochemical activity and performance compared to film.

The result of CV test for RGO/CS film composite with different weight ratios showed that the supercapacitor contains RGO/CS (w/w: 90/10) exhibits the largest CV area, indicating that it has the largest specific capacitance (872.74 ± 68.35 F g^{-1} at 5 mV s^{-1}) between all of the symmetrical solid-state supercapacitors. The result of GCD test for this supercapacitor shows that the discharge curve is nearly a straight line, exhibits quick and short current response times, meaning a good electric double layer (EDL) performance which is consistent with the literatures [39, 40].

The comparison between the specific capacitance of fiber and film-based solid-state supercapacitors showed that film has the highest specific capacitance. This may be attributed to variations in the material's surface area, porosity, and accessibility of active sites [88]. Film often provides a larger surface area, more active sites for electrochemical reactions, and better accessibility of electrolyte ions to the electrode surface compared to fibers, leading to higher specific capacitance. Additionally, the film structure may offer improved electron

and ion transport within the electrode, better porous structure, and potentially of flexibility, contributing to enhanced electrochemical performance [89, 141].

Furthermore, the electrochemical impedance spectroscopy (EIS) and cycle-life and structural properties for RGO/CS film type sample were also investigated. The Nyquist plot of RGO/CS (w/w: 90/10) provided a comprehensive analysis of the EIS data, accompanied by the corresponding equivalent circuit. The charge transfer resistance (R_{ct}) and ionic resistance (R_s) of the RGO/CS electrode are much lower compared to RGO electrode, this is owing to the intrinsic high ionic conductivity and fast electron transfers in the system [90]. Moreover, in the low-frequency region, the straight line reflects the ion diffusion element within the electrodes. The line of RGO/CS electrode is more vertical suggesting that the conductive links between chitosan and RGO provide an enhanced electrical conductivity or easily accessible ion diffusion path for electrolyte ions [80].

The result of cycle-life test indicated that the specific capacitance experiences a slight decline from 64.24 Fg^{-1} to approximately 56.09 Fg^{-1} in PVA/KCl gel electrolyte after 10,000 cycles. Impressively, even after this extensive cycle count, the electrode retains an impressive 87.31% of its initial capacitance. This outcome underscores the remarkable resilience and durability of the RGO/CS electrode, a characteristic attributed to the open framework structures inherent to chitosan [39]. This structural 3D-framework facilitates the accessibility of ion charges and enables the efficient conduction and transportation of ions. Crucially, the interplay between GO sheets and chitosan chains engenders physical interactions that serve as barriers, mitigating the extent of polymer chain degradation during the repeated charge-discharge cycles. This phenomenon culminates in a substantial enhancement of both capacitance and cycle life [41, 43]. The symmetrical solid-state supercapacitor exhibits excellent energy and power densities of 234.97 W h kg^{-1} and 1499.98 kW kg^{-1}, respectively. In evaluating the cell viability of the RGO/CS composite, the results showcased a viability rate of 76.4% after 72 h. The recorded cell viability of 76.4% indicates that a notable fraction of cells retained their vitality and well-being post-exposure to the RGO/CS electrode.

Additionally, the structural properties of GO/CS film sample were studied using ATR-FTIR, UV-Vis, XRD, XPS, BET, AFM, POM, TEM, FE-SEM, Electrical conductivity, and Tensile

mechanical tests. As a summary, in the FTIR spectrum of RGO/CS, it's noteworthy that the intensity of O-H stretching and C-O stretching was lower compared to the GO/CS spectrum, indicating the reduction of GO to RGO. Subtle shifts in peaks were observed, possibly attributable to hydrogen bonds among composite components. Additionally, the presence of RGO in the composite was indicated by the peak found at 1048 cm^{-1} in the RGO/CS spectrum [9, 93].

The result of UV-Vis reveals that upon the attachment of GO with CS, the peaks associated with GO moves to the higher wavelength. This shift signifies the interaction between epoxy groups on GO and amino groups (NH$_2$) on chitosan, culminating in the formation of the GO/CS composite [142]. In the RGO/CS spectrum, there is a red-shift in peaks which is attributed to the partial restoration of electronic conjugation among aromatic carbon atoms. Collectively, these outcomes suggest that chitosan becomes conjugated with GO after reduction [143]. The comparison of XRD results and d-spacing of RGO, CS, RGO/CS confirms that the presence of chitosan might influence the stacking and arrangement of RGO layers, leading to changes in the d-spacing compared to pure RGO in RGO/CS composite, indicating the existence of an interaction or a specific arrangement of RGO and chitosan layers in the composite structure [94, 144]. The XPS result of the composites containing chitosan and either RGO or GO reflect the spectral features characteristic of both constituent materials. This observation provides strong evidence for their successful incorporation within the composite structure [145].

The AFM images of GO showed distinctive features and patterns on the surface. These images provide a clear visualization of the individual layers of GO sheets [317, 318]. The AFM findings pertaining to the GO and CS composite provide a complex and intriguing nanoscale structure. The composite material displays a heterogeneous surface marked by regions of varying roughness, a characteristic likely attributed to the coexistence of GO sheets and CS particles [143, 319].

GO sheets can exhibit liquid crystalline properties, which refers to their ability to self-assemble into ordered structures in a liquid medium. Polarized optical microscopy (POM) helps visualize and analyze these structures under the influence of polarized light, providing insights into the organization and liquid crystallinity (LC) behavior of GO [102]. The

lyotropic nematic LCs of GO clearly indicate the local orientation of GO sheets in the aqueous media in the form of the large area of Schlieren texture. The formation of LC textures of GO/CS composite occurred by their supramolecular self-ordering into ordered layers through the interaction between the oxygen and amide functional groups, which displayed the layered architectures, in line with the formation of ordered clusters of chitosan [103].

The morphologies and microstructure of the GO, RGO, GO/CS, and RGO/CS were illustrated by TEM. TEM images of the GO/CS shows a much rougher and high density surface appeared compared to GO due to the assemblage of chitosan on the surface of GO layers which clearly indicates the combination of the GO layers with chitosan to form the GO-chitosan composite [93, 108]. After reduction of GO, the surface of RGO/CS appears to be rough and clearly covered by some decorations compared to RGO, which are attributed to the coating of chitosan, indicating that the chitosan was successfully grafted onto the surface of RGO. Furthermore, few layers of graphene nanosheets wrapped up by rough chitosan chains. This indicated that the chitosan made contribution to the well-dispersion of RGO nanosheets [109, 110].

The ultimate tensile strength, toughness, and Young's modulus of GO, RGO, CS, GO/CS, and RGO/CS films from the measured stress-strain curves were obtained. In comparison to GO and RGO, the GO/CS and RGO/CS composites show 46% and 36% increment in Young's modulus and 61% and 64% growth in tensile strength, respectively. The toughness (area under the stress-strain curve) of neat GO film is 184.45±54.17 MJ m^{-3}. The GO/CS and RGO/CS nanocomposites exhibit toughening effects as high as 80% compared to GO and RGO. This suggests enhanced stiffness and structural integrity, possibly due to the synergistic effects of RGO and CS [146].

Brunauer-Emmett-Teller (BET) analysis was conducted to determine the specific surface area, total pore volume, and pore diameter of CS, RGO, and RGO/CS which these properties corresponds to the adsorption capacity of the materials. According to the classification by BDDT IUPAC classification, the adsorption-desorption isotherm graphs of RGO/CS nanocomposite tended to follow type IV with the specific flow of the hysteresis loop for mesoporous material. These properties indicated of interconnected meso- and macro-pores

like tinted bottle and the random pore distribution [97, 98]. The BET characteristics of the RGO/CS nanocomposite falls within the range observed for RGO, indicating that the addition of chitosan did not significantly alter the high surface area (13.672 m^2 g^{-1}), adsorption capacity, and porous structure. These results suggest that chitosan may act as a scaffold or binder for RGO (synergistic effects), potentially enhancing its mechanical stability, reducing the risk of structural degradation during charge-discharge cycles and facilitating the ion diffusion and charge transfer at the electrode-electrolyte interface, thereby enhancing the electrochemical performance of the solid-state supercapacitor which is consistent with the literatures [99, 100].

The field emission scanning electron microscopy (FE-SEM) images for GO, RGO, CS, GO/CS, RGO/CS were also provided. The GO-chitosan film exhibited a distinctive "sandwich" configuration. The image demonstrates that a significant portion of the GO nanosheets were fully exfoliated and uniformly dispersed within the chitosan matrix [9]. The RGO/CS composites images show the presence of graphene dispersed within chitosan, exhibiting irregularly wrinkled and sheet-like structures. The RGO sheets appear as interconnected layers or flakes, featuring a surface morphology marked by crumpling or folding [114]. The results of EDAX-Mapping of GO/CS samples show an elevated proportion of oxygen content, confirming the continued presence of unreduced graphene oxide, as well as regions with elevated nitrogen levels signifying chitosan domains. However, in RGO/CS, there are areas with higher carbon concentrations related to RGO. In contrast, regions with reduced carbon concentration indicate the prevalence of chitosan [147, 148].

The electrical conductivity of GO, RGO, CS, GO/CS, and RGO/CS samples was measured using EIS test and calculated based on the value of charge transfer resistance (R_{ct}) from the Nyquist plots at an electrode/electrolyte interface which is the primary factor affecting the impedance [149]. The reduction of GO shows that the RGO/CS sample (2.62×10^{-3} S cm^{-1}) have higher electrical conductivity than GO/CS (4.40×10^{-6} S cm^{-1}) because the reduction process removes oxygen groups from GO sheets, restoring some of the sp^2 hybridized carbon structure found in graphene which is consistent with the literatures [97, 118].

In the subsequent stage of the thesis work, flexible solid-state supercapacitors were prepared using films obtained by pouring onto PET surfaces that meet the flexibility criterion instead of the standard steel sub-layer, and electrochemical performance studies of these structures were conducted. In this production, the RGO/CS (w/w: 90/10) film poured onto PET served as the electrode, while the PVA/KCl gel (Mw=195000 g mol^{-1}, PVA/KCl (w/w:1/2)) was used as the electrolyte. The specific capacitance value was measured as 191.07±19.24 F g^{-1} at 5 mVs^{-1} (186.64±21.69 F g^{-1} at 1 A g^{-1}), and this value was significantly lower than that of the stainless steel substrate (5 mV s^{-1}'de 872.74±68.35 Fg^{-1}). Stainless steel is a conductive material, providing better electrical conductivity and potentially lower resistance compared to PET [124]. The adhesion of the RGO/CS electrode to the current collector is crucial and stainless steel, being a rigid and smooth surface, might provide better adhesion and uniformity of the electrode compared to PET, which is flexible and may have a less smooth surface [150]. Moreover, stainless steel offers better mechanical stability and support for the electrode, maintaining structural integrity during charge-discharge cycles, but PET, being more flexible, might experience deformation or structural changes that could impact performance [119, 120, 151].

In the final part of our thesis work, aiming to examine the potential use of prepared electrolyte and electrode structures in laser 3D-printing technology, RGO/CS (w/w: 90/10) electrode and PVA/KCl (Mw=195000 g mol^{-1}, PVA/KCl (w/w:1/2)) gel electrolyte were printed onto a polyimide (PI) film to provide a flexible solid-state supercapacitor. Interdigital RGO/CS electrodes exhibited comb-like formations and demonstrated exceptional adhesion properties and durability. However, despite testing with solvents such as acetic acid, acetone, ethanol, and 2-propanol, the desensitized RGO/CS film electrode portions remaining on the PI surface could not be removed. This situation was identified as a challenge to be overcome in adapting laser 3D-printing technology to the electrode and electrolyte materials prepared within the scope of the thesis, and it is discussed in the subsequent sections of the thesis.

In the light of all these results, it is thought that the film-based structures obtained within the scope of this PhD thesis can be important alternatives for supercapacitor applications, with their excellent electrochemical performance, mechanical-thermal stability and biocompatibility properties. Therefore, these findings offer a promising route towards the fabrication of stable and high-performance biocompatible electrode materials and gel

polymer electrolytes that can be used in fabrication of solid-state supercapacitors, thus laying the foundation for their integration into flexible, safer and wearable bio-electronics. Developed with environmentally friendly materials, the electrode paves the way for the production of solid-state supercapacitors with advanced electrochemical and biocompatibility properties, making them suitable for integration into sustainable next-generation biomedical devices.

In the subsequent chapter, the significance of supercapacitors, their various types, and energy storage mechanisms are initially discussed. Subsequently, the focus shifts to flexible supercapacitors, electrodes, ion conduction mechanisms, the structure of gel polymer electrolytes, and their different types. At the end of the chapter, the electrodes and electrolytes investigated in this PhD thesis are introduced.

3. GENERAL INFORMATION

3.1. Supercapacitor and its concepts

A supercapacitor is a particular type of a regular capacitor. Traditional capacitors composed of two conductive electrodes that are separated from one another by a dielectric substance. When a voltage is introduced to the capacitor, it leads to the accumulation of opposing charges on the surface of the capacitor. These charges remain separated by the dielectric material and the resultant electric field results in the energy storage. This phenomenon is illustrated in Figure 3.1 [152].
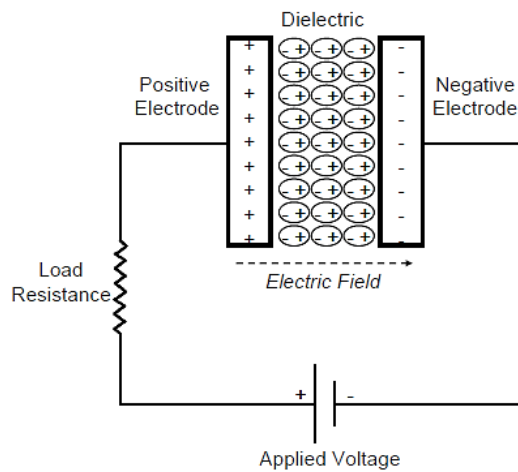
Figure 3.1. Structure of a typical capacitor [152].

Figure 3.2 shows the supercapacitor structure. Each supercapacitor is composed of two electrodes having a high specific surface area in a liquid or solid electrolyte consisting of

positive and negative ions. Also, a porous dielectric is placed as a separator between two electrodes, which is ion permeable, but avoids the charge transfer between the two electrodes. By applying voltage between two electrodes, these ions are segregated and the electrical energy is stored within the supercapacitor [152].
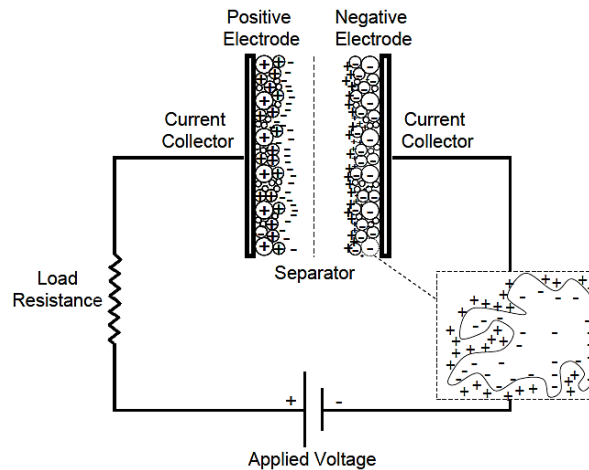
Figure 3.2. Structure of a supercapacitor [152].

3.2. Types of supercapacitors

Supercapacitors are categorized into three classifications based on their energy storage mechanism: Electric double layer capacitors (EDLC), Pseudocapacitors, Hybrid capacitors [13, 14].

In electric double-layer capacitors (EDLC), carbon materials with a high specific surface area like activated carbon, carbon nanofibers, carbon nanotubes and graphene are utilized, while in quasi-capacitors, intermediate metal oxides like manganese oxide (MnO_2) and conductive polymers such as Polypyrrole is used. In hybrid capacitors, one of the electrodes is fabricated of carbon material and the other is made of quasi-capacitive electrode (Figure 3.3) [13, 14].
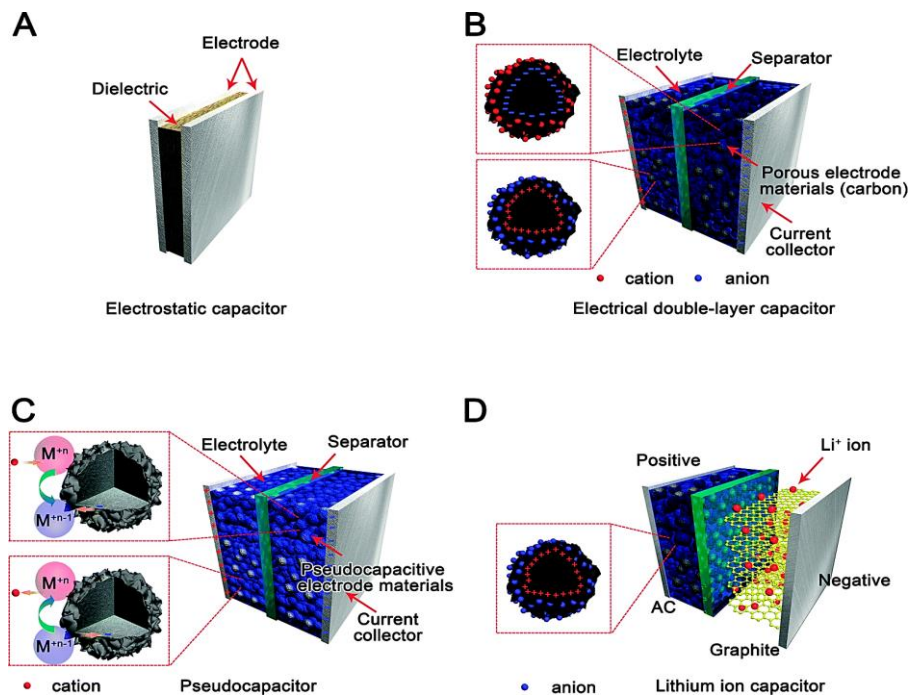
Figure 3.3.   Structure of a conventional capacitor and types of supercapacitors [14].

3.2.1   Electric double layer capacitors

In electric double layer capacitor (EDLC), the composition of electrode/electrolyte surface is changed by surface absorption of the electric charge and causes the electrode to be charged to the opposite charge of the adjacent electrolyte layer and the formation of two electric layers at the electrode-electrolyte interface is formed [13, 15]. In other words, ions accumulate at the interface of electrode/electrolyte and lead to energy storage by electrostatic process. Therefore, in this supercapacitor, due to the absence of oxidation and reduction reactions, charge storage is done by non-faradic processes. Because of high specific surface of carbon materials (about 1000-2000 $m^2\ g^{-1}$), considerable endeavors have been undertaken to enhance energy density and diminish electrical resistance (Figure 3.4) [14, 20, 152].
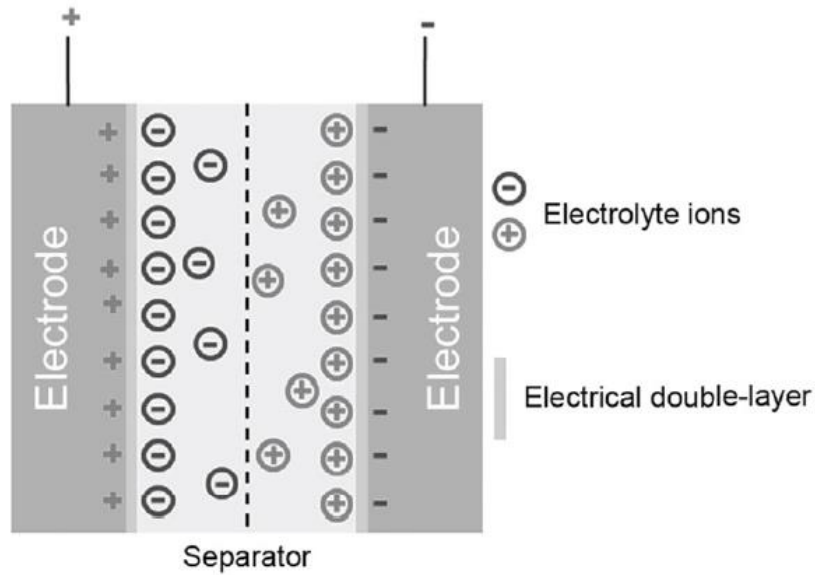
Figure 3.4. The process of absorbing ions on the surface of the electrodes and forming two electrical layers [19].

3.2.2 Pseudocapacitors

In Pseudocapacitors type, electrons are transferred between the electrode/electrolyte by oxidation-reduction reactions, and the amount of charge storage depends on the speed of reversible faradic reactions [13]. Quasi-capacitors store energy through chemical reactions, but in electric double-layer capacitors, energy is stored via physical absorption of charge without occurring of chemical reactions. Hence, chemical reactions occur in quasi-capacitors leading to system failure, reduced life-span, and long charging and discharging times [14, 20].

3.2.3 Hybrid capacitors

In hybrid systems, charge storage is done using both faradic and non-faradic processes, which can achieve higher power density and energy density than double-layer electric capacitors and quasi-capacitors [13]. On the basis of the electrode structure, hybrid systems are split into multiple groups: composite electrodes made of electric double layer type and quasi-capacitors, asymmetric electrodes, and battery-type electrodes. In the first group, carbon materials are the combination of metal oxides or conductive polymers, and the charge storage mechanism is done using both faradic and non-faradic reactions [14, 19].

34

Because of the high specific surface area, carbon materials enhance the contact between the electrode and electrolyte materials and the charge will be stored by creating an electrical double layer [13]. Quasi-capacitive materials also enhance the capacitance by performing faradic reactions. In asymmetric hybrid systems, one electrode is made of electrical double-layer material and the other one is made of quasi-capacitive material [1]. In this type, both faradic and non-faradic processes are used for charge storage. Similar to asymmetric hybrid systems, in the hybrid type based on the battery electrode, one electrode is a supercapacitor-type and the other one is a battery-type electrode. Such structures provide higher power density than batteries and higher energy density than supercapacitors [14, 152]. The cycle life of hybrid capacitors and quasi-capacitors is much less than electric double-layer capacitors due to the occurrence of faradic processes. Therefore, the electric double-layer capacitor has received extremely attention due to its great power density and superior cycle stability [13, 14]. The main challenge in electric double-layer electrodes is their low energy density. Energy density is relative to the capacitance of the electrode and the second power of the cell voltage, and the increase of each of these functions resulting in enhancement of the energy storage of supercapacitors. The maximum tolerable potential of the supercapacitor is subjected on the constant voltage range of the electrolyte, and the capacitance also enhances by increasing the ionic conductivity of electrolytes. Consequently, it is essential to develop electrodes and electrolytes with optimal structure and performance [14, 153].

3.3. Carbon-based electrode materials

The description of the main carbon-based electrode materials is introduced in this part. Due to its low expense and high accessibility, carbon-based electrode materials are the major greatly usage materials in supercapacitors [13, 28].

3.3.1 Graphene

Graphene is a thick sheet of a popular atom, composed of 2D layers all-sp^2 hybridized carbon atoms in a network of polyaromatic crystals of honeycomb framework [126, 154]. There are more fascinating characteristics such as great area to volume ratio, proper thermal properties and electrical conductivity, structural moldability, greatly adjustable surface area, minor

diffusion path, beneficial chemical durability, high mechanical stability, and broad voltage window. In addition, it benefits from a great monolayer surface area (about 2620 m^2 g^{-1}) and open hole set-up that contributes to increase the kinetic event of transportation [28, 30, 153, 155, 156].

A conventional method of producing graphene is shown in Figure 3.5, where graphite oxide is originally oxidized from graphite. This is obtained by Hummer's method [34] or modified Hummer's method [157]. Simple sonication process can be used for the production of graphene oxide (GO) sheets from fully exfoliation of graphite oxide. Chemically derived graphene is produced from GO which is reduced with hydrazine solution and heat [30, 154].
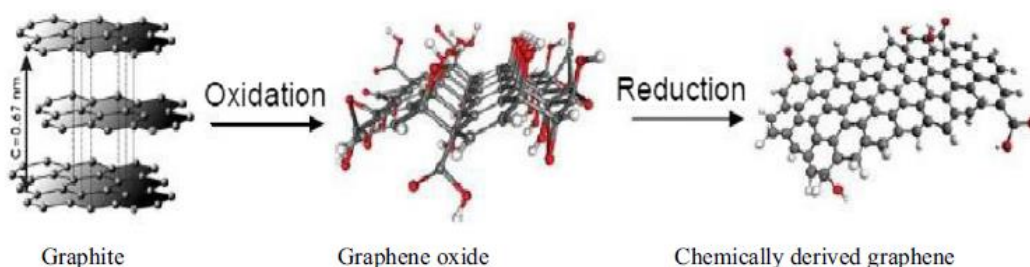
Figure 3.5. Chemical approach to synthesis of chemically derived graphene [16].

The disadvantage of graphene sheets is that they can easily form irreversible agglomerations and restacking to their graphite structure. The existence of Vander Waal interactions between the near sheets through the re-stacking of GO sheets, reducing the energy density due to the reduction of surface area. As a result determining intrinsic capacitance becomes very challenging [16, 126]. Researchers have shown that the performance of graphene could be efficiently increased by adding other materials into the graphene sheets as spacer [31]. The spacers could break the Vander Waal force between graphene sheets to hinder the graphene sheets restacking, assist ion diffusion and decrease the diffusion strength [2, 33]. The most used spacers to enhance the electrochemical performance of graphene are carbon sphere [158] , carbon black [159, 160], carbon nanotubes [161], metal oxides[162, 163], polymers [164, 165], and biomass-based carbon materials [166-170]. Various capacitance amounts were get for supercapacitor based on graphene in literatures. Ionic liquid-based supercapacitors have 31.9 Wh kg^{-1} energy density and 75 F g^{-1} specific capacitance [3]. Specific capacitances of 135 F g^{-1} and 99 F g^{-1} were reported for aqueous electrolyte and

organic electrolyte, respectively [171]. The reduced graphene sheets with less restacking in aqueous electrolyte indicated an energy density of 28.5 Wh kg^{-1} and specific capacitance of 205 F g^{-1} [36].

3.3.2. Activated Carbon

Activated carbon (AC) is the majority important material for supercapacitor electrodes. Because of their great surface area and the less expenses, they are the best electrode materials [172]. Carbon-rich organic solution is used to make such materials that can be easily obtained from sources such as wood, and fossil fuels. Moreover, AC is made from synthetic materials such as polymers [157, 173].

In literature, the reported surface area is between 1000 to 2000 m^2 g^{-1} and the specific surface area is 3000 m^2 g^{-1}. The most usage cell voltage for AC electrodes is 2.7 V which gives the specific capacitance of 100 to 120 F g^{-1} [174, 175] and volumetric capacitance of 60 F cm^{-3} [176]. Furthermore, the aqueous electrolyte showed a restricted 0.9 V cell voltage [173] and specific capacitance of 300 F g^{-1} [37].

3.3.3. Carbon nanotubes (CNTs)

CNTs are produced through the chemical breakdown of different hydrocarbons. Various nanostructured creations can be achieved by manipulating the various parameters; single-wall carbon nanotubes (SWCNTs) and multi-wall carbon nanotubes (MWCNTs) may be obtained [16]. These materials show great electrical conductivity and well-available surface area. The specific capacitance of this material can be affected by purity and morphology structure. Moreover, it can be produced without the use of any binder which decreases the resistance between the current collector and electrode material. Recent efforts suggest the producing of aligned CNT which increases the capacitance at high current density by controlling the tubes distance. By rolling graphene sheets into tube form, single-wall CNTs are produced [31]. In addition, MWCNT can be obtained by the additional graphene tubes of SWNT which consists the double-wall CNT (DWNT). CNTs have proved to be the interesting material for electrodes due to the new properties such as great specific surface

area, proper electrical conductivity, great electrolytic availability, and high charge transport ability [177, 178].

Chemical vapor deposition (CVD) method is used for the production of aligned CNT shows specific capacitance of 440 F g^{-1}, energy density of 148 Wh kg^{-1}, and power density of 315 kW kg^{-1} in ionic liquid electrolytes [179-181]. In 0.5 M H$_2$SO$_4$ electrolyte, the CNTs containing titanium nitride exhibited the specific capacitance of 81 mF cm^{-2} [181].

3.4. Electrolyte materials

The types of electrolytes that are used for fabrication of supercapacitors are divided into two groups: liquid electrolytes and solid electrolytes (Figure 3.6) [14].
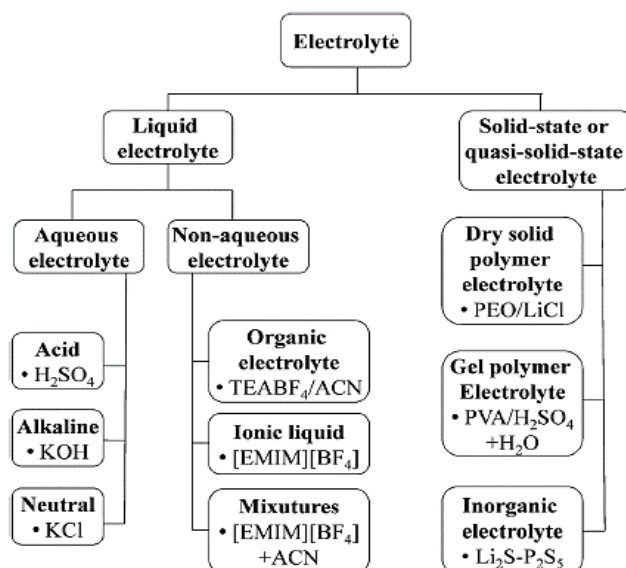
Figure 3.6.   Various types of liquid and solid electrolytes [14].

Liquid electrolyte includes aqueous and non-aqueous types. Aqueous type includes acidic, basic and neutral, which has high ionic conductivity due to the presence of water, but the electrolysis of water and gas production leads to a decrease in the voltage range of these types of electrolytes [14]. The non-aqueous type is separated into three categories: organic, ionic liquid, and a mixture of organic and ionic liquid. An organic electrolyte composed of salt dissolved in an organic solvent. The organic solvent must exhibit good solubility, low viscosity and a high level of safety. Ionic liquid electrolytes are in the form of separate ions

at room temperature. These electrolytes have high thermal and electrochemical stability and are also non-volatile and non-toxic [14, 19].

Solid or quasi-solid electrolyte includes dry polymer electrolyte (SPE), gel polymer electrolyte (GPE) and inorganic electrolyte [14]. Dry polymer electrolyte includes polymer and electrolyte salt, such as: (PEO/LiCl, polyethylene oxide/lithium chloride). Gel polymer electrolyte includes polymer and liquid electrolyte solution, such as: (PVA/H_2SO_4/H_2O, polyvinyl alcohol/ Sulfuric acid/water) [53]. Because of the existence of liquid phase in this type of electrolyte, GPE is also called a quasi-solid electrolyte, and when water is used as a solvent, the GPE called as a hydrogel. In GPE, the polymer has a 3D-network structure that is swollen by the solvent and has higher ionic conductivity than SPE. The inorganic electrolyte is Li_2S-P_2S_5 (lithium sulfide-phosphorus pentasulfide), which has good thermal stability, but this electrolyte is not useful in making flexible devices [14, 15]. Therefore, ideally an electrolyte should have high voltage range, high ionic conductivity, good chemical and electrochemical stability. In some applications, such as flexible storage devices, because of the problems caused by leakage of liquid electrolytes, they are replaced by solid or semi-solid electrolytes [14]. Among various types of solid electrolytes, gel polymer electrolyte exhibits greater ionic conductivity [2, 14].

Capacitance is defined as the ratio of stored charge (Q) to applied voltage (V) and is measured in Farads (F) [2, 14]:

$$C=Q/V \tag{3.1}$$

C is directly proportional to the surface of each electrode (A) and inversely proportional to the distance between two electrodes (d) [14, 16]:

$$C=\varepsilon_0\varepsilon_r A/d \tag{3.2}$$

ε_0 is the dielectric constant of the vacuum and ε_r is the dielectric constant of the material between two electrodes. The capacitance is defined based on the amount of material on the electrode, its surface or volume: weight capacitance (F g^{-1}), volumetric capacitance (F cm^{-3}), surface capacitance (F cm^{-2}) [14, 16].

Two important parameters of any energy storage system are power density and energy density. Energy density expresses the ability of energy stored by electrodes, and its unit is Wh kg^{-1}, it is defined by the equation (3.3) [14, 161]:

$$E=CV^2/2 \tag{3.3}$$

In relation (1.3), "V" is the voltage and "C" is the capacitance of the electrode.

The power density expresses the supercapacitor's stored energy transfer rate capability, and its unit is W kg^{-1}, it is defined by the equation (3.4) [14, 162]:

$$P=V^2/4ESR \tag{3.4}$$

ESR is the equivalent resistance of the circuit, which includes the resistance created by the system components, including the electrode and electrolyte. Conventional capacitors have high power density, but their energy density is lower compared to batteries and solar cells [14, 152, 182]. Supercapacitors have electrodes with a higher specific surface, which according to the relations (3.2) and (3.3), have a higher capacitance and energy density than ordinary capacitors. In addition, by reducing the total resistance, a power density comparable to conventional capacitors can be achieved [152, 162].

Ragone plot shows the power density in terms of energy density for energy storage systems. As shown in Figure 3.7, supercapacitors are in the region between batteries and conventional capacitors. Considering that supercapacitors have lower energy density, but they can be used

in medical and military devices, power supplies, wind turbines, hybrid cars, and spacecrafts that require high power density and short charging time [14-16].
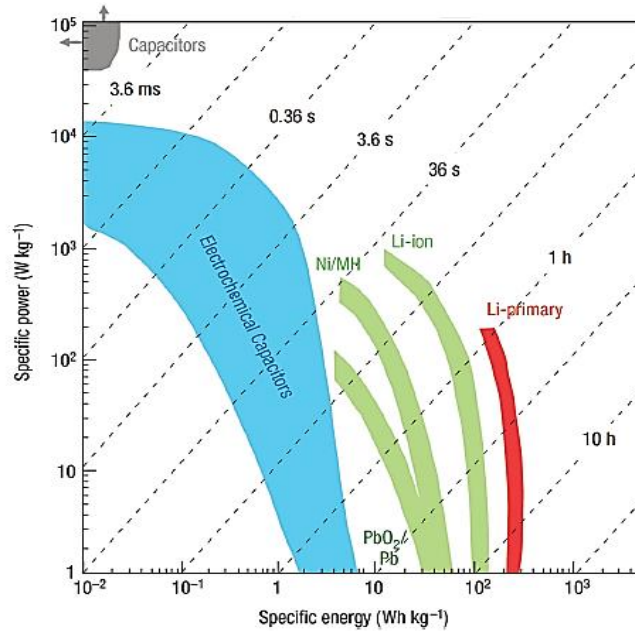
Figure 3.7. Ragone plot for energy storage systems [14].

3.5. Flexible Supercapacitors

Unlike conventional supercapacitors, flexible supercapacitors have important features such as small size, high durability and lightness. The application of portable electronic devices like mobile phones and netbooks, wearable, textiles, and flexible displays has expanded greatly, which requires lightness, excellent flexibility, and high safety of these devices [183-185] (Figure 3.8). Due to leakage and rigidity problems of liquid electrolytes, they are unsuitable for the creation of flexible supercapacitors. As a result, solid or quasi-solid electrolytes are employed as substitutes. Flexible supercapacitors integrate adaptable electrodes with a solid foundation electrolyte [14]. Carbon-based electrodes have emerged as flexible electrode options in supercapacitors, primarily due to their notable attributes such as elevated electrical conductivity, power density, cycle stability, and exceptional mechanical characteristics. In the realm of solid electrolytes, gel electrolytes stand out for their remarkable ionic conductivity and significant flexibility[13, 16].

41
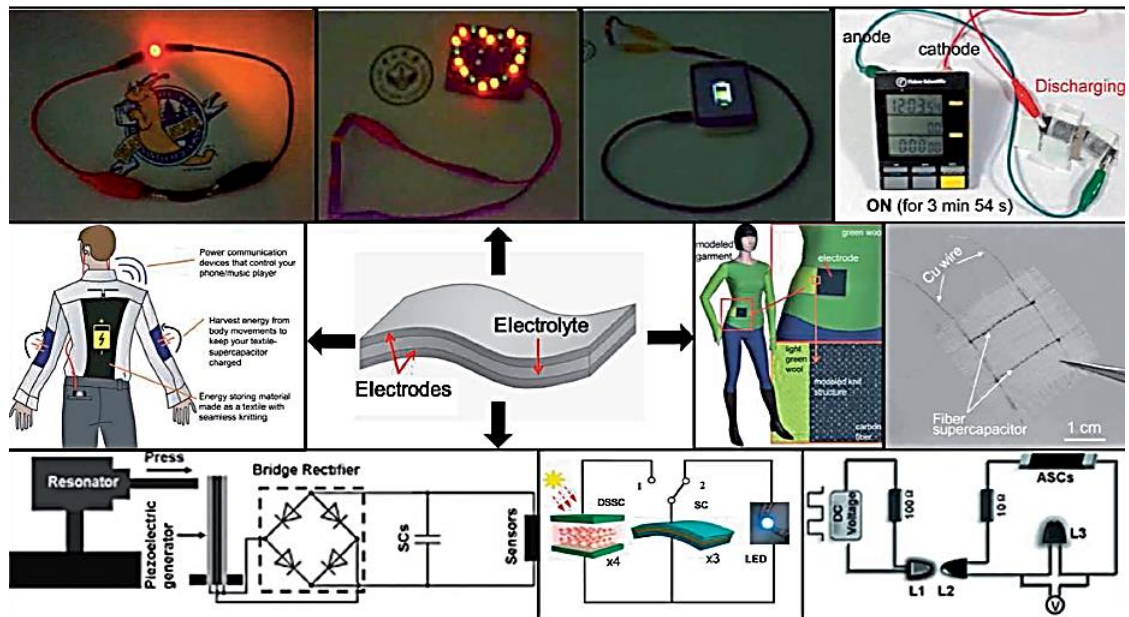
Figure 3.8. The application of flexible supercapacitors [13].

The unique features of gel electrolyte among the types of solid electrolytes for the preparation of flexible supercapacitor is discussed. In the following section, an introduction about gel electrolyte and its types, structure and ion conduction mechanisms is given. Afterwards, the electrode and gel electrolyte studied in the current PhD thesis are introduced.

3.6. Gel Polymer Electrolyte (GPE)

Gel polymer electrolyte consists of a three-dimensional network of polymer chains, ions and solvent molecules, and the solvent is trapped in the structure of this network [14]. If the solvent used is water, the gel electrolyte is also known as a hydrogel. Polymer chains are connected to each other by physical or chemical cross-links and form this three-dimensional network (Figure 3.9) [15]. In the physical type, the chains are put together by entanglements or secondary forces such as Van der Waals forces, and hydrogen or ionic interactions. The time and temperature of destruction of these types of gels are less. In the chemical type, chains are held together by strong covalent bonds by a cross-linking agent material. In this type of gel, the toxicity of materials and controlling the reaction conditions is still a challenge [16, 186].
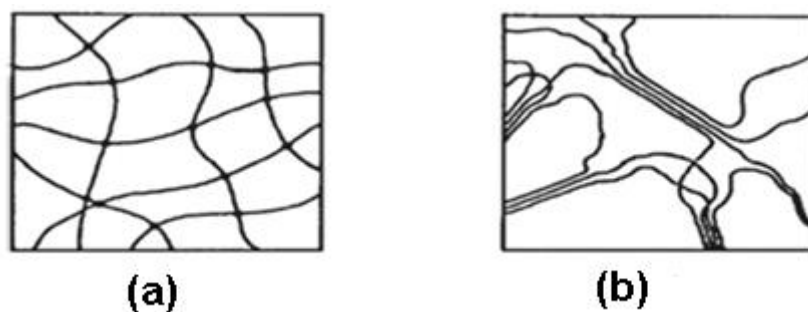
Figure 3.9. Gel electrolyte with a) chemical cross-links, b) physical cross-links [186].

3.6.1. Different types of gel electrolytes

As mentioned in the previous section, gel electrolyte contains polymer, solvent and electrolyte salt. According to the electrolyte salt, gel electrolyte is classified into four types: gel electrolyte containing lithium ion, gel electrolyte containing proton, gel electrolyte containing hydroxyl ion, gel electrolyte containing other ions or ionic liquid [14]. Gel electrolyte containing lithium ion is prepared by mixing polymer with lithium salt and organic solvent [15]. Organic solvents are often toxic, flammable and expensive. Gel electrolyte containing protons is obtained by mixing polymer with proton solvent and polar solvent. Heteroacids are commonly used as proton donors, which have higher ionic conductivities at room temperature than the lithium-containing type [187]. The gel electrolyte containing hydroxyl ions is obtained by mixing the polymer with an alkaline solution, which has a lower ionic conductivity than the protonated type [52]. Electrolyte containing ionic liquid has less ionic conductivity and is sensitive to humidity [13, 16]. The movement of protons, lithium ions, hydroxyl ions, other ions or ion samples in ionic liquids provides the ionic conductivity of the gel polymer electrolyte [187].

3.6.2. Ion conduction mechanisms in gel polymer electrolytes

Figure 3.10 shows the proton or ions conduction mechanisms. In hopping mechanism, the movement of ions through water molecules are determined by the formation and rupture of hydrogen bonds. The ion jump from one site to another site, it faces various potential energies that are separated from one another owing to the formation of strong hydrogen bonds by a small energy barrier. Consequently, the low activation energy results in an

increase in the speed of ion movement [15, 188]. Within the context of diffusion mechanism, ions form complexes with water molecules prior to permeation. The progression of permeation is impeded as hydrogen bonds are established with additional water molecules. This ion penetration process operates at a slower pace compared to ion jumping and necessitates greater activation energy [15, 187]. Conversely, the direct transfer mechanism occurs through the segmental motions of polymer chains in amorphous phase which facilitates the ions transfer [16, 187].
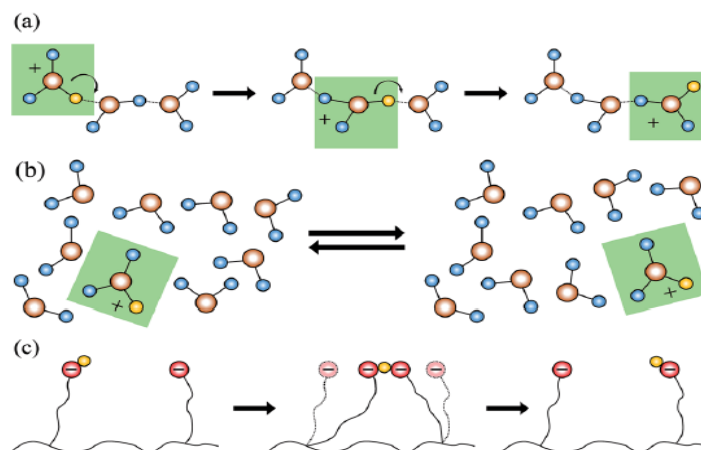
Figure 3.10.   Ion transfer mechanisms, a) Ion hopping mechanism in a system with a strong hydrogen bond, b) Diffusion mechanism of ions in a system with a weak hydrogen bond, c) Ion transfer mechanism through segmental movements of polymer chains [187].

3.7. Poly(vinyl alcohol) (PVA)

Among different types of polymers to prepare gel polymer electrolytes for supercapacitors, poly(vinyl alcohol) (PVA) is of great interest due to its good mechanical properties, water solubility, great ionic conductivity, non-toxicity, biocompatibility, biodegradability and low cost [15, 189].

Poly(vinyl alcohol) is a hydroxy polymer that has the greatest volume of synthetic resin production in the world and is a water soluble synthetic polymer. The chemical structure of this polymer is shown in Figure 3.11 [190].
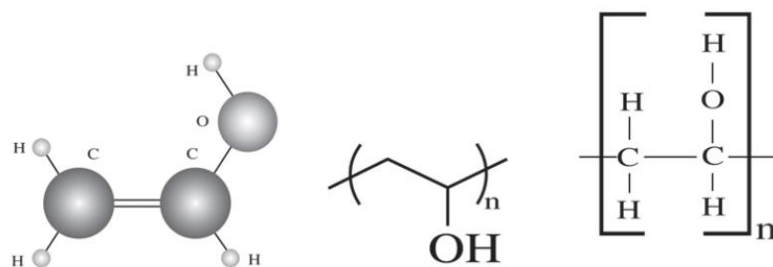
Figure 3.11. Vinyl alcohol molecule (left), chemical structure of PVA polymer (right and middle) [190].

PVA is not prepared through the synthesis of vinyl monomer, because of the monomer instability[25]. Therefore, PVA is synthesized by hydrolysis of vinyl acetate under alkaline conditions. The acetate groups of poly vinyl acetate (PVAc) is eliminated through the full or partial hydrolysis process [15]. The quantity of acetate groups which is remained in the reaction medium refers to the extent of hydrolysis. An increased degree of hydrolysis corresponds to a reduced presence of acetate groups within the polymer structure [191]. PVA is a linear polymer with hydroxyl groups, which are smaller in size compared to the acetate groups. These hydroxyl groups do not interfere with the establishment of crystalline regions within the polymer matrix. This indicates that hydroxyl groups are capable of forming hydrogen bonds with hydroxyl groups present in adjacent chains [53, 192]. Consequently, these hydroxyl groups are organized and positioned within the crystal lattice (Figure 3.12). In PVA solutions, in addition to intrachain and interchain hydrogen bonds, hydrogen bonds are also arranged between water molecules and polymer chains [15, 193].
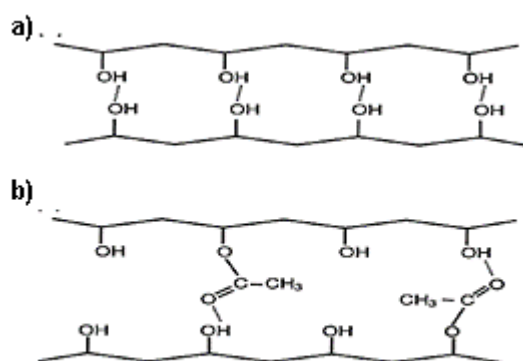
Figure 3.12. Hydrogen bonding in poly(vinyl alcohol), a) high degree of hydrolysis; many secondary hydrogen bonds are formed. b) low degree of hydrolysis; acetate groups act as barriers to prevent hydrogen bond formation [193] .

45

3.8. Graphene oxide and its synthesis method

Graphene oxide (GO) is a single layer of graphite containing various oxygen functional groups on its surface and edges [194]. The oxidation of graphite results in the formation of graphene oxide. GO is typically synthesized from graphite using various methods [126]. There are different ways for the synthesis of graphene oxide chemically by oxygenating graphite through Brody, Stadenmeier, Hoffman and Hummers' methods (Figure 3.13) [126].
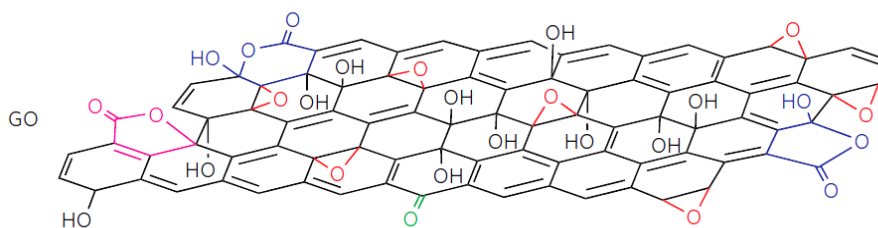
Figure 3.13. Chemical structure of graphene oxide [35].

In 1859, Brody was able to synthesize graphene oxide by adding potassium chlorate to a slurry of graphite and nitric acid. In 1899, Stadenmeyer was able to improve the reaction by adding concentrated sulfuric acid to enhance the acidity of the mixture and chlorate in equal and different proportions. The result of this method was an increase in the oxidation rate of graphene oxide in a single reaction compared to the Brody method [34, 35]. Sixty years later, Hoffmann and Hummers prepared graphite oxide by reacting expanded graphite with potassium permanganate (a strong oxidizing agent) and nitric acid in concentrated sulfuric acid. By increasing the distance between the layers, which is dependent on the amount of water washing and surface oxidation, they were able to synthesize graphene oxide. The active species resulting from the reaction of potassium permanganate with sulfuric acid is manganese heptoxide, which is produced according to the following reaction [32, 195, 196].

$$KMnO_4 + 3H_2SO_4 \rightarrow K^+ + MnO_3^+ + H_3O^+ + 3HSO_4^-$$

$$MnO_3^+ + MnO_4^- \rightarrow Mn_2O_7$$
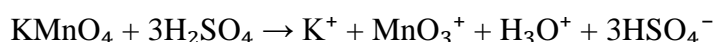
The graphene oxide produced by this approach is highly oxygenated and because of the presence of oxygenated functional groups on the surface and edges, it is very hydrophilic and easily flakes in water [35, 197]. The great distance between the graphene oxide layers facilitates the penetration of water molecules in that space and causes the distribution of plates in the aqueous environment. Graphene oxide is a single layer of graphite oxide with a very high specific surface area, contains a significant amount of oxygenated functional groups such as carbonyl, hydroxyl, carboxylic acid and epoxide on its edges and surface [35, 198]. Reduced graphene oxide which is produced through the thermal reduction of graphene oxide may be utilized as electrode materials which can improve the electrochemical and mechanical properties of supercapacitors [196].

GO is also produced by chemical vapor deposition (CVD), involving the reduction of graphene oxide using chemical vapors. GO is often prepared using Hummers' method and then reduced to graphene using a reducing agent in a CVD process. This method allows for the controlled growth of reduced graphene oxide on various substrates [199]. Another approach is utilizing the microwave irradiation during the synthesize process which can accelerate the reaction and reduce the synthesize time [200]. Hydrothermal method involves the reduction of graphite at a high-temperature [201]. Each synthesize method has its own advantages and limitations, and the choice depends on factors such as desired properties of the graphene oxide, scalability, and the specific application requirements.

3.9. Chitosan

Chitosan is a cationic polysaccharide polymer with a linear and semi-crystalline structure. It is derived from the partial deacetylation of chitin and ranks as the second-largest naturally existing biopolymer found in the natural world [1]. Generally, when the extent of deacetylation (DD) of chitin surpasses 70% following the deacetylation procedure, it is categorized as chitosan. Nevertheless, chitosan utilized for commercial applications typically falls within the range of 70–90% DD. These DD values significantly influence various attributes of chitosan. For instance, chitosan with a higher DD enhances solubility in acidic aqueous environments, and exhibits enhanced biological and chemical characteristics [14]. The exceptional structure of high-grade chitosan, coupled with its numerous outstanding attributes, has rendered it well-suited for the creation of novel hybrid

materials designed to fulfill diverse objectives across various domains. Consequently, the surge in chitosan demand in recent times has prompted researchers to explore significant chitin sources, develops efficient extraction techniques, and devise effective conversion processes from chitin to chitosan [202]. Among all of the biopolymers, chitosan has been extensively used to manufacture electrode and electrolyte materials in supercapacitors because of its excellent mechanical strength and good ionic conductivity achieved after modification because of the ability to drive ions with pairs of electrons in –NH$_2$, –OH, and C–O–C (glycosidic linkage) groups presented in its structure [203].

Through years of study and research, scientists have created a range of chitosan-based electrodes utilizing diverse carbon-rich materials such as carbon nanodots, carbon nanotubes, graphene, and porous carbon [40, 42, 204]. Nevertheless, porous carbon has emerged as a prospective substance due to its substantial porosity, expansive specific surface area at a minimal cost of production, along with its electrochemical stability, elevated conductivity, and environmentally friendly characteristics [38]. Using chitosan as a renewable and sustainable origin for fabricating porous carbon through methods that are both environmentally conscious and economically efficient has enhanced the dependability of utilizing this auspicious material. Across numerous investigations, diverse composites aimed at electrode applications have been formulated by integrating chitosan with materials like reduced graphene oxide and polyaniline [43] graphene oxide, [205] and so on.
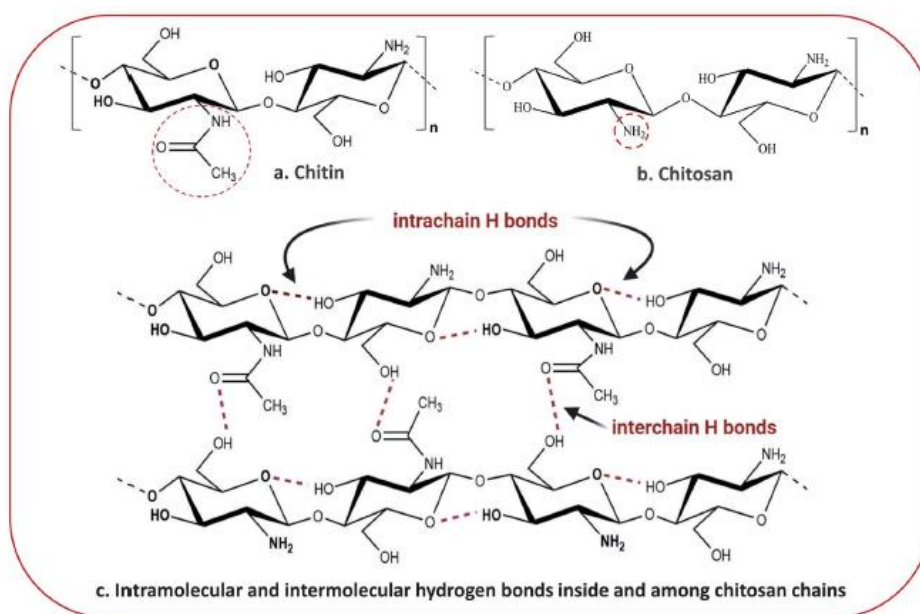
Figure 3.14. Schematic illustration of (a) chitin, (b) chitosan, (c) intermolecular and intramolecular hydrogen bonds inside and among the chitosan chain [41].

48

Within the scope of this PhD thesis, the utilization of chitosan and RGO as electrode constituents presents several advantages for supercapacitors. These advantages encompass remarkable electrochemical efficacy due to chitosan's substantial retention capacity, absence of toxicity, and adept ion adsorption onto its structure. This renders chitosan a promising contender for serving as a biocompatible electrode material, particularly in the realm of biocompatible flexible supercapacitors [39]. Hence, the primary aim of this thesis is to investigate the effect of different PVA molecular weights and PVA/KCl weight ratios on ionic conductivity and mechanical-thermal properties of gel polymer electrolytes. Secondly, how different weight ratios of chitosan in electrodes impact their morphology, structure, and electrochemical functionality of solid-state supercapacitors. The optimal weight percentage of chitosan within the RGO electrode is examined with a focus on assessing the electrode's rate capability and stability. To explore its practical applicability, a symmetric solid-state supercapacitor (RGO–chitosan//RGO–chitosan) is fabricated using PVA/KCl as the gel polymer electrolyte and subjected to comprehensive characterization.

4. LITERATURE REVIEW

In recent years, solid-state supercapacitors have had a broad range of applications in the production of wearable, textiles, and electronic equipment such as mobile phones and notebooks than conventional supercapacitors [206]. The features of these supercapacitors are small size, lightness, easy preparation, processability and convenient packaging. These supercapacitors contain flexible electrodes and solid-state electrolytes [207]. Gel polymer electrolytes among the different types of solid-state electrolytes are used to make solid-state supercapacitors due to their great ionic conductivity, proper electrochemical properties and mechanical strength [15]. Therefore, researchers have considered the electrochemical behavior of gel polymer electrolyte to increase the electrochemical performance and energy density of flexible supercapacitors. Moreover, they have prepared supercapacitors using graphene-based electrodes due to their low cost and high availability [13, 14].

In this chapter, the researches conducted in the area of gel polymer electrolytes (GPEs) and graphene-based electrodes and their effect on electrochemical performance of solid-state supercapacitors are evaluated.

4.1. Different types of gel polymer electrolytes (GPEs)

4.1.1 Proton-based gel polymer electrolytes

The supercapacitor used in flexible electronic devices must contain an electrolyte with high strainability. Zhao et al. [49] showed that the gel electrolyte with the optimum amount of acid/polymer had good ionic conductivity in different strain percentages. Figure 4.1 shows the mechanical characteristics of two gel polymer electrolytes and pure polymer.
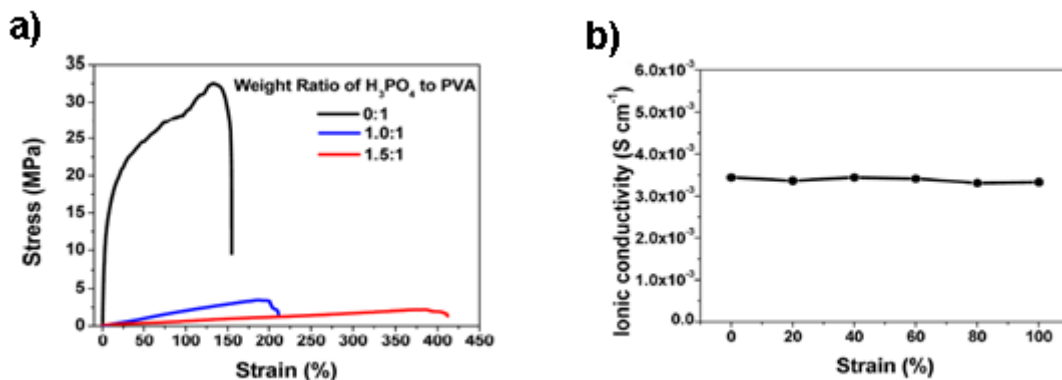
Figure 4.1. a) Stress-strain graphs of pure PVA and PVA/H_3PO_4/H_2O gel electrolytes. b) Ionic conductivity of gel electrolyte under various strains at room temperature [49].

The tensile strength and Young's modulus of the gel polymer electrolyte decrease by increasing the acid content. Moreover, the elongation at breaks increases, contributing to higher elasticity. The acid molecules enhance the amorphous phase and chain mobility of polymer. This phenomenon ultimately enhances the electrolyte's elasticity[49].

Recent studies on gel electrolytes have showed that PVA is suitable for preparing gel electrolytes due to its excellent electrochemical stability, non-toxicity and biocompatibility. In addition, the (-OH) groups on the PVA chains absorb a high water quantity and can increase ionic conductivity. Rossi et al. prepared a PVA/H_2SO_4 gel polymer electrolyte by adding various weight percentages of hydroxyethyl cellulose. Notably, the gel polymer electrolyte containing 1% weight displayed the most favorable results, demonstrating the lowest electrolyte bulk resistance alongside the highest specific capacitance of 160 F g^{-1}[26].

Due to the fast growth of portable electronic system, the request for sustainable, lightweight and flexible energy storage source is growing. Recently, there have been many efforts to design flexible supercapacitors that do not lose their electrochemical performance under different bending, twisting and tensile strains [14]. Overall performance of a flexible supercapacitor depends on electrodes, electrolyte, and cell design. Recent research shows that the improvement of the mechanical strength of flexible supercapacitors with outstanding electrochemical performance remains a major problem. Additionally, electrolyte plays a key role in supercapacitors, and solid-state electrolytes are widely utilized in manufacturing of

flexible supercapacitors because of the absence of liquid electrolyte challenge, such as leakage and corrosion [14]. Flexible supercapacitors have a multi-layer architecture, where the solid-state electrolyte is sandwiched with the electrodes. This configuration elevates the collective impedance of the complete assembly, diminishing the likelihood of effortless ion migration between the cathode and anode. Additionally, it mitigates the risk of structural deterioration when subjected to continuous stretching and folding cycles [13]. Wang et al. [74] used the in-situ polymerization method of aniline monomer in gel polymer electrolyte (PCH (PVA/H_2SO_4/Glutaraldehyde/H_2O)) with various concentrations of aniline, were able to make an integrated supercapacitor. Scanning electron microscopic images (Figure 4.2) showed that polyaniline was well distributed on the surface and sides of the electrolyte and a large amount of polyaniline nanofiber networks had grown on the electrolyte surface. The light microscope image of the cross section of the supercapacitor showed that polyaniline had penetrated well into the electrolyte and the thickness of the formed layer was 250 micrometers. The gel electrolyte had an ionic conductivity equal to 0.082 S cm^{-1}. The prepared supercapacitor showed a capacitance equal to 488 mF cm^{-2}, cycle stability up to 7000 and tensile strain equal to 300% [74].
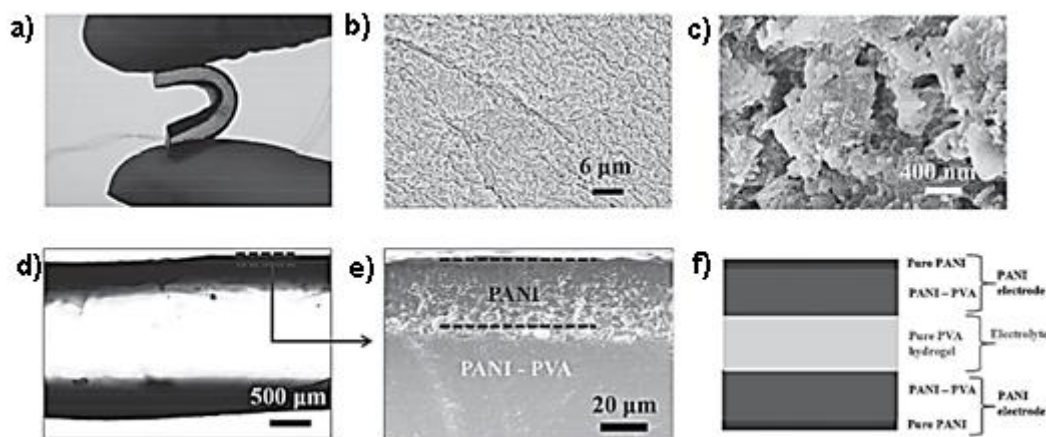
Figure 4.2. PANI-PCH film. a) PANI-PCH film, b) Surface microstructure of PANI-PCH film, c) Scanning electron microscope image with 400 nm magnification, d) Cross section of PANI-PCH film with optical microscope, e) Cross-section of PANI-PCH film with electron microscope scanning at -130 °C, f) Structural schematic of PANI-PCH film [74].

The application of carbon nanomaterials and its manufacturing methods in different shapes and sizes for supercapacitors have been widely developed. Supercapacitors consist of two electrodes and a dielectric material, which have less energy density than batteries, but a higher life cycle and power density. Recently, many efforts have been made to utilize supercapacitors in the textile industry, but preparing them in the form of fibers with the highest electrochemical efficiency is considered to be a challenge [73]. Kim et al [73] prepared fibers from carbon nanotubes and agarose. Agarose is a natural hydrophobic polymer that forms a flexible hydrogel and supplies a good conductive nature in the electrode. Electrodes were prepared using the shear extrusion process under shear force from orifices with a diameter of 0.5 to 1 mm. Carbon nanotubes were oriented to the axis of the extrusion process by applying a shear force. The smaller diameter fibers had good electrical conductivity and ions were readily available to the electrodes. Light microscope images (Figure 4.3) showed that fibers with $PVA/H_3PO_4/H_2O$ gel electrolyte are mechanically resistant and did not lose their shape under various conditions. Also, the gel electrolyte formed a coating on the surface of both electrodes without any gaps or holes and had an ionic conductivity equal to 0.056 mS cm^{-1}. Such a structure reduces the internal strength and increases the electrochemical efficiency.

The results of CV test for two different fibers with diameters of 126 and 248 micrometers are given in Figure 4.4(a). The fiber with a smaller diameter (aCNT1) had a rectangular curve, which indicates the electric double layer capacitive behavior. But for a fiber with a larger diameter (aCNT2), the shape deviates from the rectangular state and had even less current, such a system stores energy through faradic processes. Figure 4.4(b) shows the charge and discharge curves of both supercapacitors. The value of IR drop was smaller for the fiber with a smaller diameter, which indicated the good electrical properties of the electrodes and their low surface resistance against the penetration of ions. The prepared supercapacitor had a high volumetric capacitance of 1.2 F cm^{-3}, and only one percent of its capacitance reduced up to 1000 cycles under bending stress which can be used in wearable devices and textiles [73].
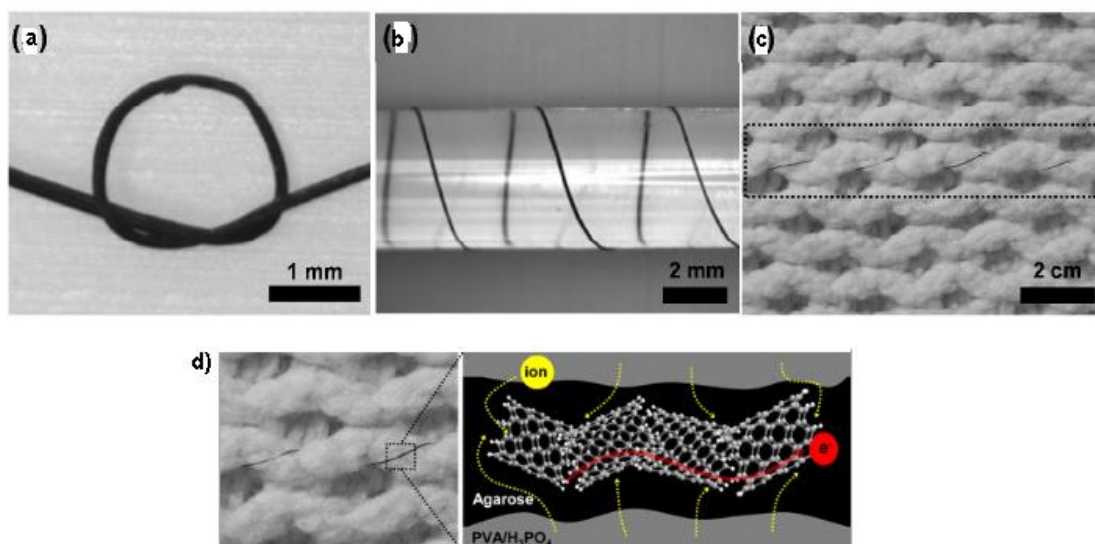
Figure 4.3. Optical microscope images of carbon nanotubes. a) tied, b) twisted around a glass rod, c) image of carbon nanotube fiber woven into a dress, d) schematic diagram of ion and electron transfer path in arranged carbon nanotubes [73].
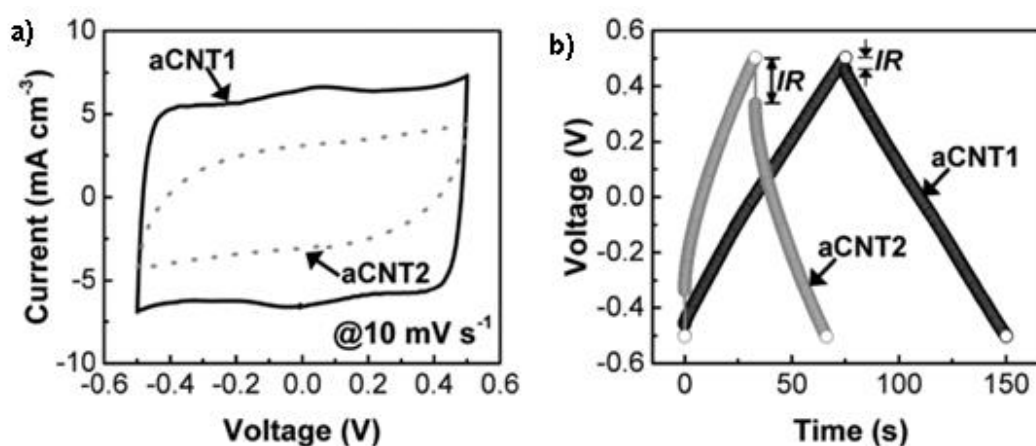
Figure 4.4. a) Cyclic voltammetry curves at 10 mV s^{-1} scan speed, b) Charge and discharge curves at 7.7 mA cm^{-3} constant current density [73].

Parajatik et al. [21] explored the influence of polyethylene glycol (PEG) as a plasticizing agent on the ionic conductivity of gel electrolyte composed of PVA/H$_3$PO$_4$. Employed X-ray diffraction identification assays, infrared spectroscopy, and differential scanning calorimetry (DSC) to examine the impact of the plasticizer on the structural characteristics of the electrolyte. The results showed that the presence of plasticizer in the electrolyte leads to an increase in the free volume as well as a reduction in glass transition temperature (T$_g$)

and an increase in ductility of the chains for the occurrence of segmental movements (Table 4.1). The optimal amount of PEG in the electrolyte was reported to be 30% by weight. More than 30% plasticizer increased the T_g and melting temperature (T_m) of the electrolyte, which is owing to the interaction between the polymer chains and the softener, increasing the crystallinity of the electrolyte. The ionic conductivity of gel electrolyte containing 30% by weight was equal to 0.086 mScm^{-1}. In fact, the presence of plasticizer increases the flexibility and ions mobility, increasing the ionic conductivity. The softener can penetrate between the polymer chains and decreases the attraction force, enhancing the chains segmental motions. A higher amount of plasticizer leads to a reduction in ionic conductivity, which is owing to a reduction in the number of ions available to pass through the polymer channels. The ionic conductivity of an electrolyte depends on temperature between 300 to 370 K which showed that as the temperature increased, the free volume of the electrolyte increased for the transport of ions through polymer chains. Also, the viscosity of the electrolyte and the activation energy for the transfer of ions from one site to another reduced and increased the ionic conductivity [21].

Table 4.1. Glass transition temperature (T_g), melting temperature (T_m) and crystallinity percentage (χ_c) for different electrolyte samples [21].

Samples	T_g (°C)	T_m (°C)	% Degree of crystallinity (χ_c)
PVA	69	224	–
PVA–H$_3$PO$_4$	65	222	35.7
PVA–H$_3$PO$_4$–10% PEG	64	220	27.1
PVA–H$_3$PO$_4$–20% PEG	57	219	21.4
PVA–H$_3$PO$_4$–30% PEG	56	219	11.8
PVA–H$_3$PO$_4$–40% PEG	68	222	30.3

4.1.2. Gel polymer electrolytes based on hydroxyl ion and salt

Due to the characteristic features of gel polymer electrolytes, they have been attracted considerable attention in fabrication of flexible energy storage devices. Gel electrolyte is a solid and flexible material that does not have the disadvantages of liquid electrolytes such as leakage and corrosion. Gel electrolyte has a network structure that holds water and increases ionic conductivity compared to solid electrolytes [14]. In general, there are two methods for preparing supercapacitors using gel electrolytes. The first method is to sandwich the electrolyte film with the electrodes. This way is easy, but the electrolyte cannot cover the surface of the active material of the electrodes well, and it leads to enhance the resistance of the whole system and decreases the energy density. The second method consists of preparing a gel electrolyte solution and adding it to the electrodes. In this method, the electrolyte solution penetrates into the electrode cavities and covers a larger surface of the electrode, reducing the interface resistance among the electrode and electrolyte, and moreover increases the durability and stability of the system [27].

Jiang et al. [27] were able to prepare a gel electrolyte using PVA/Potassium borate/KCl/H_2O on the surface of activated carbon electrodes by electrodeposition method. This method does not depend on the size and shape of the electrodes. Figure 4.5 shows the schematic of the process in which the prepared solution contains electrolyte salt, polyvinyl alcohol and boric acid, the anode is made of graphite or any other neutral metal, and the cathode is made of activated carbon. When the salt solution is electrolyzed, the pH value on the cathode surface increases and leads to the formation of barite ions ($B(OH)_4^-$). These ions create transverse connections between the polymer chains and form a three-dimensional network, and simultaneously the cations travel to the cathode under the influence of the electric field and combine with barite ions and stabilize the network centers. Eventually, a uniformly thick layer of gel is formed on the surface of the cathode [27].
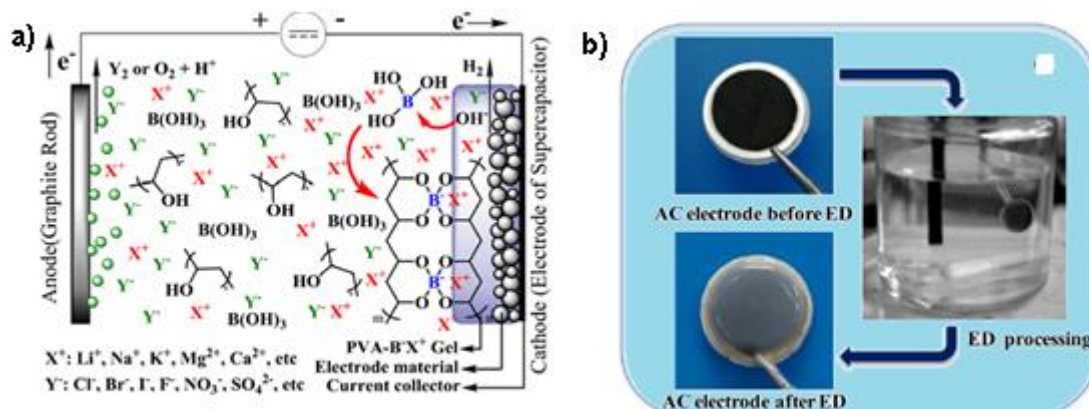
Figure 4.5. a) Schematic of the process of electric deposition of gel electrolyte, b) The surface of active carbon electrodes before and after the process of electric deposition of gel electrolyte [27].

The charge and discharge test for different concentrations of gel electrolyte salt is given in Figure 4.6(a). Electrolyte with high salt concentration had lower internal resistance and higher ionic conductivity (1.02 mS cm^{-1}) due to high charge carriers. Cyclic voltammeter graphs for different concentrations of electrolyte salt in Figure 4.6(b) were almost rectangular in shape, which showed that ions are accumulated at the interface among the electrode and electrolyte, confirming the electrical double-layer behavior. The sample with a high concentration of salt showed the highest capacitance (65.9 F g^{-1}) [27].
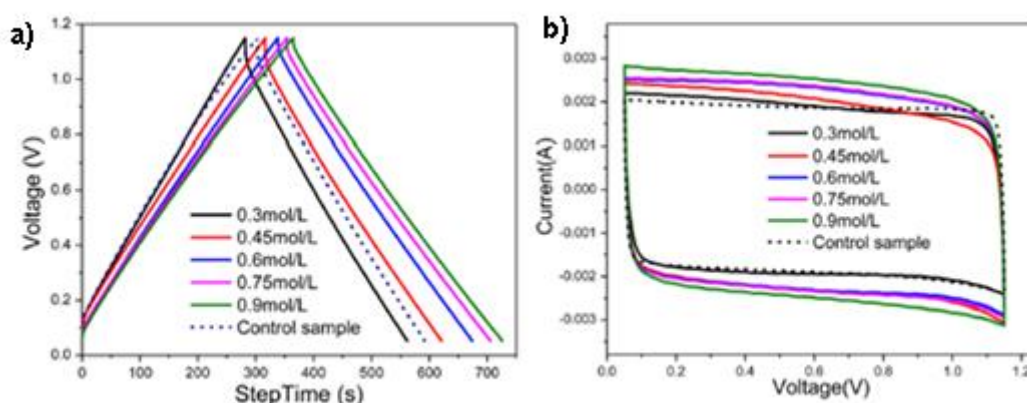
Figure 4.6. a) Supercapacitor charge and discharge curves at current density 0.1 A g^{-1}, b) Cyclic voltammeter curves at 1 mV s^{-1} scan rate [27].

In recent years, numerous efforts have been done to refine the ionic conductivity of polymer electrolytes in environmental conditions. Ions can move in amorphous phase and ionic conductivity improves by increasing the amorphous area of electrolytes. PVA has hydroxyl groups that can form hydrogen bonds and help forming the polymer electrolyte [70]. Pavani et al [70] prepared polymer electrolytes using PVA/KCl/H_2O for various weight ratios of PVA/KCl, 95/5, 90/10, 85/15. X-ray diffraction analysis (XRD) was utilized to examine the salt impact on the polymer framework. The peak at 23.6° was for pure PVA, that declined with an enhancing in the content of electrolyte salt. Hence, the crystallinity percentage of polymer decreased by increasing the amount of salt. The absence of salt-related peaks confirmed the complete dissolution of salt within the polymer matrix.

Hodge et al. highlighted a correlation between peak intensity in the XRD spectrum and polymer crystallization degree. Consequently, the decrease in peak intensity as salt content increases signifies a higher amorphous region in the polymer. The enhanced amorphous nature of the electrolyte facilitates ion penetration and improves ionic conductivity. They employed a scanning electron microscope (SEM) to investigate interfaces and phase separation within the electrolyte. By adding salt to polymer, the film's surface roughness, wrinkles and the crystalline nature of the polymer decreased. The soft morphology of the surface of the electrolytes confirms the complete dissolution of the salt in the electrolyte due to the interaction between the salt and polymer chains. The melting temperature of electrolytes had been studied by DSC test. The pure polymer showed a T_m of 465 K which was decreased by adding salt, confirming the reduction in the crystalline nature of the polymer and easy movement of the polymer chains. XRD, DSC, SEM tests confirmed the enhancement in the amorphous phase of the gel polymer electrolyte. By increasing the salt amount, ionic conductivity increased owing to the high charge carriers and ions movement and lower electrolyte bulk resistance [70].

4.1.3. Gel polymer electrolytes using ionic liquids

Supercapacitors based on liquid electrolytes, unlike solid electrolytes, always have a separator, which enhances the resistance of the entire system and its thickness. In addition, the presence of organic solvents in the electrolyte structure causes leakage and corrosion. Polymer electrolytes are of great interest because of their elasticity, flexibility, high chemical

and electrochemical stability and compatibility with electrodes. Recently, researchers showed that using ionic liquid can enhance the ionic conductivity and increase the electrochemical efficiency of the gel electrolyte owing to the enhancement of softness of polymer chains. Ionic liquids have good electrochemical and thermal stability, are non-volatile and non-flammable at room temperature. Moreover, these materials have a broad range of potential and may enhance the energy density of the supercapacitor [14, 208].

Jang et al.[208] prepared electrolytes using PVA/H_3PO_4 from ionic liquid [EMIM]BF_4 with different weight percentages of 25, 30, 75, 100 and investigated its effect on ionic conductivity. The ionic conductivity at various weight percentages of [EMIM]BF_4 is shown in Figure 4.7. The conductivity test showed that the ionic conductivity enhanced by increasing the amount of ionic liquid for the electrolyte solution and reached from 27.3 mS cm^{-1} to 39.3 mS cm^{-1} for 100% weight percentage. The highest amount of ionic conductivity of the gel is 0.78 mS cm^{-1} corresponding to 25% weight of ionic liquid. The increase of this ionic conductivity value is associated to the softening of electrolyte by the ionic liquid, which has made the polymerized chains flexible and facilitated the transfer of ions in polymer matrix. In general, electrolytes that have flexible polymer chains can increase the speed of ion movement. Additionally, the electrolyte conductivity depends on the amount of charge carriers and ion mobility. In this electrolyte, besides $H_2PO_4^-$ and H_3O^+ ions, there are also BF_4^- and EMIM$^+$ ions, which enhance the amount of charge carriers and as a result they are ionically conducted. The prepared electrolytes were combined with activated carbon electrodes and studied the electrochemical performance. The cyclic voltammeter graph of the supercapacitor containing PVA/H_3PO_4 had rectangular shape and showed the ideal double electric behavior. Incorporating an ionic liquid into the electrolyte altered the graph's shape, causing a departure from the rectangular form and resulting in broader oxidation and reduction peaks. These peaks correspond to the taking place of oxidation and reduction processes at the electrode-electrolyte interface. The electrolyte containing 50% ionic liquid by weight exhibited a significant surface area, indicating higher ionic conductivity due to the increased ion concentration in the electrolyte [208].
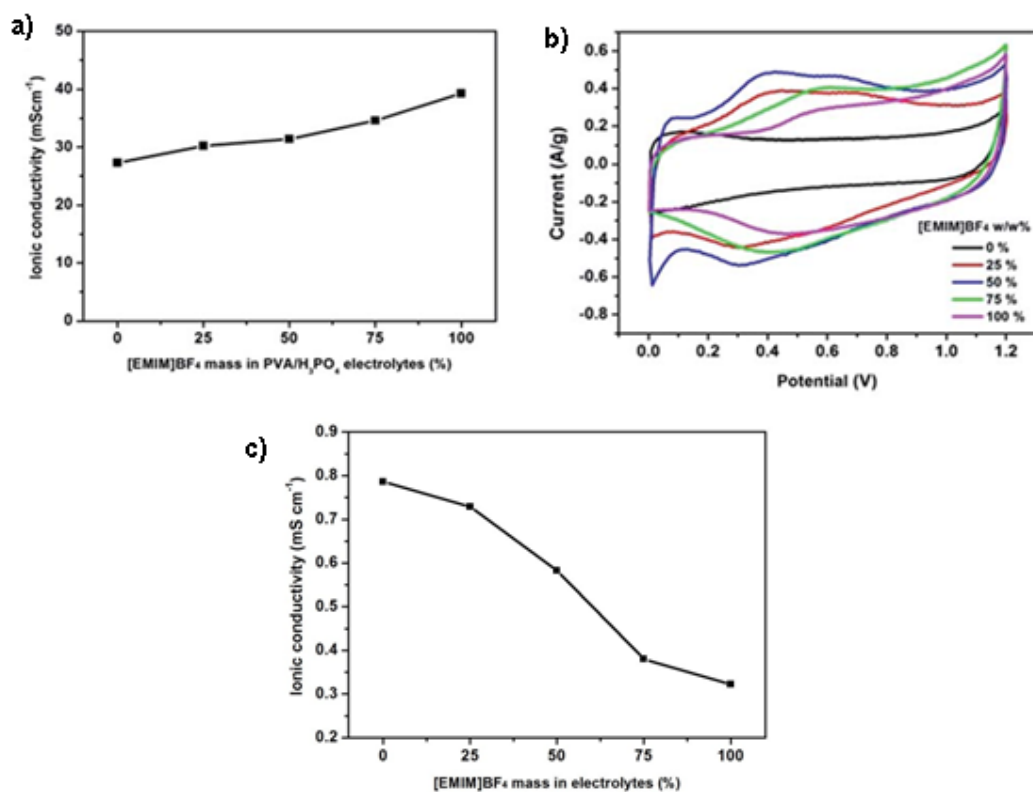
Figure 4.7. a) Ionic conductivity of electrolytes with conductivity meter in different weight percentages of [EMIM]BF$_4$ b) Cyclic voltammeter curves in various weight percentages of [EMIM]BF$_4$ for a scanning speed of 5 mV s^{-1}, c) Ionic conductivity of gel electrolytes with Impedance spectroscopy test in various weight percentages of [EMIM]BF$_4$ [208].

4.1.4. Gel polymer electrolytes containing redox active materials

To make flexible supercapacitors, besides the preparation of flexible electrodes, electrolyte development plays a key role. One of the main characteristics of an electrolyte is having sufficient mechanical strength and great ionic conductivity. Among the various types of electrolytes, gel polymer electrolyte is widely used in supercapacitors due to its good film-formation ability, flexibility, easy design, and no need for a separator. Acids and bases are used to increase the ionic conductivity because the dynamic movements of hydroxyl ions and protons are high. The redox active material increases the capacitance of the supercapacitor by performing reversible and rapid oxidation and reduction reactions [209].

Sun et al. [209] added the redox substance 2-mercapto pyridine (PySH) to PVA/H$_3$PO$_4$/H$_2$O gel electrolyte and studied the electrochemical properties and ionic conductivity performance. The electrolyte exhibited good tensile and bending characteristics and was

stretched to twice of its original length and even curved in a circular and spiral shape without breaking. All of the films had recovered to their original form and length after the tension had been cut. Also, mechanical tensile test data indicated that the elongation at the breaking point for $PVA/H_3PO_4/H_2O$ gel electrolyte is 311.93% and for the electrolyte consists of PySH is 392.17%. Thus, adding the reducing agent enhanced the mechanical properties and flexibility of the gel electrolyte. Figure 4.8 (a) exhibits the impact of PySH value on the electrolyte ionic conductivity. When the value of PySH was lower than 0.17 gr, the ionic conductivity increased and showed the optimal value of 22.57 mS cm^{-1}. Because this material performs oxidation and reversible reduction reactions at electrode surface, releasing multiple ions throughout the free volume of the polymer matrix. When the amount of PySH was more than 0.17 gr, the ion conductivity decreased due to the formation of ions clumps. The results of the cyclic voltammeter test prepared with both types of electrolyte at 10 mV s^{-1} scan rate in the voltage range of -1 to 1 V are given in Figure 4.8(b). The supercapacitor using PVA/H_3PO_4 electrolyte showed a rectangular curve, which expressed energy storage by accumulating of ions at the electrode/electrolyte interface. Furthermore, by adding reducing agent to the electrolyte, strong redox peaks occur at -0.25 and 0.25 V, associated to the oxidation and reduction of PySH. Because of the low potential difference between the oxidation and reduction peaks and the symmetry of the charge and discharge reaction, the process of oxidation and reversible reduction process had happened [209].

Figure 4.9 shows the results of the electrochemical impedance test for the supercapacitor based on both electrolytes in the frequency between 100 mHz and 100 kHz. The equivalent electric circuit is given in the appendix of the figure. R_{esr} is the equivalent series resistance, R_{ct} is the interface resistance among the electrode and electrolyte, C_{dl} is the capacitance of the two layers, and W is the Warburg element. In the impedance curve of supercapacitors, both of the electrolytes have a small high frequency semicircle and a sloping line at low frequency, which indicates the Warburg resistance of ions or the penetration of ions. The electrolyte consists of PySH not only had a less bulk resistance, but also showed a lower charge transfer resistance because it increased the interaction among the electrode and electrolyte and improved the electrochemical characteristics of the electrolyte [209].
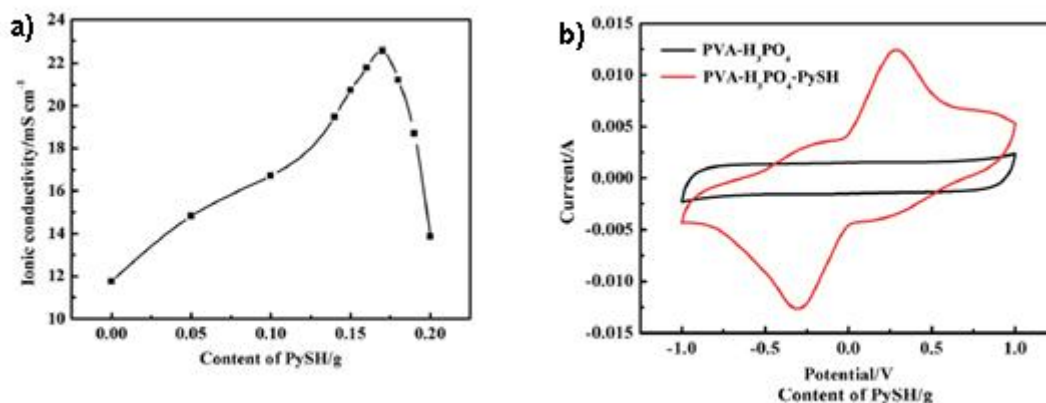
Figure 4.8. a) Ionic conductivity of the gel electrolyte for different amounts of PySH, b) Cyclic voltammeter curves of supercapacitor with PVA/H$_3$PO$_4$ and PVA/H$_3$PO$_4$/PySH gel electrolytes at 10 mV s^{-1} scan speed [209].
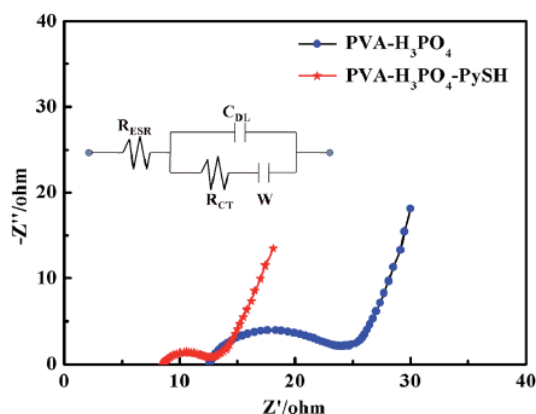
Figure 4.9. Electrochemical impedance graphs of supercapacitor with PVA/H$_3$PO$_4$/H$_2$O and PVA/H$_3$PO$_4$/PySH gel electrolytes [209].

Liquid electrolytes containing acid, base or salt are broadly utilized as electrolytes in the production of supercapacitors as they have high ionic conductivity and low price, but due to the leakage of materials, they are not useful in the preparation of flexible supercapacitors. Recent studies have been showed that adding a reducing active substance to an electrolyte can increase the supercapacitor capacitive feature. These materials directly participate in the oxidation and reduction reaction of electron transfer, and the supercapacitor electrochemical

efficiency at the electrode-electrolyte interface is enhanced by quasi-capacitance distribution of these materials [210].

Sun et al. [210] added allirazine (ARS) to PVA/H$_3$PO$_4$/H$_2$O gel electrolyte and investigated its mechanical and electrochemical properties. ARS contains hydroxyl groups and is easily soluble in water. The gel electrolyte was prepared in various amounts of ARS and indicated the highest ionic conductivity in the amount of 0.5 g. The results showed that the ionic conductivity of the electrolyte is enhanced with an adequate amount of ARS, which has a softening role, and an excessive amount of this substance causes clumping of free ions and phase separation, making the ions transfer more difficult and reduces the ionic conductivity [210].

4.1.5. Composite gel polymer electrolytes

Developing gel electrolytes with high electrochemical performance for industrial applications is growing day by day. One of the ways to enhance the electrochemical and mechanical characteristics of gel electrolyte is to use additives such as nano silica, titanium dioxide, graphene oxide, etc. The amount of specific surface area and the chemical structure of these materials have a significant effect on ionic conductivity. Adding these nanoparticles to the electrolyte forms a composite polymer electrolyte in which solid particles with a large surface area can change many of the electrolyte chemical and physical features like ionic conductivity and mechanical properties [211].

Huang et al. [211] prepared PVA-KOH-GO based polymer electrolyte composite and considered the effect of graphene oxide (GO) on electrochemical properties. The PVA chains were cross-linked with boric acid (B-PVA) in which the boron atoms can enhance the mechanical features and ionic conductivity of the electrolyte. GO with a very high specific surface area contains a significant amount of oxygenated functional groups, facilitating the ions transport and increases the ionic conductivity of electrolyte. Figure 4.10 shows the results of the infrared spectroscopy test. The peak at 654 cm^{-1} is related to the bending of O-B-O groups, and the intensity of the –OH peak in PVA is reduced by adding boron and graphene oxide. The polymer chains are limited by boron atoms and graphene oxide sheets, and even boron atoms had interacted with graphene oxide sheets, that such a structure may

have a key role in the electrolyte ionic conductivity. Figure 4.11 indicates the effect of the GO amount on ionic conductivity. For electrolyte without boric acid, it had more ionic conductivity than the liquid electrolyte, which is owing to the presence of PVA and GO, both of which consists polar groups and facilitate the ions transfer. But when the amount of graphene oxide increased, these sheets form clusters and block the ion transport pathways. By adding boric acid, the ionic conductivity increased in a lower amount of graphene oxide, because boron atoms can enter the GO structure and open the closed paths of ion movement or shorten the ion transport path and increases the ionic conductivity [211].
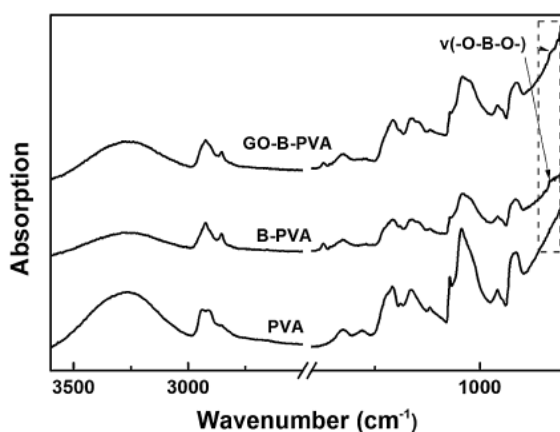
Figure 4.10.   FTIR curves of PVA, B-PVA and nanocomposite containing graphene oxide [211].
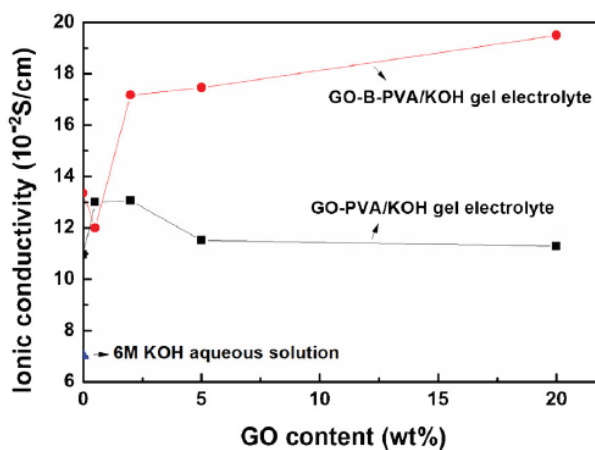
Figure 4.11.   Ionic conductivity of gel electrolyte for different amounts of graphene oxide [211].

Energy storage devices based on polymer and composite electrolytes have many advantages over liquid electrolytes, such as good thermal and chemical stability and preventing leakage and corrosion by solvents. Among the types of polymers used, PVA can be a source for forming hydrogen bonds due to its hydroxyl groups. Recently, adding inorganic fillers such as ZrO_2 (zirconium oxide), Al_2O_3 (aluminum oxide), etc. to polymer electrolytes may increase the ionic conductivity, mechanical and electrochemical stability [212]. Lim et al.[212] prepared PVA/LiClO$_4$ based electrolyte consists TiO_2 nanoparticles and investigated its impact on ionic conductivity and structural features of polymer matrix. Figure 4.12 shows the electrolyte ionic conductivity in terms of temperature for different amounts of nanofiller. The linear relation between ionic conductivity with temperature showed that the polymer electrolyte follows the Arrhenius theory and the ionic conductivity enhanced by increasing temperature. In fact, the segmental movements of polymer chains enhances and the charge carriers movement (Li^+) from one site to another nearby site increases, called mutation mechanism. The bond between oxygen atoms from the polymer chain and Li^+ at higher temperatures becomes weaker. This interaction causes the separation of charge carriers from polymer chains and forms empty sites. Therefore, the Li^+ ion moves from the adjacent site to the empty site and re-aligns itself in the chain, and the increase in temperature causes the acceleration of ions movement and increased the ionic conductivity. The activation energy, which shows the energy required to overcome the deformation of polymer chains with Li^+, is derived from the slope of the ionic conductivity curve in terms of temperature. The activation energy depends on the amount of TiO_2, and 8% by weight of this material had the lowest activation energy, and in fact, less energy is required to break the chemical bonds in the polymer network [212].

Figure 4.13(a), shows the XRD spectrum of the three components of the electrolyte. The diffraction peak at the angle of 19.8 degrees indicates that PVA has semi-crystalline character. The characteristic peaks of TiO_2 are at 2.25, 27.4, 36, 41.1, 54.2 degrees while for LiClO$_4$ they are at 21.23, 31.3, 35.7, 39.1 degrees. XRD spectra of electrolytes are given in Figure 4.13(b). While there was no TiO_2 in the gel, the characteristic peak at 31.3° corresponds to the crystalline structure of LiClO$_4$, which indicates that this material is not completely decomposed and recrystallized in the polymer matrix. From the intensity of the peak, it is possible to evaluate the properties of the electrolyte being amorphous. The intensity of the peak at the angle of 19.8° has become lower and wider, indicating that

$LiClO_4$ has changed the arrangement of the polymer segment. By adding 2 wt% of TiO_2, the intensity of the peak did not change, exhibiting there was any change in the amorphous nature of polymer, however the peak intensity decreased by increasing the amount of TiO_2. Pure PVA showed a higher amount of crystallization owing to the presence of hydroxyl groups on its side chains. The crystallinity of the polymer decreased by the addition of $LiClO_4$ and TiO_2, because the hydroxyl groups of PVA react with salt and nanofiller. The higher degree of amorphousness of the gel polymer electrolyte causes the ductility of polymer chains and enhances the ion mobility and ionic conductivity. Adding TiO_2 reduced the size of crystals, increasing the flexibility of the polymer chains and ionic conductivity. The electrolyte containing 8 wt% of TiO_2 showed a less peak intensity and a smaller crystal size, indicating the high amorphous area of the electrolyte and its ionic conductivity [212].
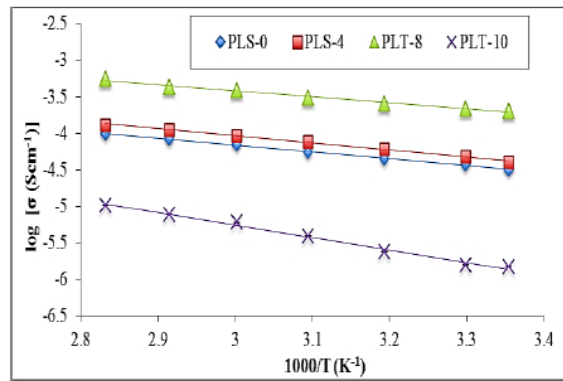
Figure 4.12.   Arrhenius curves of ionic conductivity of electrolytes with different amounts of TiO_2 [212].
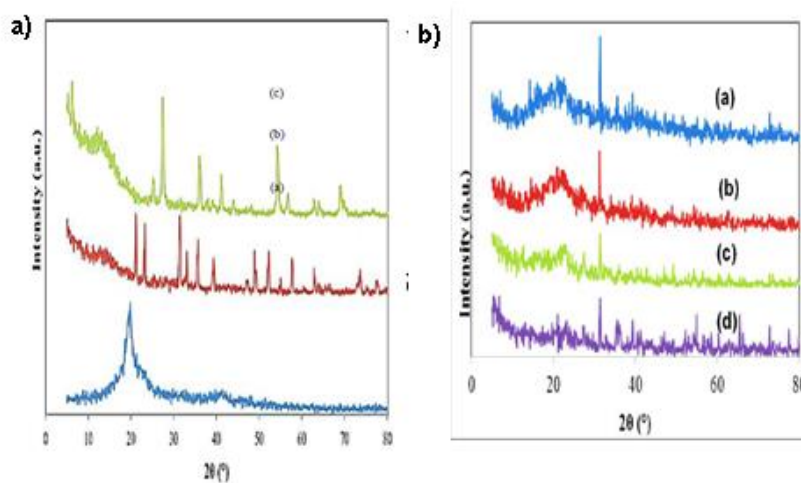
Figure 4.13. X-ray diffraction patterns a) (a) PVA, (b) $LiClO_4$, (c) TiO_2, b) PLT-0 (a), (c) PLT-8, (d) PLT-10, (b) PLT-4 [212].

Table 4.2.   Ionic conductivity of PVA- based gel polymer electrolytes.

Electrolyte	Molecular weight of polymer (g/mol)	Weight ratio (w/w) of Polymer: Electrolytic salt or other components	Ionic conductivity (mS cm^{-1})	Ref
PVA/H_3PO_4/H_2O	124,000–186,000	1:1 1: 1.5	0.96 3.44	[49]
PVA/H_3PO_4/H_2O	95,000	1: 0.8	0.056	[73]
PVA/H_3PO_4/H_2O PVA/H_3PO_4/PEG/H_2O	125,000	1: 0.4	0.00152 For 30% wt of PEG: 0.086	[21]
PVA/Potassium borate/KCl/H_2O	74,800 ± 50	…	1.02	[27]
PVA/H_3PO_4/H_2O PVA/H_3PO_4/[EMIM]BF_4 /H_2O	130,000	1: 0.8	0.78 For 100% wt of [EMIM]BF_4: 0.33	[208]
PVA/H_3PO_4/H_2O PVA/H_3PO_4/PySH/H_2O	…	1:2 1: 2	11.58 For 0.17 g of PySH: 22.57	[209]
PVA/H_3PO_4/Cellulose/H_2O	…	1:0.4	0.104	[213]
PVA/H_2SO_4/Glutaraldehyde/H_2O	…	1:0.5	82	[74]
PVA/H_2SO_4/H_2O PVA/H_2SO_4/IC/H_2O	…	1:1 1:1	7.1 20.27	[214]
PVA/H_3PO_4/SiWA/H_2O	85,000–124,000	1:1.2	8	[215]
PVA/KOH/TiO_2/Glutaral dehyde /H_2O	74,800	…	For 15% wt of TiO_2 : 48	[216]
PVA/PVP/KOH/H_2O	30,000–70,000	1:0.5	$(1.5 \pm 1.1) \times 10^{-1}$	[52]
PVA/H_3PO_4/H_2O	98,000	1:2	2.56	[53]
PVA/Boric acid/GO/KOH/H_2O	…	…	For 20% wt of GO: 195	[211]
PVA/H_2SO_4/H_2O		1:2	11.4 For 0.5 g ARS: 33.3	[210]

PVA/H_2SO_4/ARS/H_2O				
PVA/LiCLO$_4$/TiO$_2$/H_2O	…	…	For 8% wt of TiO$_2$: 0.000126	[212]
PEO/PVDF/DMF	PEO: 1000,000 PVDF: 900,000	PEO:PVDF; 0.5:1	2	[22]
PEO/LiCF$_3$SO$_3$ PEO/LiCF$_3$SO$_3$/Al$_2$O$_3$ PEO/LiCF$_3$SO$_3$/PEG PEO/LiCF$_3$SO$_3$/DOP	PEO: 6000,000 PEG:6000	1:0.15 1:0.15:0.20 1:0.15:0.20 1:0.15:0.20	0.001 ± 0.215 0.0864 ± 0.694 0.00873 ± 0.027 0.760 ± 11.473	[23]
PEO/PA-LiFTSI/THF	PEO: 450,000	PEO/PA-LiFTSI; 1:1	0.0177 at 80 °C	[217]
PEO/PMMA/Lithium iodide/iodine/4‑tert‑butyl pyridine	PEO: 100,000 PEO: 120,000	PEO/PMMA; 1:9	7	[54]
PMMA/Pr$_4$N+I/PC/EC		20/30/30/40	5.02	[24]
PVDF/PMMA/LiTFSI/EMITFSI/NMP		PVDF/PMMA; 10/90	3.097	[218]
PMMA/[Eimm]BF$_4$/ LiClO$_4$/PC PMMA/ LiClO$_4$/PC	PMMA: 996,000	PMMA/[Eimm]BF$_4$ / LiClO$_4$; 0.9/ 1/8.1	2.9 1.7	[219]
PMMA- 1-methyl-3-trimethoxysilaneimidazolium chloride, (IL)-TFSI/LiTFSI/PC	PMMA: 180,000	0.11:1	3.47	[220]
PEO/KOH PVA/PEO/KOH	PVA; 130,000 PEO; 100,000	PVA/PEO; 5/5	0.0001 10	[55]
PVDF-HFP/HDPE/DMF	PVDF-HFP; 47,000	22:1	2.97	[221]
PVDF-HFP/[EMIM]BF$_4$/GO/DMF		1/2/0.01	25	[19]
PVA/LiClO$_4$/H_2O PEO/LiClO$_4$/H_2O CMC/LiClO$_4$/H_2O			48 21 35	[56]

PVDF-HFP/([PMpyr][NTf$_2$]/THF	PVDF-HFP; 400,000	20:80	1.596	[222]
PVDF-HFP/PMIMTFSI PVDF-HFP/0.4M LiTFSI/PMIMTFSI PVDF-HFP/0.4M LiTFSI/PMIMTFSI/(EC+PC)	PVDF-HFP; 455,000	80:20 0.4M LiTFSI 60:20:20	6.09 ± 0.08 9.50 ± 0.08 14.8 ± 0.08	[223]
PVA/H$_3$PO$_4$/H$_2$O	27000 27000 61000 61000 125000 125000 195000 195000 195000	1:0.5 1:1 1:0.5 1:1 1:0.5 1:1 1:0.5 1:1 1:2	4.76±0.18 13.26±0.84 4.38±0.18 10.32±0.19 2.82±0.06 7.46±0.55 2.50±0.07 6.51±0.23 14.75±1.23	[51]
PVA/H$_3$PO$_4$/GO/H$_2$O	195000	1:2	SAGO amount: 0.01; 21.08±0.09 0.02; 23.23±1.57 0.05; 26.76±0.95 0.1; 29.21±0.06 0.2; 25.13±0.97 0.5: 22.36±0.47 1; 20.74±0.78 2; 13.46±2.90 10; 7.84±0.31 LAGO amount: 0.01; 19.45±0.78 0.02; 20.57±0.54 0.05; 23.85±0.23 0.1; 21.36±0.88 0.2; 20.84±0.72	[48]

			0.5; 19.22±0.90	
			1: 12.02±0.79	
			2; 7.29±1.70	
			10; 5.46±0.22	
B(borax)-PVA/KCl	…	…	32.6	[224]
B(borax)-PVA/KCl/GO			For 2.3 wt% GO: 47.5	
PVA-H$_3$PO$_4$-KCl	115000	…	For 25 wt% KCl: 4.38	[45]
PVA-H$_3$PO$_4$-KCl-Carbon black (CB)			For 50 wt% KCl: 7.32	
			For 75 wt% KCl: 10.71	
			For 75wt% KCl and 10 wt% CB: 11.02	
			For 75wt% KCl and 15 wt% CB: 11.73	
			For 75wt% KCl and 25 wt% CB: 12.71	
			For 75wt% KCl and 50 wt% CB: 13.65	
PVA/H$_2$SO$_4$/PEG/glutaral dehyde (GA)	PEG, molecular weight: 20000	…	67.1	[50]
PVA-KOH	…		7.5	[44]
PVA-KOH-KCl			0.43	
PVA-KOH-(0.0005)mol K$_3$[Fe(CN)$_6$]			9.1	
PVA-KOH- (0.001) mol K$_3$[Fe(CN)$_6$]		1:0.46:0.46:0.4	0.21	
PVA-KOH-KCl-(0.001) mol K$_3$[Fe(CN)$_6$]			0.71	
PVA/H$_3$PO$_4$			4.1	
PVA/H$_2$SO$_4$			5.2	

PVA/boric acid (BA)/ 1-ethyl-3-methylimidazolium chloride (EmimCl)	Polyvinyl alcohol (PVA) with an alcoholization degree of 96−98% and a polymerization degree of 1750 ± 50	…	2.43	[225]
PVA–GB- guanosine (G)–boric acid (B)	…	…	70	[226]
PVA/ KI+I_2 (Potassium iodide (KI) and iodine (I_2))	72000	…	For PVA 0.8: 8.41	[227]
Boron cross-linked(B)-PVA/KCl	PVA with average polymerization degree of 1750 ± 50 and hydrolysis degree of 97%	…	38	[228]
PEI−PVA−(4-formylphenylboronic acid (Bn)) Bn-LiCl PEI−PVA−Bn-NaCl PEI−PVA−Bn-KCl PEI−PVA−Bn-AMC	PEI (Mw = 600, 1800, 10 000 g mol^{-1}, purity 99%), PVA (type-1799, DP: 1700, Mw: ~79 000 g mol^{-1}, alcoholysis: 99.8−100%)		15.41 13.85 8.93 4.15	[75]
PVA/LiCl	…	1:1	8.2	[229]
polyvinyl alcohol (PVA) and aqueous HCl solutions	…	…	0.7-2.2	[230]
(BMIMBF$_4$)IL/PVA/H$_2$SO$_4$ PVA/H$_2$SO$_4$	…	0.5:1:1	90.09 38.36	[231]

PVA/KCl	polyvinyl alcohol (Mw. 125 000)	…	1.5 wt% KCl: K-4: 0.0544	[46]
PVA/ Methacrylic Acid Ethyl acrylate(MAA:EA)/KCl	PVA of molecular weight 17,000	42.5:42.5:1	15 wt% of KCl salt: 0.000185	[47]
PVA/KOH/ P-phenylenediamine (PPD)	PVA molecular weight 44.05 MW, alcoholysis: 99.8-100%	1:1: 0-0.16 g	0.08 g of PPD: 25	[232]
PVA-H_2SO_4	PVA (average polymerization degree: 1750 ± 50)	…	136.4	[233]
PVA-H_2SO_4	…	…	17.3	[234]
PVA/ Kappa-carrageenan (KC)/KOH	Polyvinyl alcohol (PVA 1799, molecular weight about 75000, alcoholysis: 99%)	…	210	[235]

4.2. Solid-State Supercapacitors using Graphene

Supercapacitors have been broadly utilized in portable electronic devices owing to their high power density, excellent reversibility, high capacity, low cost, and long cycle-life. Recently, many attempts have been done to develop electrode materials with superior electrochemical characteristics which play a crucial role in an electrochemical supercapacitive system [236]. He et al. [236] developed, an easy, two-step, top-to-bottom plan for making thin, (PVA/H_3PO_4) gel electrolyte and graphene/graphite paper-type electrodes. The ductile and fully robust supercapacitor are highly efficient, like after 20,000 cycles shows a large ~3.6 F cm^{-3} volumetric capacitance. In particular, the supercapacitors exhibited outstanding rate characteristic with exceptionally retention of up to 94% of specific capacitance by enhancing the current density from 0.5 to 5 A cm^{-3} [236].

Gao et al. [237] prepared chitosan (CS)/reduced graphene oxide (rGO) composite (CRG) by microwave-assisted hydrothermal process away of other carbonization. The specific surface area is improved due to the homogeneous dispersion of CS among the rGO sheet. By removing the water molecules between CS and rGO, NH-C=O groups has been formed that may assist the humidity and conductivity of the compound. CRG indicated an elevated 274 F g^{-1} specific capacitance at a current density of 0.5 A g^{-1}, as utilizing as additive-free electrode. Solid-state supercapacitor using both lignin hydrogel as electrolyte and CRG as electrode, provided a 8.4 Wh kg^{-1} energy density at 50 W kg^{-1} power density [237].
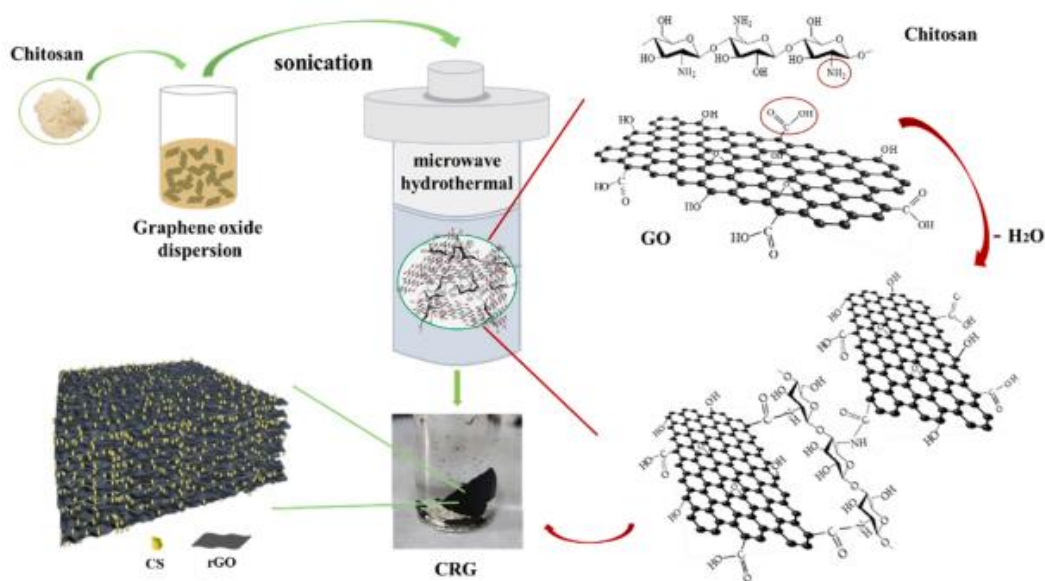
Figure 4.14.   A schematic description for the preparation process of CRG [237].

The specific capacitance of various samples are illustrated in the GCD curves at 0.5 A g^{-1} (Figure 4.15 (a)). The current response time of CS is rapid and brief, displaying a balanced and symmetric behavior characteristic of EDLC, with a specific capacitance of 72 F g^{-1} at 0.5 A g^{-1}. Both rGO and CRG exhibit symmetrical GCD curve shapes with an inflection point within the potential range of 0.4-0.6 V, indicating a combination of EDLC and pseudocapacitive behavior. At 0.5 A g^{-1}, the specific capacitance of rGO ranged at 205 F g^{-1} due to the presence of developed micro-mesopores and oxygen-containing groups. In the case of CRG, the specific capacitance reached 274 F g^{-1} at 0.5 A g^{-1}. The increased

abundance of N-5, N-6, and O-I contributes to the elevated pseudo-faradaic capacitance in an acidic electrolyte, which in turn contributes to the high capacitance of CRG. Moreover, the NH–C=O groups have the potential to enhance wettability and electrical conductivity, and the sandwich structure of CRG expands the contact area between the electrode and electrolyte, both of which positively impact capacitance. Figure 4.15 (b) shows that at 5 A g^{-1} current density, the specific capacitance of the CS, rGO and CRG samples were 55, 166 and 228 F g^{-1} and at the 0.3 A g^{-1} current density, it retains 71.4 %, 75.8 % and 76.1 % of capacitance, respectively. At a high scan rate, the micro-, meso- and macropores may facilitate the transport of electrolyte ions and capacitance retention, assuring the high rate capacity [237].
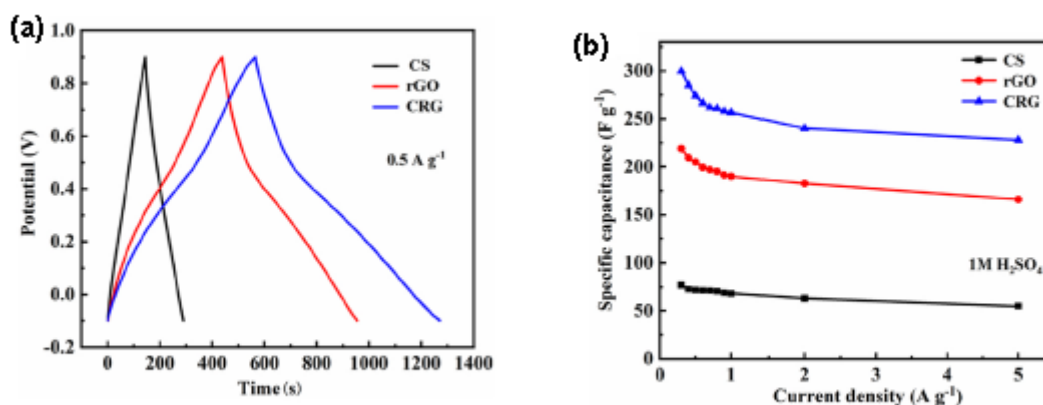
Figure 4.15. Electrochemical performance at three-electrode system for CS, rGO and CRG samples in 1 M H₂SO₄, (a) GCD curves at 0.5 A g^{-1}, (b) Specific capacitance at various current densities [237].

Recent researchers have been showed that flexible supercapacitors as wearable energy storage devices have attracted considerable attention. Graphene has been widely utilized as supercapacitor electrodes, principally because of wide specific surface area, great electrical conductivity and chemical durability. As a result, the graphene-based hydrogels with less expenses, great specific surface area, and outstanding mechanical strength is of major importance for versatile and portable energy storage devices [84]. Ren et al. [84] made oxygen-doped activated carbon/graphene compound hydrogels through a hydrothermal approach. In this hydrogel, the activated carbon has great specific surface area which is originated from chitosan containing oxygen groups which are designed within the reduced

graphene oxide (rGO) structure to strongly hinder the restacking of rGO nanosheets and achieve great surface area and conductivity of the hydrogels, resulting in outstanding energy storage performance. The optimum sample exhibited a 375.7 F g^{-1} specific capacitance at 1 A g^{-1} current density in 1 M H_2SO_4 electrolyte. Moreover, after 5000 charge/discharge cycles at 10 A g^{-1}, the supercapacitor exhibited 83% cycling stability. Figure 4.16 (a–f) shows the microstructure of the resulting material. Powdered oxygen-doped activated carbon (OAC) exhibits a granular structure with a surface covered in pore-rich honeycomb microstructures (Figure 4.16 (a and b)). This is achieved through the carbon activation method. Freeze-dried graphene hydrogels (GH) (Figure 4.17 (c)) showcase a 3D porous arrangement with varying sizes of micro- and meso-pores, facilitating the transportation of electrolyte ions. This porous structure is formed through a synergistic effect during the hydrothermal process, where GO sheets undergo reduction to form rGO. The microstructure of the composite oxygen-doped activated carbon/graphene hydrogels (GOAC2, GOAC3, and GOAC4) is depicted in Figure 4.16 (d–f). These products, denoted as GOAC2, GOAC3, and GOAC4, correspond to weight ratios of GO to OAC at 2:1, 3:1, and 4:1, respectively. It is evident that all composite hydrogels consist of a network of porous graphene nanosheets with active carbon enveloped at their core [84].
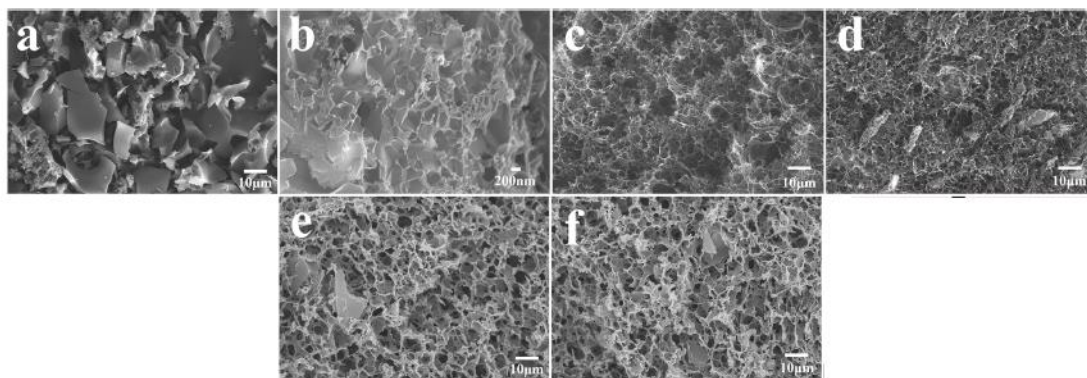
Figure 4.16. FESEM images of freeze-dried hydrogel samples (a and b). OAC; (c) GH; (d) GOAC3; (e) GOAC4; (f) GOAC2 [84].

The electrochemical performance assessment of both graphene hydrogel (GH) and composite electrodes employing 1 M H_2SO_4 as the aqueous electrolyte had been conducted through a three-electrode system. Figure 4.17(a) displays the charge-discharge (GCD) profiles of all electrodes at a current density of 1 A g^{-1}. The RGO charge-discharge curves

exhibit the characteristic symmetrical triangular shape indicative of a double-layer capacitor behavior. Comparatively, the capacitive performance of the composite oxygen-doped activated carbon/graphene (GOAC) is notably improved over GH, with GOAC3 exhibiting the most favorable capacitive performance. At 1 A g^{-1} current density, the specific capacitance values for GH, oxygen-doped activated carbon (OAC), GOAC4, GOAC3, and GOAC2 are 206.6, 215.2, 327.8, 375.7, and 235 F g^{-1}, respectively. The rate capability of GOAC3 stands out, owing to its interconnected 3D porous structure. While the introduction of OAC substantially enhances the capacitive properties of the graphene hydrogel material, increasing the ratio of GO to OAC from 3:1 to 2:1 results in reduced specific capacitance, possibly due to a reasonable addition of OAC leading to decreased cross-linking between GO sheets. Figure 4.17 (c) illustrates the cyclic voltammetry (CV) test outcomes of GH and GOAC3 electrodes. Notably, the GOAC3-based electrode at a scan rate of 5 mV s^{-1} displays larger current and integral area compared to the GH-based electrode, signifying superior electrochemical performance. Clear redox peaks are observed in both electrodes, attributed to the oxygen-containing functional groups present in OAC and GH, contributing to additional pseudo-capacitance and increased specific capacitance.

Further insight into the capacity features of the composite electrodes is gained through the Nyquist curve, as depicted in Figure 4.17 (d). Both GH and GOAC3 electrodes exhibit nearly vertical lines in the low-frequency region, indicating an almost ideal charging and discharging process. In the high-frequency region, the point of intersection with the real impedance axis reflects the ionic resistance of the electrolyte. Notably, the R_{ct} (charge transfer resistance) of the GOAC3 electrode (1.19 Ω) is smaller than that of GH (2.62 Ω), suggesting a more effective electrode/electrolyte interfacial charge transfer. The utilization of activated carbon material within graphene hydrogel facilitates ion transfer due to the larger specific surface area and sufficient space for ion migration within the porous framework. The GCD test results for the GOAC3 electrode at varying current densities (0.5–10 A g^{-1}) are presented in Figure 2.17 (e). These results exhibit nearly triangular shapes, indicating standard double-layer behavior with high columbic efficiency. Across different current densities, the specific capacitances of the GOAC3 electrode range from 389.5 to 266 F g^{-1}, showcasing an exceptional rate capacity of 68.3%. Furthermore, the CV curves of the GOAC3 electrode at various scan rates (Figure 4.17 (f)) display slightly distorted rectangular

shapes, attributed to the presence of oxygen-containing functional groups within OAC and graphene sheets [84].
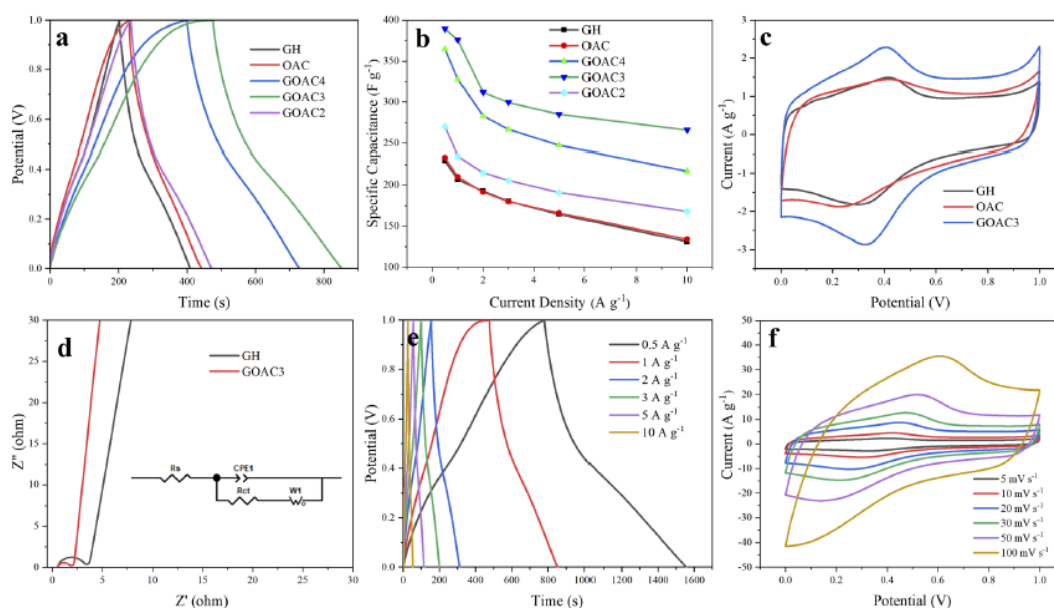
Figure 4.17. (a) GCD graphs of all electrodes at a 1 A g^{-1} current density; (b) Specific capacitance of GH, OAC, GOAC4, GOAC3 and GOAC2 electrodes at various current densities; (c) CV curves of GH, OAC, and GOAC3 electrodes at 5 mV s^{-1} scan rate; (d) Nyquist plots of GH and GOAC3 electrodes; (e) GCD curves of GOAC3 electrode at various current densities; (f) CV curves of GOAC3 electrode at various scan rates [84].

The research investigation of Salleh et al. [85] focused on evaluating the impact of varying mass percentages of chitosan as a binder in graphene electrodes on their electrochemical performance. Microstructural and structural tests were conducted to assess the homogeneity and distribution of the chitosan binder. Electrochemical efficiency and cycle-life of these electrodes for supercapacitor applications were studied using cyclic voltammetry (CV) and galvanostatic charge-discharge (GCD) tests. The optimal mass percentage of chitosan binder was found to be 10 wt%, resulting in favorable homogeneity and interaction. The electrode exhibited the highest specific capacitance of 135.65 F g^{-1} and maintained 87.2% retention over repeated charge-discharge cycles.

In the case of the asymmetric supercapacitor (MnO$_2$–graphene–chitosan//graphene–chitosan), an energy density of 80.40 Wh kg^{-1} at a power density of 2894.61 Wh kg^{-1} was

achieved. Furthermore, 74.18% of the initial capacitance was retained after 1000 cycles at 1.2 A g^{-1}. The graphene electrode containing 10 wt% chitosan binder displayed exceptional characteristics. The X-ray diffraction (XRD) pattern of graphene electrodes with varying chitosan binder content exhibited noticeable peaks (Figure 4.18 (a)). As the chitosan binder percentage increased, the intensity peaks of Ni foam became reduced and broader. This phenomenon was attributed to the chitosan binder covering the crystalline framework of Ni foam, leading to a decrease in crystallite size and an increase in diffraction width. Given the amorphous structure of the chitosan binder, its presence on the Ni foam surface contributed to impurities and a subsequent reduction in Ni foam's peak intensity. Figure 4.18 (b) confirmed the reduction in intensity peak at 44.34° (111) from Ni foam. When comparing XRD plots of the graphene electrode with 10 wt% chitosan binder and Ni foam, insignificant changes were observed. The peak intensity for the 10 wt% chitosan binder was lower, indicating that the chitosan binder did not fully cover the graphene surface. Nevertheless, it formed a robust physical bond and exhibited favorable properties [85].
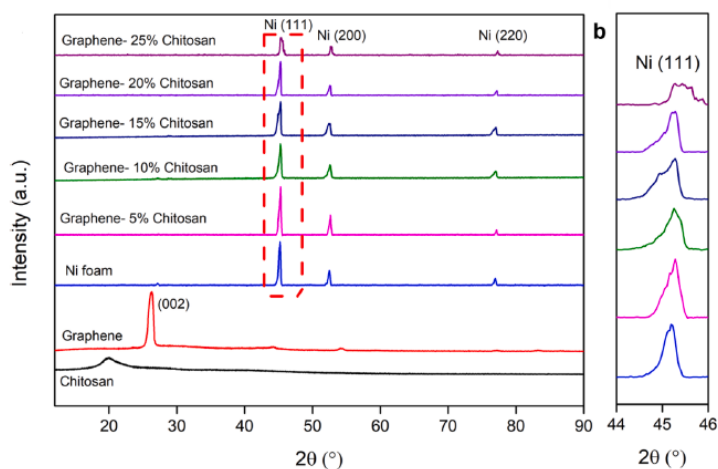
Figure 4.18. XRD plots of (a) graphene electrodes with various weight percentage of chitosan binder on Ni foam (b) enlargement of Ni (111) peaks [85].

Electrochemical impedance spectroscopy (EIS) measurements were utilized to examine the contact resistances and transport kinetics between graphene-chitosan electrodes and electrolyte (Figure 4.19). The Nyquist plots depicted the frequency response of the electrode/electrolyte system. The series resistance (Rs) of the electrolyte is defined by the contact resistance at the interface between the electrode and electrolytes. In the high-

frequency region, the Faraday interface charge transfer resistance (R_{ct}) is identified by the diameter of the semicircle, while in the low-frequency region, the standard Warburg behavior is indicated by the slope of a straight line. The double-layer capacitance is represented as a constant phase element, denoted as C. Among the graphene-based electrodes, the one containing 5 wt% chitosan binder exhibited the lowest values for both R_s (2.217 Ω) and R_{ct} (0.184 Ω). This can be attributed to the lower content of the chitosan binder, resulting in a larger active reaction surface area of the graphene. Additionally, this electrode demonstrated higher electrical and ionic conductivity compared to the other electrodes and was identified as the optimal weight percentage. Although the R_s (2.315 Ω) and R_{ct} (0.539 Ω) values for the 10 wt% chitosan binder were relatively higher than those for the 5 wt% binder, they still indicated low resistance. Thus, the 10 wt% binder can provide strong adhesion and flexibility due to its uniform spreading across the electrode's surface [85].
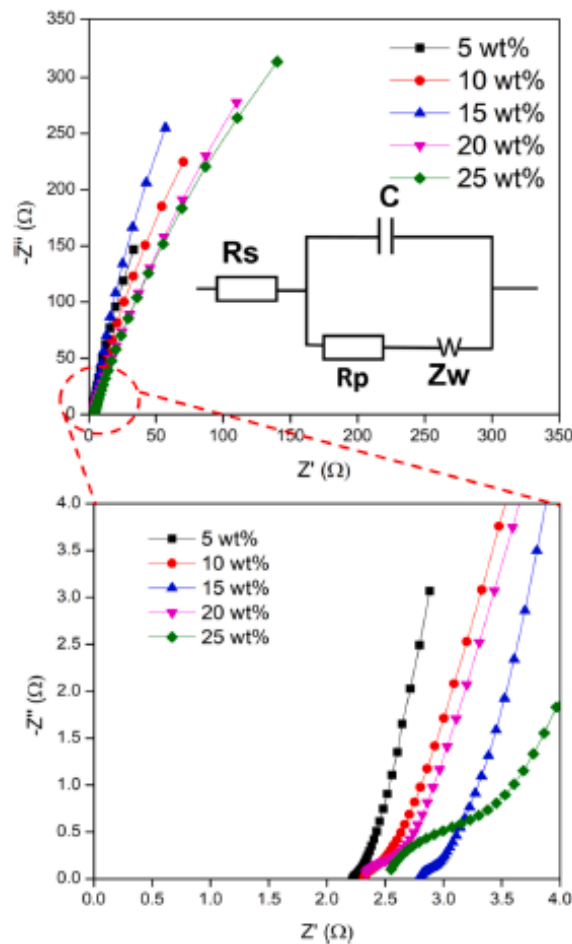
Figure 4.19. Nyquist plots and equivalent circuit (inserted) of graphene electrode at various weight percentages of chitosan binder in 1 M KOH solution[85].

Table 4.3. Electrochemical Performance of Graphene-based solid-state supercapacitors.

Electrode	Electrolyte	Specific capacitance	Energy density	Power density	Cyclic stability Or bending cycles	Ref.
$V_2O_5 \cdot 0.5H_2O$-rGO Hybrid on Carbon Cloth	PVA-KCl	136 mF cm^{-3}	102 µWh cm^{-3}	73.38 mW cm^{-3}	98% capacitance retention at 400 mV s^{-1} after 10000 cycles	[238]
reduced graphene oxide fiber fabrics (rGOFFs) polyaniline (PANI)/ rGOFFs	H_2SO_4/PVA	285 F g^{-1} at 0.1 A g^{-1} and 220 F g^{-1} at 1A g^{-1} 2812 mF cm^{-2} at 1 mA cm^{-2} 3828 mF cm^{-2} at 1 mA cm^{-2} (172 F cm^{-3})	28 µWh cm^{-2} (254 µW cm^{-2}) to 11 µWh cm^{-2} (4950 µWcm^{-2})	500 µW cm^{-2} to 5000 µW cm^{-2}	…	[81]
graphene paper-like electrode	PVA/H_3PO_4	~3.6 F cm^{-3}	…	…	remained about 98% of the initial capacitance after 20000 charge-	[236]

					discharge cycles	
three-dimensional chitosan/graphene (CS-rGO) aerogel	…	184.6 mF cm^{-3} at a current density of 2 mA cm^{-3}	32 W h kg^{-1}	1000 W kg^{-1}	89.8% retention rate of the volume capacitance after 5000 cycles at 10 mA cm^{-3}	[239]
chitosan (CS)/reduced graphene oxide (rGO) composite	1 M H$_2$SO$_4$	274 F g^{-1} at the current density of 0.5 A g^{-1}	8.4 Wh kg^{-1}	50 W kg^{-1}	high capacitance retention rate of 92.57 % after 10000 cycles	[83]
Chitosan oxygen-doped activated carbon/graphene composite	1 M H$_2$SO$_4$	375.7 F g^{-1} at a current density of 1 A g^{-1}	29.9 W h kg^{-1}	1000.4 W kg^{-1}	83% after 5000 charge/discharge cycles at 10 A g^{-1}	[84]
PANI/graphene/textile-HCl (PANI/G/T-HCl)	1 mol L^{-1} H$_2$SO$_4$ electrolyte	1601 mF cm^{-2} at the current density of 1 mA cm^{-2}	755 mWh m^{-2}	1448 mW m^{-2}	a capacitance retention more than 75% after 10000 cycles at 10 mA cm^{-2}	[240]
exfoliated graphene–chitosan hydrogel	1.0 M of H$_2$SO$_4$	153.6 Fg^{-1} at 1 mAg^{-1} current density	3.47 kWh kg^{-1}	102.07 W kg^{-1}	97% retention after 1000 cycle	[241]
Graphene / chitosan(binder)	1 M KOH aqueous electrolyte	For 10wt% chitosan: 135.65 F g^{-1} at			Capacitance retention of 87.2% over the repeated	[85]

		5 mV s^{-1} scan rat			1000charge-discharge cycle.	
MnO$_2$–graphene–chitosan//graphene–chitosan			80.40 Wh kg^{-1}	2894.61 W kg^{-1}	74.18% retention of its original capacitance after 1000 cycles at 1.2 A g^{-1}	
Chitosan/activated carbon (AC)	neutral Li$_2$SO$_4$ electrolyte	264 F g^{-1}			…	[242]
	Li$_2$SO$_4$-polyacrylamide (PAM) solid electrolyte		1.6 mWh cm^{-3}	0.8 W cm^{-1}		
N,S co-doped graphene-enhanced hierarchical porous carbon foam (N,S-GHPCF) (it contains	6 M KOH	405 F g^{-1} at 1 A g^{-1}	18.4 Wh kg^{-1}	300 W kg^{-1}	98.8% of capacitance retention after 10000 cycles	[82]

chitosan as well)						
NiO nanoparticles decorated on polypyrrole nanotube (PNT) through a chitosan (CS) layer (NiO/CS-PNT) NiO/CS-PNT//NiO/CS-PNT	KOH/PVA gel as electrolyte	934.11 Fg^{-1} at current density of 1 Ag^{-1}	27.80 Wh Kg^{-1}	4045.69 W kg^{-1}	capacitance retention of 84.90% even after 10,000 cycles	[243]
poly(3,4-ethylenedioxythiophene) (PEDOT)/screen-printed reduced graphene oxide (rGO)–chitosan (CS) bilayer material	PVA–H$_2$SO$_4$ gel electrolyte	1073.67 mF cm^{-2}	35.5 μW h cm^{-2}	2 mWcm^{-2}	A 10,000-cycle CV test showed a capacitance retention rate of 99.3% under a potential scan rate of 200 mV/s, indicating good stability	[244]
modified chitosan (M-chitosan) and holey graphene oxide (HGO)	lignin hydrogel electrolyte	420 F g^{-1} at 0.5 A g^{-1}	14.8 Wh kg^{-1}	100 W kg^{-1}	…	[245]

Fe$_3$O$_4$/graphene-oxide/chitosan aerogel (GCFA)	basic (6M KOH: cell-1), acidic (1M H$_2$SO$_4$: cell-2), & neutral (Na$_2$SO$_4$: cell-3) as electrolyte mediums	Cell-3; ~160 F g^{-1} Cell-2; ~160 F g^{-1} Cell-1; ~102 F g^{-1}	~14.6 Wh kg^{-1} ~7.84 Wh kg^{-1} ~1.54 Wh kg^{-1}	~0.77 kW kg^{-1} ~0.45 kW kg^{-1} ~0.14 kW kg^{-1}	excellent coulombic efficiency (~91%) even after 10,000 charge-discharge cycles	[246]
Light scribed graphene	PVA–H$_2$SO$_4$	4.04 mF cm^{-2} 265 F g^{-1}	1.36 mWh cm^{-3}	20 W cm^{-3}	100% bending cycles (10 000 cycles)	[247]
3D porous graphene	PVA–H$_2$SO$_4$	34 mF cm^{-2}	…	14.3 kW kg^{-1}	…	[248]
Graphene/PEDOT/PSS	PVA–H$_3$PO$_4$	448 mF cm^{-2} 49.9 F cm^{-3}	34 mWh cm^{-2}	…	100% bending cycles (10 000 cycles)	[249]
Graphene/MXene	PVA–H$_3$PO$_4$	216 F cm^{-3}	4.8 mWh cm^{-3}	0.04 W cm^{-3}	85.2% bending cycles (2500 cycles)	[250]
Graphene/PVP	PVA–H$_2$SO$_4$	31.6 mF cm^{-2} 67.4 F cm^{-3} 168.4 F g^{-1}	0.8 mWh cm^{-3}	20 W cm^{-3}	…	[251]
Graphene/ACC	PVA–KOH	1710 mF cm^{-2} 162 F g^{-1}	240 mWh cm^{-2}	156	…	[252]

				mW h cm^{-2}		
Ribbon-like graphene	PVA–H$_2$SO$_4$	3800 mF cm^{-2} 82.7 F cm^{-3} 89.9 F g^{-1}	…	12.5 W h kg^{-1}	…	[253]
Graphene/PANi	PVA–H$_2$SO$_4$	665 F g^{-1} 6.4 mF cm^{-2}	14.2 mWh cm^{-3}	…	100% bending cycles (600 cycles)	[254]
Crumpled graphene	PVA–H$_3$PO$_4$	196 F g^{-1}		…	…	[255]
Graphene–cellulose paper	PVA–H$_2$SO$_4$	46 mF cm^{-2}	15 mWh cm^{-2}	…	…	[256]
Graphene hydrogel	PVA–H$_2$SO$_4$	372 mF cm^{-2} 31 F cm^{-3}	0.61 kW h kg^{-1}	0.67 W kg^{-1}	…	[257]
Functionalized graphene hydrogel	PVA–H$_3$PO$_4$	412 F g^{-1}	34 mWh cm^{-2}	…	87% bending cycles (10^4 cycles)	[258]
Graphene/poly pyrrole hydrogel film	PVA–KOH	363 F cm^{-3}		…	…	[259]
Graphene/PA hydrogel	PVA–H$_2$SO$_4$	170.6 F g^{-1}	26.5 W h kg^{-1}	132 W kg^{-1}	…	[260]
Doped graphene hydrogel	PVA–H$_2$SO$_4$	62 F g^{-1}	8.7 W h kg^{-1}	1650 W kg^{-1}	…	[261]
Doped graphene hydrogel	PVA–H$_2$SO$_4$	345 F g^{-1}	134 W h kg^{-1}	83 kW kg^{-1}	…	[262]

Graphene/MnO$_2$ composite hydrogel film	PVA–H$_2$SO$_4$	2.96 F g^{-1}	0.27 mWh cm^{-3}	0.02 W cm^{-3}	88% bending cycle (500 cycles)	[263]
Graphene/PANi/graphene	PVA–H$_2$SO$_4$	121.5 mF cm^{-2}	5.4 mWh cm^{-3}	…	…	[264]
Paper PANi/rGO film	PVA–H$_2$SO$_4$	464 F g^{-1}		…	…	[265]
Graphene/MoS$_2$	PVA–H$_2$SO$_4$	70 mF cm^{-2} 19.44 F cm^{-3}	1.72 mWh cm^{-3}	0.062 W cm^{-3}	93% (500 cycles)	[266]

5. MATERIALS, TESTS AND METHODS

In this chapter, firstly, the purchased materials, the laboratory equipments used for sample preparation, the synthesis method of graphene oxide and gel polymer electrolyte are introduced, followed by the fabrication of RGO/CS electrodes and solid-state supercapacitors. Afterwards, the characterization tests such as structural and electrochemical tests are introduced. Supplementary images of the samples and experimental setups can be found in the appendix of this thesis.

5.1. Materials

The specifications of the chemicals utilized in this PhD thesis are outlined in the table below. All chemicals were used as received without further purification unless otherwise stated.

Table 5.1. Specifications of the materials and methods used in this PhD thesis.

Material	Chemical symbol	Manufacturer	Barcode/Specification
Poly(vinyl alcohol)	PVA	Sigma-Aldrich (Mowiol)	Mowiol 4-98 (M_w=27000 g mol^{-1}, degree of hydrolysis: 98%) Mowiol 10-98 (M_w=61000 g mol^{-1}, degree of hydrolysis: 98%) Mowiol 20-98 (M_w=125000 g mol^{-1}, degree of hydrolysis: 98%)

			Mowiol 56-98 $(M_w=195000 \text{ g mol}^{-1}$, degree of hydrolysis: 98%)
Potassium chloride	KCl	Merck	K51221736
Graphite	Graphite flakes	Asbury	3772
Sulfuric acid	H_2SO_4	Merck (95-97%)	1.00731.2511
Nitric acid	HNO_3	Chemlab (65%)	CL00.1902.2500
Potassium permanganate	$KMnO_4$	Scharlau	PO03301000
Hydrogen peroxide	H_2O_2	Chemlab (30%)	CL00.2308.1000
Hydrochloric acid	HCl	Merck (37%)	1.00317.2500
Deionized water	H_2O	Milli Q-water purification system, Millipore, Bedford, MA, USA	DI, 0.055 μS
Chitosan	$C_{18}H_{35}N_3O$	Sigma-Aldrich	448877-250G
Acetic acid	CH_3COOH	Merck	K50609263
Polyethylene Terephthalate film	PET	Sigma-Aldrich	GF76788848 Thickness; 0.5 mm
Polyimide film	PI	CMC Kleebetechnik, Germany	Kapton$^{®}$ HN 125 ± 13 μm
Acetone	$C_3 H_6 O$	Merck	K467042 14527

| Ethanol | $C_2\ H_6\ O$ | Merck | K449487 83 340 |
| 2-propanol | C_3H_8O | Merck | K519 13434 948 |

5.2. Synthesis method of Graphene oxide, Gel polymer electrolyte, and Reduced graphene oxide/Chitosan (RGO/CS) composite electrode

5.2.1. Synthesis method of Graphene oxide (GO)

GO was synthesized through modified Hummers' method [142, 267]. To initiate the synthesis of layered graphite, 2 grams of graphite flakes were added to 30 mL of concentrated sulfuric acid under continuous mixing. Subsequently, 10 mL of nitric acid was incrementally incorporated into the resultant mixture, which was then subjected to 24 hours of agitation at room temperature. Then, deionized water was added to the reaction mixture, and the resultant solution underwent centrifugation, followed by triple water washes. The precipitate was dried for one day at 60 ° C to yield layered graphite. To achieve fully oxidized graphite while retaining the initial large sheet size, the layered graphite was briefly exposed to a furnace at 1050 °C for 15 seconds. This process was followed by the addition of one gram of completely oxidized graphite to 200 mL of sulfuric acid. Subsequently, 10 grams of potassium permanganate ($KMnO_4$) was gently introduced into the mixture, resulting in the emergence of a sludge green color. In the subsequent step, the reaction mixture was carefully transferred to a water and ice bath. Gradually 200 mL of deionized water was added to the mixture, ensuring safe handling due to the risk of acid splashing. Upon reaching room temperature, the introduction of 50 mL of hydrogen peroxide to the mixture led to a color transformation from sludge green to brownish yellow or gold. In the final step, the golden mixture was subjected to centrifugation in falcon tubes at 9000 rpm for 10 minutes. The lower sedimented portion of each falcon was retained, while the upper part was discarded. The resulting mixture underwent three consecutive 10-minute washes using 1.0 M hydrochloric acid, each cycle involving thorough mixing and subsequent centrifugation to remove the top liquid. This acid washing step aimed to decrease the pH of the mixture and separate GO flakes from the salt. After the acid washing step, pour distilled water was added into the mixture in each falcon and mixed vigorously until it was uniform, then centrifuged

and discarded the top liquid each time. The washing step was repeated until the pH of the mixture reaches 5-6. The purpose of the leaching step is to separate the ions from sulfuric acid and hydrochloric acid. In this step, the GO dispersion was obtained.

Table 5.2. The role of materials utilized in the graphene oxide production.

Name of material	The role of material in the reaction
Graphite flakes	Graphene oxide nano sheets
Sulfuric acid	Reaction medium
Potassium permanganate	Oxidizing agent
Hydrogen peroxide	Reaction termination agent
Hydrochloric acid	The agent that separates the salt from the reaction medium
DI-Water	The agent that separates excess ions from the reaction medium

5.2.2. Preparation of gel polymer electrolytes based on PVA/KCl

The gel polymer electrolyte was prepared via the solution-casting method. Initially, 1 g of PVA was dissolved in 10.0 mL of DI-water at 90°C for 2 hours to achieve a homogeneous and low-viscosity solution, which was then cooled to room temperature. Aqueous KCl solution was prepared by dissolving a specific amount of KCl salt in water (2.0 M). Subsequently, under continuous stirring, KCl(aq) was incorporated into the viscous polymer solution. The mass fraction of KCl salt in the final gel, relative to PVA, was 0.1, 0.5, 1.0, 2.0, 5.0, 10.0 and 20.0. At the end, the viscous liquids were added into Teflon or polystyrene (PS)-molds and dried at ambient temperature. The dried films were separated from the molds and used for further tests.
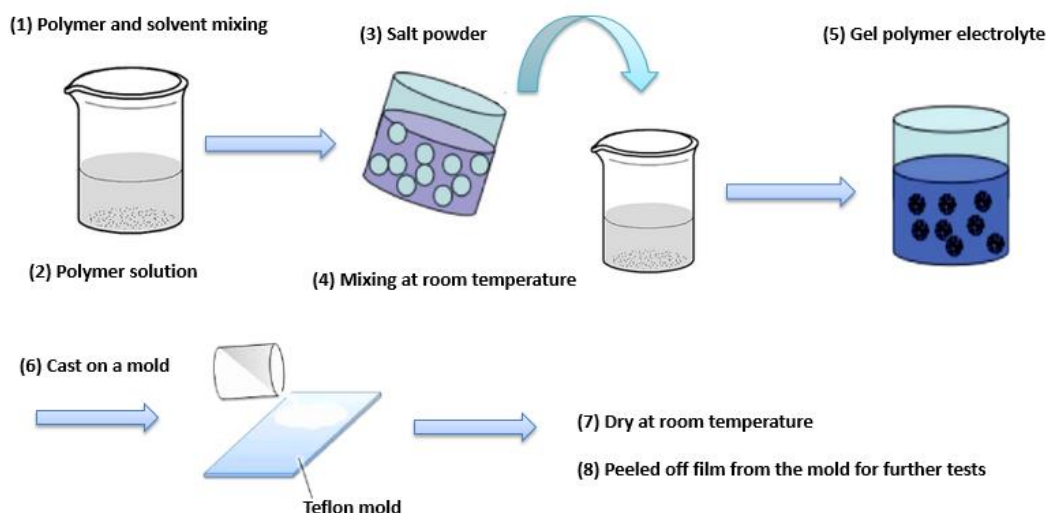
Figure 5.1. Preparation steps of gel polymer electrolyte by solution-casting method.

5.2.3. Preparation of graphene oxide/chitosan (GO/CS) solution

Initially, an aqueous-based graphene oxide solution was prepared following the procedure outlined in the preceding section. After the synthesis of graphene oxide (GO), a series of eight washing cycles were conducted, involving treating the aqueous-based GO with acetic acid through centrifugation at 12,000 rpm for 20 minutes. In each cycle, the upper portion was discarded, and fresh acetic acid was introduced, resulting in the production of acetic acid-based graphene oxide. Following this, dry chitosan powder with medium molecular weight was added to the acetic acid-based GO dispersion at a concentration of 2 mg mL^{-1}.

The difference between low, medium, and high molecular weight chitosan lies in the average size of the polymer chains, which impacts various properties, with the choice depending on the specific application. Low molecular weight chitosan features smaller-sized polymer chains, higher solubility, weak mechanical strength, and faster degradation, making it suitable for applications such as drug delivery, wound healing, and agriculture. Medium molecular weight chitosan offers a balance between solubility and stability, making it suitable for various applications. High molecular weight chitosan, on the other hand, possesses longer polymer chains, lower solubility, slower degradation, and poses challenges in processing [127]. Therefore, medium molecular weight chitosan is the best choice for preparing the electrodes as it can provide the necessary structural integrity to hold GO sheets together, ensuring a cohesive and conductive network. Moreover, it may contribute to an

optimal porous structure, allowing efficient electrolyte penetration and enhancing ion accessibility and improve the overall electrochemical performance [91].

Thus, different mass ratios of GO/CS composite solution were prepared using medium-molecular-weight CS, specifically 95/5, 90/10, 80/20, 60/40, 50/50, 20/80, 10/90, and 0/100. Homogeneity was achieved by magnetic stirring over a 4-hour period at room temperature, resulting in the formation of a uniform slurry.

5.2.4. Preparation of flexible solid-state supercapacitors based on RGO/CS fiber electrodes

According to section 5.3.3, GO/CS composite solutions with various weight ratios were prepared. These solutions were continuously injected from a syringe with an outer diameter of 0.42 mm and a length of 27 cm. Subsequently, they were coagulated in a mixture of ethanol and water (EtOH concentration: 50% by volume) using the wet-spinning method to form GO/CS fibers. After immediate air-drying, the fibers were extracted. The GO within the GO/CS fibers underwent reduction through a hydrothermal treatment [268] in an oven at 120°C for 8 hours, resulting in reduced-GO (RGO) containing fibers. Subsequently, the RGO/CS fibers were submerged just in the PVA/KCl gel electrolyte using solution dipping (Mw=195000 g mol^{-1}, PVA/KCl w/w: 1/2) which showed the highest ionic conductivity. The RGO/CS fibers were kept immersed in the PVA/KCl gel solution to ensure effective wetting and coverage of the fibers with the gel electrolyte. After 24 hours, the fibers were arranged parallel to each other in a parallel pattern and connected to the electrochemical device using silver glue for testing.

5.2.5. Preparation of solid-state supercapacitors based on RGO/CS film electrodes

The prepared slurries of GO/CS solutions with different weight ratios were coated onto stainless steel substrates which acted as a current collector with a 1×1 cm^2 coating area. These coated substrates were then subjected to a hydrothermal treatment within an oven at 120 °C for a duration of 8 hours, ultimately giving rise to the fabrication of RGO/CS electrodes [268]. The as-prepared electrolyte film was cut into pieces (1×1 cm^2 in area, 400-500 μm in thickness) and sandwiched between two electrodes to assemble face-to-face into an all-solid-state supercapacitor configuration which allowed the gel electrolyte film on

each electrode to act as a thin separator. For comparative purposes, samples of pure chitosan and pure RGO were also prepared following the aforementioned process.

5.2.6. Preparation of flexible solid-state supercapacitors based on RGO/CS film electrodes

Initially, poly(ethylene terephthalate) (PET) film underwent cleaning with ethanol and deionized (DI) water before coating. The prepared slurry of the GO/CS solution with a weight ratio of 90/10 was applied as two separate electrodes on a PET film substrate, serving as a flexible current collector with a 2×2 cm² coating area. These coated substrates were then subjected to a hydrothermal treatment in an oven at 120°C for 8 hours, resulting in the fabrication of RGO/CS electrodes. Subsequently, the sample was placed on a glass surface and then the PVA/KCl gel electrolyte (Mw=195,000 g mol^{-1}, PVA/KCl w/w: 1/2) was added with a dropper to the surface of the electrodes. After 24 hours, the sample was connected to the electrochemical device using silver glue for testing purposes.

5.2.7. Preparation of flexible solid-state supercapacitors based on RGO/CS using laser 3D-printing technology

The Laser 3D-printing machine, a compact CNC milling machine, operates within small dimensions and moves along three coordinate axes (X, Y, and Z) programmed from a computer [269]. Primarily used for artistic engraving and machining on various materials like wood, aluminum, plastic, and MDF, its significant application lies in producing precise PCB prototypes for the electronics industry [270]. Renowned for its speed, accuracy, low maintenance, energy efficiency, compact size, and standalone operation, this device is highly efficient in small-scale environments and industries [271]. In this thesis, as detailed in section 5.3.3, a GO/CS solution with a weight ratio of 90/10 was prepared. The GO/CS solution was coated onto a polyimide (PI)-based Kapton® film and air-dried at room temperature. Subsequently, laser 3D-printing was conducted on the GO/CS film on the PI surface using a mini CNC1610 laser device (Model Code: B2-01-0101A), following a predefined hair-comb GO/CS pattern generated in "artcam" software. This selective process allows controlled heating of specific areas, resulting in the reduction of GO to reduced GO in a controlled manner, ensuring the desired electrical properties. The laser can locally reduce graphene oxide to obtain a graphene structure for creating RGO/CS electrodes, offering more flexibility in patterning compared to conventional printing or lithographic

techniques. The laser settings were configured to a width of 1 mm and a gap of 1 mm, with a voltage of 12 V, current of 1.3 A, and a laser power and wavelength of 2500 mW and 450 nm, respectively. Finally, the PVA/KCl gel electrolyte (Mw=195,000 g mol^{-1}, PVA/KCl w/w: 1/2) was applied with a dropper to the surface of the electrodes.

5.3. Structural and electrochemical characterization tests

In this section, the details of structural characterization tests and measurements aimed at identifying the electrochemical performance of PVA/KCl gel electrolytes and various electrode materials including GO, RGO, CS, GO/CS, and RGO/CS are presented.

5.3.1. Attenuated Total Reflection-Fourier transform infrared spectroscopy (ATR-FTIR) analysis

ATR-FTIR analysis was employed to identify the functional groups present in graphene oxide, electrolyte, and electrodes, as well as to explore the interaction between the components of the electrolyte and electrodes. The samples were prepared in film form and subjected to analysis. Fourier transform infrared (FTIR) spectra were acquired using a PerkinElmer Spectrum Two model spectrometer operating in attenuated total reflectance (ATR) mode. Spectra were collected from solid samples with 32 scans and a resolution of 4 cm^{-1} in the wavenumber range of 500-4000 cm^{-1}.

5.3.2. Ultraviolet-Visible spectroscopy (UV-Vis) analysis

The absorbance of the samples under investigation was quantified using a UV−Vis Varian Cary100 spectrophotometer. Measurements were conducted at room temperature within a wavelength range of 190-800 nm.

5.3.3. Field emission-Scanning electron microscope (FE-SEM) analysis

FE-SEM analysis was conducted to visualize the morphology of electrolyte and electrode samples, as well as to determine the size of graphene oxide sheets. Samples were prepared in film form on SiO$_2$ substrates and subsequently imaged. The Tescan GAIA3+Oxford XMax 150 EDS device was utilized to analyze the samples at various magnifications of 5, 10, 20, 50 μm.

5.3.4. Transmission electron microscopy (TEM) analysis

The GO, RGO, GO/CS, and RGO/CS samples were further examined using TEM (FEI Tecnai G2 F30 transmission electron microscope) operated at 100 keV, with varying magnifications for analysis. For GO and GO/CS dispersions, 1-2 droplets of the sample were added to DI-water (2 mL), resulting in a very light-yellow coloration in the water. Subsequently, TEM samples were prepared by drying a droplet of the GO or GO/CS suspension on a holey carbon grid at room temperature. In the case of RGO and RGO/CS samples, the as-prepared GO and GO/CS samples on the holey carbon grid were subjected to a thermal reduction process by placing them on a heater at 120°C for approximately 8 hours. This process led to a color change from brownish-yellow to black, indicating the reduction of GO. In both cases, a thin film of materials was achieved on the TEM grid for analysis.

5.3.5. X-Ray diffraction (XRD) analysis

XRD measurements were employed to determine the distance between graphene oxide sheets and to investigate the effect of KCl on the crystalline structure of PVA, as well as the effect of GO on the crystalline structure of chitosan. A Bruker AXS model D8 Advance diffractometer was utilized, employing a Cu-Kα1 radiation source with a wavelength (λ) of 0.15406 nm. XRD data were collected over a 2θ range from 2° to 80°, with a scanning step size of 0.02°.

The crystallinity degree (χ) was determined using the following formula:

$$\chi\,(\%) = 100 \times A_c / (A_c + A_a) \tag{5.1}$$

In this equation, A_c and A_a denote the measured overall intensity values for the crystalline and amorphous phases, respectively.

The d-spacing (d) value was evaluated using the Bragg's law:

$$n\lambda = 2d\,\sin\Theta \tag{5.2}$$

where λ is the wavelength of the x-ray, "d" is the spacing of the crystal layers (path difference), θ is the incident angle (the angle between incident ray and the scatter plane), and "n" is an integer of the order of reflection.

The crystallite size (L) was calculated using the Scherrer Equation:

$$L = K\lambda/\beta\ Cos\Theta \hspace{5cm} (5.3)$$

where λ is the wavelength (nm), β is the full width at half maximum (FWHM) of peak in radian, θ is the incident angle. K is the shape factor that can be 0.62-2.08 and is usually taken as about 0.89 [272].

5.3.6. Atomic force microscopy (AFM) analysis

Tapping-mode AFM was utilized to capture images of GO and GO/CS samples under ambient conditions. The same samples prepared for SEM examination were utilized for AFM observations. A Veeco Multimode V scanning probe microscope, equipped with a Nanoscope VIII controller, was employed for AFM measurements operating in tapping mode.

5.3.7. X-Ray photoelectron spectroscopy (XPS) analysis

X-ray photoelectron spectroscopy (XPS) was utilized to assess the chemical environment and binding energies. A monochromatized Al Kα X-ray source in a Thermo spectrometer was employed for this purpose. The X-ray spot size was set at 400 μm, and pass energies of 30 eV and 200 eV were utilized for the survey and core-level scans, respectively.

5.3.8. Dynamic Mechanical Thermal Analysis (DMTA) analysis

Dynamic mechanical thermal analysis (DMTA) of the PVA gel electrolytes was conducted in the tensile mode, employing Netzsch DMA 242C device. The measurements were done at a constant frequency of 1 Hz with a 1 N preload, a heating rate of 5°C/min and a temperature range of -100 to 150 °C. The samples were prepared by the cutting of strips from the films with length of 20 mm, width of 5 mm and thickness of 0.4-0.5 mm.

5.3.9. Polarized optical microscopy (POM) analysis

Polarized optical microscopy (POM) is a technique that employs polarized light to investigate the optical properties of materials. This method utilizes a light source emitting polarized light, where the electric field vibrations occur in a specific direction. The light passes through a polarizer, allowing only light vibrating in a particular direction to pass through. Subsequently, this polarized light interacts with the sample, revealing valuable information about its optical characteristics [273]. Birefringent materials, having varying refractive indices in different directions, modify the polarization of light passing through them. Subsequently, the light encounters an analyzer, set at a specific angle to the polarizer, permitting only light vibrating in a particular direction to pass through. The observer then views the sample through an eyepiece or camera. The observed colors and patterns offer insights into the material's optical properties, crystallinity, stress, and other features [274]. In the context of GO, POM can be utilized to investigate its liquid crystalline properties. Aqueous dispersions of GO and GO/CS composite were analyzed using polarized optical microscopy (Optika B-383PLi) in transmission mode. This examination aimed to assess the homogeneity and birefringence of GO sheets.

5.3.10. Tensile mechanical analysis

The mechanical properties of the produced polymer, gel polymer electrolyte, graphene oxide, and nanocomposite films were measured using a GALDABINI Sun 2500 mechanical testing machine with 1 KN force sensor, a gauge length of 5 cm and a constant stretching rate of 50 mm/min according to the American Society for Testing and Materials (ASTM) standard for thin films (ASTM D882). The films prepared in a rectangular shape with a dimension of 1×10 cm and repeated three times for each sample. The average thickness of the samples was 0.17-0.22 mm. GO films for the tensile mechanical test were prepared by casting the as-prepared GO solution onto a Teflon substrate. To obtain RGO films, the GO films were subjected to reduction by placing them in an oven at 120°C for 8 hours. Similarly, other films were also prepared by casting their solutions onto Teflon substrate.

5.3.11. Brunauer-Emmet-Teller (BET) analysis

To analyze the specific surface area and porosity of CS, RGO, and RGO/CS samples using the BET test (BET BELSORP Mini II), the following procedure was employed: Initially, each sample underwent heating under vacuum and specific temperature conditions.

Subsequently, the samples were subjected to degassing with nitrogen gas at 120 °C. Following degassing, the cooled samples were exposed to nitrogen gas, gradually increasing the pressure. The container housing the sample was immersed in a liquid nitrogen bath to cool the sample to the boiling temperature of nitrogen, facilitating gas absorption. As nitrogen gas entered the container at a controlled rate, the exit rate was measured. Gas adsorption by the sample at different pressures of nitrogen gas allowed for the determination of its specific surface area. The BET device calculated the amount of nitrogen absorbed by the sample by analyzing the difference between input and output gas quantities. Throughout the process, nitrogen gas pressure gradually increased, enabling the BET device software to generate a graph illustrating the amount of absorbed gas versus pressure.

5.3.12. Cell Viability analysis

For the biocompatibility assessment, SPECTROstar Nano (BMG LABTECH) was employed. To ensure sterility, the samples underwent a 1-hour exposure to UVC light. Following UV treatment, no observable deformations were observed noted, thereby rendering the samples suitable for subsequent experimentation. The viability assay centered on the HeLa cell line. Cells were cultured and subsequently seeded at a density of 50,000 cells/well in a 96-well culture plate. A 72-hour incubation period was allotted for the cells to adhere to the culture plate. Subsequent to this incubation period, the UV-treated materials were introduced into the culture wells. An additional 72-hour incubation ensued, during which the cells interacted with the materials. At the conclusion of this duration, WST-1 reagent (Cayman, #600485) was added, followed by a 2-hour incubation interval. Following this, absorbance readings were taken at 450 nm utilizing a spectrophotometer.

5.3.13. Electrochemical impedance spectroscopy (EIS) analysis

Electrochemical tests, utilized in various fields like corrosion, biosensors, solar cells, batteries, and supercapacitors, involve assessing voltage, current, and other parameters to compute supercapacitor capacitance, power density, and energy density [149]. Electrochemical cells can be classified as three-electrode or two-electrode systems. In a three-electrode system, measurements are conducted using three electrodes: the working electrode (under test), the counter electrode (providing current), and the reference electrode (for potential measurement against the working electrode). Voltage is applied across the

working and reference electrodes, while current flowing between the working and counter electrodes is assessed [275, 276]. In electrochemical impedance spectroscopy, a low-amplitude sinusoidal alternating voltage is applied to the working electrode, causing system disturbance. The response, characterized by an alternating current with a time delay between voltage and current, is expressed as a phase angle [277].

$$V_{ac=} V_t = V_0 e^{j\omega t} \tag{5.4}$$

$$I = I_0 = e^{j\omega t - j\phi} \tag{5.5}$$

$$\omega = 2\pi f \tag{5.6}$$

Where, V_0 is the voltage amplitude, I_0 is the current amplitude, ϕ is the phase angle, and ω is the angular frequency.

Impedance, denoted as Z (ohm), is defined by Ohm's law as the ratio of alternating voltage to alternating current. It represents the complex resistance encountered when current flows through a circuit containing resistors, capacitors, and inductors [134, 277].

$$Z = V_t / I_t = Z_0 e^{j\phi} \tag{5.7}$$

$$Z_{real} = Z_0 \cos (\phi), \ \ Z_{img} = Z_0 \sin (\phi) \tag{5.8}$$

$$\phi = \tan^{-1} (Z_{img} / Z_{real}) \tag{5.9}$$

To analyze the behavior of a system and its components effectively, it is crucial to model the system using equivalent electrical circuits. Typically, the equivalent circuit of an electrochemical system comprises various elements like capacitors, resistors, and emitters interconnected in different configurations [134]. The complexity of the circuit corresponds to the complexity of impedance encountered. Understanding the impedance of a system requires considering three parameters: impedance magnitude, phase angle, and frequency. These parameters are often depicted in a Bode diagram (Figure 5.2) for clarity [277].
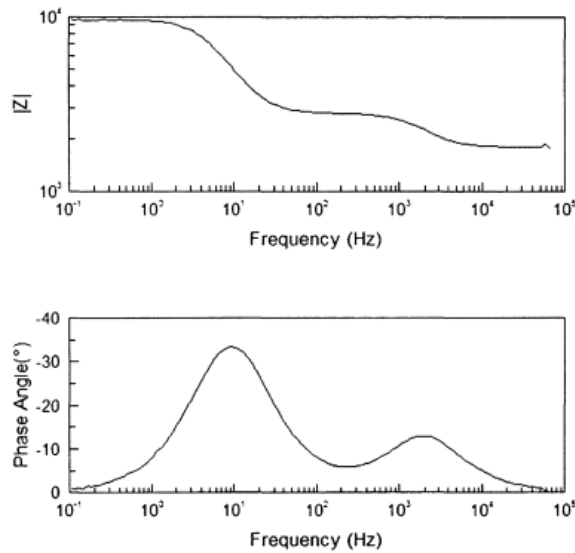
Figure 5.2. Bode diagram resulting from the electrochemical impedance spectroscopy test [277].

The Nyquist curve displays impedance vector data, plotting imaginary impedance against real impedance across a frequency range (Figure 5.3). It is a graphical representation used in impedance spectroscopy to illustrate the relationship between the real and imaginary components of impedance across a range of frequencies. It plots the complex impedance data, typically obtained from electrochemical impedance spectroscopy (EIS), with the real impedance on the x-axis (Z′ or Re (Z)) and the imaginary impedance on the y-axis (Z″ or Im (Z)). This curve provides valuable insights into the behavior of electrochemical systems, allowing to analyze factors such as charge transfer resistance, double-layer capacitance, and diffusion processes [277].
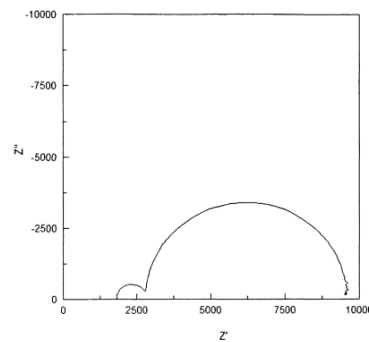
Figure 5.3. Nyquist diagram resulting from the electrochemical impedance spectroscopy test [277].

When a sinusoidal voltage traverses a circuit with resistance, the resulting current response is a sinusoidal wave in phase with it, exhibiting no phase delay, and its impedance equals R. An instance of this phenomenon is the resistance of an electrolyte solution. Table 5.4 provides the phase angle for each component of the electric circuit [277].

Table 5.3.   Some literature values of phase angle and impedance for different elements of electric circuit [149, 277].

Circuit element	Phase angle	Impedance
Resistor	0	R
Capacitor	-90	$1/j\omega C$
Inductor	+90	$j\omega L$
Warburg σ: Warburg coefficient	+45	$\omega\,\sigma(1-j)^{½}$

In the current thesis, EIS test has been utilized to determine the ionic conductivity of electrolytes and the electrochemical performance of solid-state supercapacitors. The frequency range of the test was set between 100 mHz to 100 kHz at 24 °C and a relative humidity of 22% using the BIOLOGIC, SP150 device. Conducted with a two-electrode system, the samples were sandwiched between stainless steel electrodes. The ionic conductivity of the electrolyte was calculated using the following formula:

$$\sigma = t\,/\,RA \tag{5.10}$$

where, σ is the ionic conductivity of the electrolyte (mS cm^{-1}), t is the thickness of the electrolyte layer (cm), A is the contact surface of the electrolyte and electrode (cm^2), and R is the bulk resistance of the electrolyte in ohms [278]. The electrolyte thickness ranged from 400 to 500 micrometers, with a contact surface area of 1 cm^2. Each sample underwent the test three times for accuracy.

5.3.14. Electrical conductivity analysis

The electrical conductivity of GO, RGO, CS, GO/CS, and RGO/CS samples was determined using electrochemical impedance spectroscopy (EIS) testing. Conductivity measurements were conducted across a frequency range of 100 mHz to 100 kHz at 24 °C and a relative humidity of 24% using the AUTOLAB (FRA32M) device. Electrical conductivity, denoted by σ, quantifies a material's ability to conduct electric current and is the reciprocal of specific electrical resistivity (ρ), which represents a material's resistance to current flow [149, 279]. To calculate the electrical conductivity, the material's resistivity is needed and calculated using the following formula [149]:

$$\sigma = 1/\rho \tag{5.11}$$

Resistivity depends on both the material's intrinsic properties and its dimensions [52]. It can be calculated using the (5.12) formula:

$$\rho = R \times (A/t) \tag{5.12}$$

Where, R is the charge transfer resistance of the material (ohms), A is the cross-sectional area of the material (= $1cm^2$), and t is the thickness of the material or the distance between the electrodes (=0.1cm). By measuring resistance, area, and thickness, the electrical conductivity can be calculated.

5.3.15. Cyclic Voltammetry (CV) analysis

The cyclic voltammetry test is a valuable tool for examining electrochemical reactions. In this test, a voltage ranging from V_0 to V_1 is applied to the working electrode, and the resulting current response is plotted against the applied voltage [15, 49]. As depicted in Figure 5.4, the working electrode's voltage reaches V1 with the specified scanning rate and then reverses direction to return to the initial voltage. These cycles of potential changes can be repeated as desired. The shape of the cyclic voltammograms (CV) curve indicates the type of energy storage mechanism [280]. For instance, a rectangular curve shape suggests an electrical double-layer energy storage mechanism, while deviations from the rectangular shape

indicate a shift toward quasi-capacitive behavior, where oxidation-reduction reactions occur on the electrode surfaces [281].
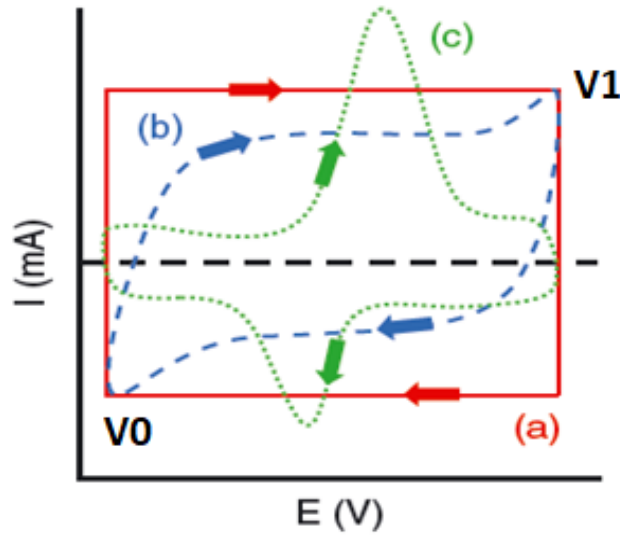
Figure 5.4. Cyclic voltammetry curve, a) ideal capacitor behavior, b) electrical double layer behavior, c) quasi-capacitive behavior [282].

The following equation is used to calculate the specific capacitance for the two-electrode system;

$$Cs = 2 \int idV /(m \times \Delta V \times v) \qquad (5.13)$$

where, "C" is capacitance, $\int$ IdV is the integral surface area of current-voltage curve in the studied voltage range, "A" is the contact surface of electrode and electrolyte, "v" is scan rate, and "ΔV" is the voltage difference [283, 284].

In this PhD thesis, cyclic voltammetry (CV) tests were conducted at varying scan rates (5, 20, 50, 100, 200, 500, 1000 mVs-1) using a DropSens Spelec cyclic voltammetry system within a potential window spanning from 0 to 1 V. Additionally, cyclic stability was evaluated by performing tests at 200 mV s^{-1} for 10,000 cycles for solid-state supercapacitors and at 200 mV s^{-1} for 5000 cycles for the gel electrolyte using the same DropSens Spelec device. These tests were conducted at the laboratory's ambient temperature and humidity conditions, with gel samples sandwiched between stainless steel electrodes, and the experiment was repeated three times using a two-electrode system.

5.3.16. Galvanostatic charge/discharge (GCD) analysis

The GCD test serves as a standard method for assessing the cyclic stability performance of supercapacitors. Each cycle involves charging the supercapacitor from voltage V_0 to V_1 under a constant current density, followed by discharge back to its original voltage or discharged with negative current density (Figure 5.5) [283].
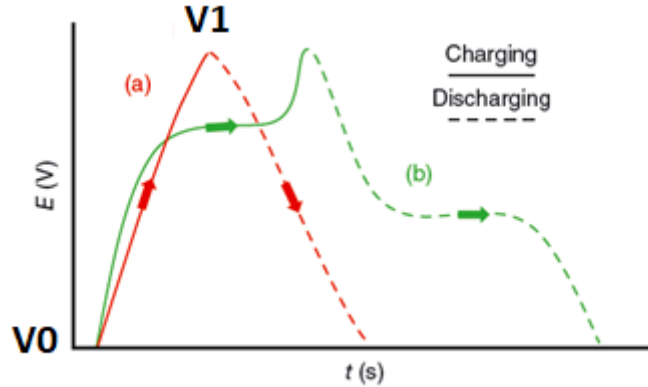
Figure 5.5. Charge-discharge curve, a) electric double layer behavior, b) quasi-capacitive behavior [282].

Specific capacitance, power density and energy density are calculated according to the following relations:

$$C_s = (2i \times \Delta t)/(m \times \Delta V) \tag{5.14}$$

Where, "C_s" is the gravimetric capacitance of the electrode in a two-electrode system (F g^{-1}), "ΔV" is the potential window (V), "Δt" is the discharge time (s), and "m" is the total mass of electrodes (g) [57, 285].

$$E = \frac{1}{2} C V^2/3.6 \tag{5.15}$$

$$P = \frac{E \times 3600}{t} \tag{5.16}$$

where, "E" is the energy density (Wh kg^{-1}), "V" is the potential window (V), "P" is the power density (W kg^{-1}), "C" is the gravimetric capacitance of the electrode in a two-electrode system (F g^{-1}), and "t" is the discharge time (s) [286].

In this PhD thesis, the GCD (Galvanostatic Charge-Discharge) method was employed to assess the specific capacitance of the solid-state supercapacitor using the BIOLOGIC VSP300 device. Charge-discharge cycles were conducted across various current densities (1, 2, 5, 10 A g^{-1}) within a potential range of 0 to 1.5 V at laboratory temperature and humidity conditions. The test was repeated three times using a two-electrode system.

6. RESULTS AND DISCUSSIONS

This chapter begins with presenting the results of various characterization tests conducted for the synthesis of gel polymer electrolyte, graphene oxide, chitosan, and graphene oxide/chitosan composites. Subsequently, the electrochemical and cycle-life properties of the gel polymer electrolyte and solid-state supercapacitors will be discussed.

6.1. Structural characterizations of the gel polymer electrolyte

Polymer gel electrolytes are characterized by their ability to conduct ions while maintaining a flexible and gel-like consistency. In this PhD study, electrolytes were prepared using polyvinyl alcohol (PVA) as the polymer matrix and potassium chloride (KCl) with varying concentrations to supply ions. The addition of KCl salt induces molecular-level changes in the polymer matrix by weakening the hydrogen bonds between polymer chains, primarily through its ionic interactions [57]. Consequently, the disruption of hydrogen bonding among the polymer chains results in an expansion of the free volume between them, thereby enhancing the overall flexibility of the polymer chains, as schematically illustrated in Scheme 6.1. Moreover, the presence of salt influences the polymer's structural characteristics, notably increasing its amorphous content while decreasing its crystallinity [287]. This phenomenon occurs as the salt disturbs the ordered structure of crystalline regions, leading to their transformation into more disordered, amorphous regions. Ultimately, the observed rise in amorphous content and reduction in crystallinity collectively contribute to the heightened flexibility exhibited by the electrolyte film [67, 287, 288].
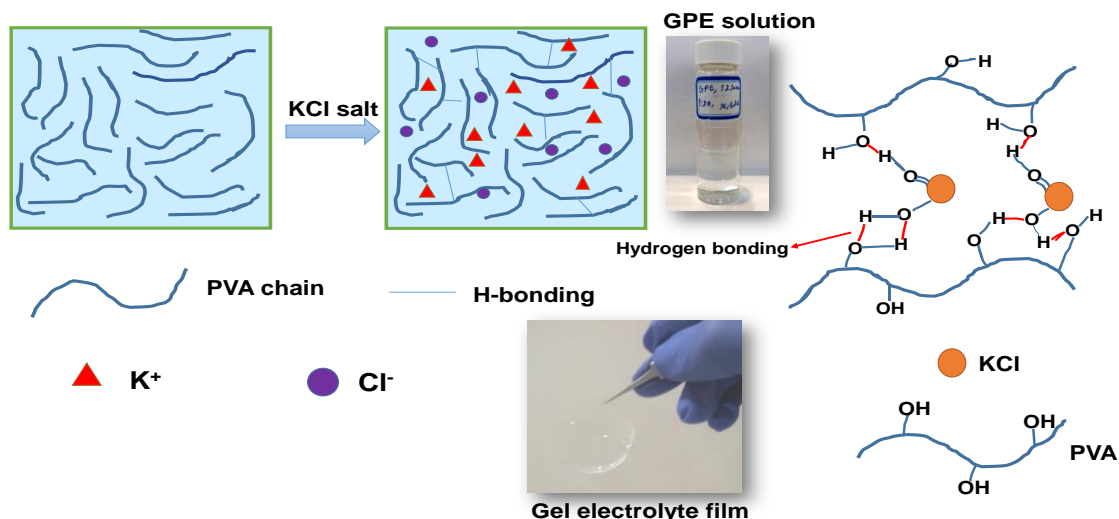
Scheme 6.1. Schematic illustration of the formation of KCl-plasticized PVA gel polymer electrolyte.

The gel electrolyte possesses a semi-crystalline structure with both crystalline and amorphous regions, as evident in the XRD pattern, a common characteristic of many polymers (Figure 6.1(a)) [134, 135]. Addition of KCl induces structural changes in the gel electrolyte, driven by fresh interactions within both its crystalline and amorphous phases. In the XRD pattern of pure PVA, two distinct diffraction peaks are noticeable at 2θ values of 9.6° and 19.6°, corresponding to d-spacing of 9.2 Å and 4.5 Å, respectively. These peaks indicate the presence of a semi-crystalline structure in PVA, featuring the (110) and (101) reflection planes. The heightened intensity of the (110) diffraction peak can be attributed to the prevalence of –OH groups in PVA side chains, fostering robust hydrogen bonding [53, 133]. However, upon the addition of KCl, the PVA crystallinity decreases from 59.87% to 40.74%. On the other hand, the crystallite size increases from 296 Å in pure PVA to 513 Å in PVA/KCl gel. These are typical beneficial effects of plasticizers, which lead to reduced polymer brittleness and enhanced flexibility, processability, and stretchability. Alterations in crystallite sizes can also be attributed to changes in molecular mobility prompted by the addition of plasticizers. The presence of KCl may contribute to an expansion in free volume, allowing for a slight enhancements in crystal growth [48, 51, 70, 136, 289]. This reduction in crystallinity and increase in crystallite size due to existence of KCl suggest a disorganization of the PVA crystalline structure, resulting in a more amorphous nature [290].

Enhanced polymer chain segmental motions within the amorphous structure promotes ion movement and contributes to elevated ionic conductivity levels.
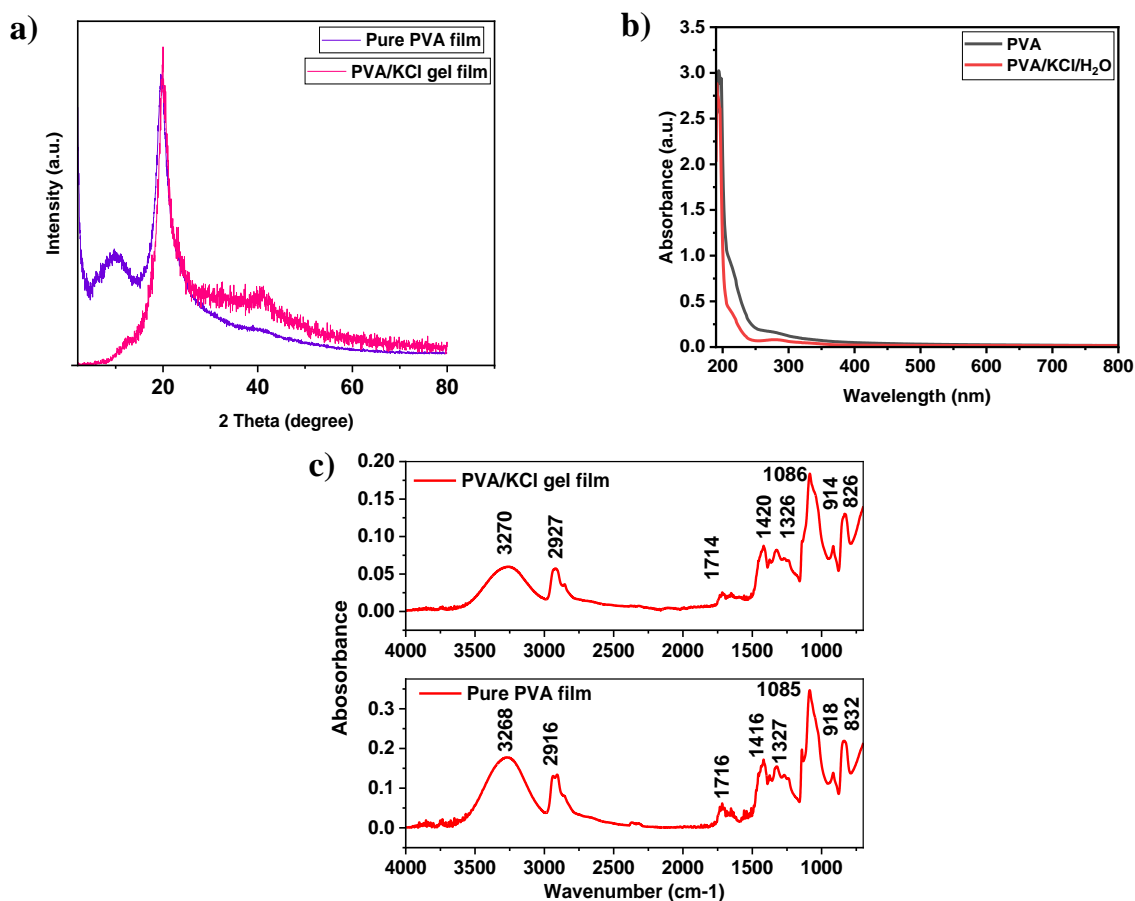
Figure 6.1. Structural characterization of pure PVA and PVA/KCl gel electrolyte (M_w = 195000 g mol^{-1}, PVA/KCl (w/w); 1/2). a) X-ray diffraction pattern with a continuous scan type covering the range from 2 to 80°, b) UV-Vis absorption spectra ranging from 190 to 800 nm, c) ATR-FTIR spectra within the 500-4000 cm^{-1} range.

This mechanism was further supported by UV-Vis results presented in Figure 6.1(b). In the case of pure PVA solution, a prominent absorption peak at 194 nm is observed in the UV region, accompanied by a shoulder at 280 nm in the visible region. These peaks correspond to the hydroxyl group transition of n → π* and π → π* transition of the carbonyl groups (C=O) linked with ethylene unsaturation (C=C) in the -(CH=CH)$_2$CO- moiety [51, 53]. Such transitions involve the excitation of electrons from the ground state to a higher energy state,

with the unshared electron pairs moving to the π^* orbital [21]. In the gel electrolyte solution, a peak at 320 nm may be attributed to n $\rightarrow \pi^*$ transition of the carbonyl groups and also a blue shift occurs in the absorption peak at 194 nm, along with a shift towards lower wavelengths in the absorption spectrum. These shifts suggest a reduction in hydrogen bonding among PVA chains, likely resulting from interactions between K^+/Cl^- ions and the polar groups within PVA [47, 291]. These observations suggest the formation of complexes between PVA and KCl, aligning with findings from the FTIR analysis (Figure 6.1(c)). The decreased peak intensity related to the (110) reflection plane signifies a decline in crystallinity. These findings align with alterations observed in FTIR and UV-Vis spectra, corroborated by prior research [51, 137], collectively indicating reduced interactions among PVA chains and the emergence of complexes formed between PVA and KCl (as illustrated in Figure 6.1(b) and Figure 6.1(c)).

In the ATR-FTIR spectrum of pure PVA film, peaks at 3268, 2916, 1718, 1415, 1327, 1085, 918, and 832 cm^{-1} (as shown in Figure 6.1(c)) are assigned to the O–H stretching, C–H stretching, C = O stretching, C–H wagging, C–O stretching of acetyl group, C–O stretching of an acetate group, and the two end peaks are related to the C–H bending; respectively [51, 53]. When PVA is combined with KCl in the gel electrolyte, these peaks undergo slight shifts, indicating potential interactions between the polymer and the salt [53]. The absorption peaks of PVA/KCl gel film at 3270, 2927, 1714, 1420, 1326, 1086, 914 and 825 cm^{-1} are attributed to the O–H stretching, C–H stretching, water absorption peak, C–H wagging, CH-OH bending, C–O stretching; respectively. The last two peaks are related to the C–H bending [291, 292]. Notably, the stretching vibrations of -OH and -CO groups experience significant modifications, with a decrease in peak intensity and a red-shift compared to pure PVA. These alterations strongly suggest the formation of complexes or interactions between the KCl and the polar groups in PVA (-OH and -CO), consistent with the previous reports [51, 137, 138, 293-296].

As a consequence of interactions between the polar groups in PVA and K^+/Cl^- ions, the gel electrolyte experiences a disturbance in its crystalline structure, resulting in an augmented predominance of the amorphous phase [291]. These interactions, likely facilitated by favorable electrostatic attractions and coordination effects between the ions of KCl and the oxygen groups within PVA in an aqueous environment, may potentially drive a hopping

mechanism, thus bolstering ionic conductivity [297]. The increased segmental mobility of polymer chains within the amorphous phase promotes ion mobility, thus supporting higher ionic conductivity. Consequently, this phenomenon greatly enhances ionic conductivity within the gel electrolyte, facilitating the smooth movement of ions (Scheme 6.2) [14, 17, 21, 70, 298]. In gel polymer electrolytes, three principal mechanisms are involved in ions conduction. The first mechanism, known as the "Grotthuss or hopping" mechanism, hinges on ion movement through the formation and disruption of hydrogen bonds between the ion and water molecules [15]. Ions "hop" between different sites characterized by varying potential energy, separated by small energy barriers arising from strong hydrogen bonding. This mechanism leads to increased ion mobility due to its low activation energy [21]. The second mechanism, diffusion, entails an ion forming a complex with water molecules before migrating through the electrolyte. The rate of ion penetration decreases as hydrogen bonds are established with other water molecules, resulting in a higher activation energy compared to the hopping mechanism [187]. The third mechanism, direct transfer, involves the displacement of polymer chains within the amorphous structure, facilitating ion transfer. In this phase, the motion of polymer chains eases ion transport. Above the glass transition temperature (T_g) of the polymer, the segmental movements of polymer chains enable ion transport within the amorphous phase. The ion conduction mechanism is influenced by temperature and humidity, with an increase in both factors, ion conduction enhances [15, 70, 299, 300].
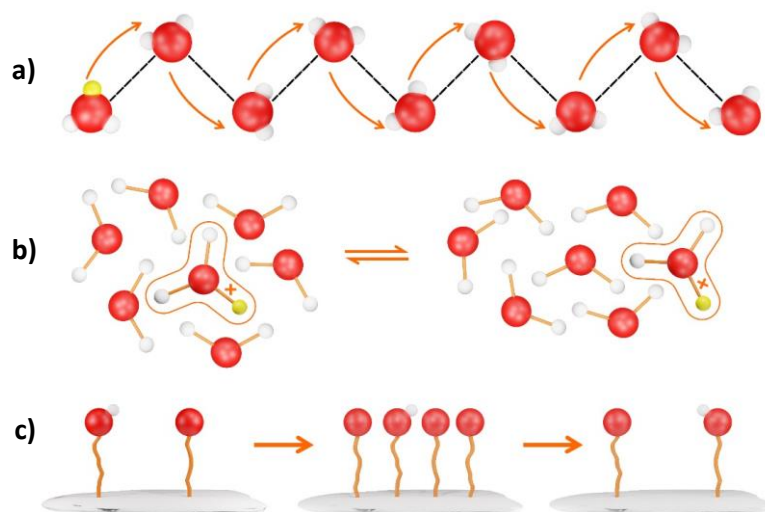
Scheme 6.2. Schematic illustration provides a visual representation of the various mechanisms responsible for proton conduction within gel polymer electrolytes. (a) Hopping

or Grotthuss Mechanism, (b) Diffusion or Vehicle Mechanism, (c) Segmental Motion of Polymer Chains.

Polymer gels are a versatile group of materials possessing various properties that fall between those of liquids and solids. They consist of a polymer and a solvent arranged in a three-dimensional cross-linked network structure [301, 302]. Physical cross-linked gels offer the advantage of not requiring the use of cross-linking agents. Their formation can be attributed to a range of physical interactions, including hydrogen bonding, crystallization, ionic bonds, molecular self-assembly, and mechanical dispersion [186]. Notably, the temporary bonds between their polymer chains can adapt themselves in response to temperature, pH, or solvent make-up. The softness of a gel can also be tuned by adjusting the spacing between crosslinks. This can be achieved by increasing the molecular weight of the polymer chain that connects the crosslinks or by diluting the gel with a liquid. The liquid component within the gel, which is not involved in the cross-linked network, is known as the sol. Commonly, the cross-linked polymer network itself is referred to as the gel [8, 15, 19].
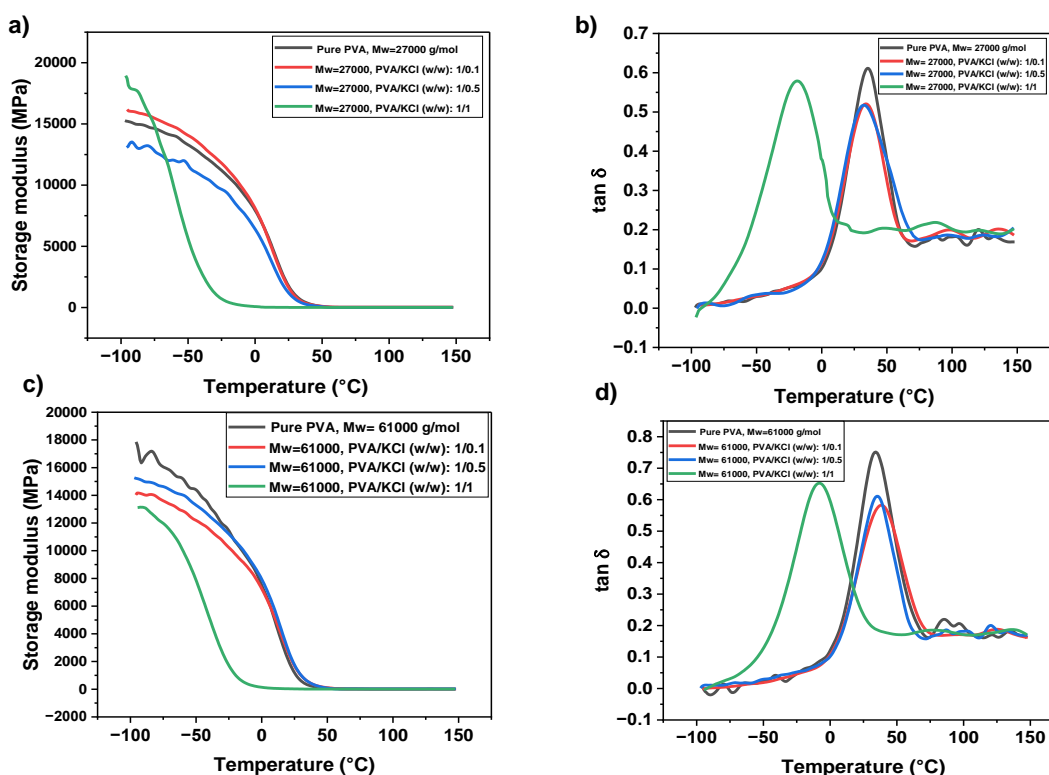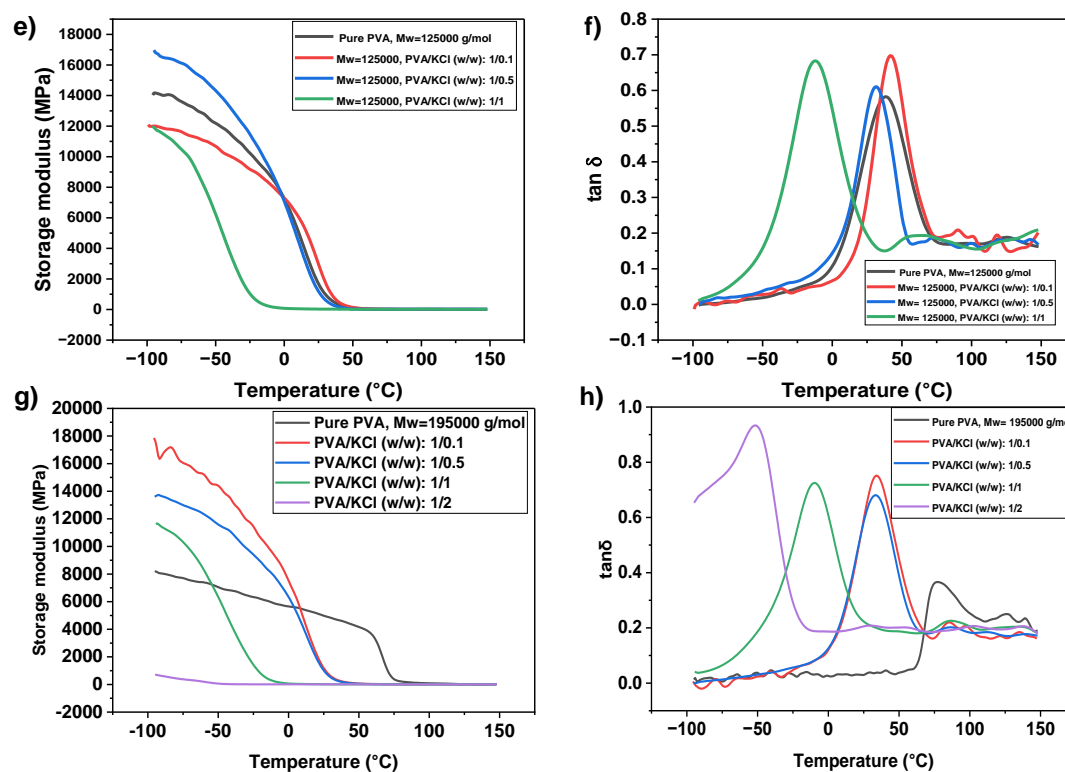
Figure 6.2. Dynamic mechanical thermal analysis (DMTA) results as storage modulus and tanδ for pure PVA and PVA/KCl gel polymer electrolyte with a,b) molecular weight of 27000 g mol^{-1}, c,d) molecular weight of 61000 g mol^{-1}, e,f) molecular weight of 125000 g mol^{-1}, g,h) molecular weight of 195000 g mol^{-1}, for different PVA/KCl weight ratios.

Dynamic Mechanical Analysis (DMA) was employed to assess the viscoelastic properties of the as-prepared gel electrolytes. A viscoelastic polymer can be described as a combination of elastic (spring-like) and viscous (dash-pot like) components [303]. DMA results offer insights into the influence of temperature on the mechanical behavior of PVA gel electrolytes, as well as on molecular relaxations and interactions within these materials [60]. The behavior of tanδ (the mechanical damping factor) and the storage modulus (E′) for both pure PVA and the gel electrolytes with different molecular weights are depicted in Figure 6.2.

PVA is classified as a semi-crystalline polymer, characterized by the presence of both crystalline ordered layers and amorphous folded chains. It exhibits a higher glass transition temperature (T_g) when compared to gel polymer electrolytes [51]. At room temperature, pure PVA typically exists in a glassy state, displaying high values for E′, indicating significant stiffness. However, when the temperature surpasses the T_g, the material undergoes a

transition into a rubbery elastic state, during which the moduli changes less with increasing temperature [57].

Interestingly, the addition of KCl to the PVA matrix did not lead to a consistent trend in the storage modulus across gels of different molecular weights. The DMA results for PVA/KCl gel electrolytes, employing PVA with molecular weights of 27000, 61000, and 125000 g mol^{-1}, and featuring PVA/KCl weight ratios of 1/0.1, 1/0.5, and 1/1, are thoughtfully illustrated in Figure 6.2 (a-f). In the tanδ versus temperature graphs for all samples, it is evident that increasing the KCl content in the gel reduces the glass transition temperature, confirming an increase in the amorphous phase of the polymer [59, 300]. In the storage modulus (E′) versus temperature graphs for M_w=27000 g mol^{-1}, there is no distinct trend in E' at lower temperatures. The addition of KCl salt to PVA leads to an increase in E' and then a decrease for weight ratios of 1/0.5 and 1/1. In contrast, for M_w=61000 g mol^{-1}, E' decreases for all samples, failing to form a stiff gel [63, 71]. For the GPE with PVA of M_w=125000 g mol^{-1}, there is no discernible trend in E'. Upon the introduction of KCl salt to the PVA, E' experiences an increase for the weight ratio of 1/0.5. However, the gels with 1/0.1 and 1/1 weight ratios exhibit lower E' in comparison to pure PVA. This phenomenon is most likely attributed to the agglomeration effect induced by the salt, resulting in viscosity increment and a behavior resembling that of a viscous substance [4, 59, 60].

Unlike purely elastic solids, polymer gels possess a viscoelastic character, meaning they can internally rearrange and dissipate energy. This characteristic is particularly pronounced in polymer gels where the polymer chain length, whether in the solvent or as part of the gel network, is substantial enough to allow the polymer to physically entangle with itself [58, 71]. Such behavior makes these gels ideal for use in flexible solid-state supercapacitors, which are often required to bend, twist, or stretch without losing their functionality. The viscoelastic behavior of the gel electrolyte allows it to deform under stress and then recover its shape when the stress is removed, which is crucial for maintaining the integrity of the supercapacitor during mechanical stress [304, 305]. In the case of the gel with M_w=195000 g mol^{-1}, the PVA demonstrated a glassy and rigid behavior at temperatures below the T_g (Figure 6.2(g)). The introduction of salt led to an increase in the elastic modulus, indicating a resistance deformation. This could be attributed to both a reinforcement effect within this temperature range and the formation of interactions between PVA chains and KCl salt [306,

307]. Additionally, a rise in the KCl salt content resulted in a decrease in E', likely due to the formation of ion aggregates that heightened viscosity and displayed characteristics close to a viscous behavior. With an increasing KCl salt content, the T_g decreased due to the plasticizing effect of the salt which in turn diminished the intermolecular and intramolecular interactions between the polymer chains [57, 61].

The influence of temperature and KCl content on the damping factor (tanδ) of the gel with M_w=195000 g mol^{-1} is also depicted in Figure 6.2(h). PVA exhibits a single transition peak at approximately 77.2 °C, attributed with relaxations in the amorphous regions of PVA, where the molecular chains exhibit attainable micro-Brownian motions [304, 307]. As expected, the addition of KCl to the gel resulted in a decrease in the glass transition temperature (T_g) due to a smaller fraction of the polymer matrix and an increase in the size of PVA crystallites. This indicates that the gelation process potentially transformed certain crystalline PVA structures into a cross-linked network, consequently limiting the mobility of the polymer chain [63, 308]. Consequently, the addition of KCl results in a shift to lower temperature in the tanδ peak, indicative of reduced restrictions to the cooperative motion of the PVA chains segmental movement. When the PVA/KCl content is 1/0.1, the glass transition temperature is 34.1 °C, indicating that KCl facilitates the relaxation process, leading to a softer system and consequently decreasing the T_g [304, 305]. This behavior can result from an increase in the mobility of the amorphous PVA molecules caused by the weak intermolecular hydrogen bonds between PVA chains. The T_g decreases further with increasing KCl, likely due to the weakening of intermolecular hydrogen bonds between PVA chains as more KCl is dispersed unevenly in the PVA matrix and the plasticizing effect of possible KCl agglomerates [62, 71].

For covalently cross-linked materials, E′ is greater than E″(loss modulus), signifying the presence of elastic properties, a characteristic feature of a gel. A similar inference can also be made for physically cross-linked gels. The higher storage modulus for the gel shows the greatest storage of deformation energy. The lowest storage modulus occurs when the PVA/KCl ratio is 1/2, demonstrating the dominance of viscous nature over elastic character and the effective solvation of the polymer backbones of the gel by water [287, 309]. Therefore, E′ gradually decreases as the amount of KCl increases. This phenomenon can be attributed to the plasticizing effect of PVA, which demonstrates its sensitivity to the presence

of salt through the disruption of hydrogen bonds and the reduction of cohesive energy between polymer chains. The introduction of KCl molecules weakens the hydrogen bonds at a molecular level, leading to increased inter-chain spaces and enhanced flexibility of the polymer chains [304, 310]. Consequently, the presence of KCl salt results in an increase in the polymer amorphous structure and a decrease in its crystallinity, thereby imparting greater flexibility to the electrolyte film. From this, it can be inferred that the movement of the polymer chains in the amorphous phase facilitates the transfer of ions with ion mobility occurring above the glass transition temperature (T_g) of the polymer. Therefore, the diffusion mechanism dominates the Grotthuss mechanism [15, 70, 299, 300].

Table 6.1, presents the ratio of E'/E'' at three different temperatures for the gel with M_w=195000 g mol^{-1}, which is indicative of the viscoelastic behavior of the gel electrolyte. At -50 °C, the E'/E'' ratio for PVA/KCl (w/w) gel electrolyte with weight ratios of 1/0.1 and 1/0.5 is higher than 10, indicating a robust gel. In contrast, the PVA/KCl (w/w) gel electrolyte with ratios of 1/1 and 1/2 have a lower E'/E'' ratio, less than 10, and are considered soft gels [4, 304]. This disparity may be attributed to the complete connection of polymer chains to crosslinks in the former case, ensuring a higher elastic modulus and a stronger gel structure. In contrast, an unequal ratio of polymer chains to cross-linkers can introduce network defects, such as loops and dangling ends, thereby yielding a softer gel [305, 310]. A gel electrolyte behaves more like a viscoelastic soft-solid at higher E'/E'' ratios, as the "long-range" rearrangements of polymer chains are very slow. However, a lower E'/E'' ratio suggests a dominant viscous behavior (liquid-like), implying that "short-range" rearrangements of polymer chains occur rapidly [4, 304]. By increasing the temperature for the PVA/KCl gel electrolyte with weight ratios (w/w) of 1/0.1 and 1/0.5, the electrolyte behaves as a soft gel. This is because higher temperatures reduce the interaction between the polymer chains and disrupt the gel network structure. However, the PVA/KCl gel electrolyte with weight ratios (w/w) of 1/1 and 1/2 still behaves as a soft gel at higher temperatures [4, 310]. The behavior of the gel electrolyte changes from being liquid-like to solid-like at the gel point. By increasing the temperature, the solid-like (elastic) behavior of the gel dominates over the liquid-like (viscous) character. The viscosity changes, making the gel softer and forming a highly cross-linked system [4, 15, 17]. Thus, the PVA/KCl gel electrolyte with a weight ratio of 1/2 is considered as a weak gel.

Table 6.1. The ratio of E′/E″ and tanδ peak for PVA/KCl/H₂O gel polymer electrolytes at different temperatures.

Gel Material	-50 °C	0 °C	50 °C	Tanδ peak (°C)
M_w=195000 g mol⁻¹, PVA/KCl(w/w): 1/0.1	42.98	8.45	2.5	34.1
M_w=195000 g mol⁻¹, PVA/KCl(w/w): 1/0.5	29.82	7.93	3.06	33.4
M_w=195000 g mol⁻¹, PVA/KCl (w/w): 1/1	5.43	1.51	6.5	-9.8
M_w=195000 g mol⁻¹, PVA/KCl (w/w): 1/2	1.04	5	8	-51.7

The mechanical properties of pure PVA film and PVA/KCl gel film are shown in Figure 6.3. PVA is a semi-crystalline polymer containing crystalline layers and amorphous folded chains with a higher tensile strength (68.5±5.35 MPa) compared to the electrolyte specimen (15.88±0.25 MPa). PVA demonstrates a relatively high strength in its elastic region, representing its ability to resist deformation under load without permanent damage. The lower Young modulus and elastic strength of the gel film suggest a more flexible and deformable nature compared to pure PVA [48, 49]. However, the highest elongation at break for the gel film signifying enhanced flexibility and stretchability.

KCl salt acts as a plasticizer and weakens the bonds between polymer chains at the molecular level. Moreover, the free volume or inter-chain spaces between PVA chains are increased, making the polymer chains more flexible. KCl salt increases the amorphous content and decreases the crystallinity of PVA, which is consistent with the results of characterization tests [45, 64]. The highest toughness of pure PVA reflects the amount of energy the material can absorb before rupturing, combining both strength and ductility. While pure PVA demonstrates higher stiffness and elastic strength, the gel sample exhibits superior flexibility

and stretchability, offering advantages in solid-state supercapacitor applications requiring conformability and deformability [65, 66].
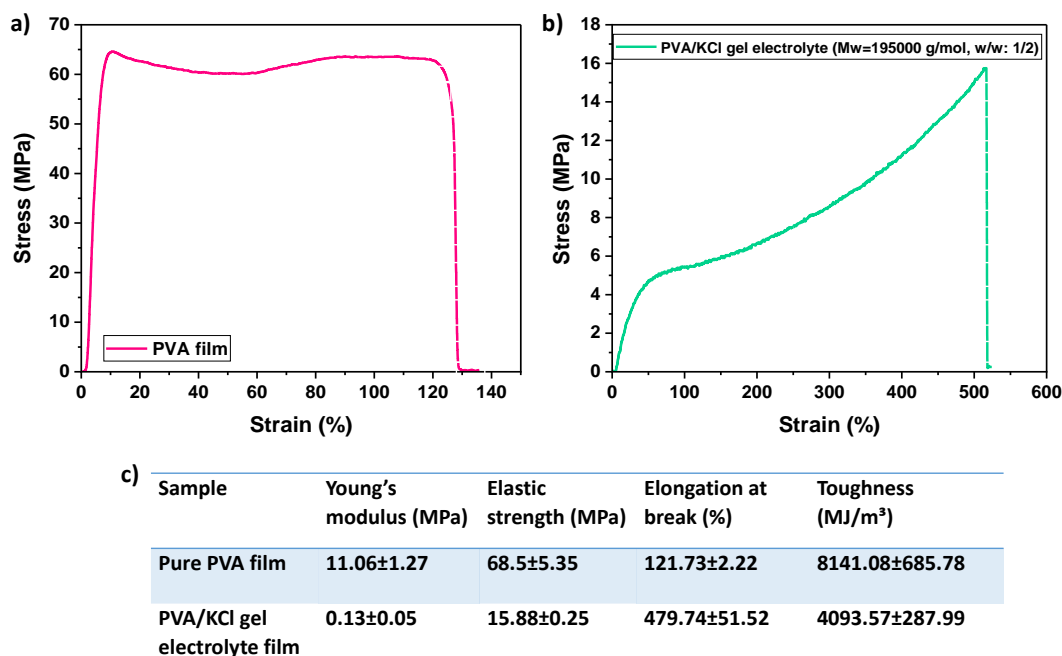
Figure 6.3. Stress-strain curve for a) pure PVA film (M_w=195000 g mol^{-1}), b) PVA/KCl gel electrolyte film (M_w=195000 g mol^{-1}, w/w: 1/2), c) Tensile properties result for pure PVA and PVA/KCl gel films.

The surface morphology and microstructure of the poly(vinyl alcohol) (PVA) film and gel films were unveiled in the field emission scanning electron microscopy (FE-SEM) image presented in Figure 6.4. The image depicts a smoother and more even surface with less roughness for the pure PVA film (Figure 6.4(a)). This indicates a compact and uniform structure, suggesting a dense arrangement of PVA molecules, which aligns with findings from similar studies, affirming the high quality and uniformity of the film [67-69].

The surface of the PVA/KCl film sample (Figure 6.4 (b and c)) displays a more textured appearance, implying the presence of dispersed potassium chloride particles within the dried PVA matrix. These particles contribute to the overall roughness and texture of the surface. [53, 311]. The SEM image further highlights a homogeneous distribution of individual KCl

117

aggregates on the surface of the dried PVA film, characterized by white dots and relatively larger spots, indicating good compatibility and interaction between PVA and KCl [69, 276]. Consequently, the combination of KCl with the PVA matrix leads to a relatively rough film surface, likely due to the disruption of hydrogen bonds and the formation of interactions between PVA and KCl. Overall, the uniform compatibility between the KCl particles and the PVA polymer throughout the entire volume suggests the formation of well-formed PVA-KCl composites, consistent with existing literature [45, 67, 70].

The images (Figure 6.4 (d-h)) depict the EDAX-Mapping results illustrating the presence of various elements in the PVA/KCl gel film. The elemental mapping is represented in different colors, with C (red), O (green), K (orange), and Cl (blue) detected within the sample. These elements correspond to carbon and oxygen from the PVA chains, as well as potassium and chlorine from the KCl salt. The high-purity condition of the prepared sample is indicated by the presence of these elements. Furthermore, the EDS mapping (Figure 6.4 (h)) demonstrates the uniform spatial distributions of C, O, K, and Cl elements within the pure polymer sample, consistent with previous findings obtained for similar samples [72, 312, 313].
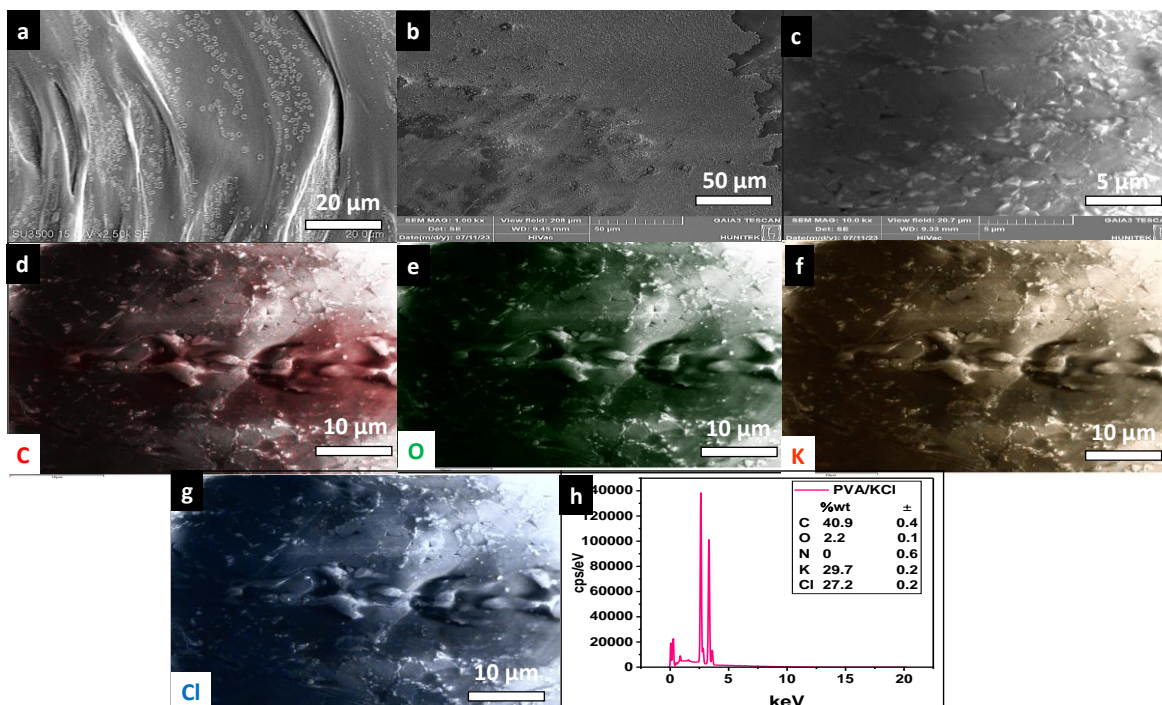
Figure 6.4. Field emission scanning electron microscopy (FE-SEM) results, where (a) represents pure PVA, while (b) and (c) depict PVA/KCl (M_w = 195000 g mol^{-1}, PVA/KCl

(w/w); 1/2) at different magnifications. SEM-EDX elemental mappings of the GPE (M_w = 195000 g mol^{-1}, PVA/KCl (w/w); 1/2) for the elements (d) carbon (C), (e) oxygen (O), (f) potassium (K), and (h) chlorine (Cl). Additionally, (h) shows the EDAX spectrum of the PVA/KCl gel film.

6.2. Structural properties of graphene oxide (GO) and GO/chitosan composite

To assess the structural properties of GO, CS, GO/CS, and RGO/CS composites, a comprehensive array of characterization techniques including ATR-FTIR, XPS, UV-Vis, AFM, XRD, BET, POM, FE-SEM, electrical conductivity, and tensile mechanical tests were employed. Scheme 6.3 illustrates the fabrication process for reduced graphene oxide/chitosan (RGO/CS) composite electrodes, involving sequential stages of CS and graphene oxide (GO) solution casting, followed by the thermal reduction of GO [314]. This thermal reduction step entails subjecting the GO/CS composite to elevated temperatures (~120 °C) to eliminate oxygen-containing functional groups present in GO through chemical reactions and desorption [315]. The outcome is the restoration of sp² carbon-carbon bonds, thereby enhancing electrical conductivity and mechanical properties, ultimately yielding RGO with characteristics similar to pristine graphene [97, 268].
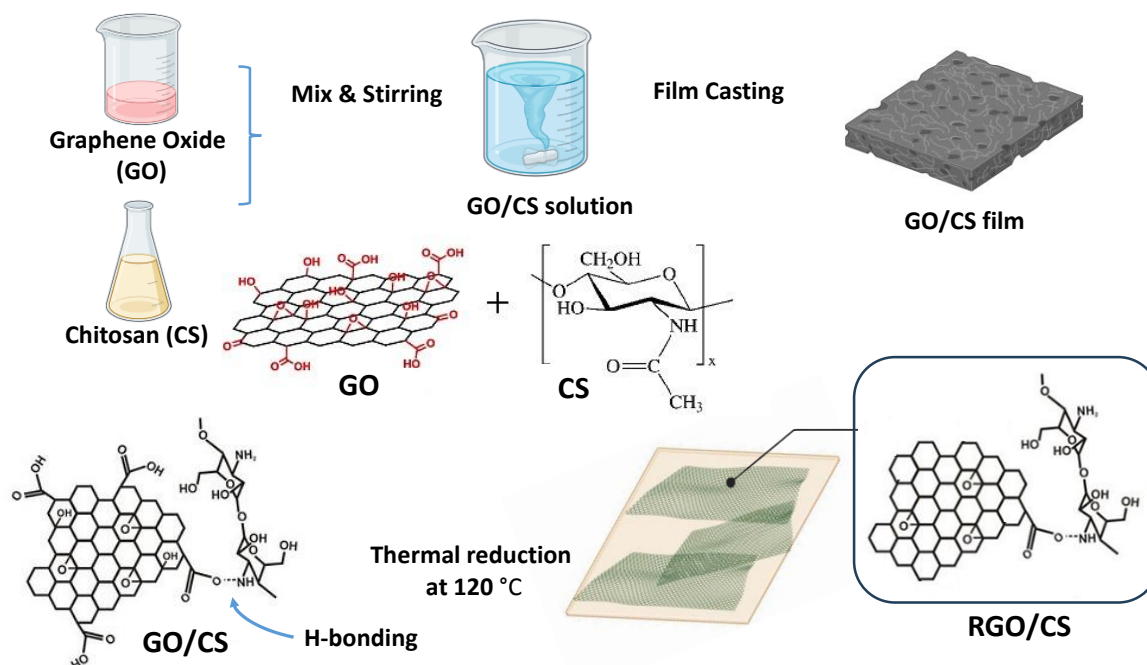
Scheme 6.3. The procedural steps for the fabrication of the RGO/CS composite electrode.

XRD analysis was employed to examine the interlayer distance of GO sheets and the crystallinity of GO/CS films. Figure 6.5 presents the XRD results for GO, CS, RGO, GO/CS, and RGO/CS films separately. The oxidation of GO is evidenced by the increased interlayer spacing compared to graphite oxide, attributed to a higher concentration of epoxy (–C–O–C–), hydroxyl (–C–OH), and carboxylic (–C–O–OH) groups on both the basal plane and edge. Analysis of the as-prepared GO dispersion reveals a 2θ value of 11.26°, confirming the complete oxidation of graphite flakes into GO, characterized by a d-spacing (d) of 7.62 Å corresponding to the (001) reflection planes of GO sheets (Figure 6.5 (a)) [142, 214].

Following the substantial removal of oxygen-containing functional groups during thermal reduction of GO, a distinct and sharp peak emerges for RGO at 2θ = 13.31° (d=6.70 Å) (Figure 6.5 (b)). This observation underscores the substantial restoration of the π-conjugated structure inherent to graphene upon the production of RGO. The appearance of the sharp peak (002) in RGO suggests the random arrangement of the crystal phase (002), a departure from the highly crystalline structure of graphite. This divergence is potentially attributed to the formation of single or only a few layers of RGO subsequent to reduction from GO [97, 316]. Additionally, the small d-spacing in RGO confirms the efficient elimination of oxygen-containing functional groups. This observation also suggests that thin RGO nanosheets are stacked to each other to form a thicker layered structure due to the presence of robust Van der Waals forces between the individual layers. Another broader and intense peak at 2θ =26.20° (d=3.40 Å) with (001) orientation can be attributed to the turbostratic band arising from disordered carbon materials or an alternative stacking arrangement in the RGO which these results are consistent with the literatures [78, 79].

Chitosan in its pristine powder exhibits two typical characteristic peaks at 10.08° (d=8.80 Å) and 21.24° (d=4.20 Å), which are well-established identifiers (Figure 6.5 (c)). These peaks may correspond to intermolecular distance and different crystalline arrangement or molecular packing within the chitosan structure [80, 93]. Upon the modification of GO with CS, the XRD analysis reveals the emergence of two distinct peaks at approximately 2θ ~ 10.72° (d=8.30 Å) and 23.68° (d=3.80 Å), confirming the successful binding of chitosan to the surface of GO (Figure 6.5 (d)). It is worth noting that, due to peak overlapping, no discernible peak related to GO is evident in the XRD patterns of GO-CS composite. The

presence of the peak at 2θ = 10.72° in GO-CS aligns with that of pure GO, indicating the persistence of stacked GO sheets within the GO-CS structure [93, 97].

Notably, the XRD pattern of RGO/CS composite showcases a shift in peak position at approximately 2θ ~24.64° (d=3.60 Å) (Figure 6.5 (e)). This peak shift, relative to the distinct chitosan and RGO peaks, confirms the interaction between the semicrystalline nature of CS and graphene nanosheets. These outcomes serve as confirmation of the formation of a nanocomposite structure between the two components [94, 144]. Figure 6.5 (f) shows the XRD results of all samples. A comparison figure of XRD results and d-spacing of RGO, CS, RGO/CS is given in Figure 6.6(a). The result of XRD test along with other research works [314, 315] confirms that the presence of chitosan might influence the stacking and arrangement of RGO layers, leading to changes in the d-spacing compared to pure RGO in RGO/CS composite, indicating the existence of an interaction or a specific arrangement of RGO and chitosan layers in the composite structure.
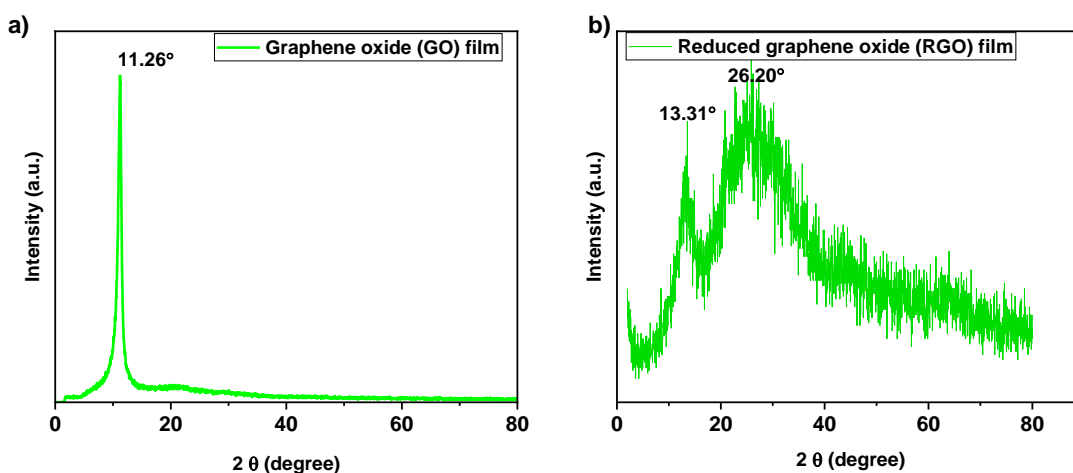
Figure 6.5. X-ray diffraction pattern of a) graphene oxide (GO), b) reduced graphene oxide (RGO), c) chitosan (CS), d) graphene oxide/chitosan (GO/CS, (w/w: 90/10)), and e) reduced graphene oxide/chitosan (RGO/CS, (w/w: 90/10)), f) All graphs in the degree range of 2° to 80°.

X-ray Photoelectron Spectroscopy (XPS) serves as a powerful analytical technique for probing the chemical environment and bonding characteristics of elements present on a material's surface to a depth of approximately 10 nm [317]. The C1s spectrum of GO, as depicted in Figure 6.6(b), exhibits multiple peaks that can be deconvoluted into five components, each corresponding to specific carbon species. The peaks located at 284.9 eV, 285.3 eV, 286.0 eV, 287.5 eV, and 288.6 eV are attributed to carbon sp^2 (C=C), C-C/C-H sp^3, epoxy/hydroxyl, C=O, and carboxylates (O-C=O) species, respectively [4, 142, 318].

These distinct peaks reflect the diverse functional groups present on the GO surface, resulting from the oxidation and exfoliation process of graphite flakes [4, 142].

Upon the reduction of GO, a pronounced decrease in the intensity of oxygenated carbon species is observed in the spectrum of RGO (Figure 6.6(c)), accompanied by a noticeable increase in the relative abundance of C=C and C-C/C-H type carbons [142, 318]. This change in spectral features provides compelling evidence for the successful reduction removing oxygen-containing functional groups effectively, thereby leading to the restoration of sp^2 carbon-carbon bonds, similar to the structure of pristine graphene [76]. Chitosan manifests specific carbon species in its C1s spectrum (Figure 6.6 (d)), including C-C, C=O, and O-C=O moieties at 283.39, 284.94, and 286.56 eV, respectively. This observation is consistent with its anticipated chemical composition [319]. The C1s spectra of the composites containing chitosan and either RGO or GO reflect the spectral features characteristic of both constituent materials (Figure 6.6 (e)). This observation provides strong evidence for their successful incorporation within the composite structure [97, 318]. Importantly, the composite containing GO exhibits higher intensities of oxygenated carbon species compared to the one containing RGO. This difference aligns with findings from previous research [76, 145, 315], as GO inherently contains more oxygen-containing functional groups due to its oxidation process.
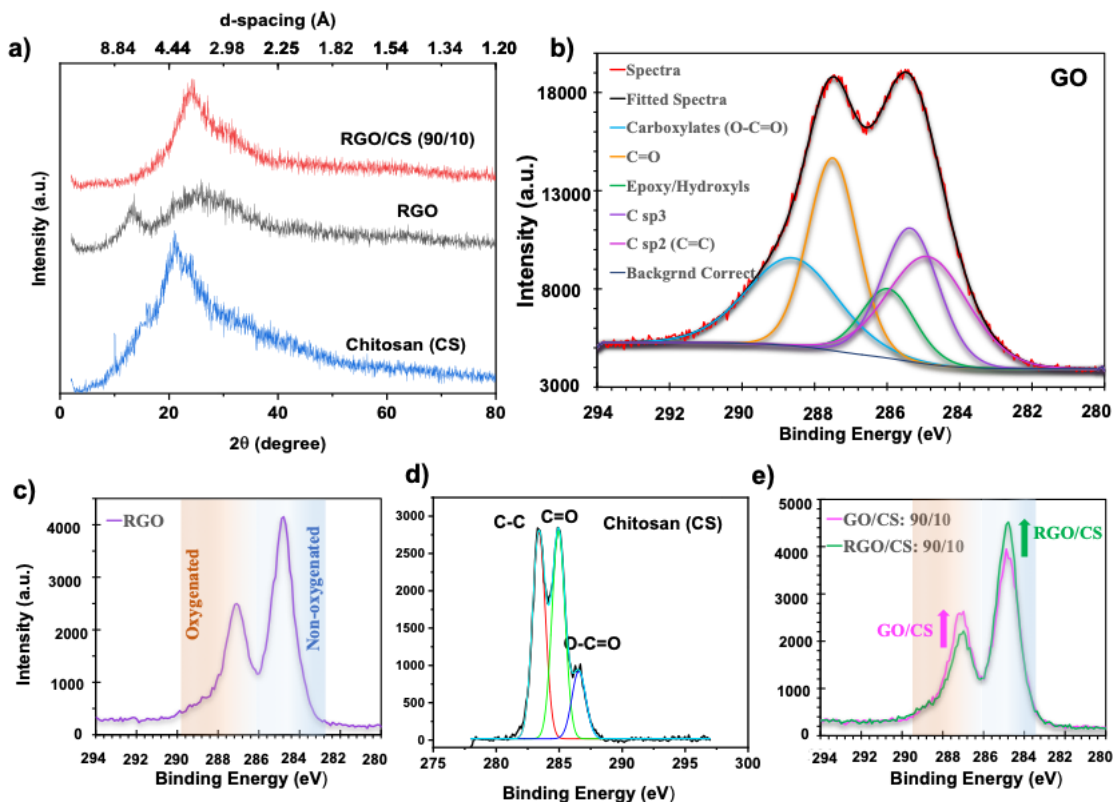
Figure 6.6. X-ray diffraction pattern of reduced graphene oxide (RGO), chitosan (CS), and reduced graphene oxide/chitosan (RGO/CS, (w/w: 90/10)). C1s core-level XPS spectra of b) Graphene Oxide (GO), c) reduced graphene oxide (RGO), d) chitosan (CS), e) comparison of GO/CS (w/w: 90/10) and RGO/CS (w/w: 90/10).

The application of ATR-FTIR serves as a robust methodology for the elucidation of component interactions, as well as for confirming the successful oxidation of graphite to produce GO. Figure 6.7 shows the ATR-FTIR spectra of pure graphene oxide (GO), chitosan (CS), RGO, GO/CS, and RGO/CS. The discernible features within the spectra unveil the characteristic absorption peaks of GO in Figure 6.7(a), situated at 3282, 2791, 2302, 1621, 1415, 1109, 969, 885 and 807 cm^{-1}. These peaks correspond to O–H stretching of carboxylic acid, asymmetrical stretching of CH$_2$, stretching of CH$_3$, C–O stretching of carboxylic acid, C–C stretching, C–O stretching of phenol group, C–O stretching of alkoxy group, and the last two peaks are related to C–H bending, respectively [48, 77, 320].

In the spectrum of chitosan (Figure 6.7(b)), a strong band at 3204 cm^{-1} signifies N-H and O-H stretching, alongside intramolecular hydrogen bonding. The bands around 2925, 2858, 2365 cm^{-1} were attributed to C-H symmetric stretching, C-H asymmetric stretching and N-

H stretching of amide II; respectively. While the presence of residual N-acetyl groups was confirmed by bands at around 1637 cm^{-1} (C=O stretching of amide I) and 1397 cm^{-1} (C-N stretching of amide III). The band at 1541 cm^{-1} was attributed to N-H bending of amide II, signifying typical N-acetyl groups. The presence of asymmetric stretching of the C-O-C bridge was noted at 1149 cm^{-1}, and bands at 1064 and 1018 cm^{-1} aligned with C-O stretching, and the last peak at 892 cm^{-1} is related to C–H bending [7, 321].

In the RGO spectrum (Figure 6.7(c)), the occurrence of peaks at 2344, 1559, 1060 cm^{-1} was associated with the asymmetrical stretching of CH$_2$, C=C stretching, C-O stretching of phenol group. All the intensities of the peaks corresponding to the oxygen containing functionalities of reduced graphene oxide were decreased as compared to the intensities of peaks of graphene oxide and even some were disappeared. Thus, after heat treatment of graphene oxide, the intensities of the OH band (3093 cm^{-1}) and C=O (1710 cm^{-1}) peaks decreased or disappeared, indicative of GO reduction [322-324].

The FTIR spectrum of the GO/chitosan composite showed a combination of characteristics peaks associated with chitosan and GO, with minor shifts (Figure 6.7(d)). This intriguing outcome suggested interactions between chitosan and GO. Peaks located at 3267, 2930, 2852, 2355, 1733, 1653, 1375, 1147, 1020, and 862 cm^{-1} were attributed to N-H and O-H stretching, C-H symmetric stretching, C-H asymmetric stretching, N-H stretching of amide II, C=O stretching of amide I, N-H bending of amide II, C-N stretching of amide III, asymmetric stretching of the C-O-C group, C–O stretching of alkoxy group, and C–H bending; respectively [93, 325]. This confluence of evidence suggested the formation of GO-chitosan composites through a reaction between epoxy groups on the GO surface and amino groups (NH$_2$) on chitosan. Moreover, it is plausible that the creation of GO-chitosan composites arises from covalent bonding subsequent to cross linking between GO and chitosan, which retards the decomposition of amine units within chitosan [127, 314].

In the FTIR spectrum of RGO/CS (Figure 6.7(e)), the observed peaks at 3212, 2933, 2851, 2369, 1717, 1560, 1223, 1158, 1048, 825 cm^{-1} were attributed to N-H and O-H stretching, C-H symmetric stretching, C-H asymmetric stretching, N-H stretching of amide II, C=O stretching of amide I, N-H bending of amide II, C–O stretching of alkoxy group, asymmetric stretching of the C-O-C group, C–O stretching of alkoxy group, and C–H bending,

respectively [97, 326]. It's noteworthy that the intensity of O-H stretching and C-O stretching was lower compared to the GO/CS spectrum, indicating the reduction of GO to RGO. Subtle shifts in peaks were observed, possibly attributable to hydrogen bonds among composite components. Additionally, the presence of RGO in the composite was indicated by the peak found at 1048 cm^{-1} in the RGO/CS spectrum [9, 93].
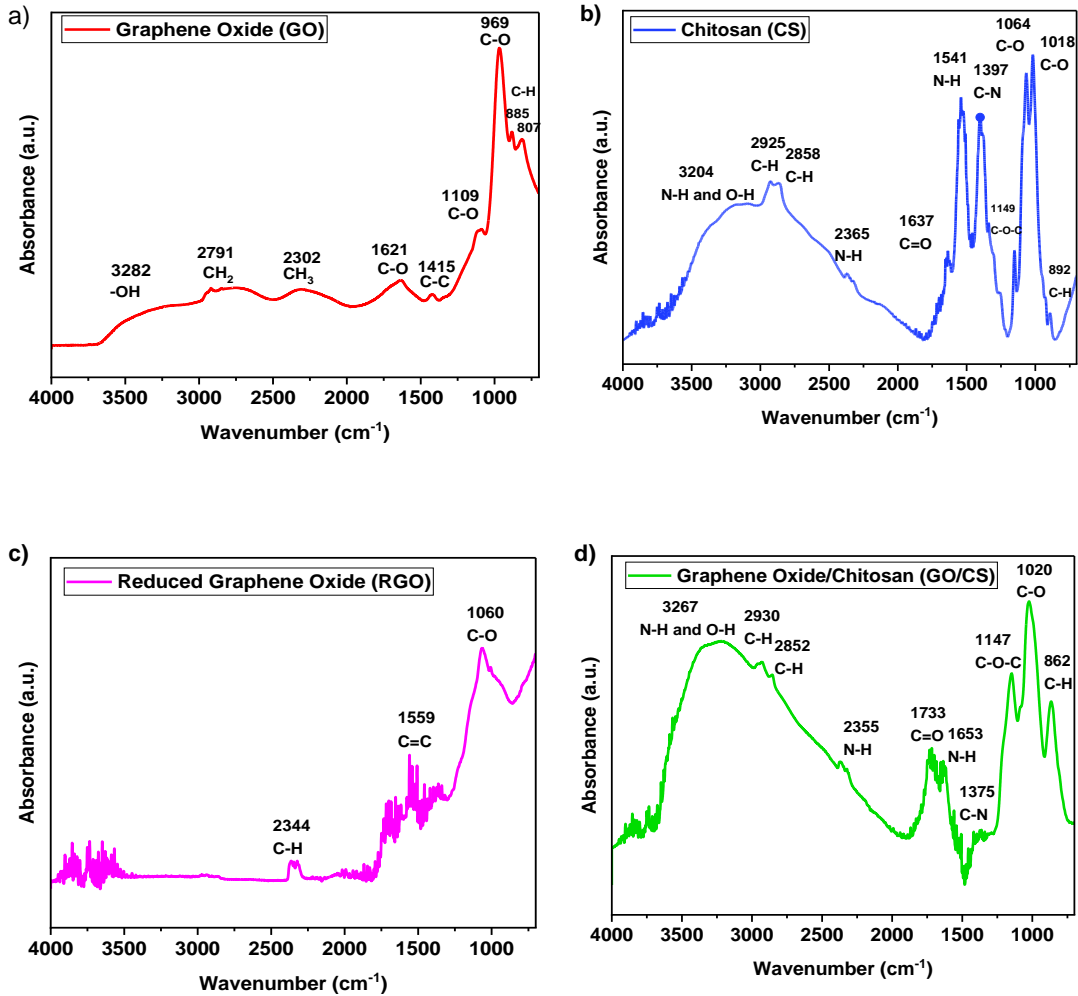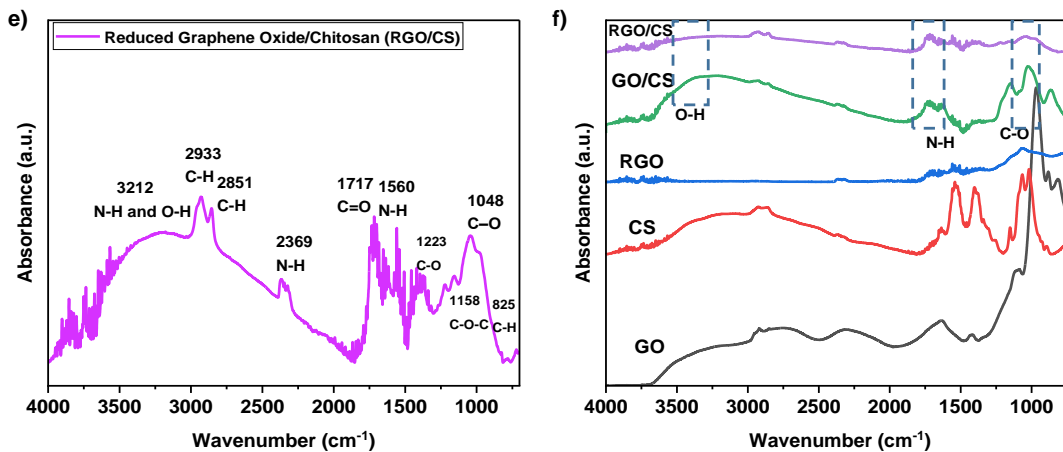
Figure 6.7. ATR-FTIR spectra of different materials: a) Graphene oxide (GO), b) chitosan (CS), c) reduced graphene oxide (RGO), d) graphene oxide/chitosan (GO/CS, (w/w: 90/10)), e) reduced graphene oxide/chitosan (RGO/CS, (w/w: 90/10)) and f) All graphs.

The UV-Vis spectra of all samples is illustrated in Figure 6.8. A distinctive peak is evident in the GO spectrum at 230 nm (Figure 6.8(a)), attributed to the π–π^* transitions inherent to the C–C aromatic bond. A small shoulder at 300 nm arises due to n–π^* transitions linked to the C=O bond [142, 318]. Notably, a shift towards longer wavelengths from 230 nm to 263 nm is observed in the absorption peak of the GO dispersion following reduction (Figure 6.8 (b)). Furthermore, a comprehensive enhancement in absorption across the entire spectral region occurs after reduction. The red-shift observed in RGO emanates from the elimination of oxygen functional groups and the consequent reinstatement of the conjugated structure which is consistent with the literatures [48, 142, 143].

UV-Visible spectroscopy is widely harnessed for the investigation of the optical properties of biopolymers. Within chitosan, the presence of two far-UV chromophoric groups, namely N-acetylglucosamine (GlcNAc) and glucosamine (GlcN), engenders nonzero extinction coefficients for wavelengths shorter than approximately 225 nm [127, 327]. As GlcNAc and GlcN residues exhibit no signs of interaction within the chitin/chitosan chain, their contributions to the overall absorbance of this polymer at a particular wavelength are additive. Specifically, the UV spectrum of chitosan in acetic acid solution manifests a peak wavelength at 200 nm (Figure 6.8(c)) [328]. Upon the attachment of GO with CS, an intriguing phenomenon emerges: the peaks associated with GO at 230 and 300 nm exhibit a rightward shift (Figure 6.8(d)). This shift signifies the interaction between epoxy groups on

GO and amino groups (NH$_2$) on chitosan, culminating in the formation of the GO/CS composite [92]. Subsequent to the chemical attachment of chitosan onto GO, the 230 nm peak experiences a red-shift to 270 nm in the RGO/CS spectrum (Figure 6.8(e)), accompanied by a conspicuous disappearance of the 300 nm shoulder. This change is attributed to the partial restoration of electronic conjugation among aromatic carbon atoms. Collectively, these outcomes suggest that chitosan becomes conjugated with GO after reduction [97, 314].
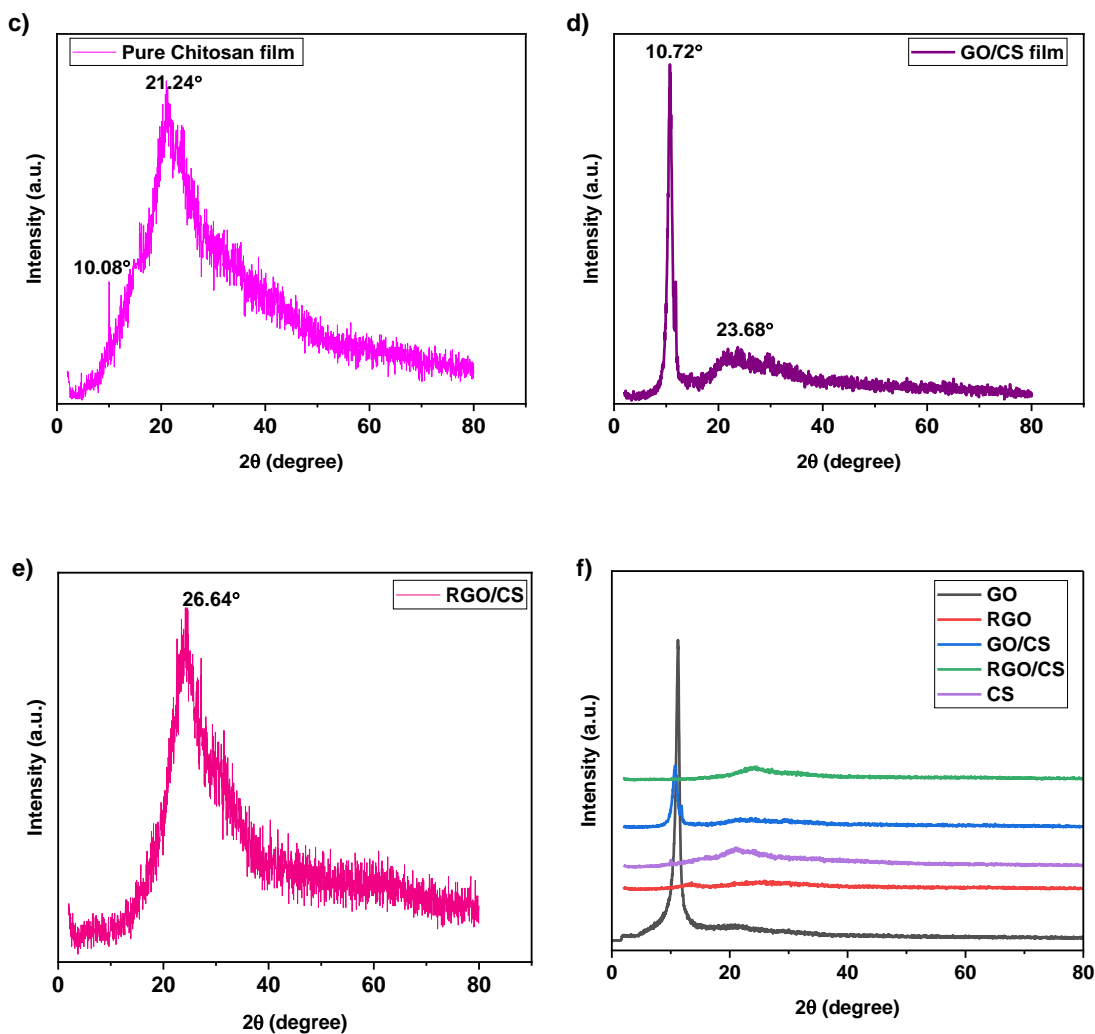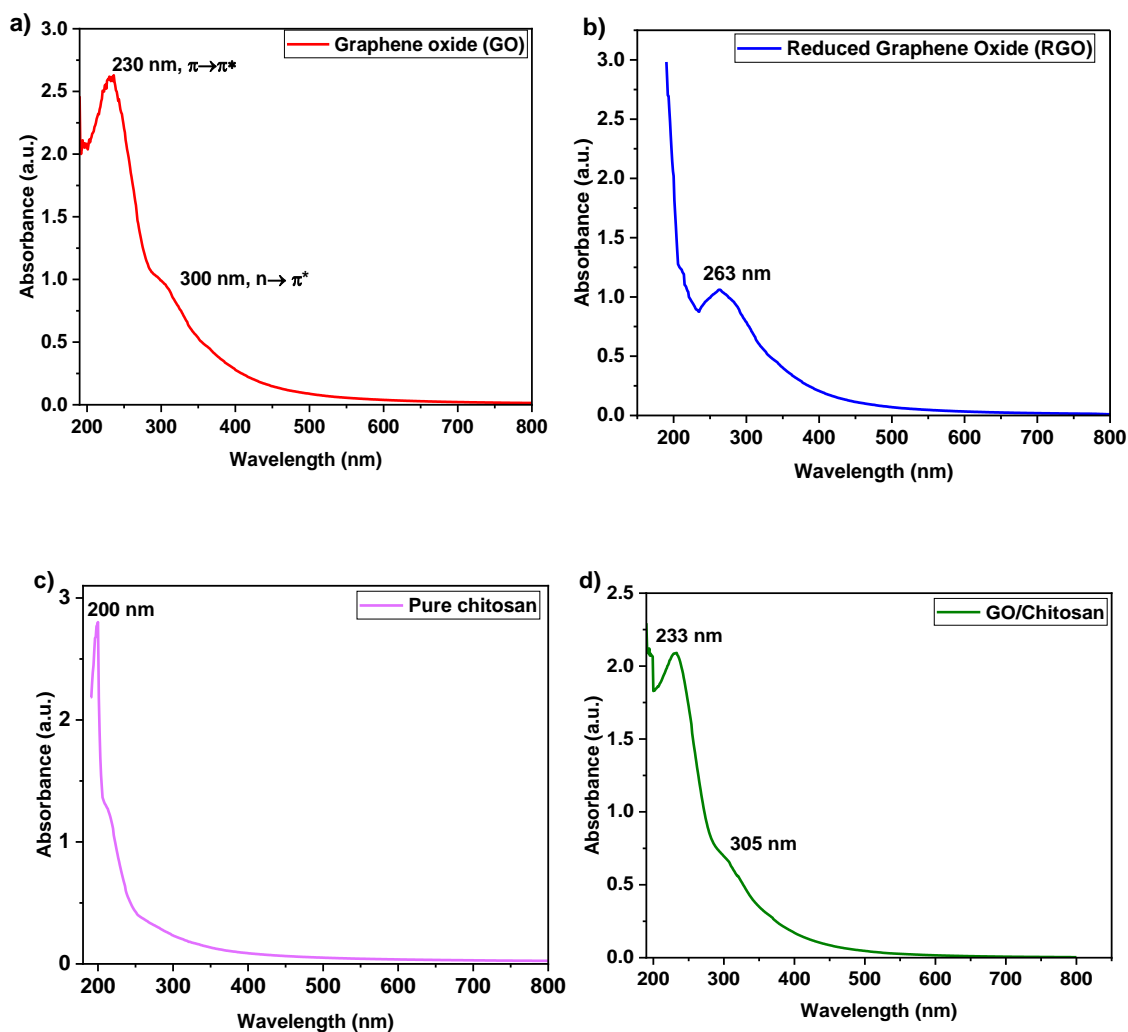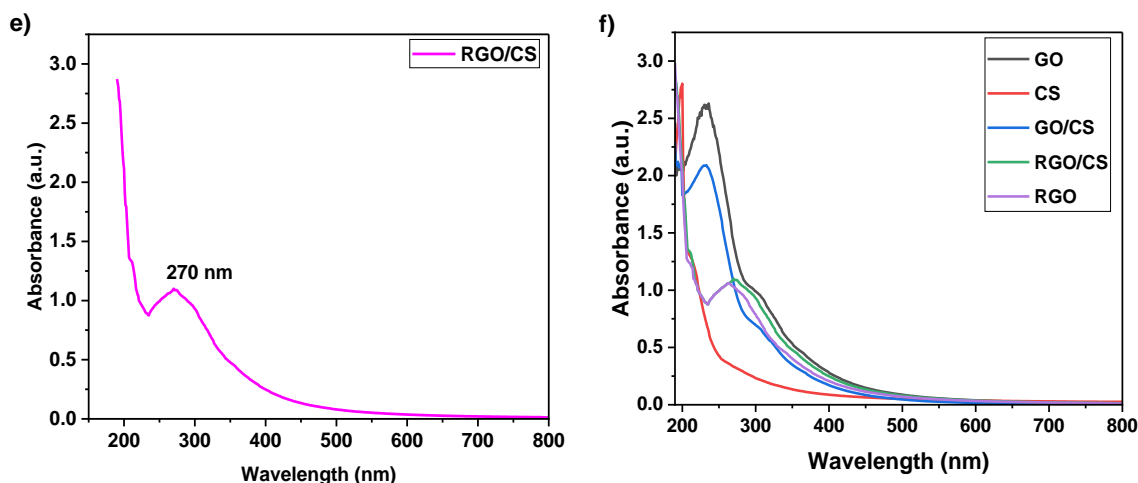
Figure 6.8. UV–Vis absorption spectra of different materials: a) graphene oxide (GO), b) reduced graphene oxide (RGO), c) chitosan (CS), d) graphene oxide/chitosan (GO/CS, (w/w: 90/10)), and e) reduced graphene oxide/chitosan (RGO/CS, (w/w: 90/10)), f)All graphs, in the spectral range from 190 to 800 nm.

Standard tensile testing was performed on rectangular shaped strips of as-synthesized films. The ultimate tensile strength, toughness, and Young's modulus of each GO, RGO, CS, GO/CS, and RGO/CS films from the measured stress-strain curves were obtained and presented in Figure 6.9. Upon comparison of RGO with GO, it can be seen that the reduction process produces an improved ductility, strength and toughness, along with a similar increase in stiffness. For the neat GO film, the Young's modulus, and tensile strength are 15.04±4.15 MPa and 2.62±0.77 MPa, respectively (Figure 6.9 (a)). For RGO, the Young's modulus and tensile strength indicate an increment of 25% and 46%, respectively (Figure 6.9 (b)). Therefore, the reduction process of GO reduces oxygen-containing functional groups in GO, leading to the restoration of a more sp^2 carbon network, resembling pristine graphene, resulting in enhanced mechanical properties [95, 96]. The reduction of GO enhances the crystallinity of RGO, reducing defects and improving the alignment of graphene layers, followed by increases stiffness and strength. Therefore, converting GO to RGO improves the interlayer interactions, reduces brittleness, provides higher ductility and elasticity, and enhanced strength in RGO [329-331].

Chitosan (CS) is a natural polymer with a long-chain structure, imparting flexibility and resilience to the material. Chitosan contains hydroxyl and amino groups, allowing for the formation of hydrogen bonds within the polymer chains which enhances tensile strength and elongation. Thus, CS has the lowest Young's Modulus (6.31±1.65 MPa), indicating lower stiffness (Figure 6.9 (c))[127, 332]. The addition of graphene materials (GO, RGO) generally increases the elastic strength and elongation at break compared to pure chitosan due to the synergistic effects of CS and GO/RGO that the chitosan's flexible and polymeric nature complements the rigid structure of graphene. The elongation at break for GO/CS and RGO/CS composites are notably higher indicating enhanced flexibility. Thus, GO or RGO is participating in the formation of an extensive interaction network with chitosan, allowing the films to withstand higher stress before fracture and to absorb a higher amount of energy before deformation. Also observed that incorporating RGO further enhanced ultimate tensile strength by 45% compared to pure chitosan, while maintaining toughness at a higher level to GO/CS film [333, 334].

In comparison to GO and RGO, the GO/CS and RGO/CS composites show 46% and 36% increment in Young's modulus and 61% and 64% growth in tensile strength, respectively. The toughness (area under stress-strain curve) of neat GO film is 184.45±54.17 mJ m^{-3}. The GO/CS and RGO/CS nanocomposites exhibit toughening effects as high as 80% as illustrated in Figure 6.9 (d and e) and Figure 6.10. This suggests enhanced stiffness and structural integrity, possibly due to the synergistic effects of RGO and CS [146]. GO nanosheets can act as cross-linking points to interconnect the chitosan chains, which can promote the interactions between the GO sheet that give rise to the enhancement of mechanical property greatly. However, when the reduction process is done on GO, the defects reduce and the alignments of GO sheets are improved, which decreases the stress concentration that leads to the increased mechanical property including Young's modulus, tensile strength and toughness in RGO/CS film. The higher elastic strength and elongation at break of RGO/CS indicates a greater ability to withstand deformation without permanent damage, signifying remarkable ductility and flexibility, which is crucial for mechanical robustness [335, 336].

Consistent with our design, the higher tensile strength of the RGO/CS compared to the GO/CS film indicates the formation of a stronger CS/GO interaction network. Further, the

observed higher strain of the RGO/CS composite compared to that of GO film suggests that under tensile stress, the chitosan chains are straightened, sliding along the GO nanosheets, thereby absorbing energy and contributing to a higher film toughness. Several factors can influence the mechanical properties of materials, and variations can arise due to differences in synthesis methods, processing conditions, and sample preparation. The hydrothermal reduction process of GO in this thesis might contribute to a more flexible and less rigid structure in RGO and RGO/CS samples, leading to a higher elongation at break. Also, the well-dispersed of GO and RGO in composites and the interaction between GO/RGO and CS could enhance flexibility.
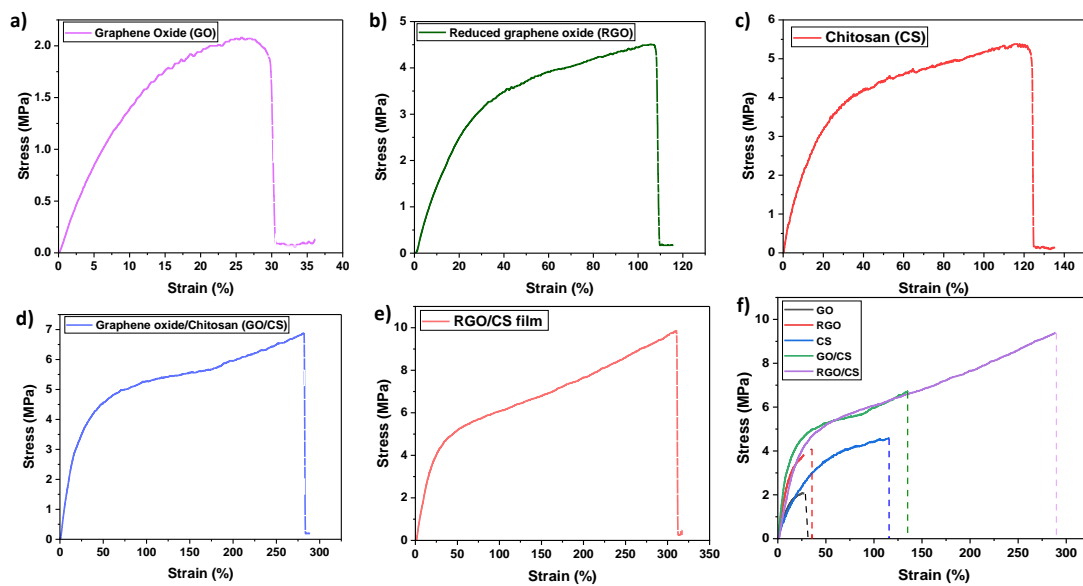
Figure 6.9. a) Stress-strain curve of a) GO, b) RGO, c) CS, d) GO/CS (w/w:90/10), and e) RGO/CS (w/w:90/10) films, f) Stress-strain curves of all samples in one graph.
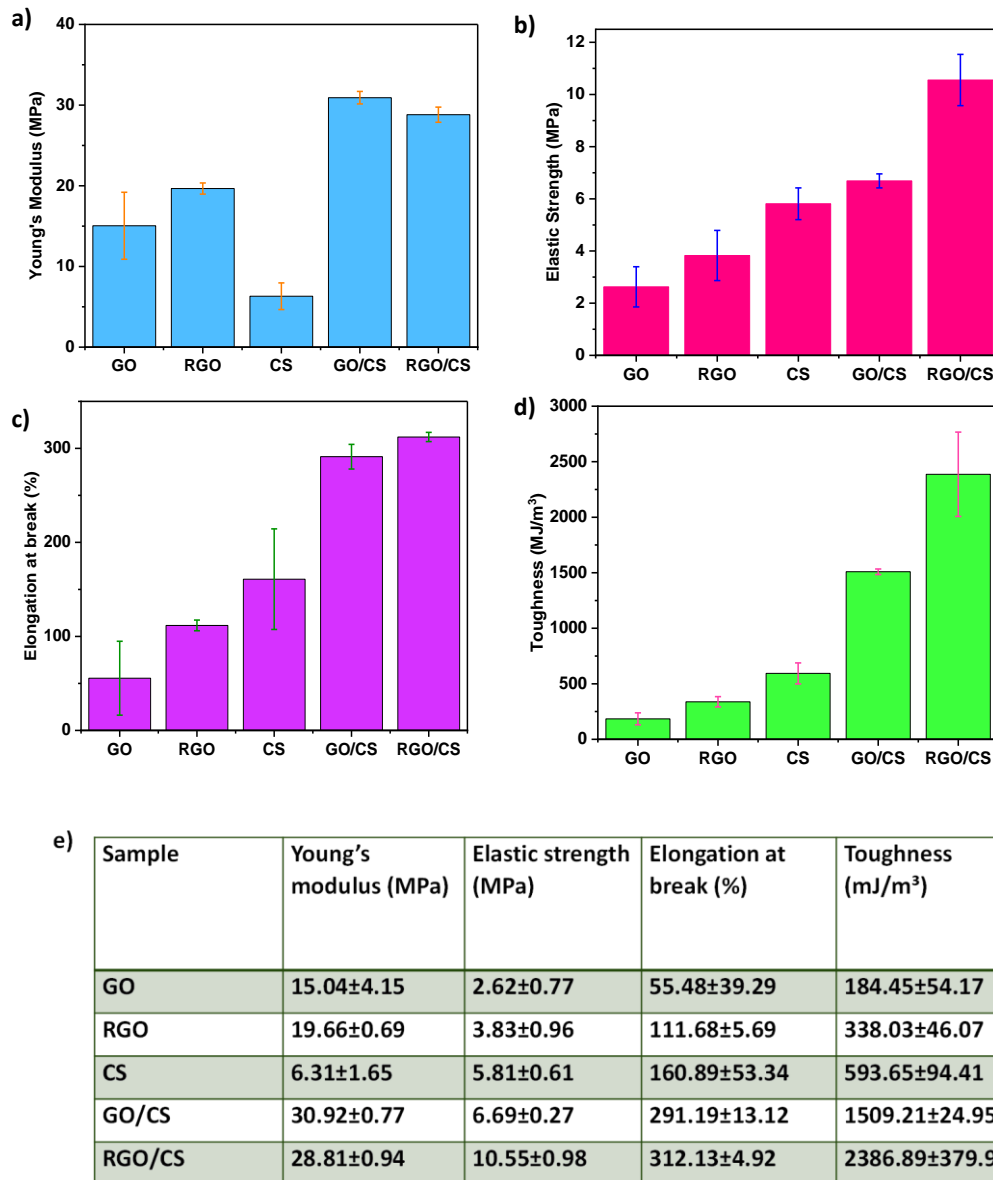
Figure 6.10. a-d) Tensile tests results as Young's modulus, Elastic strain, Elongation at break, Toughness for GO, RGO, CS, GO/CS, and RGO/CS samples. e) Detailed mechanical properties are summarized in the table.

BET analysis was conducted to determine the specific surface area, total pore volume, and pore diameter which these properties corresponds to the adsorption capacity of the materials. The BET analysis resulted from the CS, RGO, and RGO/CS nanocomposite are shown in Figure 6.11. According to the Brunei-Deming-Teller (BDDT) IUPAC classification, the pure chitosan graph was found to be of type II, which describe adsorption on macroporous

adsorbents with strong adsorbate-adsorbent interactions due to the presence of $-NH_2$ and $-OH$ active groups (Figure 6.11(a)) [337, 338]. On the other hand, the RGO followed the type IV, with the specific flow of hysteresis loop for mesoporous material that resulted in a large surface area (Figure 6.11(b)) accompanied by capillary condensation and evaporation in mesopore materials which indicated the presence of mesoporosity and macroporosity [338, 339]. According to the classification by BDDT, the adsorption-desorption isotherm graphs of RGO/CS nanocomposite in Figure 6.11(c) tended to follow type IV with the specific flow of the hysteresis loop for mesoporous material and under the low condition of relative pressure (P/P_0), the desorption and desorption graphs did not overlap which is due to the existence of metastable materials such as chitosan. These properties indicated of interconnected meso- and macro-pores like tinted bottle and the random pore distribution. As a result, the adsorption-desorption graph showed that more gases were desorbed than adsorbed which is consistent with the literatures [97, 98].

Figure 6.11(d) shows the characters of porous pure chitosan, RGO, and RGO/CS nanocomposite, including the specific surface area, the total pore volume and the average pore diameter, using the Brunauer-Emmet-Teller (BET) method. CS exhibits a relatively low specific surface area (3.032 m^2 g^{-1}) compared to graphene-based materials, which is expected due to its purely polymeric nature. The larger average pore diameter (17.028 nm) indicates the presence of relatively larger pores within the chitosan structure, likely attributed to its porous and fibrous morphology. The total pore volume (0.012908 cm^3 g^{-1}) suggests that chitosan has a moderate capacity for adsorbing ions. RGO exhibits a significantly higher specific surface area (13.267 m^2 g^{-1}) compared to chitosan, which is characteristic of graphene-based materials known for their large surface area. The smaller average pore diameter (7.2717nm) indicates the presence of relatively smaller pores within the RGO structure, likely arising from the stacked graphene and reduced interlayer spacing. The total pore volume (0.024118 cm^3 g^{-1}) suggests that RGO possesses a substantial capacity for adsorption, making it suitable for various application such as energy storage. The BET characteristics of the RGO/CS nanocomposite falls within the range observed for RGO, indicating that the addition of chitosan did not significantly alter the high surface area (13.672 m^2 g^{-1}), adsorption capacity, and porous structure.

These results along with the related research works suggest that chitosan may act as a scaffold or binder for RGO (synergistic effects), potentially enhancing its mechanical

stability, reducing the risk of structural degradation during charge-discharge cycles and facilitating the ion diffusion and charge transfer at the electrode-electrolyte interface, thereby enhancing the electrochemical performance of the solid-state supercapacitor [99, 100].
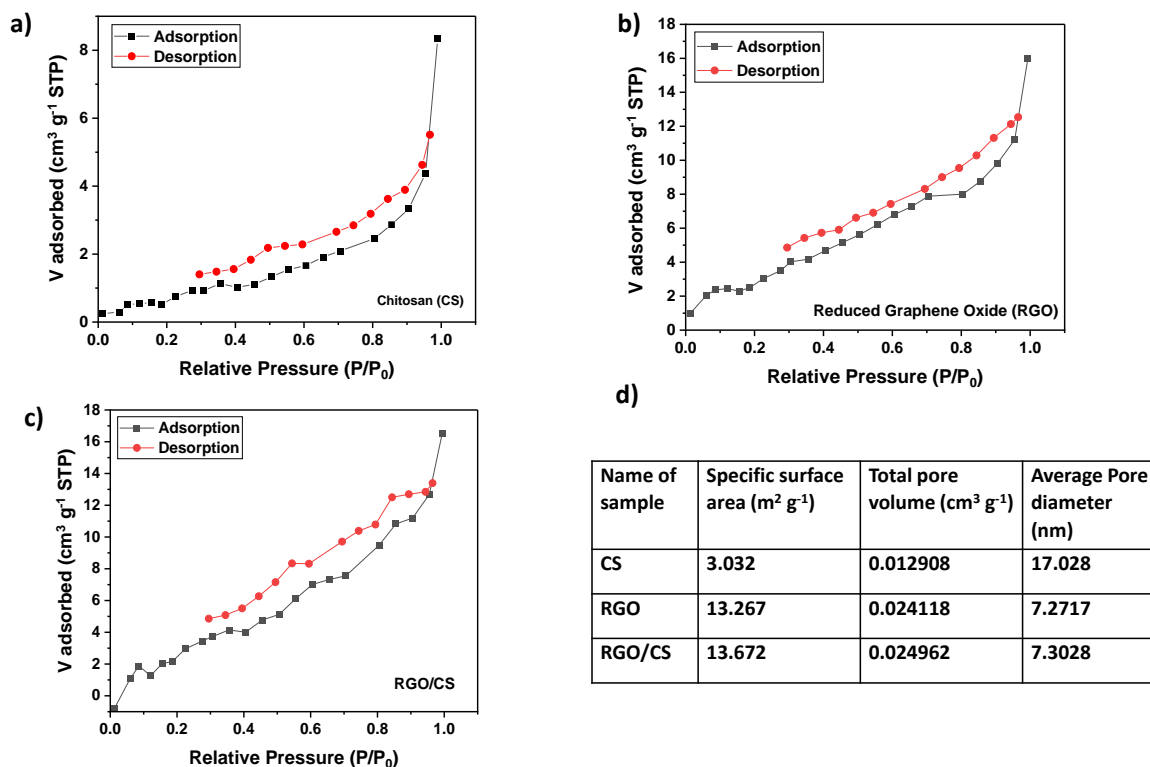
Figure 6.11. BET analysis of a) Chitosan (CS), b) Reduced Graphene Oxide (RGO), c) RGO/CS, d) BET parameters as specific surface area, total pore volume, and pore diameter for each sample.

In the AFM images of GO in Figure 6.12, distinctive features and patterns are observed on the surface. These images provide a clear visualization of the individual layers of GO sheets [340, 341]. The AFM findings pertaining to the GO and CS composite provide a complex and intriguing nanoscale structure. The composite material displays a heterogeneous surface marked by regions of varying roughness, a characteristic likely attributed to the coexistence of GO sheets and CS particles [97, 101].
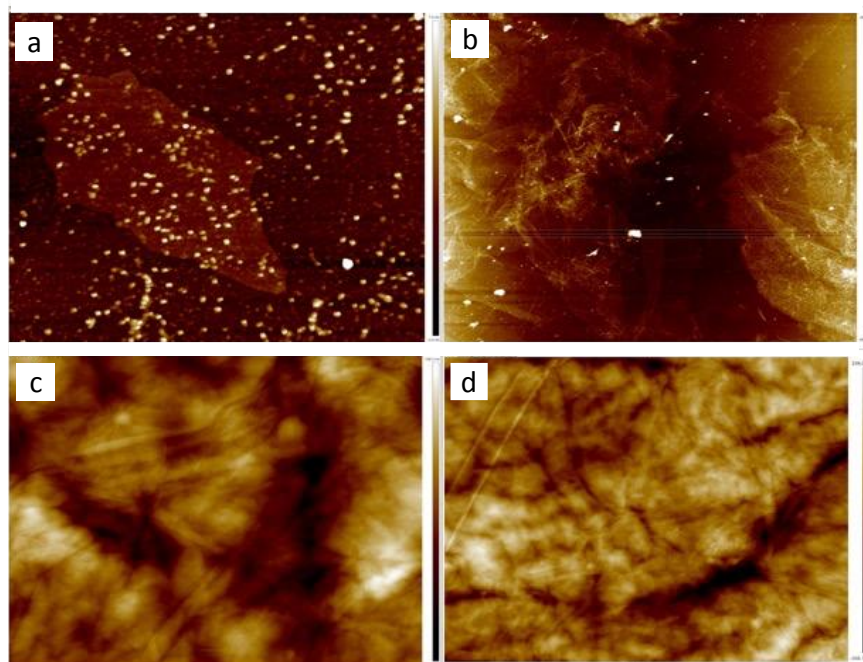
Figure 6.12. AFM images of (a, b) GO and (c, d) graphene oxide/chitosan composite (GO/CS, w/w: 90/10).

Polarized optical microscopy (POM) is a technique utilized to explore the liquid crystalline characteristics of materials such as graphene oxide (GO). It operates based on the interaction between polarized light and birefringent substances. Birefringence refers to a material's ability to exhibit varying refractive indices for light of different polarizations. Alterations in color or patterns observed through POM signify the presence of liquid crystalline phases, enabling the characterization of distinct structural attributes [273, 274]. To date, liquid crystals (LCs) of 2D colloids have not been explored, extensively. However, the recent advances in making 2D colloids of graphene [342] and graphene oxide [317, 343, 344] has opened a new set of opportunities. As a result, liquid crystal dispersions of graphene oxide are now receiving unprecedented attention [345]. The simultaneous lamellar ordering inherent in liquid crystals of 2D colloids [317, 345] can be further implemented to make lamellar structures.

GO sheets can exhibit liquid crystalline properties, which refers to their ability to self-assemble into ordered structures in a liquid medium. POM helps visualize and analyze these

structures under the influence of polarized light, providing insights into the organization and behavior of GO [102]. The selection of expanded graphite as the precursor for the synthesis of GO sheets not only gives us the advantage of obtaining monolayers with ultra-large lateral sizes, but also results in the formation of liquid crystals of GO. Their size distribution [317] indicated that the GO sheets had a lateral size predominantly on the order of 30-50 μm, and many of them being up to 100μm [346], while there are some fragments of smaller GO sheets of 5-10 μm in diameter. It was demonstrated that these ultra-large GO dispersions in aqueous media readily formed a nematic LC phase when the GO content exceeded a critical concentration of about 1mg mL^{-1} [317]. Therefore, the GO LC dispersion was considered a promising precursor of choice for the fabrication of films, fibers and nanocomposites with a highly-aligned, layered structure. While shear or external forces were usually necessary for the fabrication of highly-aligned structures using LC precursors [347], in this thesis, we were able to produce self-assembled GO films after simple evaporation of water from the LC dispersion. The 2D nature of graphene and ultra-high aspect ratio of GO sheets were the origins of self-assembly of GO sheets into LC phase and the formation of composites with a layered structure.

Typical polarized optical micrographs of GO dispersion (2 mg mL^{-1}) and GO/CS (w/w: 90/10) dispersion are given in Figure 6.13. The lyotropic nematic LCs (Figure 6.13 (a and b)) clearly indicate local orientation of the GO sheets in the aqueous media in the form of the large area of Schlieren texture. As the GO concentration increases upon evaporation of solvent, these locally oriented domains grow and form a macroscopic highly-aligned structure of GO sheets. The formation of GO/CS composite occurred by their supramolecular self-ordering into ordered layers through the interaction between the oxygen and amide functional groups. This observation was supported by the polarized light microscopy measurements, which displayed the layered architectures, in line with the formation of ordered clusters of chitosan [103]. Figure 6.13 (c and d) present LC textures in the GO/CS dispersion. Similar to the GO dispersion, the locally ordered, CS/GO sheets appear in the form of birefringence domains with a self-assembled structure. The significance of these observations is that GO sheets and polymer molecules can be formed into highly-ordered arrays of a brick-and-mortar structure with tunable GO intersheet spacing depending on the polymer content. Other polymer molecules and nanoparticles can be hybridized with GO LC

dispersion for the fabrication of multi-scale, multi-functional composites with a high degree of order, as recently demonstrated in polyacrylicacid (PAA)-GO composites [104].
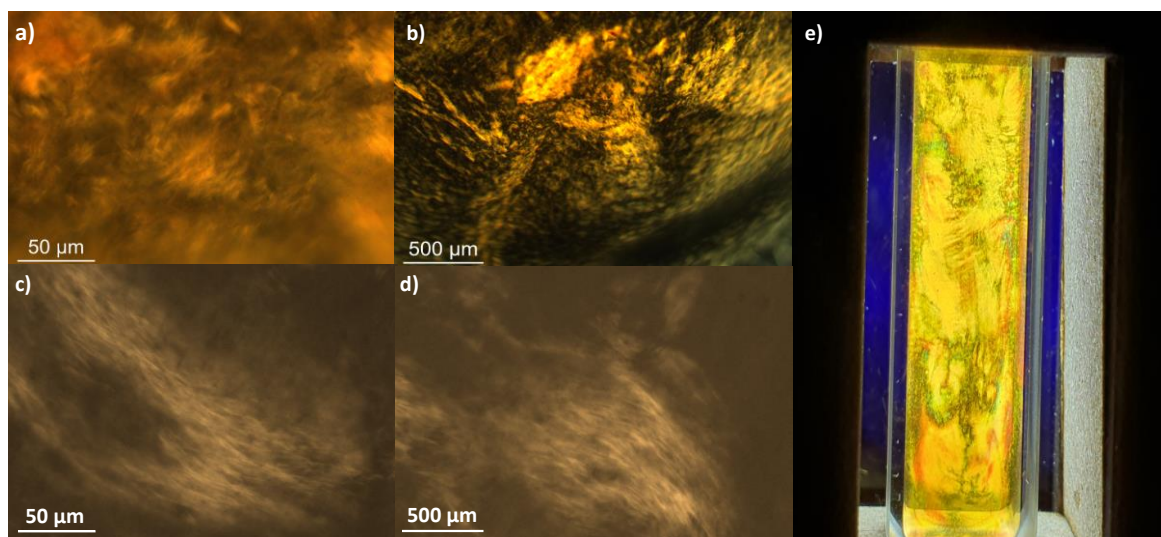
Figure 6.13. Polarized optical microscopy (POM) of a, b) Graphene oxide (GO) dispersion, c,d) Graphene oxide/chitosan (GO/CS, w/w: 90/10) solution, e) POM image of the lyotropic nematic LCs of GO.

The morphologies and microstructure of the GO, RGO, GO/CS, and RGO/CS were illustrated by TEM test. Figure 6.14 (A1-A2) shows that the GO sheets indeed consisted of single layers with several micrometers of size and fairly smooth and flattened surface, which are the characteristics of the oxidized exfoliated GO sheets. This was due to the oxygen-functional groups and electrostatic interaction of oxides on the surface that provided an extra thickness to the graphene sheets. The one edge-line clearly confirmed a monolayer GO sheet and the non-crystalline, amorphous carbon structure also suggests a highly oxygenated nature of the GO [105, 106]. In contrast, the RGO nanosheets are prone to aggregation because of the removal of oxygenated functionalized groups and the sheets may appear smoother and more condensed after reduction, as shown in Figure 6.14 (B1-B2). The inherent nature of RGO, ascribed to its 2D structure which could be considered thermodynamically stable due to rippling effect. Such type of morphology is considered to be very effective for the adsorption-desorption of electrolyte ions [106, 107]. Figure 6.14 (C1-C2) shows the TEM images of the GO/chitosan. A much rougher and a high density

surface appeared due to the assemblage of chitosan on the surface of GO layers, which strongly suggests the combination of the GO layers with chitosan to form the GO-chitosan composite [93, 108]. After GO being reduced, the RGO sheets in RGO/CS composite maintain the 2-D nanosheet morphology (Figure 6.14 (D1-D2)). In comparison to GO and RGO, the surface of RGO/CS exhibits increased roughness with noticeable decorations, attributed to the chitosan coating, indicating successful interaction with the RGO surface. Moreover, the presence of graphene nanosheets enveloped by rough chitosan chains suggests that chitosan contributes to the effective dispersion of RGO nanosheets [109, 110].
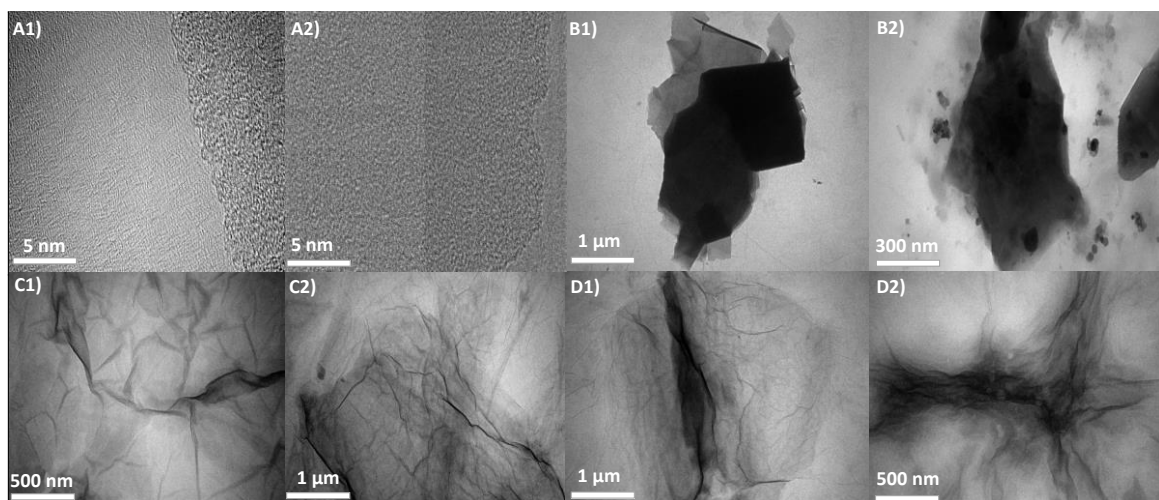
Figure 6.14. Transmission electron microscopy (TEM) of A1-A2) Graphene oxide (GO), B1-B2) Reduced graphene oxide (RGO), C1-C2) Graphene oxide/chitosan (GO/CS, w/w: 90/10) composite, D1-D2) Reduced graphene oxide/chitosan (RGO/CS, w/w: 90/10) composite.

The field emission scanning electron microscopy (FE-SEM) images provided in Figure 6.15, offer visual confirmation of the presence of GO sheets (Figure 6.15, A1-A2 image). These sheets manifest a compact, layered structure, composed of alternating fine layers. Notably, the GO sheets demonstrate a well-organized layered arrangement, with the surface morphology showcasing undulating patterns attributed to the stacking of exfoliated nanosheets. Additionally, each sheet displays a porous stacking arrangement reminiscent of a house-of-cards structure, comprised of graphene oxide layers. The imagery vividly portrays an interconnected network of sheets with a prominently stratified layout. The GO

sheets exhibit a finely alternating pattern, contributing to the formation of a densely packed lamellar structure [112, 348].
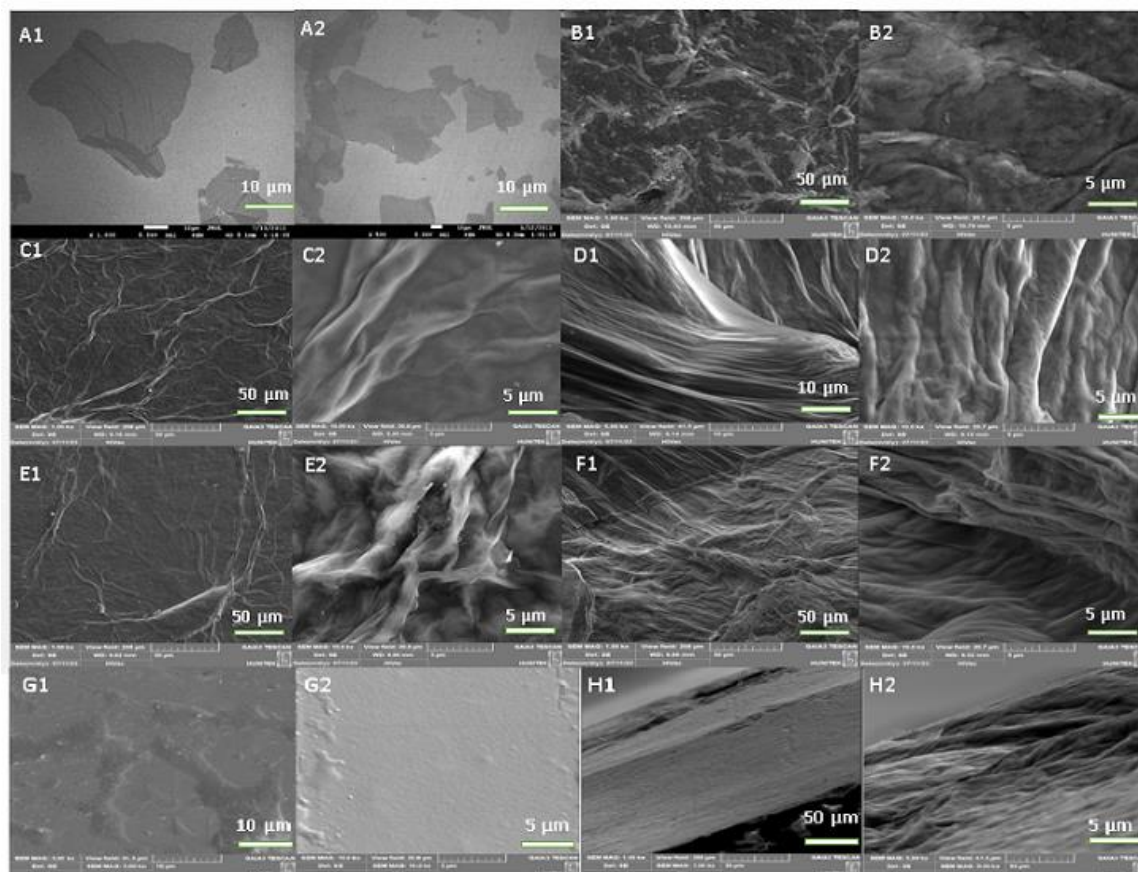
Figure 6.15. FE-SEM analysis of electrode samples, (A1-A2); Graphene oxide (GO), (B1-B2): Reduced graphene oxide (RGO), (C1-C2): Graphene oxide/chitosan (w/w:90/10), (D1-D2): Graphene oxide/chitosan (w/w:50/50), (E1-E2): Reduced graphene oxide/chitosan (w/w: 90/10), (F1-F2): Reduced graphene oxide/chitosan (w/w: 50/50), (G1-G2): Pure Chitosan, (H1-H2): Cross-section of Graphene oxide/chitosan (w/w:90/10).

The FE-SEM of RGO sheets (Figure 6.15, B1-B2 image) unveils a similar pattern of thin sheets hat have agglomerated randomly. These sheets exhibit well-defined edges, along with surfaces that are characterized by wrinkles and folds. The SEM image of RGO offers insights into the nanoscale features of this material, revealing a structured network of interconnected sheets with a highly organized and compact arrangement [349, 350]. Notably, the RGO sheets portray a smooth and continuous surface, signifying the successful reduction of GO

139

to graphene. This image highlights the presence of a highly uniform and precisely delineated structure, with the sheets tightly packed in close proximity. This compact configuration suggests the formation of a dense and interconnected network, promoting efficient charge transport and enhancing the material's conductivity [349-351].

The SEM image of the GO/CS film reveals a homogeneous composition as can be seen from the SEM images labeled as C and D in Figure 6.15. Notably, the GO-chitosan film exhibits a distinctive "sandwich" configuration. The image demonstrates that a significant portion of the GO nanosheets were fully exfoliated and uniformly dispersed within the chitosan matrix [350]. Additionally, the GO sheets are arranged in a unidirectional manner, parallel to the composite film. Therefore, the image reveals the presence of GO sheets embedded within the chitosan matrix, forming a unique interconnected network with folds and fluffy structures, attributed to wrinkles and curvatures on the surface. This depiction substantiates and corroborates the combination of chitosan and GO [315]. The GO sheets appear as thin, layered entities with irregular edges and a surface characterized by undulations. The chitosan matrix surrounds and encapsulates these GO sheets, creating a three-dimensional framework [245]. Furthermore, the images indicate a relatively uniform distribution of GO within the chitosan matrix, suggesting a favorable dispersion of the two components. The potential formation of amide linkages between GO and chitosan might facilitate dispersion of GO within the chitosan matrix, consequently influencing the electrochemical and mechanical properties of the resulting composites [9, 93].

The SEM micrographs of the composite materials formed by combining GO and chitosan at different weight ratios offer valuable insights into their morphological characteristics and structural arrangements. The image of GO/CS (w/w) composites reveals a well-dispersed and homogeneous mixture of GO and chitosan throughout the matrix. The GO sheets are discernible as thin, two-dimensional structures with irregular edges, while the chitosan matrix appears as a continuous matrix surrounding these sheets [314]. In the case of the GO/CS (w/w) 90/10 composite (Figure 6.15, C1-C2 image), the SEM image reveals the prominent presence of GO sheets. These sheets exhibit uniform distribution within the matrix, manifesting as transparent, delicate layers featuring a corrugated or crumpled surface texture [43]. Chitosan's contribution is apparent in a relatively minor proportion, constituting an interconnected web surrounding the GO sheets. This network of chitosan forms

interconnected strands or fibers, establishing a scaffold-like structure that embraces and supports the GO sheets [352]. In contrast, for the GO/CS (w/w) 50/50 composite (Figure 6.15, D1-D2 image), the SEM image indicates a more balanced coexistence of both GO and CS components. The image portrays a nearly equal distribution of GO sheets and chitosan within the composite [84]. The GO sheets retain their characteristic wrinkled morphology, while chitosan assembles into a three-dimensional network traversing the composite. The chitosan fibers intricately intertwine with the GO sheets, resulting in an interpenetrating structure. The composite exhibits a porous arrangement, with void spaces interspersed among the GO sheets and chitosan network [205]. In summation, the SEM micrographs aptly illustrate the successful incorporation of both the GO and CS components within the composites, exemplifying their effective blending. The distinct morphological characteristics observed in these samples distinctly mirror the variations in weight ratios, with the GO/CS (w/w) 90/10 composite showcasing a higher content of GO, and the GO/CS (w/w) 50/50 composite displaying a more balanced distribution [9, 113].

The SEM images of RGO/CS composites (Figure 6.15, E and F) show the presence of graphene dispersed within chitosan, exhibiting irregularly wrinkled and sheet-like structures, characterized by a broader surface area that contributes to enhanced electrical conductivity[97]. The RGO sheets appear as interconnected layers or flakes, featuring a surface morphology marked by crumpling or folding. These RGO sheets exhibit a high degree of structural disorder and roughness, typical characteristics of RGO materials [91]. The surface of the RGO sheets also exhibit irregularities and wrinkles, indicative of their intricate spatial arrangement. Within the composite matrix, the chitosan component is observed as a continuous three-dimensional scaffold-like network that envelops and provides support to the RGO sheets [114, 115].

In the case of the RGO/CS (w/w) 90/10 composite (Figure 6.15, E1-E2), the SEM image predominantly displays a structure dominated by RGO, with a few dispersed CS particles interspersed. The RGO sheets exhibit a configuration marked by layers and interconnectedness, forming a network-like arrangement. The sheets possess a wrinkled or folded surface morphology, indicating the presence of RGO [352]. The CS particles, though sparsely distributed, can be discerned as small, adhered entities on the RGO sheets. In contrast, for the RGO/CS (w/w) 50/50 sample, a more balanced distribution of RGO and CS

becomes evident. The SEM image reveals a composite structure in which RGO sheets and CS particles are evenly dispersed throughout the matrix [84]. The RGO sheets retain their layered structure, while the CS particles manifest as discrete entities of varying sizes. This image underscores the interplay between RGO and CS within the composite, showing a combination of RGO's interconnected network with the individual particulate morphology of CS [114, 115]. In its standalone form (Figure 6.15, G1-G2 image), pristine chitosan manifests as a homogeneous and continuous thin film with a smooth surface. Minor irregularities and slight roughness are observable on the film's surface, likely stemming from the intrinsic properties of chitosan and the film fabrication process [80].

The FE-SEM cross-section image of GO/CS composite (Figure 6.15, H1-H2 image) reveals distinct layers of GO and chitosan, indicating a well-defined and uniform distribution of both materials within the film [97]. The GO layers are evident as thin sheets characterized by a wrinkled and interconnected structure, which confers mechanical strength and electrical conductivity to the nanocomposite. Furthermore, the image highlights the intimate contact and robust bonding between the GO and CS components, resulting in a seamless integration of their respective properties [353].

Figure 6.16 shows the EDAX spectra and elemental mapping results for the electrode samples. RGO is derived from GO, a product of the oxidation and exfoliation of graphite. During the reduction process, oxygen-containing functional groups are eliminated from GO, resulting in a partially reduced form of graphene [354]. An EDAX analysis of RGO can reveal the presence of carbon (C) as the predominant element, emblematic of graphene's elemental composition [147]. Additionally, EDAX can detect small traces of other elements, such as oxygen (O) and nitrogen (N), along with possible impurities or residual functional groups originating from the reduction process. The mapping technique shows the uniformity and distribution of carbon and other elements throughout the entire structure of the material, providing insights into its compositional homogeneity [147, 148].

In the context of composite samples, EDAX detects C and O originating from both GO and CS, along with N inherent to CS. As depicted in Table 6.2, the EDAX analysis of GO/CS and RGO/CS samples clearly demonstrates a rise in the content of the C element compared to pristine chitosan [355]. Furthermore, it is noteworthy that the quantity of carbon (C)

within RGO-containing composites surpasses that of their GO counterparts in the same composition. The carbon/oxygen (C/O) atomic ratio serves as an indicator of graphene oxidation extent and affords insights into the oxygen functional groups' nature. The degree of oxidation of the prepared RGO was gauged through the C/O ratio, which stands at 1.24. The atomic weight ratios for C/O in the cases of GO/CS (w/w: 90/10), GO/CS (w/w: 50/50), RGO/CS (w/w: 90/10), and RGO/CS (w/w: 50/50) amount to 1.06, 1.07, 1.22, and 1.13, respectively. This outcome underscores the occurrence of a certain degree of reduction of graphene oxide sheets consequent to thermal treatment [356, 357], and aligns well with the fundamental constituents encompassing molecular framework of composites.

Table 6.2.   EDAX elemental analysis of RGO, CS, GO/CS, RGO/CS electrode samples.

Atomic percentage (w, %)	RGO	CS	GO/CS (w/w:90/10)	GO/CS (w/w:50/50)	RGO/CS (w/w:90/10)	RGO/CS (w/w:50/50)
C %	55.4± 0.0	49.1 ± 0.2	51.6± 0.2	51.7±0.1	54.9±0.1	53±0.1
O %	44.6± 0.0	44.8 ± 0.2	48.4±0.2	48.3±0.1	45.1±0.1	47±0.1
N %	0.1 ± 0.3	6 ± 0.3	0.1±1.3	0.1±0.4	0.1±0.5	0.1±0.6
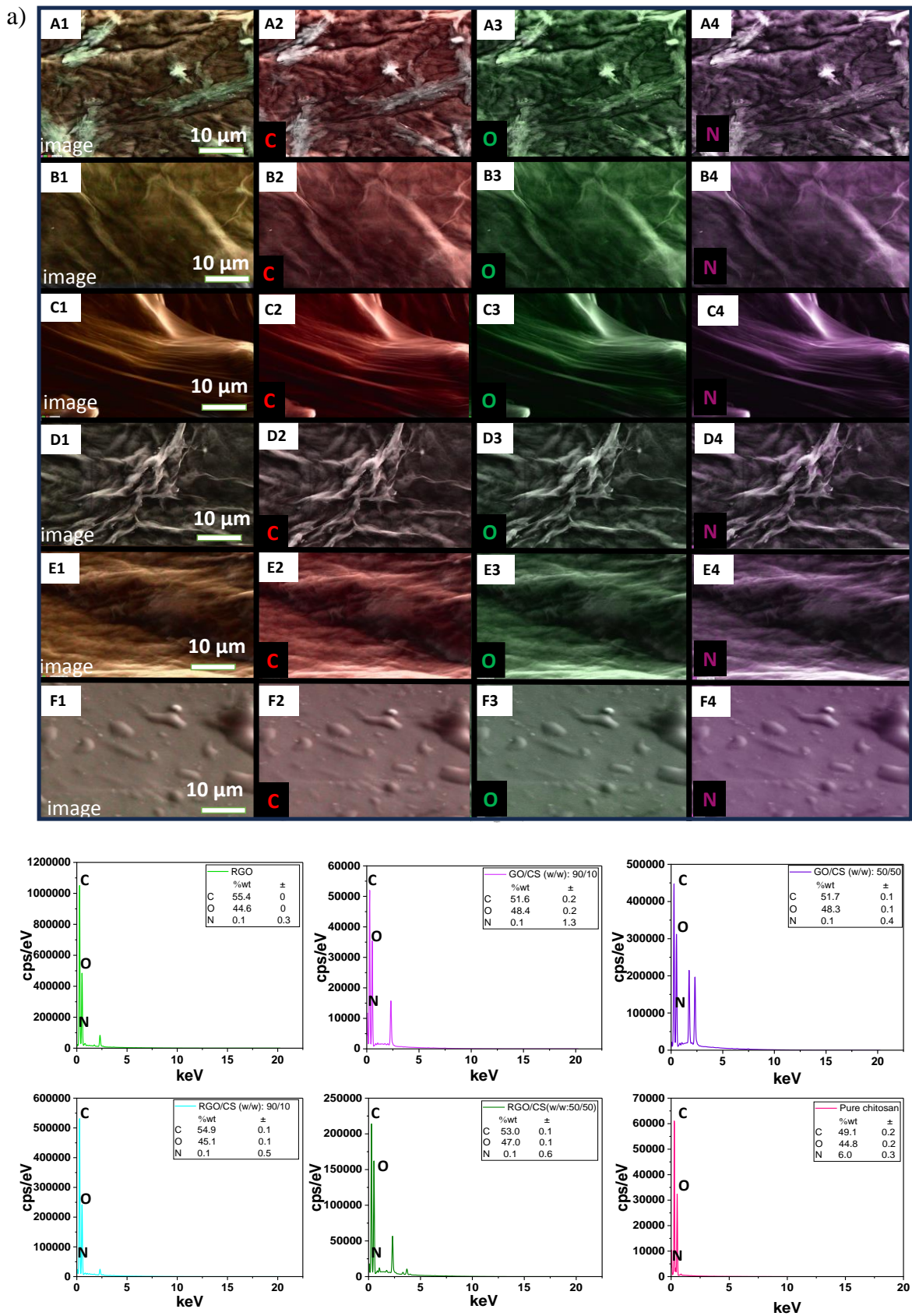
Figure 6.16. a) SEM-EDAX elemental mapping images of electrode samples, (A1-A4): Reduced graphene oxide (RGO), (B1-B4): Graphene oxide/chitosan (GO/CS, w/w:90/10),

(C1-C4): Graphene oxide/chitosan (GO/CS, w/w:50/50), (D1-D4): Reduced graphene oxide/chitosan (RGO/CS, w/w: 90/10), (E1-E4): Reduced graphene oxide/chitosan (RGO/CS, w/w: 50/50), (F1-F4): Pure Chitosan. b) EDX spectra of various samples.

Moreover, mapping shows areas with higher carbon concentrations, aligning with regions rich in RGO. In contrast, regions with reduced carbon concentration indicate the prevalence of chitosan. In comparison to RGO-containing composites, GO/CS samples demonstrate an elevated proportion of oxygen content, confirming the continued presence of unreduced graphene oxide [355]. Correspondingly, mapping reveals areas with heightened oxygen concentrations linked to graphene oxide, as well as regions with elevated nitrogen levels signifying chitosan domains. In the RGO/CS samples, the elevated carbon content is further supported by mapping, which showcases a more uniform distribution of this element [358]. Turning to the GO/CS (w/w: 50/50) and RGO/CS (w/w: 50/50) samples, the EDAX analysis reveals a more balanced distribution of C and other elements, suggesting an equitable mixture of the components.

6.3. Ionic Conductivity Characterization of the Gel Polymer Electrolyte

The gel electrolytes were prepared by dissolving a specific amount of KCl in water (2.0 M). Films with physical integrity could only be cast from solutions where the PVA/KCl ratio was 1/0.1, 1/0.5, 1/1 for all PVA molecular weights, and additionally 1/2 for 195000 g mol^{-1}. The inability to obtain a film under other conditions can be explained by the relatively reduced amount of polymer in the composition due to the high amounts of KCl and water, which are not sufficient for gel film formation [49, 291]. Electrochemical impedance spectroscopy (EIS) was utilized to study the ionic conductivity of the gel electrolytes. The EIS test results for PVA/KCl weight ratios of 1/0.1, 1/0.5, 1/1 for each molecular weight are shown in Figure 6.17, 6.18, 6.19, and 1/2 for 195000 g mol^{-1} is depicted in Figure 6.20.
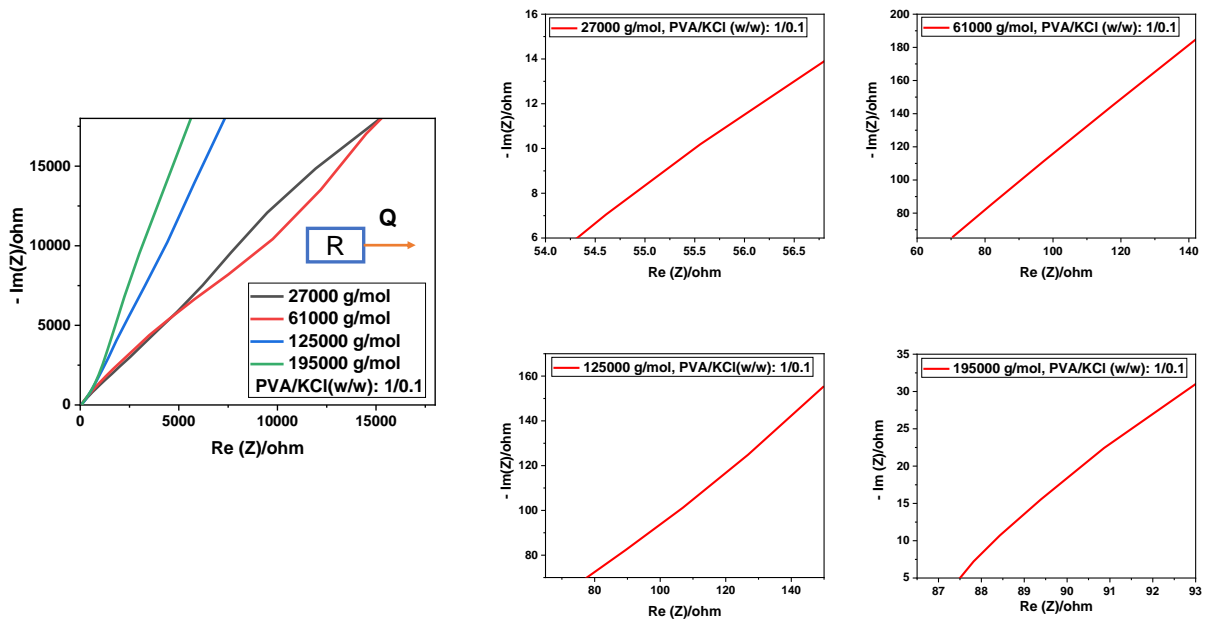
Figure 6.17. Nyquist plots of PVA/KCl/H$_2$O gel electrolyte films at different molecular weights of PVA for the weight ratio of PVA/ KCl: 1/0.1.
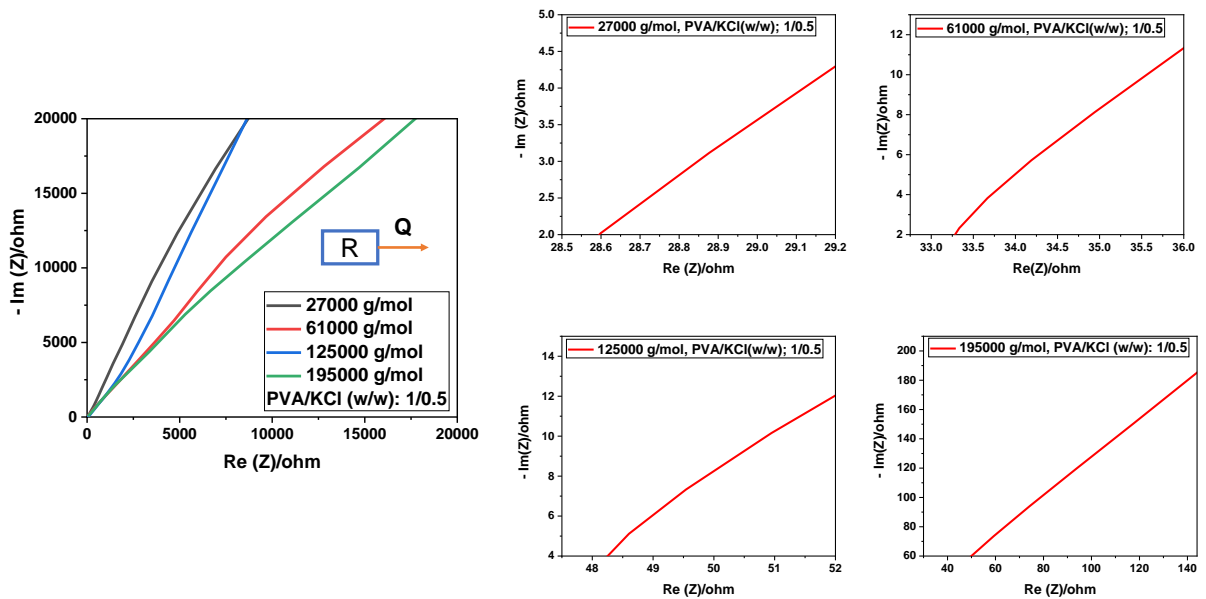
Figure 6.18. Nyquist plots of PVA/KCl/H$_2$O gel electrolyte films at different molecular weights of PVA for the weight ratio of PVA/ KCl: 1/0.5.
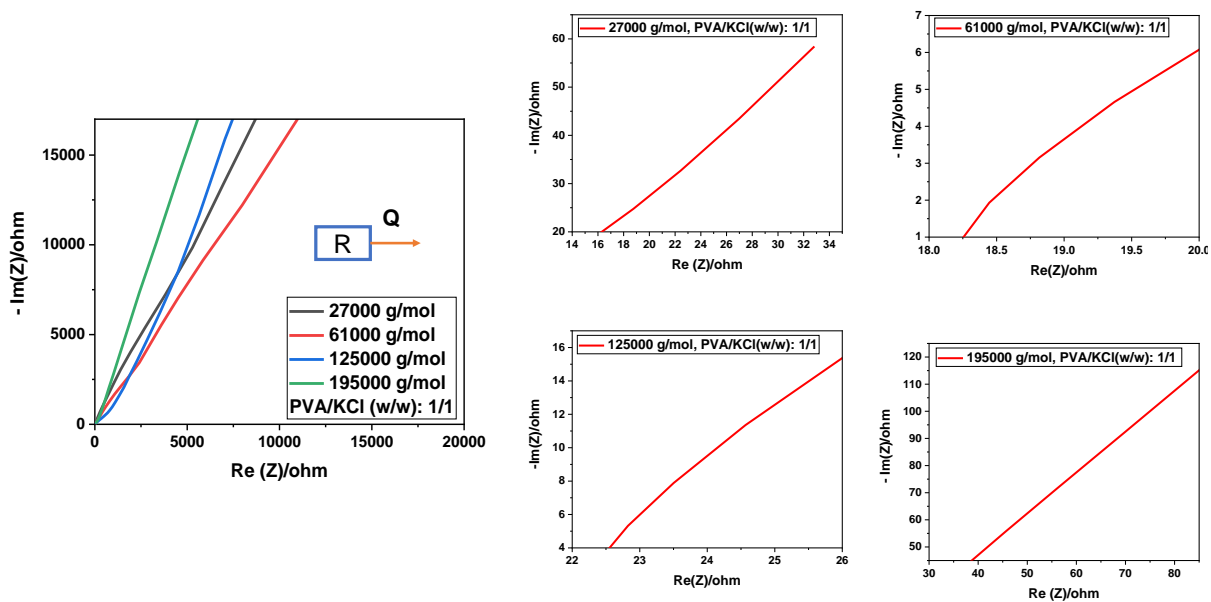
Figure 6.19. Nyquist plots of PVA/KCl/H$_2$O gel electrolyte films at different molecular weights of PVA for the weight ratio of PVA/ KCl: 1/1.
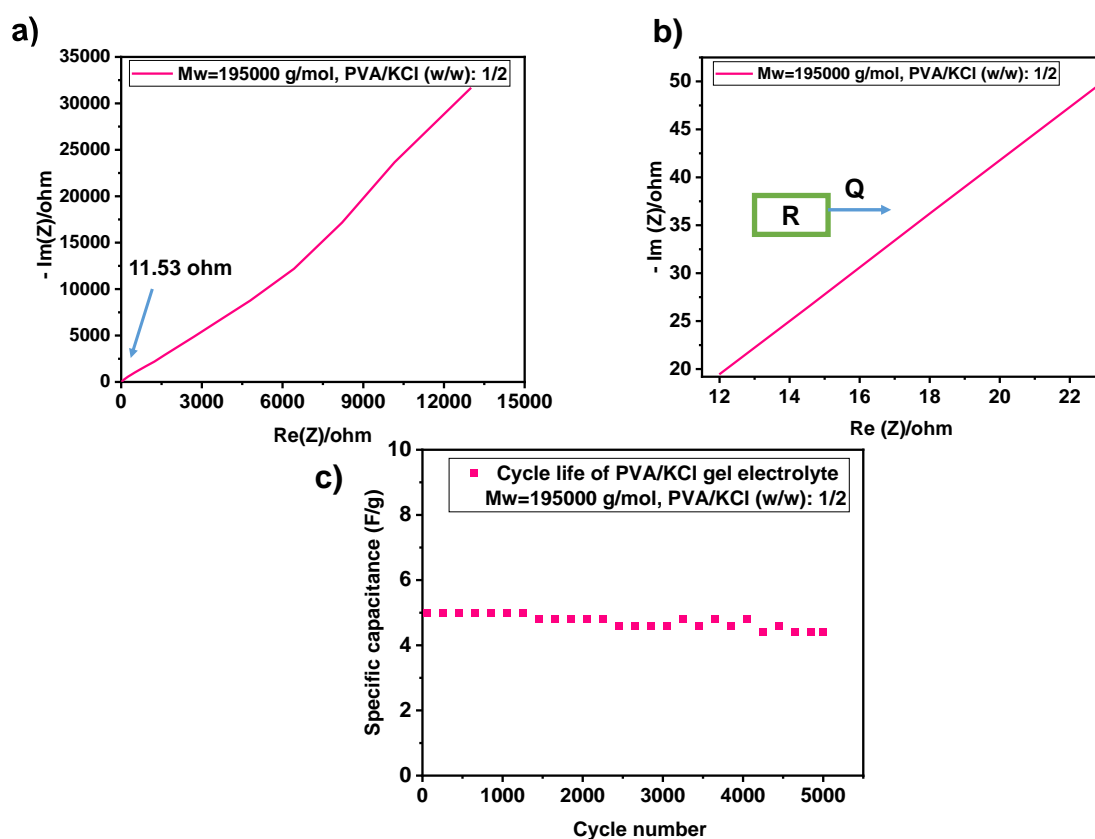
Figure 6.20. Electrochemical performance of PVA/KCl/H$_2$O gel electrolyte film (M$_w$ = 195000 g mol^{-1}, PVA/ KCl (w/w:1/2), a ,b) Nyquist plots within a frequency span of 100 mHz to 100 kHz, c) Cycle life of the gel electrolyte film after 5000 cycles.

For all samples, in the high frequency region, the gel film exhibits a resistance behavior with a non-zero intersection and in the low-frequency region, it shows the capacitive behavior with a straight line [51, 359]. According to the electrical equivalent circuit, the intersection of the figure indicates the study of impedance spectra with Z_{sim} software. The software gives information about the ohmic resistance (R) of the gel electrolytes, and constant phase element (Q) of the double layer. Based on the value of ohmic resistance, the gel electrolytes ionic conductivity was calculated [51, 291]. Thus, Table 6.3 gives the fitted data for R-value. The GPEs ionic conductivity was assessed based on equation (5.10) (chapter 5), is shown in Table 6.3, where "t" is the thickness of the film between 400-500 μm, "R" is the electrolyte ohmic resistance in ohm, and "A" is the electrolyte film contact surface area with stainless steel electrodes during the test (1 cm^2) [49, 51]. In addition, the ionic conductivity of gel electrolyte is dependent on the charge carrier concentration (n) and carrier mobility (μ), which is given by the equation (4.1) [129, 360, 361].

$$\sigma = nq\mu \tag{6.1}$$

Table 6.3, shows that at a constant weight ratio of PVA to KCl, by increasing the PVA molecular weight, the bulk resistance of the gel electrolyte and the physical interaction between the polymer chains are increased [128]. As the molecular weight of polymer increases, the relative amount of chain-ends, which are the most mobile regions of a polymer backbone, and the free-volume between the polymer chains decrease, thus the chain movements are restricted, resulting in high viscosity, low ionic motion and hence lower ionic conductivity. On the other hand, the ionic conductivity increases as the amount of KCl (charge carriers) increases because the bulk resistance reduces. This can be attributed to the increased number of charge carrier ions produced by KCl. Low-molecular-weight has more segmental motions, increasing ion mobility [129, 130]. Thus, high molecular weight is desirable for obtaining more mechanically durable films as it enhances the interactions between polymer chains. Furthermore, in our previous work, we have shown that gel electrolytes with different PVA molecular weights shows various amounts of water in their gel. High-molecular-weight PVA contains more chain entanglements, holding more water molecules. Consequently, an increased amount of water molecules leads to higher ionic conductivity, resulting in a greater quantity of dissociated free ions, which is consistent with previous reports [21, 129, 131, 132, 275, 362].

Table 6.3. Ionic conductivity of PVA/KCl/H_2O gel polymer electrolytes.

M_w (g mol^{-1})	PVA/KCl (w/w)	Thickness of the gel film (μm)	Bulk resistance (ohm)	Ionic conductivity (mS cm^{-1})
27000	1/0.1	435±10	57.07±2.76	0.76±0.03
27000	1/0.5	403±7	25.43±3.19	1.61±0.25
27000	1/1	400±5	15.43±1.22	2.61±0.25
61000	1/0.1	440±9	70.73±1.63	0.63±0.01
61000	1/0.5	410±11	34.57±2.45	1.19±0.07
61000	1/1	406±7	18.03±0.25	2.25±0.01
125000	1/0.1	463±9	77.10±3.24	0.60±0.01
125000	1/0.5	413±10	46.40±1.55	0.89±0.01
125000	1/1	402±7	20.90±1.21	1.93±0.11
195000	1/0.1	442±5	86±1.45	0.52±0.01
195000	1/0.5	419±6	49.27±1.18	0.85±0.01
195000	1/1	406±9	35.5±2.12	1.15±0.06
195000	1/2	400±3	11.53±0.68	**3.48±0.25**

*No gel films were formed for the following samples; Mw=27000 g mol^{-1}, PVA/KCl (w/w);1/2, 1/5, 1/10, 1/20, Mw=61000 g mol^{-1}, PVA/KCl (w/w);1/2, 1/5, 1/10, 1/20, Mw=125000 g mol^{-1}, PVA/KCl (w/w);1/2, 1/5, 1/10, 1/20, Mw=195000 g mol^{-1}, PVA/KCl (w/w);1/5, 1/10, 1/20.

Cyclic stability of the flexible gel electrolyte was evaluated at 200 mV s^{-1} for 5000 cycles (Figure 6.20(c)). The specific capacitance which is calculated based on equation (5.11) (chapter 5), reduces from 5 to about 4.4 mF g^{-1} after 5000 cycles. Thus, after 5000 cycles, the gel maintains %88 of initial capacitance. Therefore, the gel electrolyte containing PVA with M_w=195000 g mol^{-1} and PVA/KCl (w/w): 1/2, shows the greatest ionic conductivity and better cyclic stability which is a promising candidate for making the flexible and wearable energy storage devices.
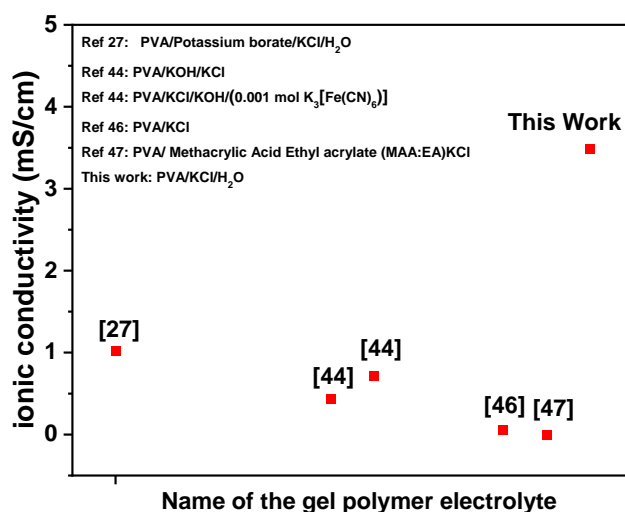
Figure 6.21. Comparison of ionic conductivity among various PVA-KCl gel polymer electrolytes.

Table 6.4 and 6.5 provide a comprehensive comparative analysis of the reported ionic conductivities of various gel electrolytes, with a primary focus on those based on PVA and several other commonly utilized polymers. Figure 6.21 visually summarizes and highlights selected studies from this dataset, offering a side-by-side comparison with our GPE. The further much-needed development of implantable medical devices for everyday use, as health monitoring devices not only for elderlies and people with chronic diseases but also for wider impact for general health monitoring of the population, relies heavily on the realization of biocompatible, miniaturized, flexible, light, yet mechanically robust energy storage and energy harvesting systems for their power up [8, 363]. In light of that, the main purpose of this study is to design and fabricate a self-assembled multifunctional biocompatible, yet flexible all solid-state gel polymer electrolyte, based on PVA/KCl/H_2O, capable of powering up the implantable medical devices. Notably, the ionic conductivity of the as-prepared gel electrolyte is significantly higher (3.48 ± 0.25 mS cm^{-1}) than that of other reported gel electrolytes based on PVA/KCl. This can be attributed to the high concentration of salt and water in the gel, which enhances the ionic conductivity. The unique gel-like structure of PVA/KCl allows for the retention of a significant amount of water, which is crucial for ion conduction. The interconnected network of the gel facilitates the diffusion of ions, leading to higher ionic conductivity [45, 291].

150

Table 6.4. Comparison of ionic conductivity of gel electrolytes based on various polymers for simple ternary systems with different reported compositions.

Electrolyte	Molecular weight of polymer (g mol^{-1})	Weight ratio (w/w) of polymer to electrolytic salt or other components	Ionic conductivity (mS cm^{-1})	Ref
PVA/H$_3$ PO$_4$ /H$_2$ O	124,000– 186,000	1:1 1: 1.5	0.96 3.44	[49]
PVA/H$_3$ PO$_4$ /H$_2$ O	95,000	1: 0.8	0.056	[73]
PVA/H$_3$ PO$_4$ /H$_2$ O PVA/H$_3$ PO$_4$ /PEG/H$_2$ O	125,000	1: 0.4	0.00152 For 30% wt of PEG: 0.086	[21]
PVA/Potassium borate/KCl/H$_2$ O	74,800 ± 50	…	1.02	[27]
PVA/H$_3$ PO$_4$ /H$_2$ O PVA/H$_3$ PO$_4$ /[EMIM]BF$_4$ /H$_2$ O	130,000	1: 0.8	0.78 For 100% wt of [EMIM]BF$_4$: 0.33	[208]
PVA/H$_3$ PO$_4$ /H$_2$ O PVA/H$_3$ PO$_4$ /PySH/H$_2$ O	…	1:2 1: 2	11.58 For 0.17 g of PySH: 22.57	[209]
PVA/H$_3$ PO$_4$ /Cellulose/H$_2$ O	…	1:0.4	0.104	[213]
PVA/H$_2$ SO$_4$ /Glutaraldehyde/H$_2$ O	…	1:0.5	82	[74]
PVA/H$_2$ SO$_4$ /H$_2$ O PVA/H$_2$ SO$_4$ /IC/H$_2$ O	…	1:1 1:1	7.1 20.27	[214]
PVA/H$_3$ PO$_4$ /SiWA/H$_2$ O	85,000– 124,000	1:1.2	8	[215]
PVA/KOH/TiO$_2$ /Glutaraldehyde /H$_2$ O	74,800	…	For 15% wt of TiO$_2$: 48	[216]
PVA/PVP/KOH/H$_2$ O	30,000–70,000	1:0.5	$(1.5 ± 1.1)×10^{-1}$	[52]
PVA/H$_3$ PO$_4$ /H$_2$ O	98,000	1:2	2.56	[53]

PVA/Boric acid/GO/KOH/H$_2$O	…	…	For 20% wt of GO: 195	[211]
PVA/H$_2$SO$_4$/H$_2$O PVA/H$_2$SO$_4$/ARS/H$_2$O		1:2	11.4 For 0.5 g ARS: 33.3	[210]
PVA/LiCLO$_4$/TiO$_2$/H$_2$O	…	…	For 8% wt of TiO$_2$: 0.000126	[212]
PEO/PVDF/DMF	PEO: 1000,000 PVDF: 900,000	PEO:PVDF; 0.5:1	2	[22]
PEO/LiCF$_3$SO$_3$ PEO/LiCF$_3$SO$_3$/Al$_2$O$_3$ PEO/LiCF$_3$SO$_3$/PEG PEO/LiCF$_3$SO$_3$/DOP	PEO: 6000,000 PEG:6000	1:0.15 1:0.15:0.20 1:0.15:0.20 1:0.15:0.20	0.001 ± 0.215 0.0864 ± 0.694 0.00873 ± 0.027 0.760 ± 11.473	[23]
PEO/PA-LiFTSI/THF	PEO: 450,000	PEO/PA-LiFTSI; 1:1	0.0177 at 80 °C	[217]
PEO/PMMA/Lithium iodide/iodine/4‑tert‑butyl pyridine	PEO: 100,000 PEO: 120,000	PEO/PMMA;1:9	7	[54]
PMMA/Pr$_4$N+I/PC/EC		20/30/30/40	5.02	[24]
PVDF/PMMA/LiTFSI/EMI TFSI/NMP		PVDF/PMMA; 10/90	3.097	[218]
PMMA/[Eimm]BF$_4$/ LiClO4/PC PMMA/ LiClO$_4$/PC	PMMA: 996,000	PMMA/[Eimm]BF$_4$/ LiClO4; 0.9/ 1/8.1	2.9 1.7	[219]
PMMA- 1-methyl-3-trimethoxysilaneimidazolium chloride, (IL)-TFSI/LiTFSI/PC	PMMA: 180,000	0.11:1	3.47	[220]
PEO/KOH PVA/PEO/KOH	PVA; 130,000 PEO; 100,000	PVA/PEO; 5/5	0.0001 10	[55]
PVDF-HFP/HDPE/DMF	PVDF-HFP; 47,000	22:1	2.97	[221]

PVDF-HFP/[EMIM]BF$_4$/GO/DMF		1/2/0.01	25	[19]
PVA/LiClO$_4$/H$_2$O PEO/LiClO$_4$/H$_2$O CMC/LiClO$_4$/H$_2$O			48 21 35	[56]
PVDF-HFP/([PMpyr][NTf$_2$]/THF	PVDF-HFP; 400,000	20:80	1.596	[222]
PVDF-HFP/PMIMTFSI PVDF-HFP/0.4M LiTFSI/PMIMTFSI PVDF-HFP/0.4M LiTFSI/PMIMTFSI/(EC+PC)	PVDF-HFP; 455,000	80:20 0.4M LiTFSI 60:20:20	6.09 ± 0.08 9.50 ± 0.08 14.8 ± 0.08	[223]
PVA/H$_3$PO$_4$/H$_2$O	27000 27000 61000 61000 125000 125000 195000 195000 195000	1:0.5 1:1 1:0.5 1:1 1:0.5 1:1 1:0.5 1:1 1:2	4.76±0.18 13.26±0.84 4.38±0.18 10.32±0.19 2.82±0.06 7.46±0.55 2.50±0.07 6.51±0.23 14.75±1.23	[51]
PVA/H$_3$PO$_4$/GO/H$_2$O	195000	1:2	SAGO amount: 0.01; 21.08±0.09 0.02; 23.23±1.57 0.05; 26.76±0.95 0.1; 29.21±0.06 0.2; 25.13±0.97 0.5: 22.36±0.47 1; 20.74±0.78 2; 13.46±2.90 10; 7.84±0.31 LAGO amount: 0.01; 19.45±0.78	[48]

			0.02; 20.57±0.54	
			0.05; 23.85±0.23	
			0.1; 21.36±0.88	
			0.2; 20.84±0.72	
			0.5; 19.22±0.90	
			1: 12.02±0.79	
			2; 7.29±1.70	
			10; 5.46±0.22	
B(borax)-PVA/KCl B(borax)-PVA/KCl/GO	…	…	32.6 For 2.3 wt% GO: 47.5	[224]
PVA-H$_3$PO$_4$-KCl PVA-H$_3$PO$_4$-KCl-Carbon black (CB)	115000	…	For 25 wt% KCl: 4.38 For 50 wt% KCl: 7.32 For 75 wt% KCl: 10.71 For 75wt% KCl and 10 wt% CB: 11.02 For 75wt% KCl and 15 wt% CB: 11.73 For 75wt% KCl and 25 wt% CB: 12.71 For 75wt% KCl and 50 wt% CB: 13.65	[45]
PVA/H$_2$SO$_4$/PEG/glutarald ehyde (GA)	PEG, molecular weight: 20000	…	67.1	[50]
PVA-KOH PVA-KOH-KCl PVA-KOH-(0.0005)mol K$_3$[Fe(CN)$_6$]	…		7.5 0.43 9.1 0.21	[44]
		1:0.46:0.46:0.4	0.71	

PVA-KOH- (0.001) mol K$_3$[Fe(CN)$_6$]			4.1	
PVA-KOH-KCl-(0.001) mol K$_3$[Fe(CN)$_6$]			5.2	
PVA/H$_3$PO$_4$				
PVA/H$_2$SO$_4$				
PVA/boric acid (BA)/ 1-ethyl-3-methylimidazolium chloride (EmimCl)	PVA, alcoholysis: 96−98%, polymerization degree: 1750 ± 50	…	2.43	[225]
PVA–GB- guanosine (G)–boric acid (B)	…	…	70	[226]
PVA/ KI+I$_2$ (Potassium iodide (KI) and iodine (I$_2$))	72000	…	For PVA 0.8: 8.41	[227]
Boron cross-linked(B)-PVA/KCl	PVA with polymerization degree of 1750 ± 50 and hydrolysis degree of 97%	…	38	[228]
PEI−PVA−(4-formylphenylboronic acid (Bn)) Bn-LiCl	PEI (Mw = 600, 1800, 10 000 g mol^{-1}, purity 99%), PVA (type-1799, DP: 1700, Mw: ∼79 000 g mol^{-1} , alcoholysis: 99.8− 100%)		15.41	[75]
PEI−PVA−Bn-NaCl			13.85	
PEI−PVA−Bn-KCl			8.93	
PEI−PVA−Bn-AMC			4.15	
PVA/LiCl	…	1:1	8.2	[229]

polyvinyl alcohol (PVA) and aqueous HCl solutions	…	…	0.7-2.2	[230]
(BMIMBF4)IL/PVA/H₂SO₄ PVA/H₂SO₄	…	0.5:1:1	90.09 38.36	[231]
PVA/KCl	PVA (Mw. 125 000)	…	1.5 wt% KCl: K-4: 0.0544	[46]
PVA/ Methacrylic Acid Ethyl acrylate(MAA:EA)/KCl	PVA (Mw. 17,000)	42.5:42.5:1	15 wt% of KCl salt: 0.000185	[47]
PVA/KOH/ P-phenylenediamine (PPD)	PVA (Mw. 44.05, alcoholysis: 99.8-100%	1:1: 0-0.16 g	0.08 g of PPD: 25	[232]
PVA-H₂SO₄	PVA (average polymerization degree: 1750 ± 50)	…	136.4	[233]
PVA-H2SO4	…	…	17.3	[234]
PVA/ Kappa-carrageenan (KC)/KOH	PVA (Mw. 75000, alcoholysis: 99%)	…	210	[235]

Table 6.4 highlights differences between our approach and other research studies. While some prior studies employed chemically cross-linked PVA structures or introduced additional salts like H3PO4 alongside KCl, others combined PVA with polymers like PEI or employed nanofillers such as carbon black or graphene oxide to increase the quantity of charge carriers, which may not be suitable for biocompatible gel electrolytes. [48, 53, 75]. Gel electrolytes of this nature pose challenges for biocompatibility due to their corrosive nature, cytotoxicity, lack of biodegradability, potential interactions with biological molecules, and the risk of eliciting inflammatory responses in living systems [364, 365]. To

address these concerns, alternative materials with lower toxicity, neutral pH, and biodegradability should be explored for biomedical applications.

Table 6.5 provides a comparative overview of the ionic conductivity achieved in this thesis with previous PVA/KCl-based gel electrolytes. It's worth noting that comparing our results with previous studies has limitations. Some studies did not report the molecular weight of PVA used, which is a crucial factor systematically investigated in this thesis for determining gel electrolyte properties. Without this information, making a reliable comparison between our work and these studies is challenging. Nonetheless, the table demonstrates the significant potential of our electrolyte for potential flexible electronic devices.

Table 6.5.   Comparison of ionic conductivity of PVA/KCl-based gel electrolytes with the present thesis.

Electrolyte	Molecular weight of polymer (g mol^{-1})	Weight ratio (w/w) of polymer to electrolytic salt or other components	Ionic conductivity (mS cm^{-1})	Ref
PVA/Potassium borate/KCl/H$_2$O	74,800 ± 50	…	1.02	[27]
B(borax)-PVA/KCl B(borax)-PVA/KCl/GO	…	…	32.6 For 2.3 wt% GO: 47.5	[224]
PVA-H$_3$PO$_4$-KCl PVA-H$_3$PO$_4$-KCl-Carbon black (CB)	115000	…	For 25 wt% KCl: 4.38 For 50 wt% KCl: 7.32 For 75 wt%, KCl: 10.71 For 75wt% KCl and 10 wt% CB: 11.02	[45]

			For 75wt% KCl and 15 wt% CB: 11.73	
			For 75wt% KCl and 25 wt% CB: 12.71	
			For 75wt% KCl and 50 wt% CB: 13.65	
PVA-KOH	…		7.5	[44]
PVA-KOH-KCl			0.43	
PVA-KOH-(0.0005)mol $K_3[Fe(CN)_6]$			9.1	
			0.21	
PVA-KOH- (0.001) mol $K_3[Fe(CN)_6]$		1:0.46:0.46:0.4	0.71	
			4.1	
PVA-KOH-KCl-(0.001) mol $K_3[Fe(CN)_6]$			5.2	
PVA/H_3PO_4				
PVA/H_2SO_4				
Boron cross-linked(B)-PVA/KCl	PVA, polymerization degree 1750 ± 50, hydrolysis: 97%	…	38	[228]
PVA/KCl	polyvinyl alcohol (Mw. 125 000)	…	1.5 wt% KCl: K-4: 0.0544	[46]
PVA/ Methacrylic Acid Ethyl acrylate(MAA:EA)/KCl	PVA (Mw 17,000)	42.5:42.5:1	15 wt% of KCl salt: 0.000185	[47]
PVA/KCl/H_2O	195000	1:2	3.48±0.25 mS/cm	**This Work**

6.4. Electrochemical characterization of graphene oxide-chitosan based supercapacitors

RGO/CS composite emerge as a promising option for electrode fabrication without the inclusion of conductive additives or binders. This is due to their remarkable conductivity, effective internal cross-linking, and the layered structure with a propensity for homogeneous dispersion [38, 366-368]. In the context of this thesis, the electrochemical assessments were carried out within a PVA/KCl gel polymer electrolyte using a two-electrode system. An initial step in evaluating supercapacitor performance typically involves cyclic voltammetry (CV). CV serves as a primary diagnostic tool to explore the electrochemical behavior of the system.

The fiber-based solid-state supercapacitors were initially prepared using various GO/CS weight ratios. RGO/CS fibers were then created through wet-spinning of the GO/CS dispersion, with GO synthesized via graphite oxidation using a modified Hummers' method. Chitosan was introduced to enhance spinnability. Schematically depicted in Scheme 6.4, the GO/CS fiber immersed in a coagulation bath resulted in the absorption of the GO/CS network. This facilitated the combination of chitosan and GO nanosheets, yielding a GO/CS fiber with a wrinkled surface structure due to intermolecular forces. This wet-spinning process enabled the production of GO/CS fibers extending several meters in length. The RGO/CS fibers were subsequently obtained through thermal reduction, as described earlier.
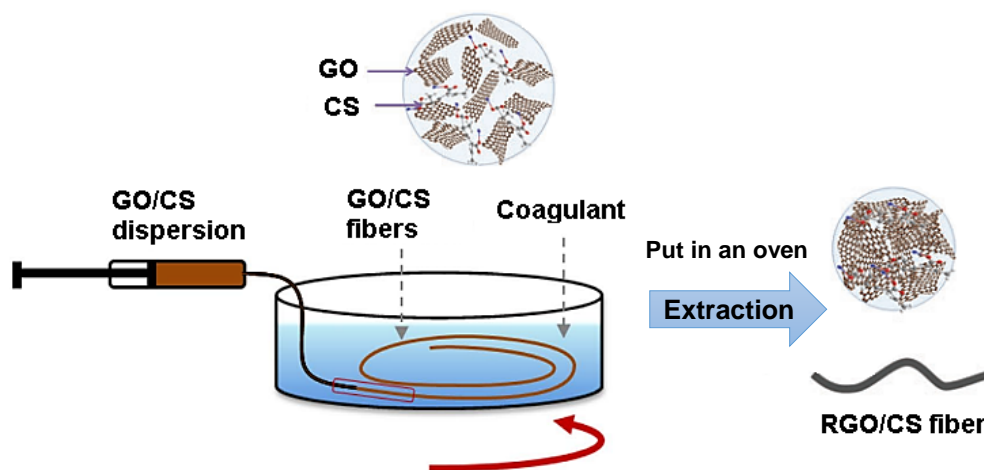
Scheme 6.4. Scheme of the wet-spinning method to prepare the RGO/CS fiber.

In the CV measurements of the RGO fibers, a notable deviation from the typical rectangular pattern, especially at higher scan rates, was observed, as depicted in Figure 6.22(a). This deviation could likely be attributed to pseudocapacitance effects, which originate predominantly from the involvement of the remaining oxygen-rich functional groups on GO surface after reduction. Notably, these functional groups, including hydroxyl, carboxyl, epoxy, and carbonyl groups situated on the surface and edges of GO sheets, contribute significantly to this pseudocapacitance behavior. Comparing the CV curves of RGO to GO reveals that RGO exhibits higher specific capacitance and electrical conductivity. The deviation from the rectangular shape in the CV curve of RGO, attributed to the remaining oxygen functional groups post-reduction, indicates not only the behavior of an electric double-layer capacitor (EDLC) but also pseudocapacitance effects [3, 369]. The RGO/CS fiber composite exhibits a larger enclosed area within the CV curve compared to RGO (85.34 ± 19.02 F g^{-1} at 5 mV s^{-1}) at lower amount of chitosan, demonstrating its remarkably high specific capacitance that arises from the synergistic interplay of both EDLC and pseudocapacitive behavior (Figure 6.22 (b-f)) [5, 81]. The exceptional capacitive response of RGO/CS spans a range of scan rates, from 5 to 100 mV s^{-1}, indicating its proficiency in facilitating rapid ion transport and reversible charge storage. This favorable behavior arises from the composite's well- developed porosity and good wettability, which collectively encourage efficient ion diffusion and facilitate the charge storage [6, 139]. The integrity of the CV curve shape for the RGO/CS composite is maintained even at a considerably high scan rate of 1000 mV s^{-1}, signifying its robust capacitive performance. This remarkable behavior reflects its adeptness in enabling the rapid diffusion of electrolyte ions from the solution into the pores of the modified electrode. The composite's low equivalent series resistance (ESR) is also implicated in this behavior, supporting its excellent charge storage capability [9, 41].

Upon analysis of the specific capacitance at a scan rate of 5 mV s^{-1}, the values recorded were as follows: 157.95 ± 29.22F g^{-1} for RGO/CS (w/w: 95/5), 523.06 ± 53.57 F g^{-1} for RGO/CS (w/w: 90/10), 397.63 ± 77.65 F g^{-1} for RGO/CS (w/w: 80/20), 267.08 ± 143.71 F g^{-1} for RGO/CS (w/w: 60/40), 46.40 ± 25.43 F g^{-1} for RGO/CS (w/w: 50/50), 0.95 ± 0.16 F g^{-1} for RGO/CS (w/w: 20/80), 0.20 ± 0.04 F g^{-1} for RGO/CS (w/w: 10/90), and 0.09 ± 0.05 F g^{-1} for RGO/CS (w/w: 0/100). Table S1, featured in the appendix of this thesis, provides specific capacitance values at various scan rates for all fiber samples. Notably, the composite

containing RGO/CS (w/w: 90/10) exhibited the highest specific capacitance. This phenomenon can be attributed to the combined effect of RGO's superior conductivity and CS's remarkable porosity, resulting in a synergistic behavior that enables enhanced charge storage and ion penetration to the electrode surface as evidenced by the distinct shape of the CV curve at high scan rates [1, 139].

The tendency of GO sheets to agglomerate often leads to a reduction in the accessible surface area for ion exchange and electrical double-layer formation and reduces the specific capacitance ((Figure 6.22 (g-i)) [140]. The RGO/CS (w/w: 90/10) composite displayed the highest specific capacitance among the samples. However, with a further increase in RGO concentration, as seen in the RGO/CS (w/w: 95/5) composition, a reduction in conductivity occurred. This decrease might be attributed to the development of isolated RGO aggregates, which limited the transport of ions across the conductive network. Interestingly, at an optimal concentration of chitosan, it acted as a spacer between RGO sheets, effectively increasing the distance between them [17, 18]. This effect was also evidenced in the aforementioned XRD results. This spatial arrangement contributed to enhanced capacitance by expanding the effective surface area available for charge storage and facilitating channels for ion exchange. The presence of $-NH_2$ and $-OH$ groups in the chitosan structure contributes significantly to minimizing ion permeable resistance at the electrode-electrolyte interface [25, 31]. Across all samples, the highest specific capacitance values were consistently observed at a scan rate of 5 mV s^{-1}, with values decreasing gradually as scan rates increased. This behavior aligns with the anticipated trend due to diffusion limitations within the electrode surface pores [1].
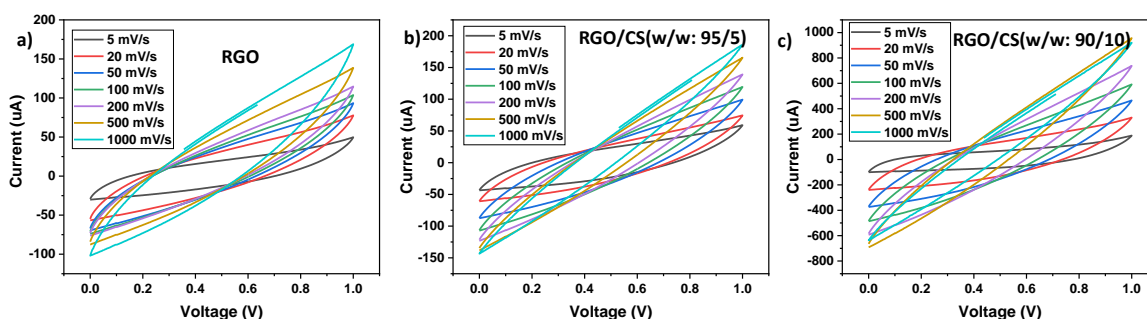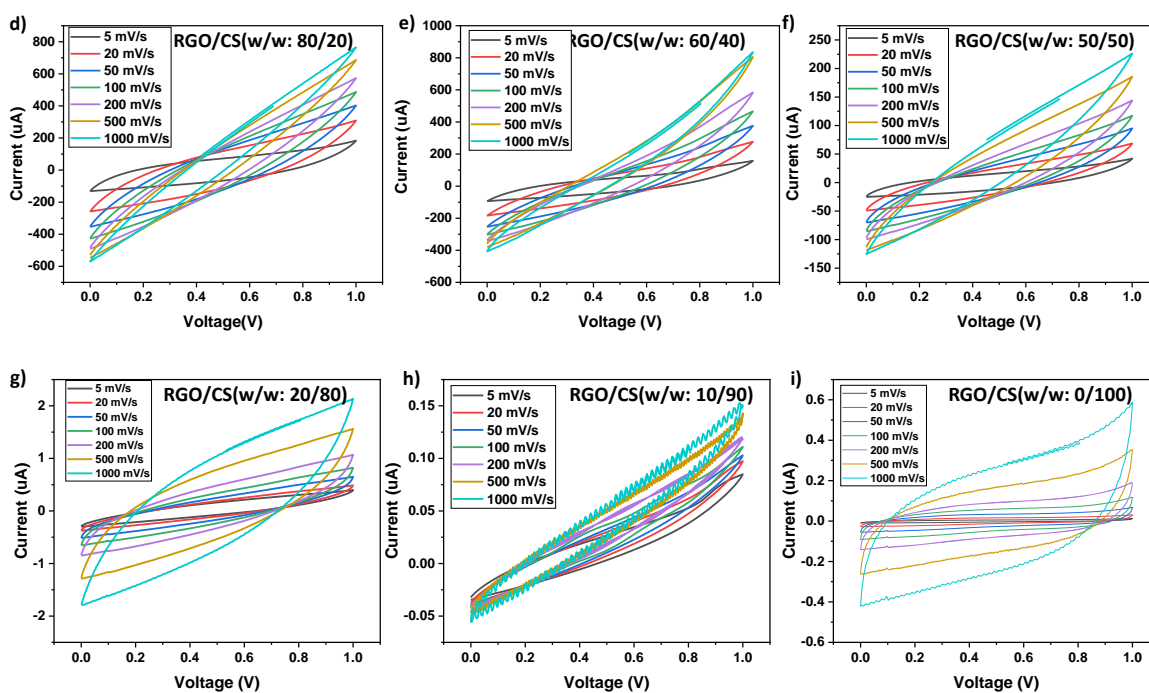
Figure 6.22. (a) Cyclic voltammetry (CV) of the supercapacitor based on reduced graphene oxide (RGO) fiber, (b-i) CV of the solid-state supercapacitors based on reduced graphene oxide /chitosan (RGO/CS) fiber composites with various weight ratios at different scan rates (5, 20, 50, 100, 200, 500, 1000 mV s^{-1}), (GPE: PVA/KCl, M$_w$=195000 g mol^{-1}, w/w:1/2).

After conducting the CV analysis of fiber composites, as depicted in Figure 6.23, we proceeded to evaluate the electrochemical performances of film-form electrodes constructed from CS, RGO, and the RGO/CS composites. The resulting CV curves, recorded at different scan rates, offer valuable insights into the electrochemical characteristics of CS, RGO, and RGO/CS film electrodes across various weight ratios. These findings are graphically depicted in Figure 6.23 and Figure 6.24.
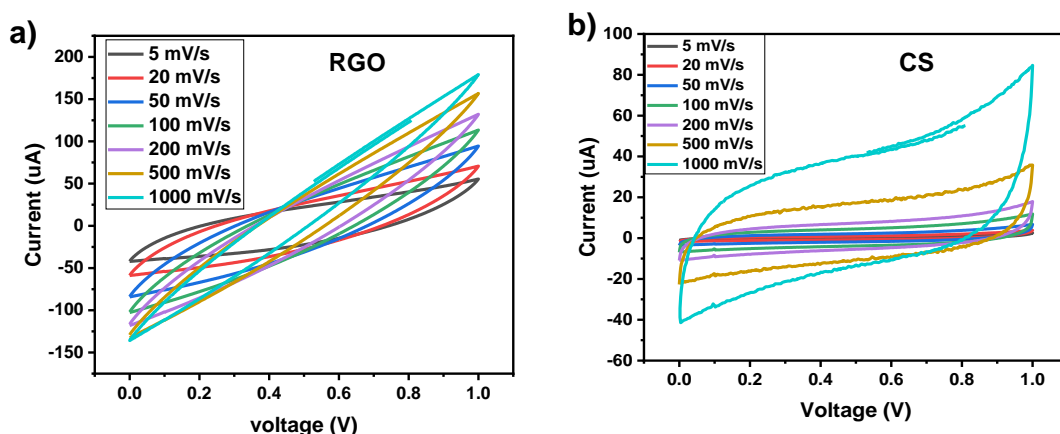
Figure 6.23. Cyclic voltammetry (CV) of the supercapacitor based on a) reduced graphene oxide (RGO) and b) chitosan (CS) films at different scan rates.

The CV curves displayed in Figure 6.23 for both CS and RGO film electrodes exhibit a distinctive rectangular-like shape, characteristic of carbon-based materials and indicative of electric double layer capacitor (EDLC) behavior [33]. However, an interesting departure from this rectangular pattern is observed in the CV curve of RGO, particularly at higher scan rates (Figure 6.23 (a)). This deviation could likely be attributed to pseudocapacitance effects, which originate predominantly from the involvement of oxygen-rich functional groups. Notably, these functional groups, including hydroxyl, carboxyl, epoxy, and carbonyl groups situated on the surface and edges of GO sheets, contribute significantly to this behavior [37]. To provide a quantitative assessment of the specific capacitance, the calculations are conducted based on the recorded CV curves at a scan rate of 5 mVs^{-1}, which yielded specific capacitance values of 5.23 ± 0.75 for CS and 174.03 ± 38.25 F g^{-1} for RGO. These results underscore the considerable enhancement in specific capacitance achieved with the incorporation of RGO compared to CS (Figure 6.23 (b)), highlighting the advantageous of electrical conductivity nature and pseudocapacitance contribution stemming from the oxygen-functionalized groups present in the RGO structure [39, 40].

The electrochemical performance of film-based solid-state supercapacitors for various weight ratios of GO/CS was also studied. The result of CV test is given in Figure 6.24 (a-h) at different scan rates from 5 to 1000 mV s^{-1}. In Figure 6.24, the RGO/CS composite exhibits a larger enclosed area within the CV curve, demonstrating its remarkably high specific

capacitance that arises from the synergistic interplay of both EDLC and pseudocapacitive behavior [36]. The exceptional capacitive response of RGO/CS spans a range of scan rates, from 5 to 100 mV s^{-1}, indicating its proficiency in facilitating rapid ion transport and reversible charge storage. This phenomenon can be attributed to the combined effect of RGO's superior conductivity and CS's remarkable porosity, resulting in a synergistic behavior that enables enhanced charge storage and ion penetration to the electrode surface as evidenced by the distinct shape of the CV curve at high scan rates [41]. The stretched rectangle shape of the CV curves can be due to the redox processes and delocalized electrons. The larger specific capacitance of RGO/CS is mainly due to the redox reactions, benefiting from higher O contents [42]. Therefore, the higher porous carbon structure of RGO/CS is more effective in contributing a high surface area, result in a higher charge storage density and higher diffusion rate of ions, contributed the most to capacitive capacitance [43]. It is easy to understand that the higher pseudocapacitance from the diffusion process in RGO/CS is due to the rich O sites which confirmed by FTIR and XRD analysis. The functional groups in RGO/CS are more efficient in attracting the electrolyte ions into the pores and onto the carbon surfaces, which exhibited the faster dynamics of the electrolytes within the carbons, a stronger interaction between electrolyte and carbon improves the electrode surface wetting and increases specific capacitance [41, 76].

Upon analysis of the specific capacitance at a scan rate of 5 mV s^{-1}, the values recorded were as follows: 312.01± 28.48 F g^{-1} for RGO/CS (w/w: 95/5), 872.75± 68.35 F g^{-1} for RGO/CS (w/w: 90/10), 459.24± 23.39 F g^{-1} for RGO/CS (w/w: 80/20), 204.27± 17.03 F g^{-1} for RGO/CS (w/w: 60/40), 159.63± 24.34 F g^{-1} for RGO/CS (w/w: 50/50), 113.07±3.31F g^{-1} for RGO/CS (w/w: 20/80), 81.86±8.82 F g^{-1} for RGO/CS (w/w: 10/90), and 5.28±0.75 F g^{-1} for RGO/CS (w/w: 0/100). Table S2 in the appendix of the thesis presents specific capacitance values at different scan rates for all film samples. Notably, the composite containing RGO/CS (w/w: 90/10) exhibited the highest specific capacitance. This phenomenon can be attributed to the combined effect of RGO's superior conductivity and CS's remarkable porosity, resulting in a synergistic behavior that enables enhanced charge storage and ion penetration to the electrode surface as evidenced by the distinct shape of the CV curve at high scan rates which is consistent with the literatures [1, 158].

The agglomeration of GO sheets leads to a reduction in the accessible surface area for ion exchange and electrical double-layer formation [159]. The RGO/CS (w/w: 90/10) composite displayed the highest specific capacitance among the samples. However, with a further increase in RGO concentration, as seen in the RGO/CS (w/w: 95/5) composition, a reduction in conductivity occurred. This decrease might be attributed to the development of isolated RGO aggregates, which limited the transport of ions across the conductive network [370]. Interestingly, at an optimal concentration of chitosan, it acted as a spacer between RGO sheets, effectively increasing the distance between them. This effect was also evidenced in the aforementioned XRD results [239]. This spatial arrangement contributed to enhanced capacitance by expanding the effective surface area available for charge storage and facilitating channels for ion exchange. The presence of $-NH_2$ and $-OH$ groups in the chitosan structure contributes significantly to minimizing ion permeable resistance at the electrode-electrolyte interface [352]. Across all samples, the highest specific capacitance values were consistently observed at a scan rate of 5 mV s^{-1}, with values decreasing gradually as scan rates increased. This behavior aligns with the anticipated trend due to diffusion limitations within the electrode surface pores [371]. Therefore, when the chitosan content surpasses 10%, a reduction in conductivity is observed. Beyond this ratio, a decrease in specific surface area, a trait that fosters the creation of an extremely efficient ion transport network and consequently enhances specific capacitance, is noticeable at higher chitosan concentrations. Conversely, at chitosan levels below the optimum, the spacing between RGO sheets becomes insufficient, adversely affecting conductivity [1, 88].
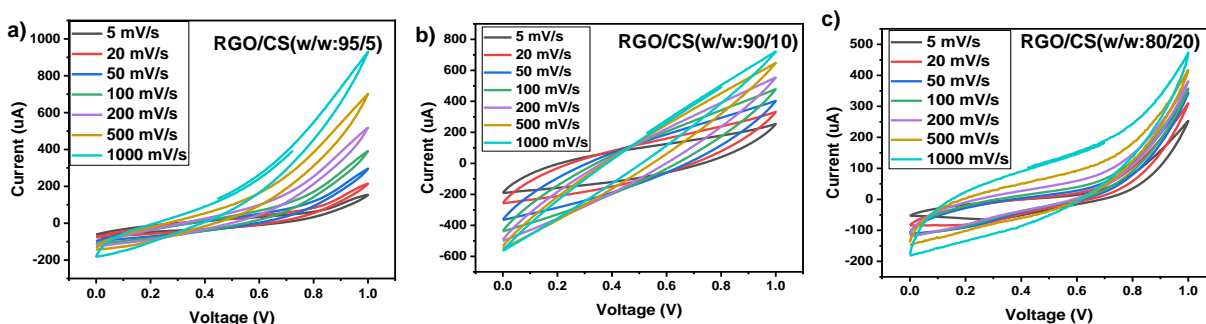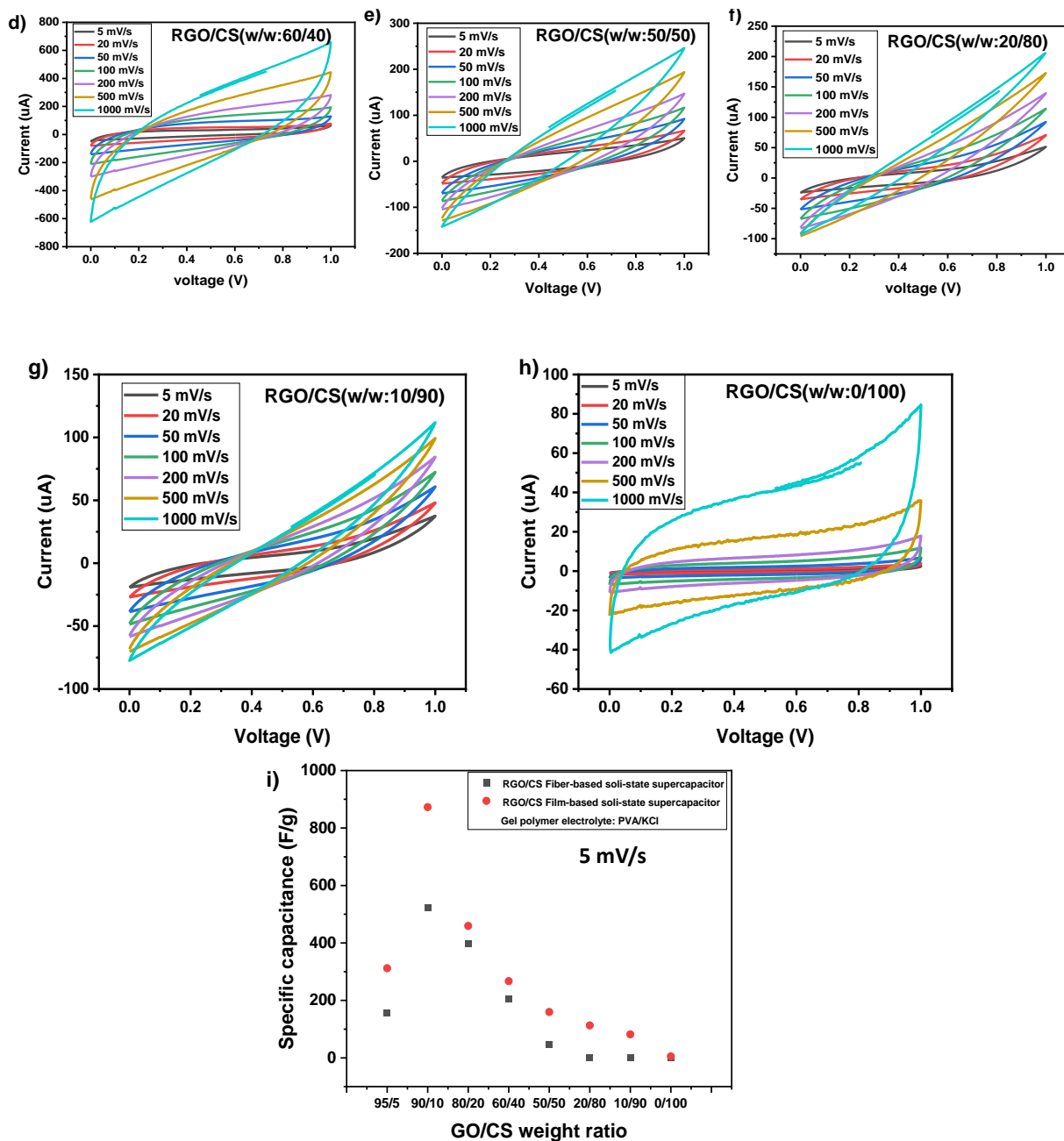
Figure 6.24. (a-h) Cyclic voltammetry (CV) of the supercapacitor based on reduced graphene oxide/chitosan (RGO/CS) film composites with various weight ratios at different scan rates, (i) specific capacitance versus GO/CS weight ratio at 5 mVs^{-1} scan rate for film and fiber-based solid-state supercapacitors; respectively. (GPE: PVA/KCl, M$_w$=195000 g mol^{-1}, w/w:1/2).

Figure 6.24 (i and j) shows the specific capacitance versus GO/CS weight ratio for film and fiber based solid-state supercapacitors; respectively. The result reveals that film form has the highest specific capacitance. This may be attributed to variations in the material's surface

166

area, porosity, and accessibility of active sites. Films often provide a larger surface area , more active sites for electrochemical reactions, and better accessibility of electrolyte ions to the electrode surface compared to fibers, leading to higher specific capacitance. Additionally, the film structure may offer improved electron and ion transport within the electrode, better porous structure, and potentially of flexibility, contributing to enhanced electrochemical performance [88, 89, 141]. The synergy effect of GO and CS is related to GO/CS amount in the composite, electrical conductivity of RGO, porous structure and pseudocapacitance of chitosan (Scheme 6.5). RGO provides high electrical conductivity due to its graphene structure, facilitating rapid charge transfer.

Chitosan contributes to the overall conductivity and acts as a binder, enhancing the structural integrity of the composite. Chitosan can undergo faradic reactions, leading to additional pseudocapacitance, complementing the double-layer capacitance of RGO [97, 372]. At GO/CS weight ratio of 90/10, there is a balance between the conductivity of RGO and the capacitive properties of chitosan, resulting in the highest specific capacitance. The 90/10 ratio likely creates an optimal porous structure, allowing efficient electrolyte penetration and promoting high ion accessibility. Chitosan at this ratio serves as an effective binder, holding the RGO sheets together without compromising conductivity [352]. At higher amount of chitosan, electrical conductivity may limit and reducing the overall capacitance and might lead to increased resistance and decreased charge transfer. At higher amount of RGO, the structure may lack stability, cohesiveness, and pseudocapacitance contribution due to the lower amount of chitosan. Therefore, chitosan as a hydrophilic polymer, enhances the ion conductivity by facilitating ion movement within the composite and this synergy can be attributed to the balanced electrical conductivity, optimized porosity, and beneficial interactions between RGO and CS, consistent with prior findings [245, 352].
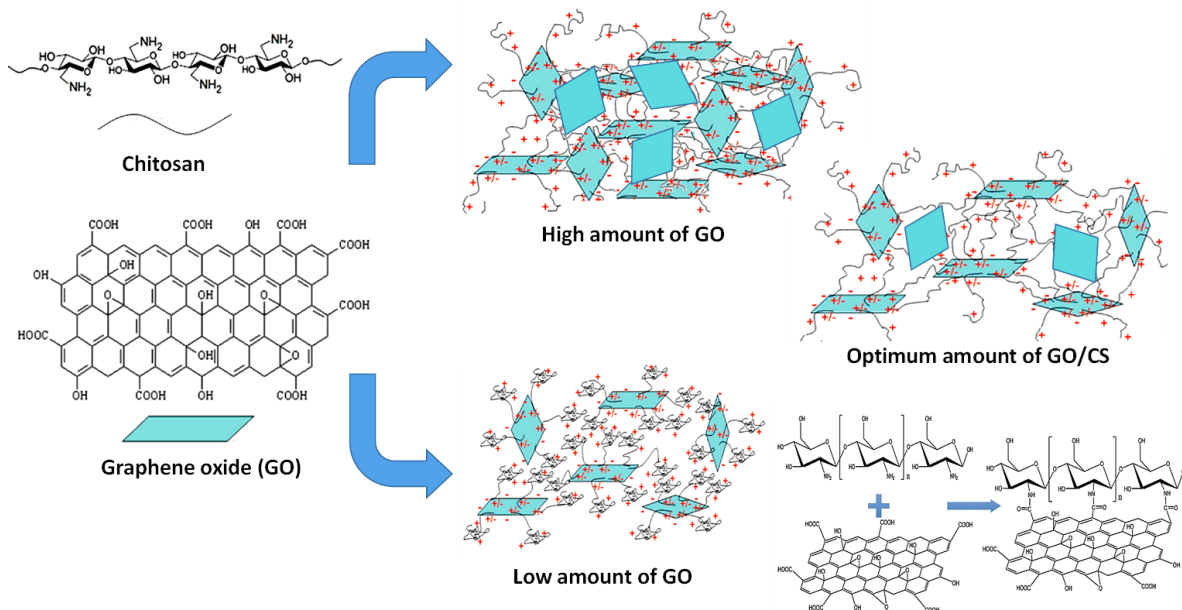
Scheme 6.5. Illustration of graphene oxide (GO) and chitosan (CS) interaction at different GO concentration.

The GCD curves of RGO/CS (w/w: 90/10) fiber composite at various current densities in Figure 6.25 (a), displays a perfect linear profile, and all the charge curves are almost ideal symmetrical with their corresponding discharge curves within the potential window (0-1.5V). This demonstrates that the supercapacitor have remarkable capacitive performance and rapid current–voltage response [141]. Furthermore, specific capacitance was observed to decrease with increasing current density which could be due to insufficient time for the electrolyte ions to diffuse into the inner pores of the electrode (Figure 6.25 (b)). Figure 6.25 (c) shows the specific capacitance versus scan rate, by increasing scan rate, the integral area decreases which could be due to insufficient time for the electrolyte ions to complete the electrochemical reaction at higher scan rates and consequently lowers the specific capacitance [160, 161].

The charge-discharge curves of RGO/CS film composite in Figure 6.25 (d) exhibits quick and short current response times, exhibiting commendable symmetry that confirms their EDLC behavior [162]. Meanwhile, the GCD profiles display relatively symmetrical shapes with inflection points and lower internal resistance (IR) drops, indicative of a harmonious combination of EDLC and pseudocapacitive behavior [163]. The specific capacitance of film type supercapacitor was measured as 751.91 ± 112.26 F g^{-1} at 1 A g^{-1} which is higher than fiber type (405.26 ± 1.44 F g^{-1} at 1 A g^{-1}). This outcome can be attributed to well-developed

168

micro-mesopores and oxygen-containing functional groups on GO and chitosan structures. The GCD results are in consistent with the CV results [352]. Figure 6.25 (e) shows the specific capacitance versus current density. The specific capacitance was observed to decrease with increasing current density which could be due to insufficient time for the electrolyte ions to diffuse into the inner pores of the electrode [165]. Figure 6.25 (f) indicates the specific capacitance versus scan rate, by increasing scan rate, the integral area decreases which could be due to insufficient time for the electrolyte ions to complete the electrochemical reaction at higher scan rates and consequently lowers the specific capacitance [1].

The abundant $-NH_2$ and -OH groups in film type electrodes contribute to increased faradaic pseudo-capacitance within an acidic-based polymer electrolyte, thereby contributing significantly to the elevated capacitance of RGO/CS [332]. Additionally, the impressive hierarchical porous structure, characterized by micro-, meso-, and macropores, played a pivotal role. Micropores can enhance the specific capacitance directly, while meso- and macropores accelerate ion diffusion [91]. Furthermore, the NH–C–O groups improved wettability and electrical conductivity, while the sandwich-like RGO/CS film configuration increased the accessible interface area between the electrolyte and the active material. This combined effect positively influenced the overall capacitance [42]. The intricate network of micro-, meso- and macropores not only facilitated the electrolyte ion transport but also upheld capacitance retention even at a high scan rate, underlining the composite's robust rate capability [39, 91].
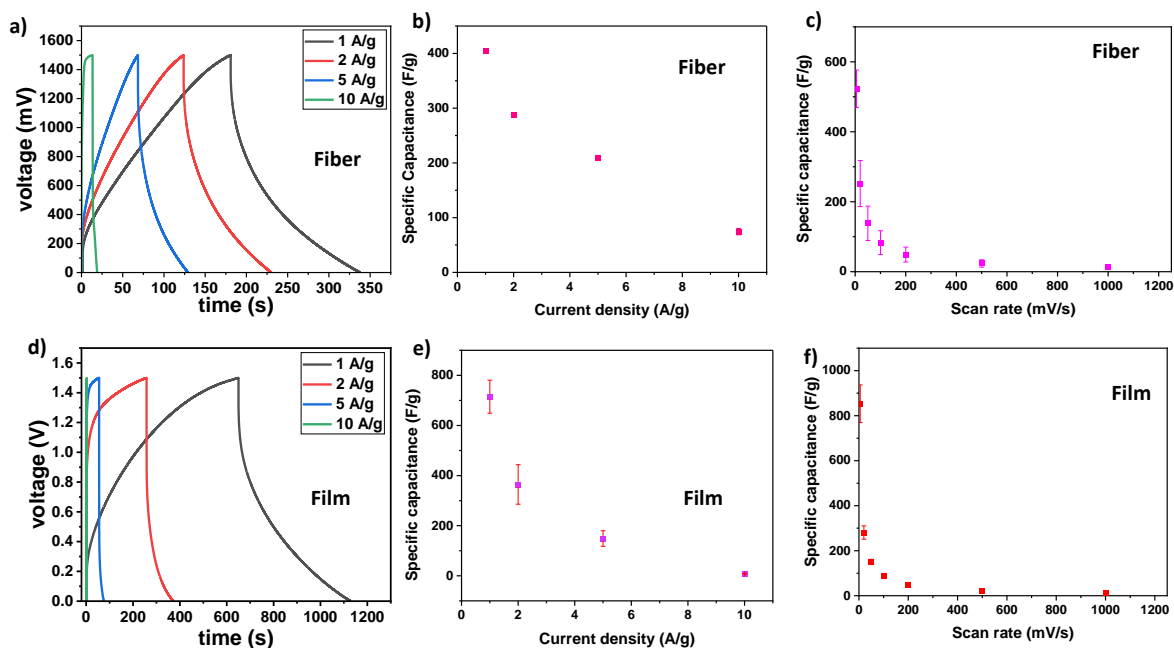
Figure 6.25. a) Galvanostatic charge-discharge (GCD) curves of the solid-state supercapacitor based on RGO/CS (w/w: 90/10) fiber composite at various current densities within potential window of 0 to 1.5 V, b) Specific capacitance versus current density for fiber-based solid-state supercapacitor, c) Specific capacitance versus scan rate for fiber-based solid-state supercapacitor, d) GCD curves of the solid-state supercapacitor based on RGO/CS (w/w: 90/10) film composite at various current densities within potential window of 0 to 1.5 V, e) Specific capacitance versus current density for film-based solid-state supercapacitor, f) Specific capacitance versus scan rate for film-based solid-state supercapacitor, (GPE: PVA/KCl, M_w=195000 g mol^{-1}, w/w:1/2).

The Nyquist plot of RGO and RGO/CS (w/w: 90/10) composite film solid-state supercapacitors in Figure 6.26 (a and b), provides a comprehensive analysis of the electrochemical impedance spectroscopy (EIS) data, accompanied by the corresponding equivalent circuit. According to the electrical equivalent circuit with Z_{sim} software, each Nyquist graph was fitted with an equivalent circuit. The software gives information about charge transfer resistance (R_{ct} or R_2) of the electrode, the ohmic or ionic resistance (R_1) of the gel electrolyte, capacitive element (C) of the electrodes, and Warburg diffusion coefficient (W). The charge transfer resistance (R_{ct}) and ionic resistance of electrolyte (R_s) values (Table 6.6) of the RGO/CS electrode are much lower than that of RGO electrode, this is owing to the intrinsic high ionic conductivity and fast electron transfers in the system [39]. Moreover, in the low-frequency region, the straight line reflects the ion diffusion resistance

within the electrodes. The line of RGO/CS electrode is more vertical compared to that of RGO suggesting that the conductive links between chitosan and RGO provide an enhanced electrical conductivity or easily accessible ion path for electrolyte ions [90, 91].

Upon subjecting of solid-state supercapacitor based on RGO/CS (w/w: 90/10) composite electrode film to a rigorous test of 10,000 charge-discharge cycles (as illustrated in Figure 6.26(c), a notable observation emerges: the calculated specific capacitance (Cs), as per the computation outlined in equation (5.11) (chapter 5), experiences a slight decline from 64.24 to approximately 56.09 F g^{-1} in PVA/KCl gel electrolyte (M$_w$=195000 g mol^{-1}, w/w: 1/2). Impressively, even after this extensive cycle count, the electrode retains an impressive 87.31% of its initial capacitance. This outcome underscores the remarkable resilience and durability of the RGO/CS electrode, a characteristic attributed to the open framework structures inherent to chitosan [39]. This structural framework facilitates the accessibility of ion charges and enables the efficient conduction and transportation of ions [41]. Crucially, the interplay between GO sheets and chitosan chains engenders physical interactions that serve as barriers, mitigating the extent of polymer chain degradation during the repeated charge-discharge cycles [43]. This phenomenon culminates in a substantial enhancement of both capacitance and cycle life. In terms of quantifying performance metrics, the supercapacitor attains an energy density of 234.97 Wh kg^{-1} and a power density of 1499.98 W kg^{-1} at 1 Ag^{-1}. These metrics underscore the formidable energy storage capabilities of the RGO/CS electrode, solidifying its position as a robust and high-performing energy storage devices [244, 352].
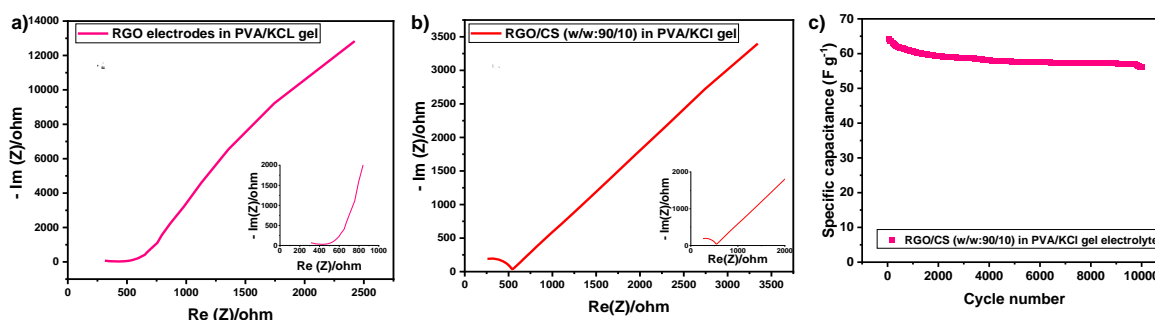
Figure 6.26. Electrochemical impedance spectroscopy (EIS) curves of a) reduced graphene oxide (RGO) film, b) RGO/CS (w/w: 90/10) composite film solid-state supercapacitors,

within the frequency range of 100 mHz to 100 kHz, c) Cycle life of the solid-state supercapacitor based on RGO/CS (w/w:90/10) composite film over 10000 cycles, (GPE: PVA/KCl, M_w=195000 g mol^{-1}, w/w:1/2).

Table 6.6. Equivalent circuit parameters for RGO/CS and RGO film-based solid-state supercapacitors.

Sample	Rs (ohm)	R_{ct} (ohm)	Diffusion element	χ^2	P value
RGO/CS (w/w: 90/10)	126.5 ±1.71	381.9 ±1.67	12728 ± 0.07 (ohm s$^{-1/2}$)	0.77	0.95
RGO	395.4 ±0.22	968±3.45	0.11± 0.40×10^{-3} (s)	0.50	0.90

The results of impedance test for GO, CS, and GO/CS samples are given in Figure 6.27 (a-c). The electrical conductivity is calculated using the value of charge transfer resistance (R_{ct}) from the Nyquist plots as the charge transfer at an electrode/electrolyte interface which is the primary factor affecting the impedance [149]. The results indicate that RGO has the higher electrical conductivity (1.10×10^{-4} S cm^{-1}) compared to GO (6.89×10^{-5} S cm^{-1}) that can be attributed to the thermal reduction process. GO is derived from graphene by the introduction of oxygen-containing functional groups, which imparts semiconducting or insulating properties to the material [373]. These functional groups disrupt the sp^2 carbon network of pristine graphene. The reduction of GO involves removing or reducing these oxygen-containing groups, effectively restoring the sp^2 carbon structure closer to graphene's pristine form [374]. This reduction process enhances the material's electrical conductivity. Moreover, the reduction reduces the band-gap, allowing for better charge carrier mobility and higher electrical conductivity [375].

Chitosan typically exhibits lower electrical conductivity compared to graphene-based materials due to its inherently insulating nature. Chitosan is a polysaccharide derived from chitin, and it lacks the extended π-conjugated structure that graphene possesses. The lack of highly conductive carbon framework in chitosan results in lower conductivity (3.15×10^{-9} S cm^{-1}) [127]. The combination of chitosan with GO or RGO aims to benefit from the advantageous properties of both materials. The GO/CS composite has lower conductivity

than GO because the oxygen-containing groups in GO disrupt the sp^2 carbon network and introduce insulating regions in the material. Chitosan being inherently insulating, further contributes to the decrease in electrical conductivity compared to pure GO [376, 377]. However, GO/CS has higher conductivity (4.40×10^{-6} S cm^{-1}) than CS which is attributed to the presence of graphene oxide sheets in the composite compared to pure chitosan. In this composite, graphene sheets can bridge or connect regions in the chitosan that would otherwise be insulating. This bridging effect facilitates the movement of charge carriers, resulting in enhanced conductivity while the conductivity of GO/CS might not reach the levels of pristine graphene due to the insulating nature of chitosan [83, 378].

The reduction of GO shows that RGO and RGO/CS samples have higher electrical conductivity than GO/CS because the reduction process removes oxygen groups from GO sheets, restoring some of the sp^2 hybridized carbon structure found in graphene [378]. As a result, RGO has a more graphitic structure than GO, leading to improved conductivity. Moreover, the reduction process increases the size of graphitic domains and promotes better inter-sheet connectivity within the RGO, allowing for better charge carrier mobility [97].

Finally, the RGO/CS composite has higher electrical conductivity (2.62×10^{-3} S cm^{-1}) than RGO which is due to the synergistic effect of RGO and CS. The conductive nature of RGO complements the insulating nature of CS, resulting in a composite with improved overall conductivity (Figure 6.27 (e and f)) [116, 117]. The combination of RGO and CS likely improves the interconnectivity of graphene sheets within the composite. This enhanced connectivity facilitates the movement of charge carriers to higher electrical conductivity. Furthermore, the incorporating chitosan into RGO network may contribute to a more stable and well-connected structure, further improving the electrical conductivity [97, 118].
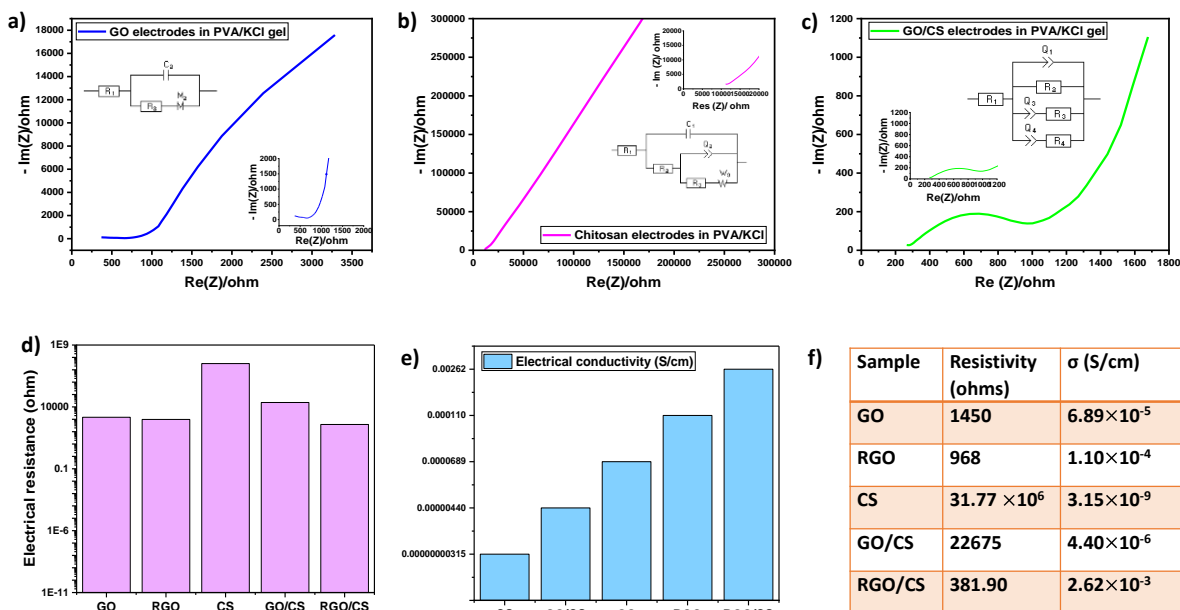
Figure 6.27. Electrochemical impedance spectroscopy (EIS) curves of a) graphene oxide (GO) film, b) Chitosan (CS) film, c) GO/CS (w/w: 90/10) composite film within the frequency range of 100 mHz to 100 kHz, d) Electrical resistance (R) in "ohms" for all of the samples, e) Electrical conductivity (σ) in "S cm^{-1}" for all of the samples, f) The R and σ data for each sample.

6.5. Comparison of the electrochemical performance of graphene-based solid-state supercapacitors

Figure 6.28 presents a comparative analysis of the electrochemical performance exhibited by various graphene-based supercapacitors employing solid-state electrolytes [379-386]. While liquid electrolytes possess higher ionic conductivity, they suffer from issues such as leakage, rendering them unsuitable for wearable electronic applications [15]. Graphene stands out as a superior carbon-based electrode material when evaluated against other contenders [43]. In the realm of chitosan/graphene-based supercapacitors, our electrode manifest notably higher specific capacitance (Figure 6.28(a)). This could be attributed to the facile preparation method, where the existence of oxygen-containing functional groups on both graphene and chitosan surfaces facilitates pseudocapacitance behavior [39]. These functional groups, encompassing hydroxyl and amino groups, serve as active sites for redox reactions, contributing to an additional charge storage capacity beyond the electric double-

layer capacitance [40]. Moreover, the GO/CS structures prepared in our investigation boast a comprehensive array of micro-, meso-, and macropores, fostering pathways for efficient ion transport and effective electrolyte permeation [41]. This dual effect not only bolsters ion accessibility but also maintains a high capacitance even at elevated scan rates. The interactions between graphene and chitosan, including hydrogen bonding and π-π stacking, further augments the overall stability of the composite. This synergy prevents the restacking of graphene sheets and upholds the material's structural integrity throughout charge-discharge cycles [42]. Figure 6.28(b), summarizes the electrochemical performance of the present work with other published results for graphene-based solid-state supercapacitors in a Ragone plot. The all-solid-state supercapacitors employing PVA-based hydrogel as the electrolyte exhibited much higher energy density compared to ionic liquids [15]. Furthermore, by employing PVdF-HFP/EMITf/Al(Tf)$_3$ ionogel as the electrolyte, the graphene nano-platelet (GNP)-based solid-state supercapacitor showed an energy density of 19.6 W h kg^{-1} at a power density of 49.6 W kg^{-1} [385]. The obtained energy density for the present work was among the highest values achieved for any type of graphene-based solid-state supercapacitor, highlighting its compelling and promising potential.
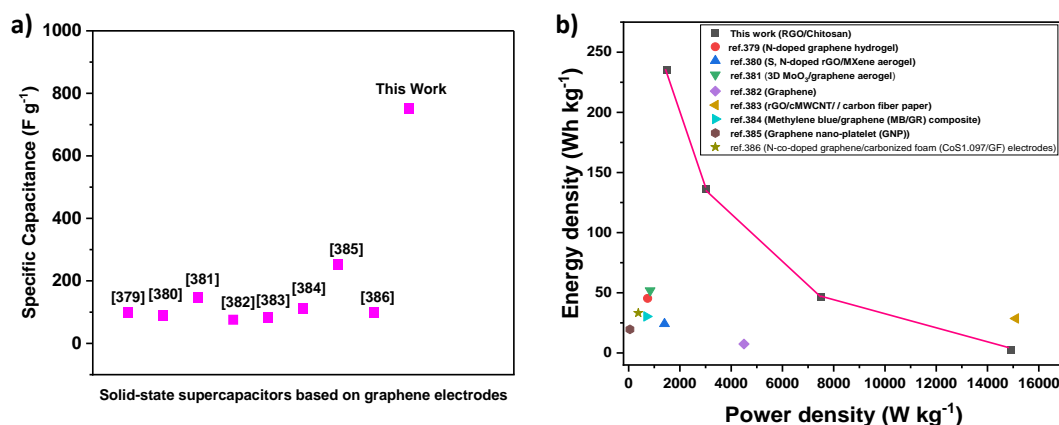
Figure 6.28. Comparing the electrochemical performance of graphene-based solid-state supercapacitors, a) Specific capacitance in F g^{-1}, b) Ragone plot.

6.6. Electrochemical performance of flexible solid-state supercapacitors on PET substrate

All the aforementioned tests were conducted using stainless steel as the current collector substrate, a well-known and widely-applied material in electrochemical measurements. All-flexible-solid-state supercapacitors are crucial for integration with micro-sensors and micro-electronics, requiring excellent mechanical properties for optimal performance [119]. If these devices exhibit desired electrochemical performance alongside good mechanical properties and biocompatibility, they hold significant promise for applications in flexible, safe, and wearable electronics [387, 388]. In this subsequent phase of the PhD thesis, we introduced polyethylene terephthalate (PET) as a flexible substrate instead of stainless steel. While stainless steel has been extensively utilized in electrochemical measurements, a limited number of previous studies have explored similar flexible substrates. For instance, Kang et al. fabricated flexible supercapacitors using carbon nanotubes (CNTs) as electrodes and PET films as the substrate [150]. They enhanced the adhesion properties of PET films through reactive ion etching (RIE), resulting in improved interfacial adhesion and overall device performance. The supercapacitors exhibited favorable cyclability, retaining 87.5% of specific capacitance after 10,000 charge/discharge cycles, along with notable performance metrics. Specifically, they demonstrated a specific capacitance of 70 F g^{-1}, an energy density of 21.1 Wh kg^{-1}, and a power density of 3.0 kW kg^{-1}.

In a study by Wang et al., flexible micro-supercapacitors (MSCs) were fabricated using zinc oxide (ZnO) nanorod/titanium (Ti)/titanium nitride (TiN) core-shell nanostructures and metallic interdigits on a PET substrate, with PVA/LiCl serving as the gel polymer electrolyte. These MSCs demonstrated a power density of 432 W kg^{-1}, an energy density of 0.24 Wh kg^{-1}, and exhibited capacitance retention of over 98% after 5000 cycles, indicating excellent stability [389].

Ghoniem et al. developed flexible supercapacitors using reduced and patterned graphene oxide (GO) films supported on a PET substrate, with PVA/H_3PO_4 as the gel electrolyte, employing a high-powered CO_2 laser system. The resulting electrodes, including rGO and MnO_2/rGO, showcased specific capacitance ranging from 82-107 Fg^{-1} and 172-368 Fg^{-1}, respectively, across an applied current range of 0.1-1.0 mA cm^2. These electrodes retained

98% and 95% of their initial capacitances after 2000 cycles at a current density of 1.0 mA cm^2 [121]. Moreover, Xue et al. developed a straightforward method for the multi-scale, in-plane patterning of graphene oxide and reduced graphene oxide (GO-rGO) electrodes, along with PVA/H$_3$PO$_4$ as the gel electrolyte, for flexible supercapacitors. The resulting symmetric and in-plane supercapacitors exhibited a specific capacitance of 141.2 F g^{-1} at a current density of 1 A g^{-1} [122].

In this PhD thesis, a straightforward method was developed to fabricate symmetrical, flexible, and all-solid-state supercapacitors using flexible PET film as the substrate, as depicted in Scheme 6.6. The flexible PET film served as a flexible current collector, while GO/CS (w/w: 90/10) functioned as the electrode material, and PVA/KCl (Mw=195000 g mol^{-1}, w/w: 1/2) served as the gel electrolyte. Notably, the supercapacitor exhibited excellent electrochemical performance without the need for organic binders or conductive additives in the electrode preparation, owing to the easy access of ions to the active material. Additionally, the PET film demonstrated remarkable properties including flexibility, durability, and resistance to corrosion, enhancing the device's resilience to outer chemical environments and prolonging its lifetime [119, 150, 390].
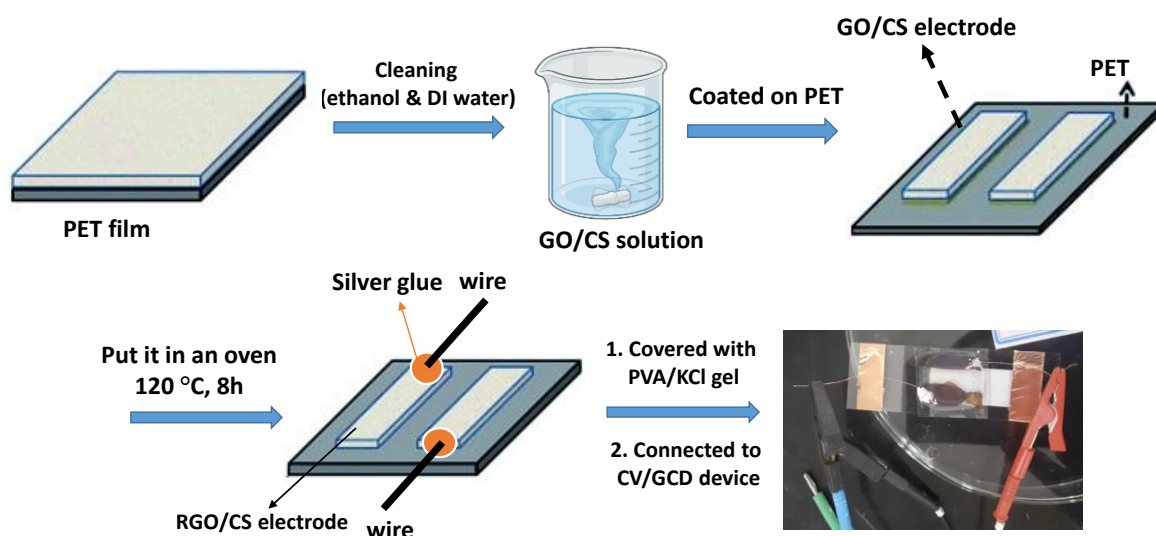
Scheme 6.6. Scheme preparation of a flexible solid-state supercapacitor based on RGO/CS on PET substrate.

The electrochemical performance of the flexible solid-state supercapacitor, based on RGO/CS (w/w: 90/10) on a PET substrate, is presented in Figure 6.29. The CV curves in Figure 6.29(a) exhibit nearly rectangular shapes, indicative of the double-layer capacitance (EDLC) characteristic. In Figure 6.29(b), it is evident that the specific capacitance decreases with increasing scan rate, attributed to the reduced diffusion of electrolyte ions into the electrode material due to faster redox reactions occurring at higher scan rates. Specifically, the specific capacitance at 5 mVs^{-1} was measured at 191.07$\pm$19.24 F g^{-1}, which is significantly lower compared to that measured using stainless steel.

The binder-free flexible solid-state supercapacitor developed on a flexible PET substrate in this study demonstrated a higher specific capacitance compared to other related research works [121-124]. This improvement can be attributed to the specific interaction and synergy between RGO and chitosan, which enhance the charge storage capability. Additionally, the excellent conductivity of RGO and the pseudocapacitance contribution from chitosan, along with effective adhesion between the RGO/CS and PET substrate, likely contributed to the enhanced electrochemical performance [97, 150]. Moreover, the PVA/KCl gel electrolyte used exhibited the highest ionic conductivity, further enhancing charge storage. To further enhance the specific capacitance on PET, optimizing process parameters such as deposition techniques and substrate treatment could be beneficial [124, 391]. Thus, the developed supercapacitor in this study offers advantages for applications requiring mechanical flexibility, as PET provides both flexibility and mechanical stability, making it a suitable platform for flexible and biocompatible solid-state supercapacitors.

Obviously, the GCD curves (Figure 6.29(c)) are nearly symmetric and shows a small voltage drop confirming the good reversibility, rapid charge/discharge behavior, and small resistance of the RGO/CS electrodes. Figure 6.29(d) presents the specific capacitance versus current density, showing a reduction in capacitance with increasing current density. This decrease is attributed to insufficient time for electrolyte ions to penetrate the electrode channels and utilize all surface areas at higher current densities. Consequently, the charge storage and capacitance of the supercapacitor are primarily determined by the number of large micropores in the electrode [391, 392]. The RGO/CS film on PET exhibits a specific capacitance of 186.64$\pm$21.69 F g^{-1} at a current density of 1 A g^{-1} (191.07$\pm$19.24 F g^{-1} at 5 mVs^{-1}), which is lower than that achieved with a stainless-steel substrate (872.74$\pm$68.35 F g^{-}

^{1} at 5 mV s^{-1} or 751.91 ± 112.26 F g^{-1} at 1 A g^{-1}). Stainless steel, being highly conductive, offers superior electrical conductivity and potentially lower resistance compared to PET [124]. Its rigid nature and higher surface energy likely promote better adhesion and uniformity of the electrode compared to the flexible, potentially less adhesive surface of PET, particularly towards the RGO/CS composite electrode [150]. Additionally, stainless steel provides superior mechanical stability and serves as a robust support for the electrodes, ensuring structural integrity throughout charge/discharge cycles. This stability facilitates uniform adhesion of the RGO/CS composite material and promotes efficient charge transfer, ultimately enhancing overall durability and electrochemical performance [119, 120, 151]. In contrast, PET, being more flexible, may undergo deformation or structural changes that could affect performance.
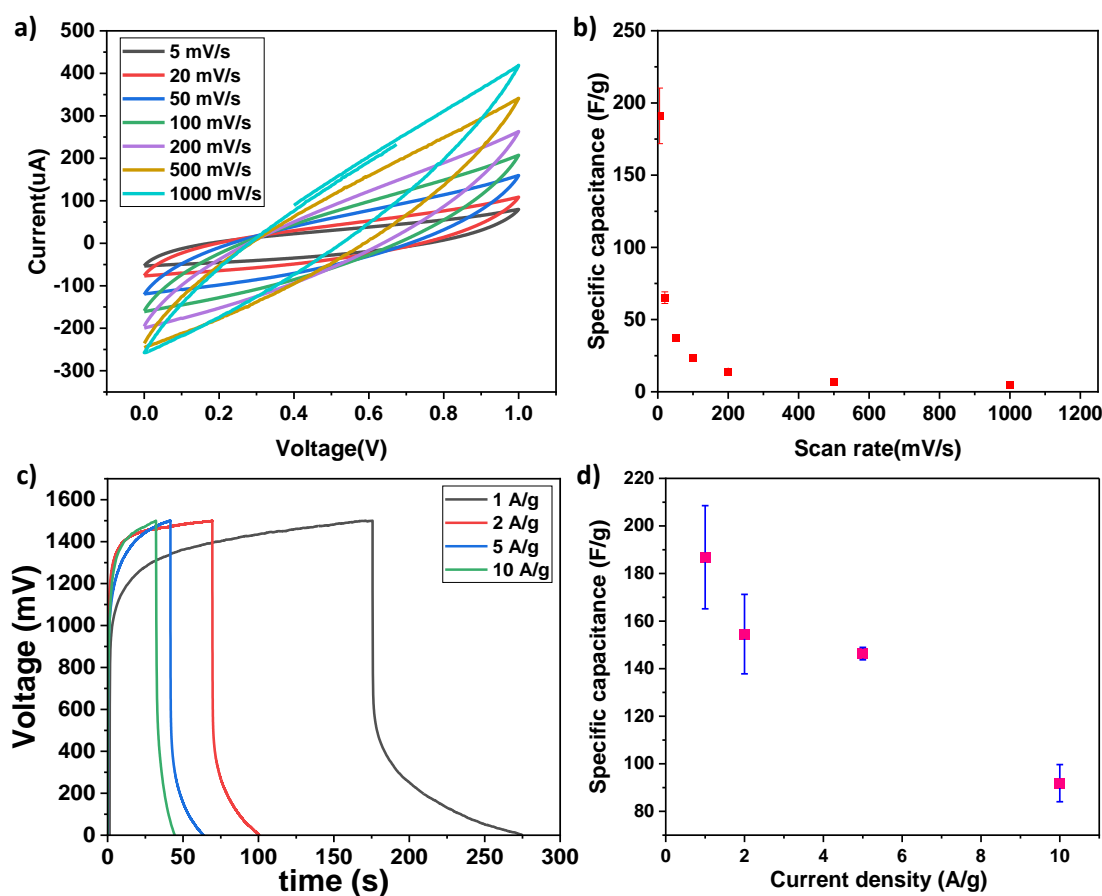
Figure 6.29. Electrochemical performance of flexible solid-state supercapacitor based on reduced graphene oxide/chitosan (RGO/CS, w/w: 90/10) film on PET substrate, a) Cyclic voltammetry (CV) at different scan rates, b) Specific capacitance versus scan rate (mV s^{-1}), c) Galvanostatic charge-discharge (GCD) at different current densities, d) Specific capacitance versus current density (A g^{-1}), (GPE: PVA/KCl, M$_w$=195000 g mol^{-1}, w/w:1/2).

6.7. Cell viability test

To assess the biocompatibility of the RGO/CS electrode material and PVA/KCl gel electrolyte, cytotoxicity studies were conducted using HeLa cells as the test subject, as depicted in Figure 6.30. The cell viability test conducted on the PVA/KCl gel electrolyte yielded a viability rate of 72.3% relative to control samples following a 72 h exposure. This rate stands as an indication of the proportion of cells that remained viable and unaffected by the presence of PVA/KCl in the culture environment. It serves as a critical gauge of the material's compatibility with living cells [364, 393]. A viability rate of 72.3% suggests that a substantial majority of cells maintained their metabolic activity and overall health during the 72-hour incubation period in the presence of PVA/KCl. A cell viability rate of 72.3% observed for PVA/KCl can be considered as moderate. However, the assessment of whether this percentage is deemed "favorable" or not depends on the context and intended application. In the realm of cell viability tests, a higher percentage of cell viability is generally favored, ideally nearing 100%, as it signifies the well-being of cells in the presence of the evaluated material.

In evaluating the cell viability of the RGO/CS composite, the results showcased a viability rate of 76.4% after 72 h. The recorded cell viability of 76.4% indicates that a notable fraction of cells retained their vitality and well-being post-exposure to the RGO/CS electrode. While this value falls short of the ideal 100% viability, it still indicates a significant degree of biocompatibility. Essentially, the composite material, comprising RGO and chitosan components, did not induce considerable detrimental effects on the cells during the 72-h test period which is consistent with the literatures [12, 364, 394].
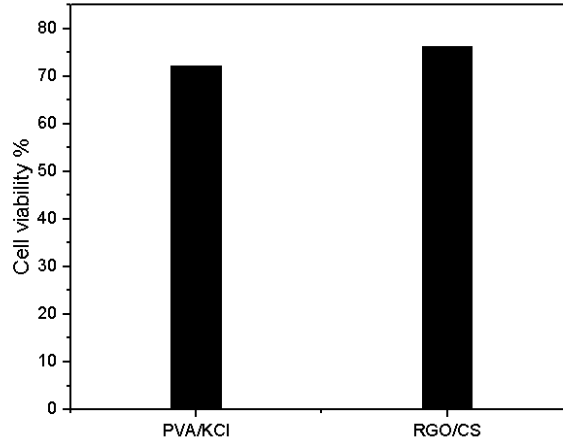
Figure 6.30. Cell viability after 72-h incubation with PVA/KCl gel polymer electrolyte and RGO/CS electrode.

6.8. Electrochemical stability of the solid-state supercapacitors based on RGO/CS

Typically, the voltage window for a solid-state supercapacitor is determined by the range within which the electrode and electrolyte materials can effectively operate without undergoing undesirable reactions [14]. Moreover, the selection of a specific voltage window for a supercapacitor is often a balance between maximizing energy storage and ensuring the stability and longevity of the device components [15]. Cyclic voltammetry measures the current response while sweeping the voltage linearly. It provides information about the capacitive and Faradic processes occurring during both the oxidation and reduction cycles. The CV curve is a plot of current against voltage and reflects the dynamic electrochemical behavior [285]. Galvanostatic charge/discharge applies a constant current and measures the resulting voltage changes over time. It offers insights into the capacitance, energy storage, and relaxation behaviors of the supercapacitor. The GCD curve typically shows the voltage response as a function of time during charge and discharge process [395]. It is common for the voltage window to slightly differ between CV and GCD tests due to the different experimental setups and techniques. In CV, the voltage window is defined by the upper and lower limits of the applied voltage during the cyclic scan. However, in GCD, the voltage window is influenced by the duration of charge and discharge, and the voltage may naturally extend beyond the defined window during certain stages of the process [396, 397].

In CV test, for RGO/CS solid-state supercapacitor, the suitable voltage range as electrochemical stability window was 0-1V. By increasing the voltage to 1.5V, the shape of the CV curve was changed. Expanding the voltage range might introduce additional redox reactions or alter the kinetics of existing reactions, affecting the shape of the CV curve. The involvement of Faradic reactions, where electrons are transferred between the electrode and electrolyte, causing chemical changes. This can introduce peaks or features in the CV curve that are not present in a purely capacitive behavior [398, 399].

In GCD test, for RGO/CS solid-state supercapacitor, the suitable voltage range as electrochemical stability window was 0-1.5V. Firstly, increasing the voltage window provides higher energy density for a supercapacitor. Therefore, in GCD, the voltage window was increased to 1.5V and provides a normal triangular shape indicates a predominantly capacitive behavior, where the charge/discharge process is primarily governed by the electrostatic storage of ions in the electric double layer [400, 401].

The voltage window range developed for the solid-state supercapacitor in this thesis. exhibited a specific capacitance of 872.74 ± 68.35 Fg^{-1} at 5 mV s^{-1} (751.91 ± 112.26 F g^{-1} at 1 A g^{-1}), energy density of 234.97 Wh kg^{-1} and a power density of 1499.98 W kg^{-1} at 1 Ag^{-1}, and maintained 87.31% of its initial capacitance after 10,000 cycles which is a common and reasonable range for many applications, especially in electronic devices.

Consumer electronics such as smartphones, tablets, and laptops where rapid charge/discharge are essential [402]. Medical devices such as implantable medical devices, portable diagnostic equipment, or wearable health monitoring device that require compact and efficient power sources [403]. Aerospace applications that supercapacitors can be used in aerospace for applications like satellite systems, unmanned aerial vehicles (UAVs), or space probes [404]. Thus, before deployment the supercapacitor in specific applications, it is crucial to conduct further testing and validation under conditions relevant to the intended use. Consider factors such as operating environment, size constraints, and safety requirements. Additionally, compliance with industry standards and regulations is essential, especially for applications in consumer electronics and medical devices [405, 406].

For instance, Maxwell Company is one of the biggest company of supercapacitors manufacturing in the world. Maxwell Technologies pioneered the design, development and deployment of ultra-capacitor energy storage technology to address the energy gap for fast-response, high power delivery solutions. Their latest achievement includes the development of a supercapacitor boasting a 3V voltage window and a capacitance of 540F. This addition to Maxwell's comprehensive range of energy storage solutions is specifically engineered to support the evolving needs of various sectors, including renewable energy, wind turbine pitch control systems, small UPS systems, consumer electronics, industrial equipment, and medical devices [407].

Therefore, the biocompatible solid-state supercapacitor developed in this thesis, utilizing RGO/CS electrodes and PVA/KCl gel electrolyte, holds promise for implantable biomedical devices. The operational voltage range aligns with safety standards, ensuring patient well-being and device functionality. Its low-voltage operation coupled with high electrochemical performance mitigates potential safety hazards and enhances compatibility with biological tissues. Collaboration with biomedical engineering experts and adherence to medical device regulations are imperative for designing and implementing solid-state supercapacitors for implantable biomedical devices, prioritizing patient safety and welfare above all else.

6.9. Fabrication of flexible solid-state supercapacitors through laser 3D-priting method

A 3D printer is a highly versatile fabrication machine capable of transforming software designs into physical objects. One of its key advantages is the ability to produce objects with intricate geometries without the need for specialized fabrication tools. Laser 3D printing, also known as stereolithography, is a common manufacturing method used in 3D printing, where a laser source plays a central role in the fabrication process [408, 409]. This technique was pioneered in the mid-1980s by Dr. Carl Deckard and Dr. Joe Beaman at the University of Texas at Austin and has since been adapted to work with a wide range of materials, including plastics, metals, glass, ceramics, and various composite material powders [409-411].

Laser 3D-printing offers several advantages over conventional methods for preparing a solid-state supercapacitor such as high precision and control of electrode fabrication, enabling the deposition of complex and customized electrode designs with high accuracy

and reproducibility [412, 413]. Laser printing can be used to create electrodes on various substrates, including flexible and transparent materials, expanding the range of potential applications. The additive manufacturing process of laser printing is highly efficient and scalable, enabling rapid prototyping and production of supercapacitors with minimal material waste and cost [414, 415]. Furthermore, laser printing eliminates the need for multiple processing steps, such as masking and etching, required in conventional lithography-based methods, streamlining the fabrication process and reducing production time and costs [412].

In the context of this thesis, a flexible solid-state supercapacitor based on RGO/CS (w/w: 90/10) as electrode materials and PVA/KCl as gel electrolyte (Mw=195000 g mol^{-1}, PVA/KCl w/w: 1/2) was developed using laser 3D-printing technology as an additive manufacturing method. The preparation of the flexible solid-state supercapacitor, termed micro-supercapacitors, is outlined in Scheme 6.7. Initially, a film of GO/CS (w/w: 90/10) was coated on the polyimide (PI)-based Kapton® substrate with a thickness of 125 μm and allowed to dry at room temperature. Subsequently, a laser beam was directed over the surface to create the desired hair comb pattern, selectively irradiating certain areas to induce solidification while avoiding others.
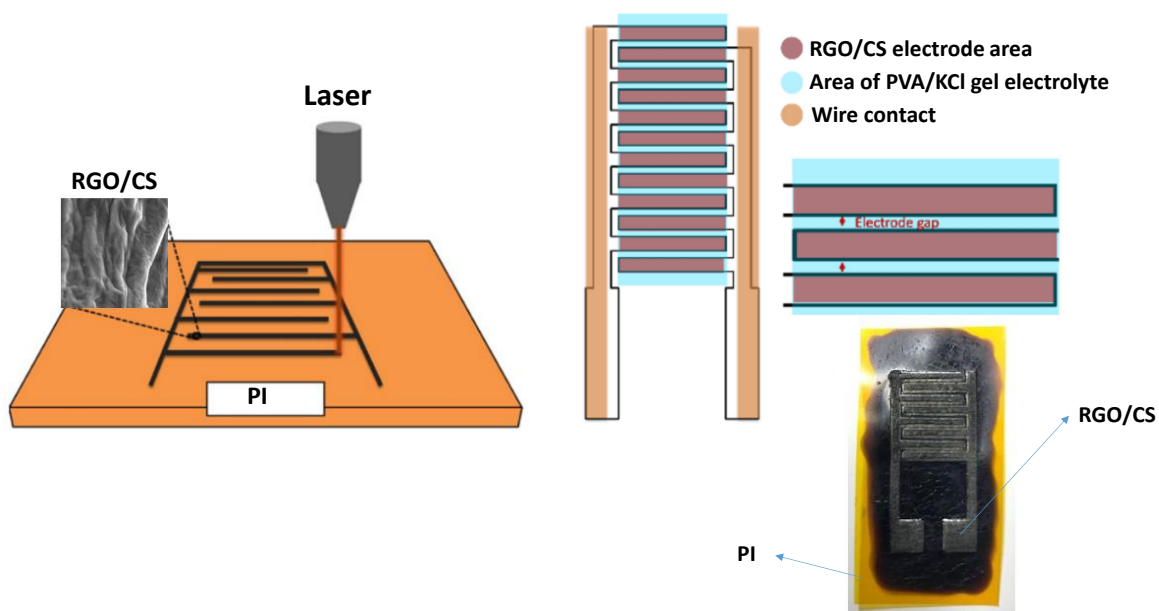
Scheme 6.7. Preparation of a flexible solid-state supercapacitor based on RGO/CS through laser 3D-printing technology.

The hair comb-like pattern created by laser 3D-printing as electrodes offers several benefits, including a higher surface area, which provides more active sites for electrochemical reactions, ultimately enhancing the electrode's capacitance and energy storage capacity [414, 415]. Additionally, this pattern promotes improved contact and interaction between the electrode and electrolyte, facilitating ion diffusion and reducing resistance at the interface, thereby improving charge/discharge kinetics [412, 413].

Therefore, among the various 3D-printing technologies, laser printing stands out for its high precision and resolution, enabling the creation of intricate patterns with fine details. This precision is essential for designing complex electrode structures to optimize the performance of supercapacitors [416, 417]. The selective heating process in laser printing allows for controlled reduction of graphene oxide to graphene, ensuring desired electrical properties [5, 247]. Compared to conventional printing or lithographic techniques, laser printing offers more flexibility in patterning. Additionally, laser sintering is more material-efficient, as it reduces waste by focusing energy only where necessary, promoting cost-effectiveness and sustainability [418]. Moreover, the localized high temperatures achieved in laser printing facilitate strong bonding between graphene layers, resulting in electrodes with enhanced mechanical strength and electrical conductivity [419].

In this thesis, the interdigital RGO/CS electrodes exhibited a hair comb formation, featuring 8 branches measuring 7.5×0.8 mm, evenly distributed on each bar of the comb. Laser parameters included a scanning speed of 200 mm min^{-1} and a laser power of 2500 W, with a lens-to-substrate distance of 55 mm. Manufacturing occurred at room temperature and in ambient air. The resultant flat active electrode structure was then coated with a thin layer of PVA/KCl gel electrolyte (Mw=195000 g mol^{-1}, w/w: 1/2). Copper wires were subsequently attached to the electrodes using silver glue for electrochemical testing.

The RGO/CS composite exhibited excellent adhesive properties and durability on the PI surface. However, attempts to remove the remaining un-patterned RGO/CS electrodes from the PI surface using solvents such as acetic acid, acetone, ethanol, and 2-propanol were unsuccessful. These un-patterned areas pose a risk of short-circuiting when connected to the electrochemical tests using wires. Therefore, addressing this challenge requires further

investigation to identify the best material or method for removing these areas to enable successful electrochemical testing.

Consequently, further improvement is needed in the mechanical properties and substrate preparation procedure to ensure that the electrical response remains unchanged under mechanical loading. A more effective method for measuring mechanical flexibility and characterizing electrode material and gel electrolyte features during mechanical deformation is required. Additionally, for printing techniques, more research is necessary to engineer the formulations of printing inks and protocols to enhance cost-effective fabrication, improve printing resolution, and make methods more environmentally friendly.

Sustainability is becoming increasingly important in materials studies. The RGO/CS electrodes and PVA/KCl gel polymer electrolyte developed in this thesis are eco-friendly, biocompatible materials, and the low-cost manufacturing methods can be utilized for the fabrication of flexible micro-supercapacitors. Moreover, the structure of RGO/CS composite provides excellent electrical conductivity and active sites for ion accumulation. The developed PVA/KCl gel electrolyte exhibits excellent ionic conductivity, thermal stability, and higher cycling stability, enhancing the energy and power density of the micro-supercapacitors and reducing the internal resistance between electrode and electrolyte. In conclusion, although our systems show promising potential in harnessing 3D laser printing technology for micro-supercapacitor production, it is imperative to tackle current limitations and obstacles to fully capitalize on the promise offered by RGO/CS composites and PVA/KCl gel electrolytes in energy storage applications using 3D laser printing.

7. CONCLUSIONS

In conclusion, this PhD thesis highlights the significant progress made in the development of all-solid-state supercapacitors for biomedical applications. Gel polymer electrolytes (GPEs), particularly those based on polyvinyl alcohol (PVA) and potassium chloride (KCl), have emerged as promising candidates due to their versatility, lightweight nature, ease of production, strong adhesion, and wide potential window.

The primary objective of this doctoral study was to design high-performance solid-state supercapacitors utilizing graphene oxide/chitosan (GO/CS) electrodes and PVA/KCl gel polymer electrolytes. The optimization of key gel electrolyte properties, such as ionic conductivity, film formation, thermal behavior, and biocompatibility, was a focal point. By systematically investigating the influence of KCl concentration and polymer molecular weight (Mw) on ionic conductivity, this research achieved gel electrolytes with high ionic conductivity, thermal stability, mechanical resilience, and flexibility—attributes essential for flexible supercapacitor applications.

Moreover, the development of symmetric fiber and film-shaped solid-state supercapacitors employing GO/CS composite electrodes and PVA/KCl gel polymer electrolytes demonstrated a synergistic enhancement in performance. This integrated approach may open new avenues for enhanced feasibility and efficacy of solid-state supercapacitor systems, representing significant progress in energy storage for biomedical applications.

The main results obtained in this PhD thesis are summarized as follows:

- For evaluation the structural properties of the gel electrolyte, the ATR-FTIR, UV-VIS, XRD, DMTA, FE-SEM and Tensile mechanical tests were done. The XRD result shows that gel electrolyte possesses a semi-crystalline structure with both crystalline and amorphous regions. The presence of KCl may contribute to an expansion in free volume, allowing for a slight enhancement in crystal growth, enhancing polymer chain segmental motions within the amorphous structure promotes ion movement and contributes to elevated ionic conductivity levels.

- The blue shift in UV-Vis spectra of the gel electrolyte suggests a reduction in hydrogen bonding among PVA chains, likely resulting from interactions between K^+/Cl^- ions and the polar groups within PVA and confirms the formation of complexes between PVA and KCl.

- The ATR-FTIR spectrum result of gel film indicates that the stretching vibrations of -OH and -CO groups experience significant modifications, with a decrease in peak intensity and a red-shift compared to pure PVA. These alterations strongly suggest the formation of complexes or interactions between the KCl and the polar groups in PVA (-OH and –CO). The increased segmental mobility of polymer chains within the amorphous phase promotes ion mobility, thus supporting higher ionic conductivity.

- PVA is a semi-crystalline polymer with a higher tensile strength (68.5±5.35 MPa) compared to the PVA/KCl gel film specimen (15.88±0.25 MPa). KCl salt acts as a plasticizer and weakens the bonds between polymer chains at the molecular level. The lower Young modulus and elastic strength of the gel film suggest a more flexible and deformable nature compared to pure PVA.

- The DMA result showed that the introduction of a small amount of KCl to PVA leads to an increase in the elastic modulus, indicating a higher deformation resistance of the gel. This could be attributed to both a reinforcement effect within this temperature range and the formation of interactions between PVA chains and KCl salt. Moreover, the addition of KCl results in a reduction in T_g and a shift in the tanδ peak to lower temperature, indicative of reduced restrictions to the cooperative motion of the PVA chains segmental movement. This behavior can result from an increase in the mobility of the amorphous PVA molecules caused by the weak intermolecular hydrogen bonds between PVA chains.

- The surface morphology and microstructure of the PVA/KCl sample by FE-SEM test highlights the uniform distribution of potassium chloride particles throughout the PVA matrix, indicating good compatibility and interaction between PVA and KCl. The EDAX and mapping results suggest that the gel sample is in high-purity condition and good spatial distributions of C, O, K, Cl elements in pure polymer sample.

- The GPE with a M_w=195000 g mol^{-1} and PVA/KCl (w/w: 1/2) has the greatest ionic conductivity of 3.48 ±0.25 mS cm^{-1} and maintains 88% of its initial capacitance after

5000 cycles. Moreover, the gel electrolyte exhibited exceptional biocompatibility, evident in a cell viability test where 72.3% of cells remained unaffected after 72 h of exposure to PVA/KCl gel. The results also highlight the potential of these gel electrolytes in enhancing the safety and longevity of supercapacitors, due to their reduced likelihood of leakage compared to liquid electrolytes.

- The electrochemical properties of GO/CS fiber and film electrodes were evaluated by CV, EIS, and GCD tests. The result of CV test for RGO/CS fiber composite with different GO/CS weight ratios exhibits a larger enclosed area within the CV curve compared to RGO, demonstrating its remarkably high specific capacitance that arises from the synergistic interplay of both EDLC and pseudocapacitive behavior. At an optimum concentration of chitosan, the supercapacitor containing RGO/CS fiber (w/w: 90/10) showed the highest specific capacitance of 523.06 ± 53.57 F g^{-1} at scan rate of 5 mV s^{-1} (405.26 ± 1.44 F g^{-1} at 1 A g^{-1}). The utilization of RGO as an electrode component demonstrated exceptional electrochemical properties, with high surface area and excellent electrical conductivity leading to impressive specific capacitance and rapid charge-discharge rates. Furthermore, the incorporation of chitosan, renowned for its biocompatibility and eco-friendly attributes, into the RGO matrix yielded enhancements in mechanical robustness and ion diffusion kinetics. Thus, chitosan effectively prevents re-stacking of GO nanosheets and provides high specific surface area and high conductivity, thus leading to excellent energy storage performance.

- In particular, the RGO/CS film-based solid-state supercapacitor demonstrated a high specific capacitance of 872.75 ± 68.35 F g^{-1} at 5 mVs^{-1} (751.91 ± 112.26 F g^{-1} at 1 A g^{-1}) compared to fiber type electrodes, which is among the highest values achieved for any type of solid-state supercapacitors. This may be attributed to variations in the material's surface area, porosity, and accessibility of active sites. Films often provide a larger surface area, more active sites for electrochemical reactions, and better accessibility of electrolyte ions to the electrode surface compared to fiber, leading to higher specific capacitance. Additionally, the film structure may offer improved electron and ion transport within the electrode, better porous structure, and potentially of flexibility, contributing to enhanced electrochemical performance.

- The result of GCD test for film-based solid-state supercapacitor shows that the discharge curve is nearly a straight line, exhibits quick and short current response times, meaning a good electric double layer (EDL) performance.

- The result of EIS test for film-based solid-state supercapacitor exhibits that the charge transfer resistance (Rct) and ionic resistance of electrolyte (Rs) values of the RGO/CS electrode are much lower than RGO, this is owing to the intrinsic high ionic conductivity and fast electron transfers in the system.

- In evaluating the cell viability of the RGO/CS film composite, the results showed a viability rate of 76.4% after 72 hours. The recorded cell viability of 76.4% indicates that a significant proportion of cells maintained their viability and well-being after exposure to the RGO/CS electrode. The film composite electrode retained 87.31% of its initial capacitance even after undergoing 10,000 cycles. The symmetrical solid-state supercapacitor exhibits excellent energy and power densities of 234.97 W h kg^{-1} and 1499.98 kW kg^{-1}, respectively.

- Additionally, the structural properties of GO/CS film sample were studied using ATR-FTIR, UV-Vis, XRD, XPS, AFM, POM, TEM, BET, FE-SEM, Electrical conductivity, and Tensile mechanical tests. In the ATR-FTIR spectrum of RGO/CS, it's noteworthy that the intensity of O-H stretching, and C-O stretching was lower compared to the GO/CS spectrum, indicating the reduction of GO to RGO. Subtle shifts in peaks were observed, possibly attributable to hydrogen bonds among composite components. Additionally, the presence of RGO in the composite was indicated by the peak found at 1048 cm^{-1} in the RGO/CS spectrum.

- The result of UV-Vis spectrum of RGO/CS reveals that there is a red-shift in peaks. This change is attributed to the partial restoration of electronic conjugation among aromatic carbon atoms, suggesting that chitosan becomes conjugated with GO after reduction.

- The comparison of XRD results and d-spacing of RGO, CS, RGO/CS confirms that the presence of chitosan might influence the stacking and arrangement of RGO layers, leading to changes in the d-spacing compared to pure RGO in RGO/CS composite, indicating the existence of an interaction or a specific arrangement of RGO and chitosan layers in the composite structure.

- The C1s spectrum of GO exhibits multiple peaks at 284.9 eV, 285.3 eV, 286.0 eV, 287.5 eV, and 288.6 eV are attributed to carbon sp^2 (C=C), C-C/C-H sp^3, epoxy/hydroxyl, C=O, and carboxylates (O-C=O) species, respectively. Chitosan manifests specific carbon species in its C1s spectrum, including C-C, C=O, and O-C=O moieties at 283.39, 284.94, and 286.56 eV, respectively. The XPS result of the composites containing chitosan and either RGO or GO reflect the spectral features characteristic of both constituent materials. Importantly, the composite containing GO exhibits higher intensities of oxygenated carbon species compared to the one containing RGO.

- In the AFM images of GO, a clear visualization of the individual layers of GO sheets are observed. The GO/CS displays a heterogeneous surface marked by regions of varying roughness, a characteristic likely attributed to the coexistence of GO sheets and CS particles.

- Polarized optical microscopy (POM) indicates the ability of GO to self-assemble into ordered liquid crystalline (LC) structure in a liquid medium. The lyotropic nematic LCs of GO clearly indicate local orientation of the GO sheets in the aqueous media in the form of the large area of Schlieren texture. The formation of LC textures of GO/CS composite occurred by their supramolecular self-ordering into ordered layers through the interaction between the oxygen and amide functional groups, which displayed the layered architectures, in line with the formation of ordered clusters of chitosan.

- The TEM images reveal distinct characteristics of the graphene oxide (GO) and reduced graphene oxide (RGO) sheets. The GO sheets exhibit single-layer structures with smooth and flattened surfaces, typical of oxidized exfoliated GO sheets, while RGO nanosheets tend to aggregate post-reduction, resulting in smoother and more condensed appearances. The GO/chitosan (GO/CS) composite displays a rougher surface with a higher density, indicating successful assembly of chitosan onto the GO layers. Following reduction, the RGO/CS surface appears rough and decorated, attributed to the chitosan coating, with chitosan contributing to the dispersion of RGO nanosheets, facilitating their well-dispersion.

- The FE-SEM images of GO-chitosan film exhibits a distinctive "sandwich" configuration. The image demonstrates that a significant portion of the GO

nanosheets were fully exfoliated and uniformly dispersed within the chitosan matrix. The RGO/CS composites images show the presence of graphene dispersed within chitosan, exhibiting irregularly wrinkled and sheet-like structures. The RGO sheets appear as interconnected layers or flakes, featuring a surface morphology marked by crumpling or folding. The results of EDAX-Mapping GO/CS samples shows an elevated proportion of oxygen content, confirming the continued presence of unreduced graphene oxide, as well as regions with elevated nitrogen levels signifying chitosan domains. In RGO/CS, there are areas with higher carbon concentrations related to RGO. In contrast, regions with reduced carbon concentration indicate the prevalence of chitosan.

- The tensile properties of RGO and GO film show that for the neat GO, the Young's modulus, and tensile strength are 15.04±4.15 MPa and 2.62±0.77 MPa, respectively. For RGO, the Young's modulus and tensile strength indicate an increment of 25% and 46% compared to GO, respectively. Therefore, the reduction process of GO reduces oxygen-containing functional groups in GO, leading to the restoration of a more sp^2 carbon network, resembling pristine graphene, resulting in enhanced mechanical properties. In comparison to GO and RGO, the GO/CS and RGO/CS composites show 46% and 36% increment in Young's modulus and 61% and 64% growth in tensile strength, respectively. The toughness (area under stress-strain curve) of neat GO film is 184.45±54.17 mJ m^{-3}. The GO/CS and RGO/CS nanocomposites exhibit toughening effects as high as 80%. This suggests enhanced stiffness and structural integrity, possibly due to the synergistic effects of RGO and chitosan.

- Brunauer-Emmett-Teller (BET) analysis was conducted to determine the specific surface area, total pore volume, and pore diameter of CS, RGO, and RGO/CS samples. According to the classification by BDDT IUPAC classification, the adsorption-desorption isotherm graphs of RGO/CS nanocomposite tended to follow type IV with the specific flow of the hysteresis loop for mesoporous material. The BET characteristics of the RGO/CS nanocomposite falls within the range observed for RGO, indicating that the addition of chitosan did not significantly alter the high surface area (13.672 m^2 g^{-1}), adsorption capacity, and porous structure, suggesting that chitosan may act as a scaffold or binder for RGO (synergistic effects), potentially enhancing its mechanical stability, reducing the risk of structural degradation during

charge-discharge cycles and facilitating the ion diffusion and charge transfer at the electrode-electrolyte interface.

- The electrical conductivity results indicate that RGO (1.10×10^{-4} S/cm) has the higher electrical conductivity compared to GO (6.89×10^{-5} S/cm) that can be attributed to the thermal reduction process which reduces the band-gap, allowing for better charge carrier mobility and higher electrical conductivity. RGO/CS composite has higher electrical conductivity (2.62×10^{-3} S/cm) than RGO which is due to the synergistic effect of RGO and CS. The conductive nature of RGO complements the insulating nature of CS, resulting in a composite with improved overall conductivity.

- A flexible solid-state supercapacitor based on RGO/CS (w/w: 90/10) and PVA/KCl gel electrolyte (Mw=195000 g/mol, PVA/KCl (w/w:1/2)) was fabricated using PET as a flexible current collector substrate. The specific capacitance value is 191.07 ± 19.24 F g^{-1} at 5 mVs^{-1} (186.64 ± 21.69 F g^{-1} at 1 A g^{-1}), and this value is lower than that of the stainless steel substrate. Stainless steel is a conductive mateial, providing better electrical conductivity and potentially lower resistance compared to PET. The adhesion of the RGO/CS electrode to the current collector is crucial and stainless steel, being a rigid and smooth surface, might provide better adhesion and uniformity of the electrode compared to PET, which is flexible and may have a less smooth surface. Moreover, stainless steel offers better mechanical stability and support for the electrode, maintaining structural integrity during charge/discharge cycles, but PET, being more flexible, might experience deformation or structural changes that could impact performance. Therefore, the stable platform for uniform adhesion of RO/CS composite material to stainless steel surface and good electricity conductor of stainless steel which is beneficial for efficient charge transfer and overall excellent durability and electrochemical performance.

- A flexible solid-state supercapacitor based on RGO/CS (w/w: 90/10) and PVA/KCl gel electrolyte (Mw=195000 g mol^{-1}, PVA/KCl (w/w:1/2)) was fabricated using laser 3D-printing technology on polyimide (PI) film. The interdigital RGO/CS electrodes displayed a hair comb formation and showed an outstanding adhesive properties and durability.

In conclusion, the film-based electrode structures derived from environmentally friendly polymers present a compelling alternative for supercapacitor applications. Their exceptional electrochemical performance, coupled with mechanical, thermal stability, and biocompatibility properties, underscore their potential significance. These findings offer a promising route towards the development of stable and high-performance electrode materials and gel polymer electrolytes, laying the foundation for next-generation energy storage devices. These advancements hold promise for flexible, safer, and wearable biomedical applications, offering enhanced energy density and cycling stabilities.

8. REFERENCES

[1] A. Borenstein, O. Hanna, R. Attias, S. Luski, T. Brousse, D. Aurbach, Carbon-based composite materials for supercapacitor electrodes: a review, Journal of Materials Chemistry A 5(25) (2017) 12653-12672, https://doi.org/10.1039/C7TA00863E.

[2] J. Yan, T. Wei, B. Shao, F. Ma, Z. Fan, M. Zhang, C. Zheng, Y. Shang, W. Qian, F. Wei, Electrochemical properties of graphene nanosheet/carbon black composites as electrodes for supercapacitors, Carbon 48(6) (2010) 1731-1737, https://doi.org/10.1016/j.carbon.2010.01.014.

[3] S. Vivekchand, C.S. Rout, K. Subrahmanyam, A. Govindaraj, C.N.R. Rao, Graphene-based electrochemical supercapacitors, Journal of Chemical Sciences 120(1) (2008) 9-13, https://doi.org/10.1007/s12039-008-0002-7.

[4] S. Naficy, R. Jalili, S.H. Aboutalebi, R.A. Gorkin III, K. Konstantinov, P.C. Innis, G.M. Spinks, P. Poulin, G.G. Wallace, Graphene oxide dispersions: tuning rheology to enable fabrication, Materials Horizons 1(3) (2014) 326-331, https://doi.org/10.1039/c3mh00144j.

[5] M.F. El-Kady, R.B. Kaner, Scalable fabrication of high-power graphene micro-supercapacitors for flexible and on-chip energy storage, Nature communications 4(1) (2013) 1475, https://doi.org/10.1038/ncomms2446.

[6] J.S. Chae, N.-S. Heo, C.H. Kwak, W.-S. Cho, G.H. Seol, W.-S. Yoon, H.-K. Kim, D.J. Fray, A.E. Vilian, Y.-K. Han, A biocompatible implant electrode capable of operating in body fluids for energy storage devices, Nano Energy 34 (2017) 86-92, https://doi.org/10.1016/j.nanoen.2017.02.018.

[7] A. Drabczyk, S. Kudłacik-Kramarczyk, M. Głąb, M. Kędzierska, A. Jaromin, D. Mierzwiński, B. Tyliszczak, Physicochemical investigations of chitosan-based hydrogels containing Aloe Vera designed for biomedical use, Materials 13(14) (2020) 3073, https://doi.org/10.3390/ma13143073.

[8] M. Chelu, A.M. Musuc, Polymer gels: Classification and recent developments in biomedical applications, Gels 9(2) (2023) 161, https://doi.org/10.3390/gels9020161.

[9] P.-P. Zuo, H.-F. Feng, Z.-Z. Xu, L.-F. Zhang, Y.-L. Zhang, W. Xia, W.-Q. Zhang, Fabrication of biocompatible and mechanically reinforced graphene oxide-chitosan nanocomposite films, Chemistry Central Journal 7 (2013) 1-11, https://doi.org/10.1186/1752-153X-7-39.

[10] S. He, Y. Hu, J. Wan, Q. Gao, Y. Wang, S. Xie, L. Qiu, C. Wang, G. Zheng, B. Wang, Biocompatible carbon nanotube fibers for implantable supercapacitors, Carbon 122 (2017) 162-167, https://doi.org/10.1016/j.carbon.2017.06.053.

[11] H.J. Sim, C. Choi, D.Y. Lee, H. Kim, J.-H. Yun, J.M. Kim, T.M. Kang, R. Ovalle, R.H. Baughman, C.W. Kee, Biomolecule based fiber supercapacitor for implantable device, Nano Energy 47 (2018) 385-392, https://doi.org/10.1016/j.nanoen.2018.03.011.

[12] S. Chakraborty, N. Mary, Biocompatible supercapacitor electrodes using green synthesised ZnO/Polymer nanocomposites for efficient energy storage applications, Journal of Energy Storage 28 (2020) 101275, https://doi.org/10.1016/j.est.2020.101275.

[13] X. Lu, M. Yu, G. Wang, Y. Tong, Y. Li, Flexible solid-state supercapacitors: design, fabrication and applications, Energy & Environmental Science 7(7) (2014) 2160-2181, https://doi.org/10.1039/C4EE00960F.

[14] C. Zhong, Y. Deng, W. Hu, J. Qiao, L. Zhang, J. Zhang, A review of electrolyte materials and compositions for electrochemical supercapacitors, Chemical Society Reviews 44(21) (2015) 7484-7539, https://doi.org/10.1039/C5CS00303B.

[15] S. Alipoori, S. Mazinani, S.H. Aboutalebi, F. Sharif, Review of PVA-based gel polymer electrolytes in flexible solid-state supercapacitors: Opportunities and challenges, Journal of Energy Storage 27 (2020) 101072, https://doi.org/10.1016/j.est.2019.101072.

[16] R. Dubey, V. Guruviah, Review of carbon-based electrode materials for supercapacitor energy storage, Ionics 25(4) (2019) 1419-1445, https://doi.org/10.1007/s11581-019-02874-0.

[17] S.H. Aboutalebi, R. Jalili, D. Esrafilzadeh, M. Salari, Z. Gholamvand, S. Aminorroaya Yamini, K. Konstantinov, R.L. Shepherd, J. Chen, S.E. Moulton, High-performance multifunctional graphene yarns: toward wearable all-carbon energy storage textiles, ACS nano 8(3) (2014) 2456-2466, https://doi.org/10.1021/nn406026z.

[18] X. Chen, R. Paul, L. Dai, Carbon-based supercapacitors for efficient energy storage, National Science Review 4(3) (2017) 453-489, https://doi.org/10.1093/nsr/nwx009.

[19] X. Yang, F. Zhang, L. Zhang, T. Zhang, Y. Huang, Y. Chen, A high-performance graphene oxide-doped ion gel as gel polymer electrolyte for all-solid-state supercapacitor applications, Advanced Functional Materials 23(26) (2013) 3353-3360, https://doi.org/10.1002/adfm.201203556.

[20] Y. Kumar, G. Pandey, S. Hashmi, Gel polymer electrolyte based electrical double layer capacitors: comparative study with multiwalled carbon nanotubes and activated carbon electrodes, The Journal of Physical Chemistry C 116(50) (2012) 26118-26127, https://doi.org/10.1021/jp305128z.

[21] G. Prajapati, R. Roshan, P. Gupta, Effect of plasticizer on ionic transport and dielectric properties of PVA–H3PO4 proton conducting polymeric electrolytes, Journal of Physics and Chemistry of Solids 71(12) (2010) 1717-1723, https://doi.org/10.1016/j.jpcs.2010.08.023.

[22] J. Xi, X. Qiu, J. Li, X. Tang, W. Zhu, L. Chen, PVDF–PEO blends based microporous polymer electrolyte: effect of PEO on pore configurations and ionic conductivity, Journal of power sources 157(1) (2006) 501-506, https://doi.org/10.1016/j.jpowsour.2005.08.009.

[23] S. Klongkan, J. Pumchusak, Effects of nano alumina and plasticizers on morphology, ionic conductivity, thermal and mechanical properties of PEO-LiCF3SO3 solid polymer electrolyte, Electrochimica Acta 161 (2015) 171-176, https://doi.org/10.1016/j.electacta.2015.02.074.

[24] Y. Jayathilake, K. Perera, K. Vidanapathirana, L. Bandara, Ionic conductivity of a PMMA based gel polymer electrolyte and its performance in solid state electrochemical cells, Sri Lankan Journal of Physics 15 (2014) 11-17, http://doi.org/10.4038/sljp.v15i0.6638.

[25] H. Fei, C. Yang, H. Bao, G. Wang, Flexible all-solid-state supercapacitors based on graphene/carbon black nanoparticle film electrodes and cross-linked poly (vinyl alcohol)–H2SO4 porous gel electrolytes, Journal of Power Sources 266 (2014) 488-495, https://doi.org/10.1016/j.jpowsour.2014.05.059.

[26] F.I. M. Rosi, M. Abdullah, Khairurrijal, , Hydrogel-Polymer Electrolytes Based on Polyvinyl Alcohol and Hydroxyethylcellulose for Supercapacitor Applications, International Journal of Electrochemical Science, 9(2014) 4251-6, https://doi.org/10.1016/S1452-3981(23)08089-6.

[27] M. Jiang, J. Zhu, C. Chen, Y. Lu, Y. Ge, X. Zhang, Poly (vinyl alcohol) borate gel polymer electrolytes prepared by electrodeposition and their application in electrochemical supercapacitors, ACS applied materials & interfaces 8(5) (2016) 3473-3481, https://doi.org/10.1021/acsami.5b11984.

[28] T.J. Booth, P. Blake, R.R. Nair, D. Jiang, E.W. Hill, U. Bangert, A. Bleloch, M. Gass, K.S. Novoselov, M.I. Katsnelson, Macroscopic graphene membranes and their extraordinary stiffness, Nano letters 8(8) (2008) 2442-2446, https://doi.org/10.1021/nl801412y.

[29] C. Lee, X. Wei, J.W. Kysar, J. Hone, Measurement of the elastic properties and intrinsic strength of monolayer graphene, science 321(5887) (2008) 385-388, https://doi.org/10.1126/science.1157996.

[30] Z.G. Wu Z-S, Yin L-C, Ren W, Li F, Cheng H-M,, Graphene/metal oxide composite electrode materials for energy storage, (2012) . Nano Energy 1(1):107–131. https://doi.org/10.1016/j.nanoen.2011.11.001.

[31] N. Díez, M. Qiao, J.L. Gómez-Urbano, C. Botas, D. Carriazo, M.M. Titirici, High density graphene–carbon nanosphere films for capacitive energy storage, Journal of Materials Chemistry A 7(11) (2019) 6126-6133, http://doi.org/10.1039/C8TA12050A.

[32] W.B. P. D. R. Dreyer, and R. S. Ruoff, , Graphene-based polymer nanocomposites, Polymer, Volume 52, Issue 1, 7 January 2011, Pages 5-25, https://doi.org/10.1016/j.polymer.2010.11.042.

[33] M. Alhabeb, M. Beidaghi, K.L. Van Aken, B. Dyatkin, Y. Gogotsi, High-density freestanding graphene/carbide-derived carbon film electrodes for electrochemical capacitors, Carbon 118 (2017) 642-649, https://doi.org/10.1016/j.carbon.2017.03.094.

[34] S. William, J. Hummers, R.E. Offeman, Preparation of graphitic oxide, J. Am. Chem. Soc 80(6) (1958) 1339-1339, https://doi.org/10.1021/ja01539a017.

[35] R.K. Singh, R. Kumar, D.P. Singh, Graphene oxide: strategies for synthesis, reduction and frontier applications, Rsc Advances 6(69) (2016) 64993-65011, https://doi.org/10.1039/C6RA07626B.

[36] Y. Wang, Z. Shi, Y. Huang, Y. Ma, C. Wang, M. Chen, Y. Chen, Supercapacitor devices based on graphene materials, The Journal of Physical Chemistry C 113(30) (2009) 13103-13107, https://doi.org/10.1021/jp902214f.

[37] R. Wang, M. Han, Q. Zhao, Z. Ren, X. Guo, C. Xu, N. Hu, L. Lu, Hydrothermal synthesis of nanostructured graphene/polyaniline composites as high-capacitance electrode materials for supercapacitors, Scientific reports 7(1) (2017) 1-9, https://doi.org/10.1038/srep44562.

[38] B. Li, Y. Cheng, L. Dong, Y. Wang, J. Chen, C. Huang, D. Wei, Y. Feng, D. Jia, Y. Zhou, Nitrogen doped and hierarchically porous carbons derived from chitosan hydrogel via rapid microwave carbonization for high-performance supercapacitors, Carbon 122 (2017) 592-603, https://doi.org/10.1016/j.carbon.2017.07.009.

[39] X. He, P. Song, X. Shen, Y. Sun, Z. Ji, H. Zhou, B. Li, Chitosan-assisted synthesis of wearable textile electrodes for high-performance electrochemical

energy storage, Cellulose 26(17) (2019) 9349-9359, https://doi.org/10.1007/s10570-019-02727-z.

[40] P. Hao, Z. Zhao, Y. Leng, J. Tian, Y. Sang, R.I. Boughton, C. Wong, H. Liu, B. Yang, Graphene-based nitrogen self-doped hierarchical porous carbon aerogels derived from chitosan for high performance supercapacitors, Nano Energy 15 (2015) 9-23, https://doi.org/10.1016/j.nanoen.2015.02.035.

[41] B.K. Roy, I. Tahmid, T.U. Rashid, Chitosan-Based Materials for Supercapacitor Application-A Review, J. Mater. Chem. A, 2021,9, 17592-17642, https://doi.org/10.1039/D1TA02997E. (2021).

[42] M. Yuan, Y. Zhang, B. Niu, F. Jiang, X. Yang, M. Li, Chitosan-derived hybrid porous carbon with the novel tangerine pith-like surface as supercapacitor electrode, Journal of Materials Science 54(23) (2019) 14456-14468, https://doi.org/10.1007/s10853-019-03911-z.

[43] Y.-C.C. Jui-Chen Hsin, Meng-Jiy Wang, Cheng-Che Hsu, I-Chun Cheng & Jian-Zhang Chen,, Ar dielectric barrier discharge jet (DBDjet) plasma treatment of reduced graphene oxide (rGO)–polyaniline (PANI)–chitosan (CS) nanocomposite on carbon cloth for supercapacitor application,   Volume 5, pages 134–140, (2020), https://doi.org/10.1007/s40974-019-00131-8.

[44] A. Hany, M. Mousa, T. El-Essawy, Studies on AC electrical conductivity, dielectric properties and ion transport in PVA polymeric electrolytes, Journal of Basic and Environmental Sciences 4 (2017) 298-304, https://doi.org/10.4236/ampc.2015.58029.

[45] C.P. Sugumaran, A flexible, cost-effective, and eco-friendly solid state supercapacitor based on PVA/KCl/Carbon black nanocomposite, Ionics 26(3) (2020) 1465-1473, https://doi.org/10.1007/s11581-019-03307-8.

[46] B. Chatterjee, N. Kulshrestha, P. Gupta, Electrical properties of starch-PVA biodegradable polymer blend, Physica Scripta 90(2) (2015) 025805, https://doi.org/10.1088/0031-8949/90/2/025805.

[47] S. Tellamekala, P. Ojha, G. NO, R. Ch, Effect of K+ ion doping on structural and physical properties of PVA/MAA: EA polymer blend electrolytes, Materials Research Innovations 25(5) (2021) 287-299, https://doi.org/10.1080/14328917.2020.1795336.

[48] S. Alipoori, M. Torkzadeh, M.M. Moghadam, S. Mazinani, S.H. Aboutalebi, F. Sharif, Graphene oxide: An effective ionic conductivity promoter for phosphoric acid-doped poly (vinyl alcohol) gel electrolytes, Polymer 184 (2019) 121908, https://doi.org/10.1016/j.polymer.2019.121908.

[49] C. Zhao, C. Wang, Z. Yue, K. Shu, G.G. Wallace, Intrinsically stretchable supercapacitors composed of polypyrrole electrodes and highly stretchable gel electrolyte, ACS applied materials & interfaces 5(18) (2013) 9008-9014, https://doi.org/10.1021/am402130j.

[50] L. Guo, W.-B. Ma, Y. Wang, X.-Z. Song, J. Ma, X.-D. Han, X.-Y. Tao, L.-T. Guo, H.-L. Fan, Z.-S. Liu, A chemically crosslinked hydrogel electrolyte based all-in-one flexible supercapacitor with superior performance, Journal of Alloys and Compounds 843 (2020) 155895, https://doi.org/10.1016/j.jallcom.2020.155895.

[51] S. Alipoori, M. Torkzadeh, S. Mazinani, S.H. Aboutalebi, F. Sharif, Performance-tuning of PVA-based gel electrolytes by acid/PVA ratio and PVA molecular weight, SN Applied Sciences 3(3) (2021) 1-13, https://doi.org/10.1007/s42452-021-04182-7.

[52] F. Hatta, M. Yahya, A. Ali, R. Subban, M. Harun, A. Mohamad, Electrical conductivity studies on PVA/PVP-KOH alkaline solid polymer blend electrolyte, Ionics 11(5) (2005) 418-422, https://doi.org/10.1007/BF02430259.

[53] L. Sa'adu, M. Hashim, M.B. Baharuddin, Conductivity studies and characterizations of PVA-orthophosphoric electrolytes, Journal of Materials Science Research 3(3) (2014) 48, https://doi.org/10.5539/jmsr.v3n3p48.

[54] H. Yu, J. Wu, L. Fan, K. Xu, X. Zhong, Y. Lin, J. Lin, Improvement of the performance for quasi-solid-state supercapacitor by using PVA–KOH–KI polymer gel electrolyte, Electrochimica Acta 56(20) (2011) 6881-6886, https://doi.org/10.1016/j.electacta.2011.06.039.

[55] C.-C. Yang, Polymer Ni–MH battery based on PEO–PVA–KOH polymer electrolyte, Journal of Power Sources 109(1) (2002) 22-31, https://doi.org/10.1016/S0378-7753(02)00038-1.

[56] N.R. Chodankar, D.P. Dubal, A.C. Lokhande, C.D. Lokhande, Ionically conducting PVA–LiClO4 gel electrolyte for high performance flexible solid state supercapacitors, Journal of colloid and interface science 460 (2015) 370-376, https://doi.org/10.1016/j.jcis.2015.08.046.

[57] E. Qua, P. Hornsby, H.S. Sharma, G. Lyons, R. McCall, Preparation and characterization of poly (vinyl alcohol) nanocomposites made from cellulose nanofibers, Journal of Applied Polymer Science 113(4) (2009) 2238-2247, https://doi.org/10.1002/app.30116.

[58] S.K.M. Patel, S.; Cohen, C.; Gillmor, J. R. & Colby, R. H. ,, Elastic Modulus and Equilibrium Swelling of Poly(dimethylsiloxane) Networks., Macromolecules, 1992, Vol. 25, pp. 5241-5251, https://doi.org/10.1021/ma00046a021.

[59] M.M.S. Quiambao, D.D. Laplana, M.I.D. Abobo, A.G. Jancon, S.D. Salvador, H.C. Siy, D.P. Penaloza Jr, Rheological characterization of the curing process for a water-based epoxy added with polythiol crosslinking agent, Építöanyag (Online) (5) (2019) 162-167, https://doi.org/10.14382/epitoanyag-jsbcm.2019.28.

[60] G. Stojkov, Z. Niyazov, F. Picchioni, R.K. Bose, Relationship between structure and rheology of hydrogels for various applications, Gels 7(4) (2021) 255, https://doi.org/10.3390/gels7040255.

[61] J. Liu, R.K. Yuen, Y. Hu, Tunable Properties of Exfoliated Polyvinylalcohol Nanocomposites by In Situ Coprecipitation of Layered Double Hydroxides, IOP Conference Series: Materials Science and Engineering, IOP Publishing, 2017, pp. 012001, https://doi.org/10.1088/1757-899X/241/1/012001.

[62] M. Naebe, T. Lin, M.P. Staiger, L. Dai, X. Wang, Electrospun single-walled carbon nanotube/polyvinyl alcohol composite nanofibers: structure–property relationships, Nanotechnology 19(30) (2008) 305702, https://doi.org/10.1088/0957-4484/19/30/305702.

[63] H. Peng, X. Gao, K. Sun, X. Xie, G. Ma, X. Zhou, Z. Lei, Physically cross-linked dual-network hydrogel electrolyte with high self-healing behavior and mechanical strength for wide-temperature tolerant flexible supercapacitor, Chemical Engineering Journal 422 (2021) 130353, https://doi.org/10.1016/j.cej.2021.130353.

[64] L. Yosefi, M. Haghighi, Fabrication of nanostructured flowerlike p-BiOI/p-NiO heterostructure and its efficient photocatalytic performance in water treatment under visible-light irradiation, Applied Catalysis B: Environmental 220 (2018) 367-378, https://doi.org/10.1016/j.apcatb.2017.08.028.

[65] Y.-X. Ju, R.-Z. Hu, P.-Y. Wang, Y.-S. Shen, F.-F. Shuang, J. Wang, P. Song, W.-G. Zhao, X.-H. Yao, D.-Y. Zhang, Strong silk fibroin/PVA/chitosan hydrogels with high water content inspired by straw rammed earth brick structures, ACS Sustainable Chemistry & Engineering 10(39) (2022) 13070-13080, https://doi.org/10.1021/acssuschemeng.2c03255.

[66] M. Gomaa, Y. Elsharkawy, M. Abdel-Hamed, E. Abdel-Hady, Synthesis and characterization of PVA/sPTA proton exchange membranes for fuel cell applications, IOP Conference Series: Materials Science and Engineering, IOP Publishing, 2021, pp. 012011, https://doi.org/10.1088/1757-899X/1046/1/012011.

[67] Z. Jahan, M.B.K. Niazi, Ø.W. Gregersen, Mechanical, thermal and swelling properties of cellulose nanocrystals/PVA nanocomposites membranes, Journal of industrial and engineering chemistry 57 (2018) 113-124, https://doi.org/10.1016/j.jiec.2017.08.014.

[68] S. Maphutha, K. Moothi, M. Meyyappan, S.E. Iyuke, A carbon nanotube-infused polysulfone membrane with polyvinyl alcohol layer for treating oil-containing waste water, Scientific reports 3(1) (2013) 1509, https://doi.org/10.1038/srep01509.

[69] L. Zhai, H.C. Kim, J.W. Kim, J. Kim, Green nanocomposites made with polyvinyl alcohol and cellulose nanofibers isolated from recycled paper, Journal of Renewable Materials 7(7) (2019) 621, https://doi.org/10.32604/jrm.2019.06466.

[70] Y. Pavani, M. Ravi, S. Bhavani, A. Sharma, V. Narasimha Rao, Characterization of poly (vinyl alcohol)/potassium chloride polymer electrolytes for electrochemical cell applications, Polymer Engineering & Science 52(8) (2012) 1685-1692, https://doi.org/10.1002/pen.23118.

[71] B. Guo, D. Zha, B. Li, P. Yin, P. Li, Polyvinyl alcohol microspheres reinforced thermoplastic starch composites, Materials 11(4) (2018) 640,https://doi.org/10.3390/ma11040640.

[72] W.H. Eisa, T. Abdel-Baset, E.M. Mohamed, S. Mahrous, Crosslinked PVA/PVP supported silver nanoparticles: a reusable and efficient heterogeneous catalyst for the 4-nitrophenol degradation, Journal of Inorganic and Organometallic Polymers and Materials 27 (2017) 1703-1711, https://doi.org/10.1007/s10904-017-0632-7.

[73] S.-K. Kim, H.-J. Koo, J. Liu, P.V. Braun, Flexible and Wearable Fiber Microsupercapacitors Based on Carbon Nanotube–Agarose Gel Composite Electrodes, ACS applied materials & interfaces 9(23) (2017) 19925-19933, https://doi.org/10.1021/acsami.7b04753.

[74] K. Wang, X. Zhang, C. Li, X. Sun, Q. Meng, Y. Ma, Z. Wei, Chemically crosslinked hydrogel film leads to integrated flexible supercapacitors with superior performance, Advanced materials 27(45) (2015) 7451-7457, https://doi.org/10.1002/adma.201503543.

[75] J. Liu, J. Huang, Q. Cai, Y. Yang, W. Luo, B. Zeng, Y. Xu, C. Yuan, L. Dai, Design of slidable polymer networks: a rational strategy to stretchable, rapid self-healing hydrogel electrolytes for flexible supercapacitors, ACS applied materials & interfaces 12(18) (2020) 20479-20489, https://doi.org/10.1021/acsami.0c03224.

[76] F.T. Johra, W.-G. Jung, Hydrothermally reduced graphene oxide as a supercapacitor, Applied Surface Science 357 (2015) 1911-1914, https://doi.org/10.1016/j.apsusc.2015.09.128.

[77] E. Andrijanto, S. Shoelarta, G. Subiyanto, S. Rifki, Facile synthesis of graphene from graphite using ascorbic acid as reducing agent, AIP Conference

Proceedings, AIP Publishing LLC, 2016, pp. Volume: 1725, 020003, https://doi.org/10.1063/1.4945457.

[78] N. Hidayah, W.-W. Liu, C.-W. Lai, N. Noriman, C.-S. Khe, U. Hashim, H.C. Lee, Comparison on graphite, graphene oxide and reduced graphene oxide: Synthesis and characterization, AIP conference proceedings, AIP Publishing LLC, 2017, pp. 150002, https://doi.org/10.1063/1.5005764.

[79] B. Gupta, N. Kumar, K. Panda, V. Kanan, S. Joshi, I. Visoly-Fisher, Role of oxygen functional groups in reduced graphene oxide for lubrication, Scientific reports 7(1) (2017) 1-14, https://doi.org/10.1038/srep45030.

[80] S. Kumar, J. Koh, Physiochemical, optical and biological activity of chitosan-chromone derivative for biomedical applications, International journal of molecular sciences 13(5) (2012) 6102-6116, https://doi.org/10.3390/ijms13056102.

[81] F. Shao, N. Hu, Y. Su, L. Yao, B. Li, C. Zou, G. Li, C. Zhang, H. Li, Z. Yang, Non-woven fabric electrodes based on graphene-based fibers for areal-energy-dense flexible solid-state supercapacitors, Chemical Engineering Journal 392 (2020) 123692, https://doi.org/10.1016/j.cej.2019.123692.

[82] L. Ma, J. Liu, S. Lv, Q. Zhou, X. Shen, S. Mo, H. Tong, Scalable one-step synthesis of N, S co-doped graphene-enhanced hierarchical porous carbon foam for high-performance solid-state supercapacitors, Journal of Materials Chemistry A 7(13) (2019) 7591-7603, https://doi.org/10.1039/C9TA00038K.

[83] L.W. Mingming Gao, Baozheng Zhao, Xinglong Gu, Tong Li, Lang Huang, Qiong Wu, Shitao Yu, Shiwei Liu, , Sandwich construction of chitosan/reduced graphene oxide composite as additive-free electrode material for high-performance supercapacitors, Carbohydrate Polymers, Volume 255, 1 March 2021, 117397, https://doi.org/10.1016/j.carbpol.2020.117397.

[84] R. Ren, Y. Zhong, X. Ren, Y. Fan, Chitosan-based oxygen-doped activated carbon/graphene composite for flexible supercapacitors, RSC advances 12(39) (2022) 25807-25814, https://doi.org/10.1039/D2RA03949D.

[85] N.A. Salleh, S. Kheawhom, A.A. Mohamad, Chitosan as biopolymer binder for graphene in supercapacitor electrode, Results in Physics 25 (2021) 104244, https://doi.org/10.1016/j.rinp.2021.104244.

[86] S.u. Haque, A. Nasar, Inamuddin, M.M. Rahman, Applications of chitosan (CHI)-reduced graphene oxide (rGO)-polyaniline (PAni) conducting composite electrode for energy generation in glucose biofuel cell, Scientific Reports 10(1) (2020) 10428.

[87] L. Chai, Q. Qu, L. Zhang, M. Shen, L. Zhang, H. Zheng, Chitosan, a new and environmental benign electrode binder for use with graphite anode in lithium-ion batteries, Electrochimica Acta 105 (2013) 378-383, https://doi.org/10.1016/j.electacta.2013.05.009.

[88] Q. Zhang, D. Liu, H. Pei, W. Pan, Y. Liu, S. Xu, S. Cao, Swelling-reconstructed chitosan-viscose nonwoven fabric for high-performance quasi-solid-state supercapacitors, Journal of Colloid and Interface Science 617 (2022) 489-499, https://doi.org/10.1016/j.jcis.2022.03.011.

[89] F. Meng, Q. Li, L. Zheng, Flexible fiber-shaped supercapacitors: design, fabrication, and multi-functionalities, Energy Storage Materials 8 (2017) 85-109, https://doi.org/10.1016/j.ensm.2017.05.002.

[90] C. He, S. Qiu, S. Sun, Q. Zhang, G. Lin, S. Lei, X. Han, Y. Yang, Electrochemically active phosphotungstic acid assisted prevention of graphene

restacking for high-capacitance supercapacitors, Energy & Environmental Materials 1(2) (2018) 88-95, https://doi.org/10.1002/eem2.12007.

[91] R. Vinodh, Y. Sasikumar, H.-J. Kim, R. Atchudan, M. Yi, Chitin and chitosan based biopolymer derived electrode materials for supercapacitor applications: A critical review, Journal of Industrial and Engineering Chemistry 104 (2021) 155-171, https://doi.org/10.1016/j.jiec.2021.08.019.

[92] M. Shu, F. Gao, M. Zeng, C. Yu, X. Wang, R. Huang, J. Yang, Y. Su, N. Hu, Z. Zhou, Microwave-assisted chitosan-functionalized graphene oxide as controlled intracellular drug delivery nanosystem for synergistic antitumour activity, Nanoscale Research Letters 16(1) (2021) 75, https://doi.org/10.1186/s11671-021-03525-y.

[93] W.M. El Rouby, A.A. Farghali, M. Sadek, W.F. Khalil, Fast removal of Sr (II) from water by graphene oxide and chitosan modified graphene oxide, Journal of Inorganic and Organometallic Polymers and Materials 28 (2018) 2336-2349, https://doi.org/10.1007/s10904-018-0885-9.

[94] S. Dhanavel, T. Revathy, T. Sivaranjani, K. Sivakumar, P. Palani, V. Narayanan, A. Stephen, 5-Fluorouracil and curcumin co-encapsulated chitosan/reduced graphene oxide nanocomposites against human colon cancer cell lines, Polymer Bulletin 77 (2020) 213-233, https://doi.org/10.1007/s00289-019-02734-x.

[95] S. Lee, H. Lee, J.H. Sim, D. Sohn, Graphene oxide/poly (acrylic acid) hydrogel by γ-ray pre-irradiation on graphene oxide surface, Macromolecular Research 22 (2014) 165-172, https://doi.org/10.1007/s13233-014-2025-x.

[96] D. Rajamani, E. Balasubramanian, A. Ziout, M. Alkahtani, Synergistic effect of r-GO on the mechanical, microstructural and high velocity impact behaviour of synthetic fibre reinforced NiTi intermetallic laminates, Journal of Materials Research and Technology (2023).

[97] S.u. Haque, A. Nasar, Inamuddin, M.M. Rahman, Applications of chitosan (CHI)-reduced graphene oxide (rGO)-polyaniline (PAni) conducting composite electrode for energy generation in glucose biofuel cell, Scientific Reports 10(1) (2020) 10428, https://doi.org/10.1038/s41598-020-67253-6.

[98] Z. Li, X. Song, S. Cui, Y. Jiao, C. Zhou, Fabrication of macroporous reduced graphene oxide composite aerogels reinforced with chitosan for high bilirubin adsorption, RSC advances 8(15) (2018) 8338-8348.

[99] F. Alakhras, H. Ouachtak, E. Alhajri, R. Rehman, G. Al-Mazaideh, I. Anastopoulos, E.C. Lima, Adsorptive removal of cationic rhodamine B dye from aqueous solutions using chitosan-derived schiff base, Separation Science and Technology 57(4) (2022) 542-554.

[100] Q. Chen, Y. Tian, P. Li, C. Yan, Y. Pang, L. Zheng, H. Deng, W. Zhou, X. Meng, Study on shale adsorption equation based on monolayer adsorption, multilayer adsorption, and capillary condensation, Journal of Chemistry 2017 (2017).

[101] S. Saleviter, Y.W. Fen, N.A.S. Omar, W.M.E.M.M. Daniyal, J. Abdullah, M.H.M. Zaid, Structural and optical studies of cadmium sulfide quantum dot-graphene oxide-chitosan nanocomposite thin film as a novel SPR spectroscopy active layer, Journal of Nanomaterials 2018 (2018) 1-8, https://doi.org/10.1155/2018/4324072.

[102] Q. Luo, C. Wirth, E. Pentzer, Efficient sizing of single layer graphene oxide with optical microscopy under ambient conditions, Carbon 157 (2020) 395-401, https://doi.org/10.1016/j.carbon.2019.10.047.

[103] L. Marin, M. Popa, A. Anisiei, S.-A. Irimiciuc, M. Agop, T.-C. Petrescu, D. Vasincu, L. Himiniuc, A Theoretical Model for Release Dynamics of an Antifungal Agent Covalently Bonded to the Chitosan, Molecules 26(7) (2021) 2089, https://doi.org/10.3390/molecules26072089.

[104] L. Lu, W. Chen, Large-Scale Aligned Carbon Nanotubes from Their Purified, Highly Concentrated Suspension, ACS Nano 4(2) (2010) 1042-1048.

[105] K. Yang, X. Huang, L. Fang, J. He, P. Jiang, Fluoro-polymer functionalized graphene for flexible ferroelectric polymer-based high-k nanocomposites with suppressed dielectric loss and low percolation threshold, Nanoscale 6(24) (2014) 14740-14753.

[106] S. Ahmad, A. Ahmad, S. Khan, S. Ahmad, I. Khan, S. Zada, P. Fu, Algal extracts based biogenic synthesis of reduced graphene oxides (rGO) with enhanced heavy metals adsorption capability, Journal of Industrial and Engineering Chemistry 72 (2019) 117-124.

[107] M.N. Vara Prasad, H.M. de Oliveira Freitas, Metal hyperaccumulation in plants: biodiversity prospecting for phytoremediation technology, Electronic journal of biotechnology 6(3) (2003) 285-321.

[108] X. Qin, H. Zhang, Z. Wang, Y. Jin, Magnetic chitosan/graphene oxide composite loaded with novel photosensitizer for enhanced photodynamic therapy, RSC advances 8(19) (2018) 10376-10388.

[109] T. Wei, W. Tu, B. Zhao, Y. Lan, J. Bao, Z. Dai, Electrochemical monitoring of an important biomarker and target protein: VEGFR2 in cell lysates, Scientific Reports 4(1) (2014) 3982.

[110] H. Chang, X. Wu, C. Wu, Y. Chen, H. Jiang, X. Wang, Catalytic oxidation and determination of β-NADH using self-assembly hybrid of gold nanoparticles and graphene, Analyst 136(13) (2011) 2735-2740.

[111] K. Gerani, H.R. Mortaheb, B. Mokhtarani, Enhancement in performance of sulfonated PES cation-exchange membrane by introducing pristine and sulfonated graphene oxide nanosheets synthesized through hummers and staudenmaier methods, Polymer-Plastics Technology and Engineering 56(5) (2017) 543-555, https://doi.org/10.1080/03602559.2016.1233260.

[112] S. Gurunathan, J. Hyun Park, Y.-J. Choi, J. Woong Han, J.-H. Kim, Synthesis of graphene oxide-silver nanoparticle nanocomposites: an efficient novel antibacterial agent, Current Nanoscience 12(6) (2016) 762-773, https://doi.org/10.2174/1573413712666160721143424.

[113] N. Azimi, A. Gandomkar, M. Sharif, Relationship between production condition, microstructure and final properties of chitosan/graphene oxide–zinc oxide bionanocomposite, Polymer Bulletin 80(6) (2023) 6455-6469, https://doi.org/10.1007/s00289-022-04277-0.

[114] Z. Guo, X.-k. Luo, Y.-h. Li, Q.-N. Zhao, M.-m. Li, Y.-t. Zhao, T.-s. Sun, C. Ma, Simultaneous determination of trace Cd (II), Pb (II) and Cu (II) by differential pulse anodic stripping voltammetry using a reduced graphene oxide-chitosan/poly-l-lysine nanocomposite modified glassy carbon electrode, Journal of colloid and interface science 490 (2017) 11-22, https://doi.org/10.1016/j.jcis.2016.11.006.

[115] L. Liu, S. Jiang, L. Wang, Z. Zhang, G. Xie, Direct detection of microRNA-126 at a femtomolar level using a glassy carbon electrode modified with chitosan,

graphene sheets, and a poly (amidoamine) dendrimer composite with gold and silver nanoclusters, Microchimica Acta 182 (2015) 77-84, https://doi.org/10.1007/s00604-014-1273-y.

[116] Q. Pan, Z. Xu, S. Deng, F. Zhang, H. Li, Y. Cheng, L. Wei, J. Wang, B. Zhou, A mechanochemically synthesized porous organic polymer derived CQD/chitosan–graphene composite film electrode for electrochemiluminescence determination of dopamine, RSC advances 9(67) (2019) 39332-39337, https://doi.org/10.1039/C9RA06912G.

[117] Y. Wang, W. Cao, L. Wang, Q. Zhuang, Y. Ni, Electrochemical determination of 2, 4, 6-trinitrophenol using a hybrid film composed of a copper-based metal organic framework and electroreduced graphene oxide, Microchimica Acta 185 (2018) 1-9, https://doi.org/10.1007/s00604-018-2857-8.

[118] C.S.R. Vusa, S. Berchmans, S. Alwarappan, Facile and green synthesis of graphene, RSC Advances 4(43) (2014) 22470-22475, https://doi.org/10.1039/C4RA01718H.

[119] K. Zhang, H. Hu, W. Yao, C. Ye, Flexible and all-solid-state supercapacitors with long-time stability constructed on PET/Au/polyaniline hybrid electrodes, Journal of Materials Chemistry A 3(2) (2015) 617-623, https://doi.org/10.1039/C4TA05605A.

[120] S. Teng, G. Siegel, W. Wang, A. Tiwari, Carbonized wood for supercapacitor electrodes, ECS Solid State Letters 3(5) (2014) M25, https://doi.org/10.1149/2.005405ssl.

[121] E. Ghoniem, S. Mori, A. Abdel-Moniem, Low-cost flexible supercapacitors based on laser reduced graphene oxide supported on polyethylene terephthalate substrate, Journal of Power Sources 324 (2016) 272-281, https://doi.org/10.1016/j.jpowsour.2016.05.069.

[122] Y. Xue, L. Zhu, H. Chen, J. Qu, L. Dai, Multiscale patterning of graphene oxide and reduced graphene oxide for flexible supercapacitors, Carbon 92 (2015) 305-310, https://doi.org/10.1016/j.carbon.2015.04.046.

[123] T. Aytug, M.S. Rager, W. Higgins, F.G. Brown, G.M. Veith, C.M. Rouleau, H. Wang, Z.D. Hood, S.M. Mahurin, R.T. Mayes, Vacuum-assisted low-temperature synthesis of reduced graphene oxide thin-film electrodes for high-performance transparent and flexible all-solid-state supercapacitors, ACS applied materials & interfaces 10(13) (2018) 11008-11017] https://doi.org/10.1021/acsami.8b01938.

[124] B.C. Kim, H.T. Jeong, C.J. Raj, Y.-R. Kim, B.-B. Cho, K.H. Yu, Electrochemical performance of flexible poly (ethylene terephthalate)(PET) supercapacitor based on reduced graphene oxide (rGO)/single-wall carbon nanotubes (SWNTs), Synthetic Metals 207 (2015) 116-121, https://doi.org/10.1016/j.synthmet.2015.05.022.

[125] K. Deshmukh, M.B. Ahamed, R.R. Deshmukh, S.K. Pasha, K. Chidambaram, K.K. Sadasivuni, D. Ponnamma, M.A.-A. AlMaadeed, Eco-friendly synthesis of graphene oxide reinforced hydroxypropyl methylcellulose/polyvinyl alcohol blend nanocomposites filled with zinc oxide nanoparticles for high-k capacitor applications, Polymer-Plastics Technology and Engineering 55(12) (2016) 1240-1253.

[126] Y. Zhu, S. Murali, W. Cai, X. Li, J.W. Suk, J.R. Potts, R.S. Ruoff, Graphene and graphene oxide: synthesis, properties, and applications, Advanced materials 22(35) (2010) 3906-3924, https://doi.org/10.1002/adma.201001068.

[127] E.S. de Alvarenga, Characterization and properties of chitosan, Biotechnology of biopolymers 91 (2011) 48-53, ISBN 978-953-307-179-4, https://doi.org/10.5772/17020.

[128] S.B. Aziz, R.M. Abdullah, M.F.Z. Kadir, H.M. Ahmed, Non suitability of silver ion conducting polymer electrolytes based on chitosan mediated by barium titanate (BaTiO3) for electrochemical device applications, Electrochimica Acta 296 (2019) 494-507, https://doi.org/10.1016/j.electacta.2018.11.081.

[129] S.B. Aziz, R.M. Abdullah, M.A. Rasheed, H.M. Ahmed, Role of ion dissociation on DC conductivity and silver nanoparticle formation in PVA: AgNt based polymer electrolytes: Deep insights to ion transport mechanism, Polymers 9(8) (2017) 338, https://doi.org/10.3390/polym9080338.

[130] S.B. Aziz, M. Hamsan, M. Brza, M. Kadir, R.T. Abdulwahid, H.O. Ghareeb, H. Woo, Fabrication of energy storage EDLC device based on CS: PEO polymer blend electrolytes with high Li+ ion transference number, Results in Physics 15 (2019) 102584, https://doi.org/10.1016/j.rinp.2019.102584.

[131] H. Gao, K. Lian, Effect of SiO2 on Silicotungstic Acid-H3PO4-poly (vinyl alcohol) Electrolyte for Electrochemical Supercapacitors, Journal of The Electrochemical Society 160(3) (2013) A505-A510, http://doi.org/10.1149/2.053303jes.

[132] Q. Chen, X. Li, X. Zang, Y. Cao, Y. He, P. Li, K. Wang, J. Wei, D. Wu, H. Zhu, Effect of different gel electrolytes on graphene-based solid-state supercapacitors, RSC Advances 4(68) (2014) 36253-36256, https://doi.org/10.1039/C4RA05553E.

[133] C.-M. Tang, Y.-H. Tian, S.-H. Hsu, Poly (vinyl alcohol) nanocomposites reinforced with bamboo charcoal nanoparticles: mineralization behavior and characterization, Materials 8(8) (2015) 4895-4911, https://doi.org/10.3390/ma8084895.

[134] S.B. Aziz, R.T. Abdulwahid, M.H. Hamsan, M.A. Brza, R.M. Abdullah, M.F. Kadir, S.K. Muzakir, Structural, impedance, and EDLC characteristics of proton conducting chitosan-based polymer blend electrolytes with high electrochemical stability, Molecules 24(19) (2019) 3508, https://doi.org/10.3390/molecules24193508.

[135] P. Lobitz, H. Füllbier, A. Reiche, J. Illner, H. Reuter, S. Höring, Ionic conductivity in poly (ethylene oxide)-poly (alkylmethacrylate)-block copolymer mixtures with LiI, Solid State Ionics 58(1-2) (1992) 41-48, https://doi.org/10.1016/0167-2738(92)90008-D.

[136] F. Santos, J.P. Tafur, J. Abad, A.J.F. Romero, Structural modifications and ionic transport of PVA-KOH hydrogels applied in Zn/Air batteries, Journal of Electroanalytical Chemistry 850 (2019) 113380, https://doi.org/10.1016/j.jelechem.2019.113380.

[137] M.L. Sheqnab, R.S. Alnayli, Effect Of Cdte Nanoparticles On Linear And Nonlinear Optical Property Of Polyvinyl Alcohols PVA Film, Journal of Education for Pure Science 9(2) (2019, : http://doi.org/10.32792/utq.jceps.09.02.28).

[138] W.H. Eisa, A. Shabaka, Ag seeds mediated growth of Au nanoparticles within PVA matrix: An eco-friendly catalyst for degradation of 4-nitrophenol, Reactive and Functional Polymers 73(11) (2013) 1510-1516, https://doi.org/10.1016/j.reactfunctpolym.2013.07.018.

[139] W. Ma, S. Chen, S. Yang, W. Chen, Y. Cheng, Y. Guo, S. Peng, S. Ramakrishna, M. Zhu, Hierarchical MnO2 nanowire/graphene hybrid fibers with

excellent electrochemical performance for flexible solid-state supercapacitors, Journal of Power Sources 306 (2016) 481-488, https://doi.org/10.1016/j.jpowsour.2015.12.063.

[140] G.-Q. Wu, X.-Y. Yang, J.-H. Li, N. Sheng, C.-Y. Hou, Y.-G. Li, H.-Z. Wang, Highly stretchable and conductive hybrid fibers for high-performance fibrous electrodes and all-solid-state supercapacitors, Chinese Journal of Polymer Science 38 (2020) 531-539, https://doi.org/10.1007/s10118-020-2381-2.

[141] M.S. Rostami, M.M. Khodaei, Recent advances of chitosan-based nanocomposites for supercapacitor applications: Key challenges and future research directions, Journal of Energy Storage 72 (2023) 108344, https://doi.org/10.1016/j.est.2023.108344.

[142] S.H. Aboutalebi, M.M. Gudarzi, Q.B. Zheng, J.K. Kim, Spontaneous formation of liquid crystals in ultralarge graphene oxide dispersions, Advanced Functional Materials 21(15) (2011) 2978-2988, https://doi.org/10.1002/adfm.201100448.

[143] S. Sunderrajan, L.R. Miranda, G. Pennathur, Improved stability and catalytic activity of graphene oxide/chitosan hybrid beads loaded with porcine liver esterase, Preparative Biochemistry and Biotechnology 48(4) (2018) 343-351, https://doi.org/10.1080/10826068.2018.1446153.

[144] S. Dhanavel, T. Revathy, A. Padmanaban, V. Narayanan, A. Stephen, Highly efficient catalytic reduction and electrochemical sensing of hazardous 4-nitrophenol using chitosan/rGO/palladium nanocomposite, Journal of Materials Science: Materials in Electronics 29 (2018) 14093-14104, https://doi.org/10.1007/s10854-018-9541-y.

[145] X. Yang, X. Niu, Z. Mo, R. Guo, N. Liu, P. Zhao, Z. Liu, Perylene-functionalized graphene sheets modified with chitosan for voltammetric discrimination of tryptophan enantiomers, Microchimica Acta 186 (2019) 1-12, https://doi.org/10.1007/s00604-019-3442-5.

[146] X. Wang, H. Bai, Z. Yao, A. Liu, G. Shi, Electrically conductive and mechanically strong biomimetic chitosan/reduced graphene oxide composite films, Journal of Materials Chemistry 20(41) (2010) 9032-9036, https://doi.org/10.1039/C0JM01852J.

[147] L. Feng, G. Gao, P. Huang, X. Wang, C. Zhang, J. Zhang, S. Guo, D. Cui, Preparation of Pt Ag alloy nanoisland/graphene hybrid composites and its high stability and catalytic activity in methanol electro-oxidation, Nanoscale research letters 6 (2011) 1-10, https://doi.org/10.1186/1556-276X-6-551.

[148] H. Kalil, S. Maher, T. Bose, M. Bayachou, Manganese oxide/hemin-functionalized graphene as a platform for peroxynitrite sensing, Journal of The Electrochemical Society 165(12) (2018) G3133, https://doi.org/10.1149/2.0221812jes.

[149] B.T. M.E. Orazem, Electrochemical impedance spectroscopy, John Wiley & Sons; 2011, https://doi.org/10.1002/9780470381588.

[150] Y.J. Kang, H. Chung, M.-S. Kim, W. Kim, Enhancement of CNT/PET film adhesion by nano-scale modification for flexible all-solid-state supercapacitors, Applied Surface Science 355 (2015) 160-165, https://doi.org/10.1016/j.apsusc.2015.07.108.

[151] X. Guan, L. Pan, Z. Fan, Flexible, transparent and highly conductive polymer film electrodes for all-solid-state transparent supercapacitor applications, Membranes 11(10) (2021) 788, https://doi.org/10.3390/membranes11100788.

[152] M. Halper, J. Ellenbogen, C-Supercapacitors: A brief overview, The MITRE Corporation, McLean, Virginia, Technical report 06-0667, 2006, https://www.mitre.org/sites/default/files/pdf/06_0667.pdf.

[153] J. Xia, F. Chen, J. Li, N. Tao, Measurement of the quantum capacitance of graphene, Nature Nanotechnol. 4, 505 (2009), https://doi.org/10.1038/nnano.2009.177.

[154] S. Park, R.S. Ruoff, Chemical methods for the production of graphenes, Nature nanotechnology 4(4) (2009) 217-224, https://doi.org/10.1038/nnano.2009.58.

[155] W.X. Lee C, Kysar JW, Hone J Measurement of the Elastic Properties and Intrinsic Strength of Monolayer Graphene, SCIENCE, 18 Jul 2008, Vol 321, Issue 5887, pp. 385-388, https://doi.org/10.1126/science.1157996.

[156] K.S. Novoselov, A.K. Geim, S.V. Morozov, D.-e. Jiang, Y. Zhang, S.V. Dubonos, I.V. Grigorieva, A.A. Firsov, Electric field effect in atomically thin carbon films, science 306(5696) (2004) 666-669, https://doi.org/10.1126/science.1102896.

[157] N.I. Kovtyukhova, P.J. Ollivier, B.R. Martin, T.E. Mallouk, S.A. Chizhik, E.V. Buzaneva, A.D. Gorchinskiy, Layer-by-layer assembly of ultrathin composite films from micron-sized graphite oxide sheets and polycations, Chemistry of materials 11(3) (1999) 771-778, https://doi.org/10.1021/cm981085u.

[158] C.X. Guo, C.M. Li, A self-assembled hierarchical nanostructure comprising carbon spheres and graphene nanosheets for enhanced supercapacitor performance, Energy & Environmental Science 4(11) (2011) 4504-4507, https://doi.org/10.1039/C1EE01676H.

[159] Y. Wang, J. Chen, J. Cao, Y. Liu, Y. Zhou, J.-H. Ouyang, D. Jia, Graphene/carbon black hybrid film for flexible and high rate performance supercapacitor, Journal of Power Sources 271 (2014) 269-277, https://doi.org/10.1016/j.jpowsour.2014.08.007.

[160] G. Wang, R. Liang, L. Liu, B. Zhong, Improving the specific capacitance of carbon nanotubes-based supercapacitors by combining introducing functional groups on carbon nanotubes with using redox-active electrolyte, Electrochimica Acta 115 (2014) 183-188, https://doi.org/10.1016/j.electacta.2013.10.165.

[161] N. Díez, C. Botas, R. Mysyk, E. Goikolea, T. Rojo, D. Carriazo, Highly packed graphene–CNT films as electrodes for aqueous supercapacitors with high volumetric performance, Journal of Materials Chemistry A 6(8) (2018) 3667-3673, https://doi.org/10.1039/C7TA10210K.

[162] L. Sheng, L. Jiang, T. Wei, Z. Fan, High volumetric energy density asymmetric supercapacitors based on well-balanced graphene and graphene-MnO2 electrodes with densely stacked architectures, Small 12(37) (2016) 5217-5227, https://doi.org/10.1002/smll.201601722.

[163] Z. Zhang, F. Xiao, L. Qian, J. Xiao, S. Wang, Y. Liu, Facile synthesis of 3D MnO2–graphene and carbon nanotube–graphene composite networks for high-performance, flexible, all-solid-state asymmetric supercapacitors, Advanced Energy Materials 4(10) (2014) 1400064, https://doi.org/10.1002/aenm.201400064.

[164] X. He, H. Zhang, H. Zhang, X. Li, N. Xiao, J. Qiu, Direct synthesis of 3D hollow porous graphene balls from coal tar pitch for high performance supercapacitors, Journal of Materials Chemistry A 2(46) (2014) 19633-19640, https://doi.org/10.1039/C4TA03323J.

[165] X. He, N. Zhang, X. Shao, M. Wu, M. Yu, J. Qiu, A layered-template-nanospace-confinement strategy for production of corrugated graphene

nanosheets from petroleum pitch for supercapacitors, Chemical Engineering Journal 297 (2016) 121-127, https://doi.org/10.1016/j.cej.2016.03.153.

[166] D. Wu, S. Hu, H. Xue, X. Hou, H. Du, G. Xu, Y. Yuan, Protonation and microwave-assisted heating induced excitation of lone-pair electrons in graphitic carbon nitride for increased photocatalytic hydrogen generation, Journal of Materials Chemistry A 7(35) (2019) 20223-20228, https://doi.org/10.1039/C9TA05135J.

[167] Q. Wu, M. Gao, S. Cao, J. Hu, L. Huang, S. Yu, A.J. Ragauskas, Chitosan-based layered carbon materials prepared via ionic-liquid-assisted hydrothermal carbonization and their performance study, Journal of the Taiwan Institute of Chemical Engineers 101 (2019) 231-243, https://doi.org/10.1016/j.jtice.2019.04.039.

[168] Q. Wu, M. Gao, G. Zhang, Y. Zhang, S. Liu, C. Xie, H. Yu, Y. Liu, L. Huang, S. Yu, Preparation and application performance study of biomass-based carbon materials with various morphologies by a hydrothermal/soft template method, Nanotechnology 30(18) (2019) 185702, http://doi.org/10.1088/1361-6528/ab0042.

[169] Z. Wu, C. Xu, C. Ma, Z. Liu, H.M. Cheng, W. Ren, Synergistic effect of aligned graphene nanosheets in graphene foam for high-performance thermally conductive composites, Advanced Materials 31(19) (2019) 1900199, https://doi.org/10.1002/adma.201900199.

[170] Q. Wu, G. Zhang, M. Gao, L. Huang, L. Li, S. Liu, C. Xie, Y. Zhang, S. Yu, N-doped porous carbon from different nitrogen sources for high-performance supercapacitors and CO2 adsorption, Journal of Alloys and Compounds 786 (2019) 826-838, https://doi.org/10.1016/j.jallcom.2019.02.052.

[171] M.D. Stoller, S. Park, Y. Zhu, J. An, R.S. Ruoff, Graphene-based ultracapacitors, Nano letters 8(10) (2008) 3498-3502, https://doi.org/10.1021/nl802558y.

[172] J. Gamby, P. Taberna, P. Simon, J. Fauvarque, M. Chesneau, Studies and characterisations of various activated carbons used for carbon/carbon supercapacitors, Journal of power sources 101(1) (2001) 109-116, https://doi.org/10.1016/S0378-7753(01)00707-8.

[173] P. Simon, A. Burke, Nanostructured carbons: double-layer capacitance and more, The electrochemical society interface 17(1) (2008) 38, https://www.electrochem.org/dl/interface/spr/spr08/spr08_p38-43.pdf.

[174] C.V.-G. K. Jurewicz , E. Frackowiak , S. Saadallah , M. Reda , J. Parmentier , J. Patarin , F. Béguin Capacitance properties of ordered porous carbon materials prepared by a templating procedure, Journal of Physics and Chemistry of Solids Volume 65, Issues 2–3, March 2004, Pages 287-293, https://doi.org/10.1016/j.jpcs.2003.10.024.

[175] J. Fernández, T. Morishita, M. Toyoda, M. Inagaki, F. Stoeckli, T.A. Centeno, Performance of mesoporous carbons derived from poly (vinyl alcohol) in electrochemical capacitors, Journal of Power Sources 175(1) (2008) 675-679, https://doi.org/10.1016/j.jpowsour.2007.09.042.

[176] C. Portet, P. Taberna, P. Simon, C. Laberty-Robert, Modification of Al current collector surface by sol–gel deposit for carbon–carbon supercapacitor applications, Electrochimica Acta 49(6) (2004) 905-912, https://doi.org/10.1016/j.electacta.2003.09.043.

[177] S. Talapatra, S. Kar, S. Pal, R. Vajtai, L. Ci, P. Victor, M. Shaijumon, S. Kaur, O. Nalamasu, P. Ajayan, Direct growth of aligned carbon nanotubes on bulk

metals, Nature nanotechnology 1(2) (2006) 112-116, https://doi.org/10.1038/nnano.2006.56.

[178] V.L. Pushparaj, M.M. Shaijumon, A. Kumar, S. Murugesan, L. Ci, R. Vajtai, R.J. Linhardt, O. Nalamasu, P.M. Ajayan, Flexible energy storage devices based on nanocomposite paper, Proceedings of the National Academy of Sciences 104(34) (2007) 13574-13577, https://doi.org/10.1073/pnas.0706508104.

[179] Y. Rangom, X. Tang, L.F. Nazar, Carbon nanotube-based supercapacitors with excellent ac line filtering and rate capability via improved interfacial impedance, ACS nano 9(7) (2015) 7248-7255, https://doi.org/10.1021/acsnano.5b02075.

[180] L. Gao, A. Peng, Z.Y. Wang, H. Zhang, Z. Shi, Z. Gu, G. Cao, B. Ding, Growth of aligned carbon nanotube arrays on metallic substrate and its application to supercapacitors, Solid State Communications 146(9-10) (2008) 380-383, https://doi.org/10.1016/j.ssc.2008.03.034.

[181] C.L. Pint, N.W. Nicholas, S. Xu, Z. Sun, J.M. Tour, H.K. Schmidt, R.G. Gordon, R.H. Hauge, Three dimensional solid-state supercapacitors from aligned single-walled carbon nanotube array templates, Carbon 49(14) (2011) 4890-4897, https://doi.org/10.1016/j.carbon.2011.07.011.

[182] J. Yan, Q. Wang, T. Wei, Z. Fan, Recent advances in design and fabrication of electrochemical supercapacitors with high energy densities, Advanced Energy Materials 4(4) (2014) 1300816, https://doi.org/10.1002/aenm.201300816.

[183] L. Wang, Q. Wu, Z. Zhang, Y. Zhang, J. Pan, Y. Li, Y. Zhao, L. Zhang, X. Cheng, H. Peng, Elastic and wearable ring-type supercapacitors, Journal of Materials Chemistry A 4(9) (2016) 3217-3222, https://doi.org/10.1039/C5TA10461K. .

[184] K. Jost, D. Stenger, C.R. Perez, J.K. McDonough, K. Lian, Y. Gogotsi, G. Dion, Knitted and screen printed carbon-fiber supercapacitors for applications in wearable electronics, Energy & Environmental Science 6(9) (2013) 2698-2705, https://doi.org/10.1039/C3EE40515J.

[185] X. Chen, L. Qiu, J. Ren, G. Guan, H. Lin, Z. Zhang, P. Chen, Y. Wang, H. Peng, Novel electric double-layer capacitor with a coaxial fiber structure, Advanced Materials 25(44) (2013) 6436-6441, https://doi.org/10.1002/adma.201301519.

[186] S.S. N. Choudhury, A. Shukla,, Hydrogel-polymer electrolytes for electrochemical capacitors: an overview, Energy Environ. Sci., 2009, 2, 55-67, https://doi.org/10.1039/B811217G.

[187] H. Gao, K. Lian, Proton-conducting polymer electrolytes and their applications in solid supercapacitors: a review, RSC advances 4(62) (2014) 33091-33113, https://doi.org/10.1039/C4RA05151C.

[188] G. Wei, J. Yu, M. Gu, T.B. Tang, Dielectric relaxation and hopping conduction in reduced graphite oxide, Journal of Applied Physics,https://doi.org/10.1063/1.4953357. 119(22) (2016).

[189] S. Sekhon, Conductivity behaviour of polymer gel electrolytes: Role of polymer, Bulletin of Materials Science 26(3) (2003) 321-328, https://doi.org/10.1007/BF02707454.

[190] D.J. Vannessa Goodship, Erich Okoth Ogur, Polyvinyl alcohol: materials, processing and applications, Smithers rapra technology2009.

[191] L. Chongad, A. Jain, G. Mukherjee, M. Banerjee, Optical Properties of CuS Nanoparticles Embedded Polyvinyl Alcohol (PVA) Films, (2021) Vol. 13 No 1, 01023(4pp), https://doi.org/10.21272/jnep.13(1).01023.

[192] S.N. Bhad, V. Sangawar, Synthesis and study of PVA based gel electrolyte, Chem Sci Trans 1(3) (2012) 653-657, https://doi.org/10.7598/cst2012.253.

[193] J. Tao, Effects of Molecular weight and Solution Concentration on Electrospinning of PVA, Worcester Polytechnic Institute, USA, (2003). (

).

[194] L. Shahriary, A.A. Athawale, Graphene oxide synthesized by using modified hummers approach, Int. J. Renew. Energy Environ. Eng 2(01) (2014) 58-63, ISSN 2348-0157, https://doi.org/10.1016/j.proeng.2017.04.118.

[195] W. Gao, N. Singh, L. Song, Z. Liu, A.L.M. Reddy, L. Ci, R. Vajtai, Q. Zhang, B. Wei, P.M. Ajayan, Direct laser writing of micro-supercapacitors on hydrated graphite oxide films, Nature nanotechnology 6(8) (2011) 496-500, https://doi.org/10.1038/nnano.2011.110.

[196] J.J. Shao, W. Lv, Q.H. Yang, Self-assembly of graphene oxide at interfaces, Advanced Materials 26(32) (2014) 5586-5612, https://doi.org/10.1002/adma.201400267.

[197] N. Zaaba, K. Foo, U. Hashim, S. Tan, W.-W. Liu, C. Voon, Synthesis of graphene oxide using modified hummers method: solvent influence, Procedia engineering 184 (2017) 469-477, https://doi.org/10.1016/j.proeng.2017.04.118.

[198] R.K. Joshi, S. Alwarappan, M. Yoshimura, V. Sahajwalla, Y. Nishina, Graphene oxide: the new membrane material, Applied Materials Today 1(1) (2015) 1-12, https://doi.org/10.1016/j.apmt.2015.06.002.

[199] M. Saeed, Y. Alshammari, S.A. Majeed, E. Al-Nasrallah, Chemical vapour deposition of graphene—Synthesis, characterisation, and applications: A review, Molecules 25(17) (2020) 3856, https://doi.org/10.3390/molecules25173856.

[200] P. Pareek, H. Dave, L. Ledwani, Microwave assisted modification of graphene oxide: Characterization and application for adsorptive removal of cationic dye, Materials Today: Proceedings 43 (2021) 3277-3285, https://doi.org/10.1016/j.matpr.2021.01.956.

[201] L. Agusu, L. Ahmad, M. Nurdin, S. Mitsudo, H. Kikuchi, Hydrothermal synthesis of reduced graphene oxide using urea as reduction agent: Excellent X-band electromagnetic absorption properties, IOP Conference Series: Materials Science and Engineering, IOP Publishing, 2018, pp. 012002, https://doi.org/10.1088/1757-899X/367/1/012002. .

[202] A. Yu, V. Chabot, J. Zhang, Electrochemical supercapacitors for energy storage and delivery: fundamentals and applications, Taylor & Francis, https://doi.org/10.1201/b14671.2013.

[203] M. Hamsan, S.B. Aziz, M. Kadir, M. Brza, W.O. Karim, The study of EDLC device fabricated from plasticized magnesium ion conducting chitosan based polymer electrolyte, Polymer Testing 90 (2020) 106714, https://doi.org/10.1016/j.polymertesting.2020.106714.

[204] R. Teimuri-Mofrad, R. Hadi, H. Abbasi, R. Fadakar Bajeh Baj, Synthesis, characterization and electrochemical study of carbon nanotube/chitosan-ferrocene nanocomposite electrode as supercapacitor material, Journal of Electronic Materials 48(7) (2019) 4573-4581, https://doi.org/10.1007/s11664-019-07226-2.

[205] S. Selvam, B. Balamuralitharan, S. Jegatheeswaran, M.-Y. Kim, S. Karthick, J.A. Raj, P. Boomi, M. Sundrarajan, K. Prabakar, H.-J. Kim, Electrolyte-imprinted graphene oxide–chitosan chelate with copper crosslinked composite electrodes for intense cyclic-stable, flexible supercapacitors, Journal of Materials Chemistry A 5(4) (2017) 1380-1386, https://doi.org/10.1039/C6TA09905J.

[206] X. Li, T. Zhao, Q. Chen, P. Li, K. Wang, M. Zhong, J. Wei, D. Wu, B. Wei, H. Zhu, Flexible all solid-state supercapacitors based on chemical vapor deposition derived graphene fibers, Physical Chemistry Chemical Physics 15(41) (2013) 17752-17757, https://doi.org/10.1039/C3CP52908H.

[207] I. Shown, A. Ganguly, L.C. Chen, K.H. Chen, Conducting polymer-based flexible supercapacitor, Energy Science & Engineering 3(1) (2015) 2-26, https://doi.org/10.1002/ese3.50.

[208] H.S. Jang, C.J. Raj, W.-G. Lee, B.C. Kim, K.H. Yu, Enhanced supercapacitive performances of functionalized activated carbon in novel gel polymer electrolytes with ionic liquid redox-mediated poly (vinyl alcohol)/phosphoric acid, RSC advances 6(79) (2016) 75376-75383, https://doi.org/10.1039/C6RA15070E.

[209] K. Sun, M. Dong, E. Feng, H. Peng, G. Ma, G. Zhao, Z. Lei, High performance solid state supercapacitor based on a 2-mercaptopyridine redox-mediated gel polymer, RSC Advances 5(29) (2015) 22419-22425, https://doi.org/10.1039/C4RA15484C.

[210] K. Sun, F. Ran, G. Zhao, Y. Zhu, Y. Zheng, M. Ma, X. Zheng, G. Ma, Z. Lei, High energy density of quasi-solid-state supercapacitor based on redox-mediated gel polymer electrolyte, RSC advances 6(60) (2016) 55225-55232, https://doi.org/10.1039/C6RA06797B.

[211] Y.-F. Huang, P.-F. Wu, M.-Q. Zhang, W.-H. Ruan, E.P. Giannelis, Boron cross-linked graphene oxide/polyvinyl alcohol nanocomposite gel electrolyte for flexible solid-state electric double layer capacitor with high performance, Electrochimica Acta 132 (2014) 103-111, https://doi.org/10.1016/j.electacta.2014.03.151.

[212] C.-S. Lim, K. H Teoh, H. M Ng, C.-W. Liew, S. Ramesh, Ionic conductivity enhancement studies of composite polymer electrolyte based on poly (vinyl alcohol)-lithium perchlorate-titanium oxide, Advanced Materials Letters 8(4) (2017) 465-471, https://doi.org/10.5185/amlett.2017.1410.

[213] M. Hashim, A. Khiar, Supercapacitor based on activated carbon and hybrid solid polymer electrolyte, Materials Research Innovations 15(sup2) (2011) s63-s66, https://doi.org/10.1179/143307511X13031890747813.

[214] S. Mallakpour, A. Abdolmaleki, S. Borandeh, Surface functionalization of GO, preparation and characterization of PVA/TRIS-GO nanocomposites, Polymer 81 (2015) 140-150, https://doi.org/10.1016/j.polymer.2015.11.005.

[215] H. Gao, K. Lian, High rate all-solid electrochemical capacitors using proton conducting polymer electrolytes, Journal of Power Sources 196(20) (2011) 8855-8857, https://doi.org/10.1016/j.jpowsour.2011.06.032.

[216] C.-C. Yang, S.-J. Chiu, K.-T. Lee, W.-C. Chien, C.-T. Lin, C.-A. Huang, Study of poly (vinyl alcohol)/titanium oxide composite polymer membranes and their application on alkaline direct alcohol fuel cell, Journal of Power Sources 184(1) (2008) 44-51, https://doi.org/10.1016/j.jpowsour.2008.06.011.

[217] M. Piszcz, O. Garcia-Calvo, U. Oteo, J.M.L. del Amo, C. Li, L.M. Rodriguez-Martinez, H.B. Youcef, N. Lago, J. Thielen, M. Armand, New single ion conducting

blend based on PEO and PA-LiTFSI, Electrochimica Acta 255 (2017) 48-54, https://doi.org/10.1016/j.electacta.2017.09.139.

[218] N. Yusoff, N. Idris, Ionic liquid based PVDF/PMMA gel polymer electrolyte for lithium rechargeable battery, Journal Of Mechanical Engineering And Sciences 11 (2017) 3152-3165, https://doi.org/10.15282/JMES.11.4.2017.18.0284.

[219] Q. Tang, H. Li, Y. Yue, Q. Zhang, H. Wang, Y. Li, P. Chen, 1-Ethyl-3-methylimidazolium tetrafluoroborate-doped high ionic conductivity gel electrolytes with reduced anodic reaction potentials for electrochromic devices, Materials & Design 118 (2017) 279-285, https://doi.org/10.1016/j.matdes.2017.01.033.

[220] Y. Li, K.W. Wong, Q. Dou, K.M. Ng, A single-ion conducting and shear-thinning polymer electrolyte based on ionic liquid-decorated PMMA nanoparticles for lithium-metal batteries, Journal of Materials Chemistry A 4(47) (2016) 18543-18550, https://doi.org/10.1039/C6TA09106G.

[221] J. He, J. Liu, J. Li, Y. Lai, X. Wu, Enhanced ionic conductivity and electrochemical capacity of lithium ion battery based on PVDF-HFP/HDPE membrane, Materials Letters 170 (2016) 126-129, https://doi.org/10.1016/j.matlet.2016.02.010.

[222] R. Muchakayala, S. Song, J. Wang, Y. Fan, M. Bengeppagari, J. Chen, M. Tan, Development and supercapacitor application of ionic liquid-incorporated gel polymer electrolyte films, Journal of industrial and engineering chemistry 59 (2018) 79-89, https://doi.org/10.1016/j.jiec.2017.10.009.

[223] P. Pal, A. Ghosh, Highly efficient gel polymer electrolytes for all solid-state electrochemical charge storage devices, Electrochimica Acta 278 (2018) 137-148, https://doi.org/10.1016/j.electacta.2018.05.025.

[224] H. Peng, Y. Lv, G. Wei, J. Zhou, X. Gao, K. Sun, G. Ma, Z. Lei, A flexible and self-healing hydrogel electrolyte for smart supercapacitor, Journal of Power Sources 431 (2019) 210-219, https://doi.org/10.1016/j.jpowsour.2019.05.058.

[225] J. Wu, G. Xia, S. Li, L. Wang, J. Ma, A flexible and self-healable gelled polymer electrolyte based on a dynamically cross-linked PVA ionogel for high-performance supercapacitors, Industrial & Engineering Chemistry Research 59(52) (2020) 22509-22519, https://doi.org/10.1021/acs.iecr.0c04741.

[226] K.-P. Wang, Y. Yang, Q. Zhang, Z. Xiao, L. Zong, T. Ichitsubo, L. Wang, Construction of supramolecular polymer hydrogel electrolyte with ionic channels for flexible supercapacitors, Materials Chemistry Frontiers 5(13) (2021) 5106-5114, https://doi.org/10.1039/D1QM00396H.

[227] S. Çavuş, E. Durgun, Poly (vinyl alcohol) based polymer gel electrolytes: investigation on their conductivity and characterization, Acta physica polonica A 129(4) (2016) 621-624, https://doi.org/10.12693/APhysPolA.129.621.

[228] K. Sun, E. Feng, G. Zhao, H. Peng, G. Wei, Y. Lv, G. Ma, A single robust hydrogel film based integrated flexible supercapacitor, ACS Sustainable Chemistry & Engineering 7(1) (2018) 165-173, https://doi.org/10.1021/acssuschemeng.8b02728.

[229] D. Li, Z. Xu, X. Ji, L. Liu, G. Gai, J. Yang, J. Wang, Deep insight into ionic transport in polyampholyte gel electrolytes towards high performance solid supercapacitors, Journal of Materials Chemistry A 7(27) (2019) 16414-16424, https://doi.org/10.1039/C9TA01208G.

[230] M. Gaele, F. Migliardini, T. Di Palma, Dual solid electrolytes for aluminium-air batteries based on polyvinyl alcohol acidic membranes and neutral hydrogels,

Journal of Solid State Electrochemistry 25(4) (2021) 1207-1216, https://doi.org/10.1007/s10008-021-04900-6.

[231] H. Du, Z. Wu, Y. Xu, S. Liu, H. Yang, Poly (3, 4-ethylenedioxythiophene) based solid-state polymer supercapacitor with ionic liquid gel polymer electrolyte, Polymers 12(2) (2020) 297, https://doi.org/10.3390/polym12020297.

[232] G. Ma, E. Feng, K. Sun, H. Peng, J. Li, Z. Lei, A novel and high-effective redox-mediated gel polymer electrolyte for supercapacitor, Electrochimica Acta 135 (2014) 461-466, https://doi.org/10.1016/j.electacta.2014.05.045.

[233] Y. Guo, K. Zheng, P. Wan, A flexible stretchable hydrogel electrolyte for healable all-in-one configured supercapacitors, Small 14(14) (2018) 1704497, https://doi.org/10.1002/smll.201704497.

[234] C. Meng, C. Liu, L. Chen, C. Hu, S. Fan, Highly flexible and all-solid-state paperlike polymer supercapacitors, Nano letters 10(10) (2010) 4025-4031, https://doi.org/10.1021/nl1019672.

[235] X. Hu, L. Fan, G. Qin, Z. Shen, J. Chen, M. Wang, J. Yang, Q. Chen, Flexible and low temperature resistant double network alkaline gel polymer electrolyte with dual-role KOH for supercapacitor, Journal of Power Sources 414 (2019) 201-209, https://doi.org/10.1016/j.jpowsour.2019.01.006.

[236] D. He, A.J. Marsden, Z. Li, R. Zhao, W. Xue, M.A. Bissett, Fabrication of a graphene-based paper-like electrode for flexible solid-state supercapacitor devices, Journal of The Electrochemical Society 165(14) (2018) A3481, http://doi.org/10.1149/2.1041814jes.

[237] M. Gao, L. Wang, B. Zhao, X. Gu, T. Li, L. Huang, Q. Wu, S. Yu, S. Liu, Sandwich construction of chitosan/reduced graphene oxide composite as additive-free electrode material for high-performance supercapacitors, Carbohydrate Polymers 255 (2021) 117397, https://doi.org/10.1016/j.carbpol.2020.117397.

[238] A. Qian, K. Zhuo, P. Karthick Kannan, C.-H. Chung, Neutral pH gel electrolytes for V2O5· 0.5 H2O-based energy storage devices, ACS Applied Materials & Interfaces 8(50) (2016) 34455-34463, https://doi.org/10.1021/acsami.6b12672.

[239] X. Wang, Y. Zhang, J. Jin, H. Wu, A. Liu, Three-dimensional chitosan/graphene aerogel with vertical alignment for high-performance all-solid-state supercapacitors, Functional Materials Letters 14(06) (2021) 2150024, https://doi.org/10.1142/S1793604721500247.

[240] P. Song, X. He, M. Xie, J. Tao, X. Shen, Z. Ji, Z. Yan, L. Zhai, A. Yuan, Polyaniline wrapped graphene functionalized textile with ultrahigh areal capacitance and energy density for high-performance all-solid-state supercapacitors for wearable electronics, Composites Science and Technology 198 (2020) 108305, https://doi.org/10.1016/j.compscitech.2020.108305.

[241] Ö. SADAK, Symmetric Supercapacitor Application of Electrochemically Exfoliated Graphene–Chitosan Hydrogel, Avrupa Bilim ve Teknoloji Dergisi (33) 133-137, https://doi.org/10.31590/ejosat.1036869.

[242] M. Genovese, H. Wu, A. Virya, J. Li, P. Shen, K. Lian, Ultrathin all-solid-state supercapacitor devices based on chitosan activated carbon electrodes and polymer electrolytes, Electrochimica Acta 273 (2018) 392-401, https://doi.org/10.1016/j.electacta.2018.04.061.

[243] H. Vijeth, S. Ashokkumar, L. Yesappa, M. Vandana, H. Devendrappa, Hybrid core-shell nanostructure made of chitosan incorporated polypyrrole nanotubes decorated with NiO for all-solid-state symmetric supercapacitor application,

Electrochimica Acta 354 (2020) 136651, https://doi.org/10.1016/j.electacta.2020.136651.

[244] C.-H. Tseng, H.-H. Lin, C.-W. Hung, I.-C. Cheng, S.-C. Luo, I.-C. Cheng, J.-Z. Chen, Electropolymerized poly (3, 4-ethylenedioxythiophene)/screen-printed reduced graphene oxide–chitosan bilayer electrodes for flexible supercapacitors, ACS omega 6(25) (2021) 16455-16464, https://doi.org/10.1021/acsomega.1c01601.

[245] C. Jiang, M. Gao, S. Zhang, S. Yu, L. Huang, Construction of Chitosan/Graphene Oxide Hybrid Hydrogel Electrode with Conductive Porous Network for High Energy Density Flexible Supercapacitor, SSRN Electronic Journal, 2022, https://doi.org/10.2139/ssrn.4105397.

[246] N. Chadha, M.Y. Bhat, S. Hashmi, P. Saini, Fe3O4/graphene-oxide/chitosan hybrid aerogel based high performance supercapacitor: effect of aqueous electrolytes on storage capacity & cell stability, Journal of Energy Storage 46 (2022) 103789, https://doi.org/10.1016/j.est.2021.103789.

[247] M.F. El-Kady, V. Strong, S. Dubin, R.B. Kaner, Laser scribing of high-performance and flexible graphene-based electrochemical capacitors, Science 335(6074) (2012) 1326-1330, https://doi.org/10.1126/science.1216744.

[248] Y. Shao, M.F. El-Kady, C.W. Lin, G. Zhu, K.L. Marsh, J.Y. Hwang, Q. Zhang, Y. Li, H. Wang, R.B. Kaner, 3D freeze-casting of cellular graphene films for ultrahigh-power-density supercapacitors, Advanced Materials 28(31) (2016) 6719-6726, https://doi.org/10.1002/adma.201506157.

[249] Y. Liu, B. Weng, J.M. Razal, Q. Xu, C. Zhao, Y. Hou, S. Seyedin, R. Jalili, G.G. Wallace, J. Chen, High-performance flexible all-solid-state supercapacitor from large free-standing graphene-PEDOT/PSS films, Scientific reports 5(1) (2015) 1-11, https://doi.org/10.1038/srep17045.

[250] H. Li, Y. Hou, F. Wang, M.R. Lohe, X. Zhuang, L. Niu, X. Feng, Flexible all-solid-state supercapacitors with high volumetric capacitances boosted by solution processable MXene and electrochemically exfoliated graphene, Adv. Energy Mater . 2017, 7, 1601847, https://doi.org/10.1002/aenm.201601847.

[251] L. Huang, C. Li, G. Shi, High-performance and flexible electrochemical capacitors based on graphene/polymer composite films, Journal of Materials Chemistry A 2(4) (2014) 968-974, https://doi.org/10.1039/C3TA14511E.

[252] K. Song, H. Ni, L.-Z. Fan, Flexible graphene-based composite films for supercapacitors with tunable areal capacitance, Electrochimica Acta 235 (2017) 233-241, https://doi.org/10.1016/j.electacta.2017.03.065.

[253] L. Sheng, J. Chang, L. Jiang, Z. Jiang, Z. Liu, T. Wei, Z. Fan, Multilayer-folded graphene ribbon film with ultrahigh areal capacitance and high rate performance for compressible supercapacitors, Advanced Functional Materials 28(21) (2018) 1800597, https://doi.org/10.1002/adfm.201800597.

[254] F. Chen, P. Wan, H. Xu, X. Sun, Flexible transparent supercapacitors based on hierarchical nanocomposite films, ACS applied materials & interfaces 9(21) (2017) 17865-17871, https://doi.org/10.1021/acsami.7b02460.

[255] J. Zang, C. Cao, Y. Feng, J. Liu, X. Zhao, Stretchable and high-performance supercapacitors with crumpled graphene papers, Scientific reports 4(1) (2014) 1-7, https://doi.org/10.1038/srep06492.

[256] Z. Weng, Y. Su, D.W. Wang, F. Li, J. Du, H.M. Cheng, Graphene–cellulose paper flexible supercapacitors, Advanced Energy Materials 1(5) (2011) 917-922, https://doi.org/10.1002/aenm.201100312.

[257] Y. Xu, Z. Lin, X. Huang, Y. Liu, Y. Huang, X. Duan, Flexible solid-state supercapacitors based on three-dimensional graphene hydrogel films, ACS nano 7(5) (2013) 4042-4049, https://doi.org/10.1021/nn4000836.

[258] Z.Y.L. Y. X. Xu, X. Q. Huang, Y. Wang, Y. Huang and X. F. Duan, , Functionalized Graphene Hydrogel-Based High-Performance Supercapacitors, Adv. Mater., 2013, 25, 5779–5784, https://doi.org/10.1002/adma.201301928.

[259] X. Wu, M. Lian, Highly flexible solid-state supercapacitor based on graphene/polypyrrole hydrogel, Journal of Power Sources 362 (2017) 184-191, https://doi.org/10.1016/j.jpowsour.2017.07.042.

[260] X. Liu, S. Zou, K. Liu, C. Lv, Z. Wu, Y. Yin, T. Liang, Z. Xie, Highly compressible three-dimensional graphene hydrogel for foldable all-solid-state supercapacitor, Journal of Power Sources 384 (2018) 214-222, https://doi.org/10.1016/j.jpowsour.2018.02.087.

[261] Z.S. Wu, A. Winter, L. Chen, Y. Sun, A. Turchanin, X. Feng, K. Müllen, Three-dimensional nitrogen and boron co-doped graphene for high-performance all-solid-state supercapacitors, Advanced Materials 24(37) (2012) 5130-5135, https://doi.org/10.1002/adma.201201948.

[262] H.Z.Z. Z. H. Pan, Y. C. Qiu, J. Yang, L. D. Xing, Q. C. Zhang, X. Y. Ding, X. S. Wang, G. G. Xu, H. Yuan, M. Chen, W. F. Li, Y. G. Yao, N. Motta, M. N. Liu and Y. G. Zhang, , Achieving commercial-level mass loading in ternary-doped holey graphene hydrogel electrodes for ultrahigh energy density supercapacitors,, Nano Energy, 2018, 46, 266–276, https://doi.org/10.1016/j.nanoen.2018.02.007.

[263] L. Xu, M. Jia, Y. Li, X. Jin, F. Zhang, High-performance MnO2-deposited graphene/activated carbon film electrodes for flexible solid-state supercapacitor, Scientific reports 7(1) (2017) 1-9, https://doi.org/10.1038/s41598-017-11267-0.

[264] N. Hu, L. Zhang, C. Yang, J. Zhao, Z. Yang, H. Wei, H. Liao, Z. Feng, A. Fisher, Y. Zhang, Three-dimensional skeleton networks of graphene wrapped polyaniline nanofibers: an excellent structure for high-performance flexible solid-state supercapacitors, Scientific reports 6(1) (2016) 1-10, https://doi.org/10.1038/srep19777.

[265] L. Liu, Z. Niu, L. Zhang, W. Zhou, X. Chen, S. Xie, Nanostructured graphene composite papers for highly flexible and foldable supercapacitors, Advanced Materials 26(28) (2014) 4855-4862, https://doi.org/10.1002/adma.201401513.

[266] N. Li, T. Lv, Y. Yao, H. Li, K. Liu, T. Chen, Compact graphene/MoS 2 composite films for highly flexible and stretchable all-solid-state supercapacitors, Journal of Materials Chemistry A 5(7) (2017) 3267-3273, https://doi.org/10.1039/C6TA10165H.

[267] M.M. Gudarzi, M.H.M. Moghadam, F. Sharif, Spontaneous exfoliation of graphite oxide in polar aprotic solvents as the route to produce graphene oxide–organic solvents liquid crystals, Carbon 64 (2013) 403-415, https://doi.org/10.1016/j.carbon.2013.07.093.

[268] M. Tas, Y. Altin, A.C. Bedeloglu, Reduction of graphene oxide thin films using a stepwise thermal annealing assisted by L-ascorbic acid, Diamond and Related Materials 92 (2019) 242-247, https://doi.org/10.1016/j.diamond.2019.01.009.

[269] V.M. Vaz, L. Kumar, 3D Printing as a Promising Tool in Personalized Medicine, AAPS PharmSciTech 22(1) (2021) 1-20, https://doi.org/10.1208/s12249-020-01905-8.

[270] J. Krause, L. Müller, D. Sarwinska, A. Seidlitz, M. Sznitowska, W. Weitschies, 3D Printing of Mini Tablets for Pediatric Use, Pharmaceuticals 14(2) (2021) 143, https://doi.org/10.3390/ph14020143.

[271] B.G. Compton, J.A. Lewis, 3D-printing of lightweight cellular composites, Advanced materials 26(34) (2014) 5930-5935, https://doi.org/10.1002/adma.201401804.

[272] A. Monshi, M.R. Foroughi, M.R. Monshi, Modified Scherrer equation to estimate more accurately nano-crystallite size using XRD, World journal of nano science and engineering 2(3) (2012) 154-160, https://doi.org/10.4236/wjnse.2012.23020.

[273] M.W. Davidson, M. Abramowitz, Optical microscopy, Encyclopedia of imaging science and technology 2(1106-1141) (2002) 120.

[274] J. Mertz, Introduction to optical microscopy, Cambridge University Press2019.

[275] S.B. Aziz, R.M. Abdullah, Crystalline and amorphous phase identification from the tanδ relaxation peaks and impedance plots in polymer blend electrolytes based on [CS: AgNt] x: PEO (x-1)(10≤ x≤ 50), Electrochimica Acta 285 (2018) 30-46, https://doi.org/10.1016/j.electacta.2018.07.233.

[276] K. Radha, S. Selvasekarapandian, S. Karthikeyan, M. Hema, C. Sanjeeviraja, Synthesis and impedance analysis of proton-conducting polymer electrolyte PVA: NH 4 F, Ionics 19 (2013) 1437-1447, https://doi.org/10.1007/s11581-013-0866-5.

[277] G. Instruments, Application Note, (2011). A snapshot of electrochemical impedance spectroscopy.

[278] K. Deshmukh, M.B. Ahamed, A.R. Polu, K.K. Sadasivuni, S.K. Pasha, D. Ponnamma, M.A.-A. AlMaadeed, R.R. Deshmukh, K. Chidambaram, Impedance spectroscopy, ionic conductivity and dielectric studies of new Li+ ion conducting polymer blend electrolytes based on biodegradable polymers for solid state battery applications, Journal of Materials Science: Materials in Electronics 27(11) (2016) 11410-11424, https://doi.org/10.1007/s10854-016-5267-x.

[279] M. Hou, M. Xu, B. Li, Enhanced electrical conductivity of cellulose nanofiber/graphene composite paper with a sandwich structure, ACS Sustainable Chemistry & Engineering 6(3) (2018) 2983-2990, https://doi.org/10.1021/acssuschemeng.7b02683.

[280] P. Campbell, M. Merrill, B. Wood, E. Montalvo, M. Worsley, T. Baumann, J. Biener, Battery/supercapacitor hybrid via non-covalent functionalization of graphene macro-assemblies, Journal of Materials Chemistry A 2(42) (2014) 17764-17770, https://doi.org/10.1039/C4TA03605K.

[281] B.K. Kim, S. Sy, A. Yu, J. Zhang, Electrochemical supercapacitors for energy storage and conversion, Handbook of clean energy systems (2015) 1-25.

[282] S.S. Brian Kihun Kim, Aiping Yu, Jinjun Zhang, Electrochemical supercapacitors for energy storage and conversion, Handbook of Clean Energy Systems, (2015, https://doi.org/10.1002/9781118991978.hces112.).

[283] G.A. Mabbott, An introduction to cyclic voltammetry, Journal of Chemical education, 60(1983) 697, https://doi.org/10.1021/ed060p697.

[284] Y. Zhu, S. Murali, M.D. Stoller, K. Ganesh, W. Cai, P.J. Ferreira, A. Pirkle, R.M. Wallace, K.A. Cychosz, M. Thommes, Carbon-based supercapacitors produced by activation of graphene, science 332(6037) (2011) 1537-1541, https://doi.org/10.1126/science.1200770.

[285] F. Marken, A. Neudeck, A.M. Bond, Cyclic voltammetry, Electroanalytical Methods: Guide to Experiments and Applications (2010) 57-106, https://doi.org/10.1007/978-3-662-04757-6_4.

[286] M.D. K. Sun, E. Feng, H. Peng, G. Ma, G. Zhao, Z. Lei, , High performance solid state supercapacitor based on a 2-mercaptopyridine redox-mediated gel polymer, RSC Adv., 2015,5, 22419-22425, https://doi.org/10.1039/C4RA15484C.

[287] A. Pan, S.G. Roy, U. Haldar, R.D. Mahapatra, G.R. Harper, W.L. Low, P. De, J.G. Hardy, Uptake and release of species from carbohydrate containing organogels and hydrogels, Gels 5(4) (2019) 43, https://doi.org/10.3390/gels5040043.

[288] S. Bhattacharya, A. Nair, A. Bag, P. Kumar Ghorai, R. Shunmugam, Engineering photo cross-linked porous network for efficient and selective removal of toxicants from wastewater, MOJ Res. Rev 2 (2019) 69-81, https://doi.org/10.15406/mojcrr.2019.02.00058.

[289] A. Mohamad, N. Mohamed, M. Yahya, R. Othman, S. Ramesh, Y. Alias, A. Arof, Ionic conductivity studies of poly (vinyl alcohol) alkaline solid polymer electrolyte and its use in nickel–zinc cells, Solid State Ionics 156(1-2) (2003) 171-177, https://doi.org/10.1016/S0167-2738(02)00617-3.

[290] Y. Farrag, L. Barral, O. Gualillo, D. Moncada, B. Montero, M. Rico, R. Bouza, Effect of Different Plasticizers on Thermal, Crystalline, and Permeability Properties of Poly (3–hydroxybutyrate–co− 3–hydroxyhexanoate) Films, Polymers 14(17) (2022) 3503, https://doi.org/10.3390/polym14173503.

[291] K. Kamani, B. Madhu, M. Nethravathi, S. Ashwini, The electrical and optical studies of the KC1 doped PVA polymer electrolyte materials, AIP Conference Proceedings, American Institute of Physics, 2013, pp. 873-874, https://doi.org/10.1063/1.4810506.

[292] B. Beenarani, C.P. Sugumaran, A flexible, cost-effective, and eco-friendly solid state supercapacitor based on PVA/KCl/Carbon black nanocomposite, Ionics 26 (2020) 1465-1473, https://doi.org/10.1007/s11581-019-03307-8.

[293] B. Kumar, G. Kaur, S. Rai, Sensitized green emission of terbium with dibenzoylmethane and 1, 10 phenanthroline in polyvinyl alcohol and polyvinyl pyrrolidone blends, Spectrochimica Acta Part A: Molecular and Biomolecular Spectroscopy 187 (2017) 75-81, https://doi.org/10.1016/j.saa.2017.06.025.

[294] K. Deshmukh, M.B. Ahamed, R.R. Deshmukh, P.R. Bhagat, S.K. Pasha, A. Bhagat, R. Shirbhate, F. Telare, C. Lakhani, Influence of K2CrO4 doping on the structural, optical and dielectric properties of polyvinyl alcohol/K2CrO4 composite films, Polymer-Plastics Technology and Engineering 55(3) (2016) 231-241, https://doi.org/10.1080/03602559.2015.1055499.

[295] A.A.A. Ahmed, A.M. Al-Hussam, A.M. Abdulwahab, A.N.A.A. Ahmed, The impact of sodium chloride as dopant on optical and electrical properties of polyvinyl alcohol, AIMS Materials Science 5(3) (2018) 533-542, https://doi.org/10.3934/matersci.2018.3.533.

[296] Z. Zhao, Y. Huang, F. Qiu, W. Ren, C. Zou, X. Li, M. Wang, Y. Lin, A new environmentally friendly gel polymer electrolyte based on cotton-PVA composited membrane for alkaline supercapacitors with increased operating voltage, Journal of Materials Science 56 (2021) 11027-11043, https://doi.org/10.1007/s10853-021-05987-y.

[297] R. Hodge, G.H. Edward, G.P. Simon, Water absorption and states of water in semicrystalline poly (vinyl alcohol) films, Polymer 37(8) (1996) 1371-1376, https://doi.org/10.1016/0032-3861(96)81134-7.

[298] V.M. Mohan, V. Raja, A. Sharma, V.N. Rao, Ionic conductivity and discharge characteristics of solid-state battery based on novel polymer electrolyte (PEO+ NaBiF4), Materials Chemistry and Physics 94(2-3) (2005) 177-181, https://doi.org/10.1016/j.matchemphys.2005.05.030.

[299] A. Kharazmi, N. Faraji, R.M. Hussin, E. Saion, W.M.M. Yunus, K. Behzad, Structural, optical, opto-thermal and thermal properties of ZnS–PVA nanofluids synthesized through a radiolytic approach, Beilstein journal of nanotechnology 6(1) (2015) 529-536, https://doi.org/10.3762/bjnano.6.55.

[300] I.M. Jipa, A. Stoica, M. Stroescu, L.-M. Dobre, T. Dobre, S. Jinga, C. Tardei, Potassium sorbate release from poly (vinyl alcohol)-bacterial cellulose films, Chemical Papers 66 (2012) 138-143, https://doi.org/10.2478/s11696-011-0068-4.

[301] N. Choudhury, A. Shukla, S. Sampath, S. Pitchumani, Cross-linked polymer hydrogel electrolytes for electrochemical capacitors, Journal of The Electrochemical Society 153(3) (2006) A614, https://doi.org/10.1149/1.2164810.

[302] X. Cheng, J. Pan, Y. Zhao, M. Liao, H. Peng, Gel polymer electrolytes for electrochemical energy storage, Advanced Energy Materials 8(7) (2018) 1702184, https://doi.org/10.1002/aenm.201702184.

[303] A.D. Azzahari, V. Selvanathan, M. Rizwan, F. Sonsudin, R. Yahya, Conductivity or rheology? Tradeoff for competing properties in the fabrication of a gel polymer electrolyte based on chitosan-barbiturate derivative, Ionics 24(10) (2018) 3015-3025, https://doi.org/10.1007/s11581-018-2515-5.

[304] T. Kittikorn, W. Chaiwong, E. Stromberg, R.M. Torro, M. Ek, S. Karlsson, Enhancement of interfacial adhesion and engineering properties of polyvinyl alcohol/polylactic acid laminate films filled with modified microfibrillated cellulose, Journal of Plastic Film & Sheeting 36(4) (2020) 368-390, https://doi.org/10.1177/875608792091574.

[305] S.K. Sahoo, J.R. Mohanty, S. Nayak, S.K. Khuntia, P.K. Jena, K.R. Panda, R. Sahu, Effectiveness of rattan fiber as a reinforcing material in polymer matrix composites: an experimental study, Journal of Natural Fibers 19(13) (2022) 6615-6624, https://doi.org/10.1080/15440478.2021.1929650. .

[306] P.R.H. M. Martini M., E. Charmicheal, H.S.S. Sharma, , Preparation and Characterisation of Cellulose Nanofibres Reinforced Polymer Composites, Australian Journal of Basic and Applied Sciences, 8(4) Special 2014, Pages: 577-592. http://ajbasweb.com/old/ajbas/2014/Special/577-592.pdf.

[307] E. Rynkowska, K. Fatyeyeva, S. Marais, J. Kujawa, W. Kujawski, Chemically and thermally crosslinked PVA-based membranes: effect on swelling and transport behavior, Polymers 11(11) (2019) 1799, https://doi.org/10.3390/polym11111799.

[308] K. Hasan, S. Bashir, R. Subramaniam, R. Kasi, K. Kamran, J. Iqbal, H. Algarni, A.G. Al-Sehemi, S. Wageh, M. Pershaanaa, Poly (Vinyl Alcohol)/Agar Hydrogel Electrolytes Based Flexible All-in-One Supercapacitors with Conducting Polyaniline/Polypyrrole Electrodes, Polymers 14(21) (2022) 4784, https://doi.org/10.3390/polym14214784.

[309] S. Nayak, J.R. Mohanty, Study of mechanical, thermal, and rheological properties of areca fiber-reinforced polyvinyl alcohol composite, Journal of Natural Fibers (2018) Journal of Natural Fibers 16(5):1-14, https://doi.org/10.1080/15440478.2018.1432000.

[310] F. Saeedi, A. Montazeri, Y. Bahari, M. Pishvaei, B. Jannat, A study on the viscoelastic behavior of chitosan-polyvinyl alcohol-graphene oxide nanocomposite films as a wound dressing, Polymers and Polymer Composites 29(8) (2021) 1259-1272, https://doi.org/10.1177/09673911209623.

[311] B.N. Hoang, T.T. Nguyen, Q.P.T. Bui, L.G. Bach, D.V.N. Vo, C.D. Trinh, X.T. Bui, T.D. Nguyen, Enhanced selective adsorption of cation organic dyes on polyvinyl alcohol/agar/maltodextrin water-resistance biomembrane, Journal of Applied Polymer Science 137(30) (2020) 48904, https://doi.org/10.1002/app.48904.

[312] S. Madhuri, K. Hemalatha, K. Rukmani, Preparation and investigation of suitability of gadolinium oxide nanoparticle doped polyvinyl alcohol films for optoelectronic applications, Journal of Materials Science: Materials in Electronics 30 (2019) 9051-9063, https://doi.org/10.1007/s10854-019-01237-9.

[313] M.A. Norouzi, M. Montazer, T. Harifi, P. Karimi, Flower buds like PVA/ZnO composite nanofibers assembly: Antibacterial, in vivo wound healing, cytotoxicity and histological studies, Polymer testing 93 (2021) 106914, https://doi.org/10.1016/j.polymertesting.2020.106914.

[314] K. Chen, Y. Ling, C. Cao, X. Li, X. Chen, X. Wang, Chitosan derivatives/reduced graphene oxide/alginate beads for small-molecule drug delivery, Materials Science and Engineering: C 69 (2016) 1222-1228, https://doi.org/10.1016/j.msec.2016.08.036.

[315] V. Karthika, M.S. AlSalhi, S. Devanesan, K. Gopinath, A. Arumugam, M. Govindarajan, Chitosan overlaid Fe3O4/rGO nanocomposite for targeted drug delivery, imaging, and biomedical applications, Scientific Reports 10(1) (2020) 18912, https://doi.org/10.1038/s41598-020-76015-3.

[316] R. Hidayat, S. Wahyuningsih, A. Ramelan, Simple synthesis of rGO (reduced graphene oxide) by thermal reduction of GO (graphene oxide), IOP Conference Series: Materials Science and Engineering, IOP Publishing, 2020, pp. 012009, https://doi.org/10.1088/1757-899X/858/1/012009.

[317] S.H. Aboutalebi, M.M. Gudarzi, Q.B. Zheng, J.-K. Kim, Spontaneous Formation of Liquid Crystals in Ultralarge Graphene Oxide Dispersions, Advanced Functional Materials 21(15) (2011) 2978-2988.

[318] R. Jalili, S.H. Aboutalebi, D. Esrafilzadeh, K. Konstantinov, J.M. Razal, S.E. Moulton, G.G. Wallace, Formation and processability of liquid crystalline dispersions of graphene oxide, Materials Horizons 1(1) (2014) 87-91, https://doi.org/10.1039/C3MH00050H.

[319] C. Shen, H. Chen, S. Wu, Y. Wen, L. Li, Z. Jiang, M. Li, W. Liu, Highly efficient detoxification of Cr (VI) by chitosan–Fe (III) complex: process and mechanism studies, Journal of hazardous materials 244 (2013) 689-697, https://doi.org/10.1016/j.jhazmat.2012.10.061.

[320] A.T. Chidembo, S.H. Aboutalebi, K. Konstantinov, D. Wexler, H.K. Liu, S.X. Dou, Liquid crystalline dispersions of graphene-oxide-based hybrids: a practical approach towards the next generation of 3D isotropic architectures for energy storage applications, Particle & Particle Systems Characterization 31(4) (2014) 465-473, https://doi.org/10.1002/ppsc.201300254.

[321] S. Yasmeen, M.K. Kabiraz, B. Saha, M. Qadir, M. Gafur, S. Masum, Chromium (VI) ions removal from tannery effluent using chitosan-microcrystalline cellulose composite as adsorbent, Int. Res. J. Pure Appl. Chem 10(4) (2016) 1-14, https://doi.org/10.9734/IRJPAC/2016/23315. .

[322] N. Kumar, S. Das, C. Bernhard, G. Varma, Effect of graphene oxide doping on superconducting properties of bulk MgB2, Superconductor Science and Technology 26(9) (2013) 095008, https://doi.org/10.1088/0953-2048/26/9/095008.

[323] T.F. Emiru, D.W. Ayele, Controlled synthesis, characterization and reduction of graphene oxide: A convenient method for large scale production, Egyptian Journal of Basic and Applied Sciences 4(1) (2017) 74-79, https://doi.org/10.1016/j.ejbas.2016.11.002.

[324] S.H. Aboutalebi, A.T. Chidembo, M. Salari, K. Konstantinov, D. Wexler, H.K. Liu, S.X. Dou, Comparison of GO, GO/MWCNTs composite and MWCNTs as potential electrode materials for supercapacitors, Energy & Environmental Science 4(5) (2011) 1855-1865, https://doi.org/10.1039/C1EE01039E.

[325] A. Javed, S.R. Abbas, M.U. Hashmi, N.U.A. Babar, I. Hussain, Graphene oxide based electrochemical genosensor for label free detection of Mycobacterium tuberculosis from raw clinical samples, International Journal of Nanomedicine (2021) 7339-7352, https://doi.org/10.2147/IJN.S326480.

[326] Y. Areerob, C. Hamontree, P. Sricharoen, N. Limchoowong, S. Laksee, W.-C. Oh, K. Pattarith, Novel gamma-irradiated chitosan-doped reduced graphene-CuInS 2 composites as counter electrodes for dye-sensitized solar cells, RSC advances 12(24) (2022) 15427-15434, https://doi.org/10.1039/D2RA01749K.

[327] W. Wang, Q. Meng, Q. Li, J. Liu, M. Zhou, Z. Jin, K. Zhao, Chitosan derivatives and their application in biomedicine, International journal of molecular sciences 21(2) (2020) 487, https://doi.org/10.3390/ijms21020487.

[328] F. Emadi, A. Amini, A. Gholami, Y. Ghasemi, Functionalized graphene oxide with chitosan for protein nanocarriers to protect against enzymatic cleavage and retain collagenase activity, Scientific reports 7(1) (2017) 1-13, https://doi.org/10.1038/srep42258.

[329] J. Chang, X. Zhou, Q. Zhao, W. Cao, M. Zhang, J. Yuan, Reduced graphene oxide-poly (ionic liquid) composite films of high mechanical performance, Frontiers in Materials 8 (2021) 635987, https://doi.org/10.3389/fmats.2021.635987.

[330] Q. Chen, J.D. Mangadlao, J. Wallat, A. De Leon, J.K. Pokorski, R.C. Advincula, 3D printing biocompatible polyurethane/poly (lactic acid)/graphene oxide nanocomposites: anisotropic properties, ACS applied materials & interfaces 9(4) (2017) 4015-4023, https://doi.org/10.1021/acsami.6b11793.

[331] Z.-R. Yu, S.-N. Li, J. Zang, M. Zhang, L.-X. Gong, P. Song, L. Zhao, G.-D. Zhang, L.-C. Tang, Enhanced mechanical property and flame resistance of graphene oxide nanocomposite paper modified with functionalized silica nanoparticles, Composites Part B: Engineering 177 (2019) 107347, https://doi.org/10.1016/j.compositesb.2019.107347.

[332] B.K. Roy, I. Tahmid, T.U. Rashid, Chitosan-based materials for supercapacitor applications: a review, Journal of Materials Chemistry A 9(33) (2021) 17592-17642, https://doi.org/10.1039/D1TA02997E.

[333] P. Terzioglu, Y. Altin, A. Kalemtas, A. Celik Bedeloglu, Graphene oxide and zinc oxide decorated chitosan nanocomposite biofilms for packaging applications, Journal of Polymer Engineering 40(2) (2020) 152-157, https://doi.org/10.1515/polyeng-2019-0240.

[334] E. Kim, X. Qin, J.B. Qiao, Q. Zeng, J.D. Fortner, F. Zhang, Graphene oxide/mussel foot protein composites for high-strength and ultra-tough thin films, Scientific reports 10(1) (2020) 19082, https://doi.org/10.1038/s41598-020-76004-6.

[335] S. Gea, J. Sari, R. Bulan, A. Piliang, S. Amaturrahim, Y. Hutapea, Chitosan/graphene oxide biocomposite film from pencil rod, Journal of Physics: Conference Series, IOP Publishing, 2018, pp. 012006, https://doi.org/10.1088/1742-6596/970/1/012006.

[336] A. Mirabedini, J. Foroughi, B. Thompson, G.G. Wallace, Fabrication of Coaxial Wet-Spun Graphene–Chitosan Biofibers, Advanced Engineering Materials 18(2) (2016) 284-293, https://doi.org/10.1002/adem.201500201.

[337] I. Fajriati, M. Mudasir, E.T. Wahyuni, Adsorption and photodegradation of cationic and anionic dyes by TiO 2-chitosan nanocomposite, Indonesian Journal of Chemistry 19(2) (2019) 441-453.

[338] M. Khalfaoui, S. Knani, M. Hachicha, A.B. Lamine, New theoretical expressions for the five adsorption type isotherms classified by BET based on statistical physics treatment, Journal of colloid and interface science 263(2) (2003) 350-356.

[339] Y. Belaustegui, I. Rincón, F. Fernández-Carretero, P. Azpiroz, A. García-Luís, D.A.P. Tanaka, Three-dimensional reduced graphene oxide decorated with iron oxide nanoparticles as efficient active material for high performance capacitive deionization electrodes, Chemical Engineering Journal Advances 6 (2021) 100094.

[340] D. Chen, L. Li, L. Guo, An environment-friendly preparation of reduced graphene oxide nanosheets via amino acid, Nanotechnology 22(32) (2011) 325601, http://doi.org/10.1088/0957-4484/22/32/325601.

[341] S. Yang, W. Yue, D. Huang, C. Chen, H. Lin, X. Yang, A facile green strategy for rapid reduction of graphene oxide by metallic zinc, Rsc Advances 2(23) (2012) 8827-8832, http://doi.org/10.1039/C2RA20746J.

[342] N. Behabtu, J.R. Lomeda, M.J. Green, A.L. Higginbotham, A. Sinitskii, D.V. Kosynkin, D. Tsentalovich, A.N.G. Parra-Vasquez, J. Schmidt, E. Kesselman, Y. Cohen, Y. Talmon, J.M. Tour, M. Pasquali, Spontaneous high-concentration dispersions and liquid crystals of graphene, Nat Nano 5(6) (2010) 406-411.

[343] J.E. Kim, T.H. Han, S.H. Lee, J.Y. Kim, C.W. Ahn, J.M. Yun, S.O. Kim, Graphene Oxide Liquid Crystals, Angewandte Chemie International Edition 50(13) (2011) 3043-3047.

[344] Z. Xu, C. Gao, Aqueous Liquid Crystals of Graphene Oxide, ACS Nano 5(4) (2011) 2908-2915.

[345] Z. Xu, C. Gao, Graphene chiral liquid crystals and macroscopic assembled fibres, Nat Commun 2 (2011) 571.

[346] Q. Zheng, W.H. Ip, X. Lin, N. Yousefi, K.K. Yeung, Z. Li, J.-K. Kim, Transparent Conductive Films Consisting of Ultralarge Graphene Sheets Produced by Langmuir–Blodgett Assembly, ACS Nano 5(7) (2011) 6039-6051.

[347] V.A. Davis, A.N.G. Parra-Vasquez, M.J. Green, P.K. Rai, N. Behabtu, V. Prieto, R.D. Booker, J. Schmidt, E. Kesselman, W. Zhou, H. Fan, W.W. Adams, R.H. Hauge, J.E. Fischer, Y. Cohen, Y. Talmon, R.E. Smalley, M. Pasquali, True solutions of single-walled carbon nanotubes for assembly into macroscopic materials, Nat Nano 4(12) (2009) 830-834.

[348] H.R.M. Kobra Gerani, and Babak Mokhtarani Enhancement in Performance of Sulfonated PES Cation-Exchange Membrane by Introducing Pristine and Sulfonated Graphene Oxide Nanosheets Synthesized through Hummers and Staudenmaier Methods POLYMER-PLASTICS TECHNOLOGY AND

ENGINEERING 2017, VOL. 56, NO. 5, 543–555, http://dx.doi.org/10.1080/03602559.2016.1233260. .

[349] D. Lin, Y. Liu, Z. Liang, H.-W. Lee, J. Sun, H. Wang, K. Yan, J. Xie, Y. Cui, Layered reduced graphene oxide with nanoscale interlayer gaps as a stable host for lithium metal anodes, Nature nanotechnology 11(7) (2016) 626-632, https://doi.org/10.1038/nnano.2016.32.

[350] A. Shalaby, D. Nihtianova, P. Markov, A. Staneva, R. Iordanova, Y. Dimitriev, Structural analysis of reduced graphene oxide by transmission electron microscopy, Bulgarian Chemical Communications 47(1) (2015) 291-295.

[351] S. Azizighannad, S. Mitra, Stepwise reduction of graphene oxide (GO) and its effects on chemical and colloidal properties, Scientific reports 8(1) (2018) 1-8, https://doi.org/10.1038/s41598-018-28353-6.

[352] C. Jiang, M. Gao, S. Zhang, L. Huang, S. Yu, Z. Song, Q. Wu, Chitosan/graphene oxide hybrid hydrogel electrode with porous network boosting ultrahigh energy density flexible supercapacitor, International Journal of Biological Macromolecules 225 (2023) 1437-1448, https://doi.org/10.1016/j.ijbiomac.2022.11.201.

[353] J. Li, N. Ren, J. Qiu, X. Mou, H. Liu, Graphene oxide-reinforced biodegradable genipin-cross-linked chitosan fluorescent biocomposite film and its cytocompatibility, International journal of nanomedicine (2013) 3415-3426, https://doi.org/10.2147/IJN.S51203.

[354] N. Bano, I. Hussain, A. El-Naggar, A. Albassam, Reduced graphene oxide nanocomposites for optoelectronics applications, Applied Physics A 125 (2019) 1-7, https://doi.org/10.1007/s00339-019-2518-8.

[355] M.A. Khapre, R.M. Jugade, Quaternary ammonium impregnated chitosan for the decontamination of wastewater from carcinogenic dyes, Environmental Processes 9(2) (2022) 24, https://doi.org/10.1007/s40710-022-00565-z.

[356] M. Mashuni, H. Ritonga, M. Jahiding, B. Rubak, F.H. Hamid, Highly sensitive detection of carbaryl pesticides using potentiometric biosensor with nanocomposite Ag/r-graphene oxide/chitosan immobilized acetylcholinesterase enzyme, Chemosensors 10(4) (2022) 138, https://doi.org/10.3390/chemosensors10040138.

[357] K. Kosowska, P. Domalik-Pyzik, M. Sekuła-Stryjewska, S. Noga, J. Jagiełło, M. Baran, L. Lipińska, E. Zuba-Surma, J. Chłopek, Gradient chitosan hydrogels modified with graphene derivatives and hydroxyapatite: physiochemical properties and initial cytocompatibility evaluation, International Journal of Molecular Sciences 21(14) (2020) 4888, https://doi.org/10.3390/ijms21144888.

[358] H. Rasti, K. Parivar, J. Baharara, M. Iranshahi, F. Namvar, Chitin from the mollusc chiton: extraction, characterization and chitosan preparation, Iranian journal of pharmaceutical research: IJPR 16(1) (2017) 366, https://doi.org/10.22037/IJPR.2017.1963.

[359] J.M. Hadi, S.B. Aziz, M.S. Mustafa, M.H. Hamsan, R.T. Abdulwahid, M.F. Kadir, H.O. Ghareeb, Role of nano-capacitor on dielectric constant enhancement in PEO: NH4SCN: xCeO2 polymer nano-composites: Electrical and electrochemical properties, Journal of Materials Research and Technology 9(4) (2020) 9283-9294, https://doi.org/10.1016/j.jmrt.2020.06.022.

[360] N.H. Ahmad, M.I.N.B.M. Isa, Ionic Conductivity And Electrical Properties Of Carboxymethyl Cellulose-NH4Cl Solid Polymer Electrolytes, Journal of

Engineering Science and Technology, 1823-4690, https://www.researchgate.net/publication/287207491, (2016).

[361] P.C. Heimenz, Principles of colloid and surface chemistry, New York M. Dekker1986.

[362] N. Kobayashi, S. Sunaga, R. Hirohashi, Effect of additive salts on ion conductivity characteristics in solid polymer electrolytes, Polymer 33(14) (1992) 3044-3048, https://doi.org/10.1016/0032-3861(92)90093-C.

[363] H. Mittal, S.S. Ray, B.S. Kaith, J.K. Bhatia, J. Sharma, S.M. Alhassan, Recent progress in the structural modification of chitosan for applications in diversified biomedical fields, European Polymer Journal 109 (2018) 402-434, https://doi.org/10.1016/j.eurpolymj.2018.10.013.

[364] A. Cano-Vicent, A. Tuñón-Molina, M. Martí, Á. Serrano-Aroca, Biocompatible Chitosan Films Containing Acetic Acid Manifested Potent Antiviral Activity against Enveloped and Non-Enveloped Viruses, International Journal of Molecular Sciences 24(15) (2023) 12028, https://doi.org/10.3390/ijms241512028.

[365] X. Li, X. Yang, Z. Wang, Y. Liu, J. Guo, Y. Zhu, J. Shao, J. Li, L. Wang, K. Wang, Antibacterial, antioxidant and biocompatible nanosized quercetin-PVA xerogel films for wound dressing, Colloids and Surfaces B: Biointerfaces 209 (2022) 112175, https://doi.org/10.1016/j.colsurfb.2021.112175.

[366] X. Li, C. Hao, B. Tang, Y. Wang, M. Liu, Y. Wang, Y. Zhu, C. Lu, Z. Tang, Supercapacitor electrode materials with hierarchically structured pores from carbonization of MWCNTs and ZIF-8 composites, Nanoscale 9(6) (2017) 2178-2187, https://doi.org/10.1039/C6NR08987A.

[367] F. Li, X. Wang, R. Sun, A metal-free and flexible supercapacitor based on redox-active lignosulfonate functionalized graphene hydrogels, Journal of Materials Chemistry A 5(39) (2017) 20643-20650, https://doi.org/10.1039/C7TA03789A.

[368] Z. Li, L. Zhang, B. Li, Z. Liu, Z. Liu, H. Wang, Q. Li, Convenient and large-scale synthesis of hollow graphene-like nanocages for electrochemical supercapacitor application, Chemical Engineering Journal 313 (2017) 1242-1250, https://doi.org/10.1016/j.cej.2016.11.018.

[369] B.T. Ho, T. Lim, M.H. Jeong, J.W. Suk, Graphene fibers containing activated graphene for high-performance solid-state flexible supercapacitors, ACS Applied Energy Materials 4(9) (2021) 8883-8890, https://doi.org/10.1021/acsaem.1c01095.

[370] S. Majumdar, P. Sen, R. Ray, High-performance graphene oxide-grafted chitosan-starch solid biopolymer electrolytes for flexible hybrid supercapacitors, Journal of Solid State Electrochemistry (2022) 1-21, https://doi.org/10.1007/s10008-021-05093-8.

[371] T. Wang, D. Wu, F. Yuan, Q. Liu, W. Li, D. Jia, Chitosan derived porous carbon prepared by amino acid proton salt for high-performance quasi-state-solid supercapacitor, Chemical Engineering Journal 462 (2023) 142292, https://doi.org/10.1016/j.cej.2023.142292.

[372] M.G. Hosseini, E. Shahryari, P. Yardani Sefidi, Polyaniline grafted chitosan/GO-CNT/Fe3O4 nanocomposite as a superior electrode material for supercapacitor application, Journal of Applied Polymer Science 138(38) (2021) 50976, https://doi.org/10.1002/app.50976.

[373] Y. Shen, T. Jing, W. Ren, J. Zhang, Z.-G. Jiang, Z.-Z. Yu, A. Dasari, Chemical and thermal reduction of graphene oxide and its electrically conductive

polylactic acid nanocomposites, Composites Science and Technology 72(12) (2012) 1430-1435, https://doi.org/10.1016/j.compscitech.2012.05.018.

[374] E. Jaafar, M. Kashif, S.K. Sahari, Z. Ngaini, Study on morphological, optical and electrical properties of graphene oxide (GO) and reduced graphene oxide (rGO), Materials Science Forum, Trans Tech Publ, 2018, pp. 112-116, https://doi.org/10.4028/www.scientific.net/MSF.917.112.

[375] K. Liu, S. Ronca, E. Andablo-Reyes, G. Forte, S. Rastogi, Unique rheological response of ultrahigh molecular weight polyethylenes in the presence of reduced graphene oxide, Macromolecules 48(1) (2015) 131-139, https://doi.org/10.1021/ma501729y.

[376] A.S. Buinov, E.R. Gafarova, E.A. Grebenik, K.N. Bardakova, B.C. Kholkhoev, N.N. Veryasova, P.V. Nikitin, N.V. Kosheleva, B.S. Shavkuta, A.S. Kuryanova, Fabrication of Conductive Tissue Engineering Nanocomposite Films Based on Chitosan and Surfactant-Stabilized Graphene Dispersions, Polymers 14(18) (2022) 3792, https://doi.org/10.3390/polym14183792.

[377] P. Feng, P. Du, C. Wan, Y. Shi, Q. Wan, Proton conducting graphene oxide/chitosan composite electrolytes as gate dielectrics for new-concept devices, Scientific Reports 6(1) (2016) 34065, https://doi.org/10.1038/srep34065.

[378] L. He, H. Wang, G. Xia, J. Sun, R. Song, Chitosan/graphene oxide nanocomposite films with enhanced interfacial interaction and their electrochemical applications, Applied surface science 314 (2014) 510-515, https://doi.org/10.1016/j.apsusc.2014.07.033.

[379] H. Wang, J. Wu, J. Qiu, K. Zhang, J. Shao, L. Yan, In situ formation of a renewable cellulose hydrogel electrolyte for high-performance flexible all-solid-state asymmetric supercapacitors, Sustainable Energy & Fuels 3(11) (2019) 3109-3115, https://doi.org/10.1039/C9SE00339H.

[380] X. Liu, Z. Lu, X. Huang, J. Bai, C. Li, C. Tu, X. Chen, Self-assembled S, N co-doped reduced graphene oxide/MXene aerogel for both symmetric liquid-and all-solid-state supercapacitors, Journal of Power Sources 516 (2021) 230682, https://doi.org/10.1016/j.jpowsour.2021.230682.

[381] K. Ghosh, C.Y. Yue, Development of 3D MoO3/graphene aerogel and sandwich-type polyaniline decorated porous MnO2− graphene hybrid film based high performance all-solid-state asymmetric supercapacitors, Electrochimica Acta 276 (2018) 47-63, https://doi.org/10.1016/j.electacta.2018.04.162.

[382] G. Pandey, A. Rastogi, Graphene-based all-solid-state supercapacitor with ionic liquid gel polymer electrolyte, MRS Online Proceedings Library (OPL) 1440 (2012) mrss12-1440-o04-05, https://doi.org/10.1557/opl.2012.1279.

[383] C. Yang, J. Shen, C. Wang, H. Fei, H. Bao, G. Wang, All-solid-state asymmetric supercapacitor based on reduced graphene oxide/carbon nanotube and carbon fiber paper/polypyrrole electrodes, Journal of Materials Chemistry A 2(5) (2014) 1458-1464, https://doi.org/10.1039/C3TA13953K.

[384] L. Deng, C. Zhou, Z. Ma, G. Fan, Methylene blue functionalized graphene as binder-free electrode for high-performance solid state supercapacitors, Journal of colloid and interface science 561 (2020) 416-425, https://doi.org/10.1016/j.jcis.2019.11.007.

[385] J. Liu, Z. Khanam, S. Ahmed, H. Wang, T. Wang, S. Song, A study of low-temperature solid-state supercapacitors based on Al-ion conducting polymer electrolyte and graphene electrodes, Journal of Power Sources 488 (2021) 229461, https://doi.org/10.1016/j.jpowsour.2021.229461.

[386] D. Jiang, H. Liang, Y. Liu, Y. Zheng, C. Li, W. Yang, C.J. Barrow, J. Liu, In situ generation of CoS 1.097 nanoparticles on S/N co-doped graphene/carbonized foam for mechanically tough and flexible all solid-state supercapacitors, Journal of Materials Chemistry A 6(25) (2018) 11966-11977, https://doi.org/10.1039/C8TA04307H.

[387] K. Wang, W. Zou, B. Quan, A. Yu, H. Wu, P. Jiang, Z. Wei, An all-solid-state flexible micro-supercapacitor on a chip, Advanced Energy Materials 1(6) (2011) 1068-1072, https://doi.org/10.1002/aenm.201100488.

[388] S. Liu, J. Xie, H. Li, Y. Wang, H.Y. Yang, T. Zhu, S. Zhang, G. Cao, X. Zhao, Nitrogen-doped reduced graphene oxide for high-performance flexible all-solid-state micro-supercapacitors, Journal of Materials Chemistry A 2(42) (2014) 18125-18131, https://doi.org/10.1039/C4TA03192J.

[389] Y. Wang, L. Sun, P. Song, C. Zhao, S. Kuang, H. Liu, D. Xiao, F. Hu, L. Tu, A low-temperature-operated direct fabrication method for all-solid-state flexible micro-supercapacitors, Journal of Power Sources 448 (2020) 227415, https://doi.org/10.1016/j.jpowsour.2019.227415.

[390] L. Liu, Y. Feng, W. Wu, Recent progress in printed flexible solid-state supercapacitors for portable and wearable energy storage, Journal of Power Sources 410 (2019) 69-77, https://doi.org/10.1016/j.jpowsour.2018.11.012.

[391] L. Chen, H.-B. Zhao, Y.-P. Ni, T. Fu, W.-S. Wu, X.-L. Wang, Y.-Z. Wang, 3D printable robust shape memory PET copolyesters with fire safety via π-stacking and synergistic crosslinking, Journal of Materials Chemistry A 7(28) (2019) 17037-17045, https://doi.org/10.1039/C9TA04187G.

[392] G. Xiong, C. Meng, R.G. Reifenberger, P.P. Irazoqui, T.S. Fisher, Graphitic petal electrodes for all-solid-state flexible supercapacitors, Advanced Energy Materials 4(3) (2014) 1300515, https://doi.org/10.1002/aenm.201300515.

[393] M. Yang, Z. Wang, M. Li, Z. Yin, H.A. Butt, The synthesis, mechanisms, and additives for bio-compatible polyvinyl alcohol hydrogels: A review on current advances, trends, and future outlook, Journal of Vinyl and Additive Technology 29(6) (2023) 939-959, https://doi.org/10.1002/vnl.21962.

[394] C. Liao, Y. Li, S.C. Tjong, Graphene nanomaterials: Synthesis, biocompatibility, and cytotoxicity, International journal of molecular sciences 19(11) (2018) 3564, https://doi.org/10.3390/ijms19113564.

[395] M. Doyle, T.F. Fuller, J. Newman, Modeling of galvanostatic charge and discharge of the lithium/polymer/insertion cell, Journal of the Electrochemical society 140(6) (1993) 1526, https://doi.org/10.1149/1.2221597.

[396] F. Licht, M. Davis, H. Andreas, Charge redistribution and electrode history impact galvanostatic charging/discharging and associated figures of merit, Journal of Power Sources 446 (2020) 227354, https://doi.org/10.1016/j.jpowsour.2019.227354.

[397] G.A. Mabbott, An introduction to cyclic voltammetry, Journal of Chemical education 60(9) (1983) 697, https://doi.org/10.1021/ed060p697.

[398] P. Karthika, N. Rajalakshmi, K.S. Dhathathreyan, Functionalized exfoliated graphene oxide as supercapacitor electrodes, (2012) Soft Nanoscience Letters, Vol. 2 No. 4, 2012, pp. 59-66. https://doi.org/10.4236/snl.2012.24011.

[399] H. Gómez, M.K. Ram, F. Alvi, P. Villalba, E.L. Stefanakos, A. Kumar, Graphene-conducting polymer nanocomposite as novel electrode for supercapacitors, Journal of Power Sources 196(8) (2011) 4102-4108, https://doi.org/10.1016/j.jpowsour.2010.11.002.

[400] H. Lee, J. Kang, M.S. Cho, J.-B. Choi, Y. Lee, MnO 2/graphene composite electrodes for supercapacitors: the effect of graphene intercalation on capacitance, Journal of Materials Chemistry 21(45) (2011) 18215-18219, https://doi.org/10.1039/C1JM13364K.

[401] X. Du, P. Guo, H. Song, X. Chen, Graphene nanosheets as electrode material for electric double-layer capacitors, Electrochimica Acta 55(16) (2010) 4812-4819, https://doi.org/10.1016/j.electacta.2010.03.047.

[402] S.K. Tiwari, A.K. Thakur, A.D. Adhikari, Y. Zhu, N. Wang, Current research of graphene-based nanocomposites and their application for supercapacitors, Nanomaterials 10(10) (2020) 2046, https://doi.org/10.3390/nano10102046.

[403] J. Arkowski, M. Obremska, K. Kędzierski, A. Sławuta, M. Wawrzyńska, Applications for graphene and its derivatives in medical devices: Current knowledge and future applications, Advances in Clinical and Experimental Medicine 29(12) (2020) 1497-1504, https://doi.org/10.17219/acem/130601.

[404] M. Al-Furjan, Z. Qi, L. Shan, A. Farrokhian, X. Shen, R. Kolahchi, Nano supercapacitors with practical application in aerospace technology: Vibration and wave propagation analysis, Aerospace Science and Technology 133 (2023) 108082, https://doi.org/10.1016/j.ast.2022.108082.

[405] Y. Huang, J. Liang, Y. Chen, An overview of the applications of graphene-based materials in supercapacitors, small 8(12) (2012) 1805-1834, https://doi.org/10.1002/smll.201102635.

[406] W. Yang, M. Ni, X. Ren, Y. Tian, N. Li, Y. Su, X. Zhang, Graphene in supercapacitor applications, Current Opinion in Colloid & Interface Science 20(5-6) (2015) 416-428, https://doi.org/10.1016/j.cocis.2015.10.009.

[407] Maxwell Technologies Company.

[408] H. Li, J. Liang, Recent development of printed micro-supercapacitors: printable materials, printing technologies, and perspectives, Advanced Materials 32(3) (2020) 1805864, https://doi.org/10.1002/adma.201805864.

[409] Y.-Z. Zhang, Y. Wang, T. Cheng, L.-Q. Yao, X. Li, W.-Y. Lai, W. Huang, Printed supercapacitors: materials, printing and applications, Chemical Society Reviews 48(12) (2019) 3229-3264, https://doi.org/10.1039/C7CS00819H.

[410] A. Su, S.J. Al'Aref, History of 3D printing, 3D printing applications in cardiovascular medicine, Elsevier2018, pp. 1-10, https://doi.org/10.1016/C2015-0-00622-0.

[411] C.K. Chua, M. Vadakke Matham, Y.-J. Kim, Lasers in 3D printing and manufacturing, World Scientific, https://doi.org/10.1142/9500.2017.

[412] K. Ghosh, M. Pumera, Free-standing electrochemically coated MoS x based 3D-printed nanocarbon electrode for solid-state supercapacitor application, Nanoscale 13(11) (2021) 5744-5756.

[413] K. Tang, H. Ma, Y. Tian, Z. Liu, H. Jin, S. Hou, K. Zhou, X. Tian, 3D printed hybrid-dimensional electrodes for flexible micro-supercapacitors with superior electrochemical behaviours, Virtual and Physical Prototyping 15(sup1) (2020) 511-519.

[414] Y. Zhang, Y. Song, Y. Shi, Y. Wang, X. Wang, X. Shi, C. Tang, J. Liu, G. Wang, Q. Tan, High-performance all-solid-state microsupercapacitors from 3D printing structure-engineered graphene-carbon sphere electrodes, Applied Surface Science 597 (2022) 153730.

[415] Y. Gao, X. Guo, Z. Qiu, G. Zhang, R. Zhu, Y. Zhang, H. Pang, Printable electrode materials for supercapacitors, ChemPhysMater 1(1) (2022) 17-38.

[416] M. Ntousia, I. Fudos, 3D printing technologies & applications: an overview, Proceedings of the CAD 2020 Conference, Singapore, 2019, pp. 248, https://doi.org/10.14733/cadconfP.2019.243-248.

[417] A. Selimis, V. Mironov, M. Farsari, Direct laser writing: Principles and materials for scaffold 3D printing, Microelectronic Engineering 132 (2015) 83-89, https://doi.org/10.1016/j.mee.2014.10.001.

[418] L. Jonušauskas, D. Gailevičius, S. Rekštytė, T. Baldacchini, S. Juodkazis, M. Malinauskas, Mesoscale laser 3D printing, Optics express 27(11) (2019) 15205-15221 https://doi.org/10.1364/OE.27.015205f.

[419] C.W. Visser, R. Pohl, C. Sun, G.W. Römer, D. Lohse, Toward 3D printing of pure metals by laser-induced forward transfer, Advanced materials (27) (2015) 4087-4092, https://doi.org/10.1002/adma.201501058.

ATTACHEMENT

APPENDIX 1 – Supplementary results of the thesis

Table S1. The specific capacitance results of the RGO/CS fiber-based solid-state supercapacitors obtained by CV test, (GPE: PVA/KCl, M_w=195000 g mol^{-1}, w/w: 1/2).

Name of sample	Integral area (µA.V)	Scan rate (mV s^{-1})	Specific capacitance (F g^{-1})
RGO	53.87	5	85.34±19.02
	70.74	20	34.15±9.44
	95.42	50	16.8±4.16
	113.66	100	9.45±2.01
	130.11	200	5.29±0.97
	149.97	500	2.51±0.52
	189.34	1000	1.69±0.41
RGO/CS(w/w: 95/5)	120.41	5	157.95±29.22
	220.64	20	50.92±10.09
	299.63	50	25.27±8.23
	364.24	100	13.95±6.73
	436.61	200	7.62±4.68
	570.63	500	3.45±2.43
	685.91	1000	2.28±1.80
RGO/CS(w/w: 90/10)	177.23	5	523.06± 53.57
	320.08	20	252.05±65.87
	436.68	50	138.46±49.01

	531.32	100	83.26±33.86
	631.84	200	48.88±21.39
	737.15	500	23.53±10.60
	762.46	1000	14.21±4.54
RGO/CS(w/w: 80/20)	145.31	5	397.63±77.65
	304.03	20	167.69±39.58
	435.76	50	102.08±22.22
	546.74	100	48.94±20.46
	664.18	200	27.67±13.87
	879.85	500	12.84±7.20
	824.02	1000	6.94±3.13
RGO/CS(w/w: 60/40)	62.70	5	204.27±17.03
	99.09	20	115.52±69.49
	146.29	50	60.93±38.86
	232.84	100	36.38±24.13
	312.13	200	21.50±14.71
	451.50	500	10.66±7.86
	718.70	1000	6.78±4.69
RGO/CS(w/w: 50/50)	33.56	5	46.40±25.43
	58.47	20	19.58±12.76
	80.72	50	10.55±7.44
	98.84	100	6.39±4.69
	119.91	200	3.84±2.89
	153.91	500	1.95±1.49
	214.80	1000	1.35±1.05

RGO/CS(w/w: 20/80)	0.34	5	0.95±0.16
	0.42	20	0.28±0.06
	0.56	50	0.14±0.05
	0.72	100	0.09±0.03
	0.97	200	0.06±0.02
	1.50	500	0.04±0.01
	2.49	1000	0.03±0.01
RGO/CS(w/w: 10/90)	0.06	5	0.20±0.04
	0.07	20	0.06±0.01
	0.07	50	0.03±0.006
	0.08	100	0.02±0.006
	0.09	200	0.01±0.001
	0.10	500	0.004±0.001
	0.14	1000	0.003±0.001
RGO/CS(w/w: 0/100)	0.04	5	0.09±0.05
	0.07	20	0.05±0.01
	0.13	50	0.03±0.001
	0.22	100	0.029±0.007
	0.36	200	0.023±0.006
	0.66	500	0.017±0.004
	1.18	1000	0.015±0.004

Table S2. The specific capacitance results of the RGO/CS film-based solid-state supercapacitors obtained by CV test, (GPE: PVA/KCl, M_w=195000 g mol^{-1}, w/w: 1/2).

Name of sample	Integral area (μA.V)	Scan rate (mV s^{-1})	Specific capacitance (F g^{-1})
CS	1.22	5	5.26 ± 0.75
	1.89	20	1.82±0.33
	4	50	1±1.40
	7.62	100	1.37±0.39
	11.31	200	1.04±0.30
	23.26	500	0.87±0.27
	50.23	1000	0.77±0.27
RGO	51.22	5	174.03±38.25
	67.70	20	57.05±13.75
	91.20	50	30.40±8.24
	108.41	100	18.04±5.13
	123.99	200	10.38±3.01
	142.62	500	4.86±1.39
	181.96	1000	3.19±0.85
RGO/CS(w/w: 95/5)	85.33	5	312.01±28.48
	112.96	20	103.26±9.47
	154.03	50	58.32±5.14
	202.46	100	37.01±3.38
	270.03	200	24.68±2.25
	377.75	500	13.81±1.26
	595.93	1000	10.89±0.99
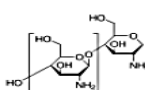
RGO/CS(w/w: 90/10)	273.63	5	872.75± 68.35
	374.54	20	291.21±27.70
	525.92	50	158.50±16.66
	650.31	100	94.62±12.63
	776.38	200	54.85±8.85
	791.69	500	23.86±2.44
	834.96	1000	13.99±0.67
RGO/CS(w/w: 80/20)	218.30	5	459.24±23.39
	285.77	20	153.16±73.62
	390.51	50	79.39±44.05
	459.59	100	46.71±25.94
	523.09	200	26.01±15.40
	591.69	500	12.09±6.68
	734.96	1000	7.89±3.79
RGO/CS(w/w: 60/40)	65.95	5	267.08±143.71
	92.17	20	81.97±6.24
	135.75	50	44.88±10.79
	173.06	100	34.88±7.04
	211.11	200	24.38±3.85
	262.32	500	14.08±1.58
	351.91	1000	11.94±1.04
RGO/CS(w/w: 50/50)	50.97	5	159.63±24.34
	82.98	20	55.04±8.25
	146.29	50	32.19±5.26
	214.91	100	20.61±3.68

	298.54	200	12.77±2.41
	446.58	500	6.52±1.27
	713.46	1000	4.47±0.87
RGO/CS(w/w: 20/80)	32.79	5	113.07±3.31
	41.61	20	37.69±4.12
	52.86	50	18.75±5.30
	61.40	100	10.55±5.15
	70.29	200	5.95±3.91
	83.19	500	2.78±2.12
	114.76	1000	2.01±1.57
RGO/CS(w/w: 10/90)	20.52	5	81.86±8.82
	30.92	20	28.39±3.43
	38.50	50	15.15±2.27
	44.53	100	9.21±1.61
	51.38	200	5.44±0.99
	61.43	500	2.60±0.47
	87.31	1000	1.72±0.26
RGO/CS(w/w: 0/100)	2.20	5	5.28±0.75
	2.33	20	1.82±0.33
	3.76	50	1.41±0.38
	7.27	100	1.37±0.39
	11.05	200	1.04±0.30
	22.60	500	0.87±0.27
	39.12	1000	0.77±0.28

The product information of chitosan polymer:

The purchased chitosan (CS) (448877-250G) with a medium molecular weight is used in pharmaceuticals applications and have good compatibility, dispersion, and lower viscosity. This chitosan has a deacetylation degree of >=75% which is soluble in acetic acid. Acetic acid can protonate the amino groups in chitosan and aiding in dissolution. Image.S1 shows the chitosan product specifications. Figure.S1 indicates the ATR-FTIR result of the synthesized chitosan by Sigma-Aldrich Company.

Product Specification

Product Name:
Chitosan - medium molecular weight

Product Number: 448877
CAS Number: 9012-76-4
MDL: MFCD00161512
Formula: C12H24N2O9

TEST	Specification
Appearance (Color)	Off White to Beige and Faint Brown to Light Brown
Appearance (Form) Powder and/or Chips	Conforms to Requirements
Deacetylation	$\geq$ 75 %
Viscosity c = 1%, 1% Acetic Acid	200 - 800 cps

Specification: PRD.2.ZQ5.10000030084

Image.S1. The product specification of chitosan by Sigma-Aldrich company.
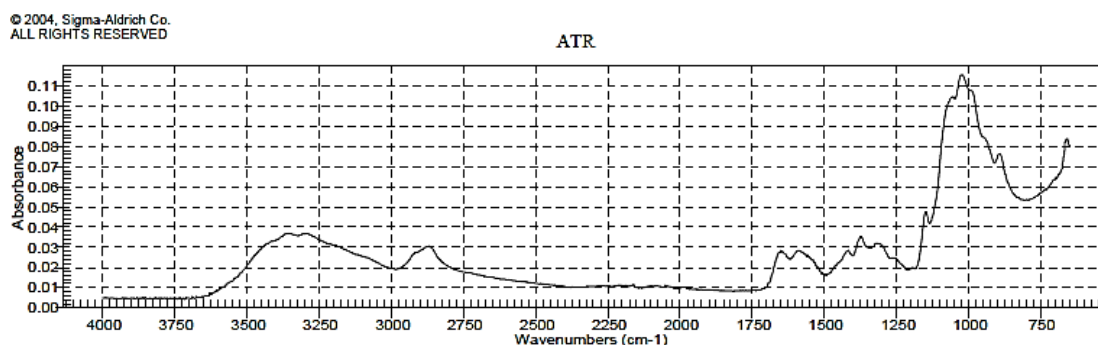
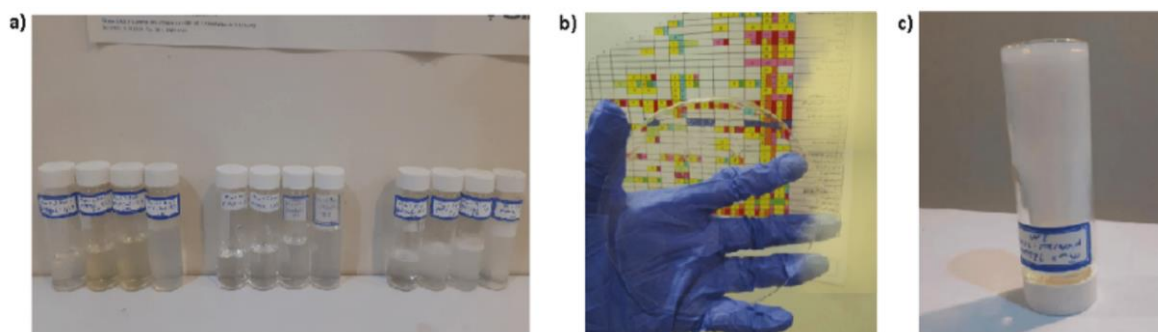Figure.S1. ATR-FTIR of pure chitosan by Sigma-Aldrich Company.

Image S2. a) Gel polymer electrolyte solutions based on PVA/KCl/H_2O, b) PVA/KCl gel film on a Petri dish, c) PVA/KCl gel sample.
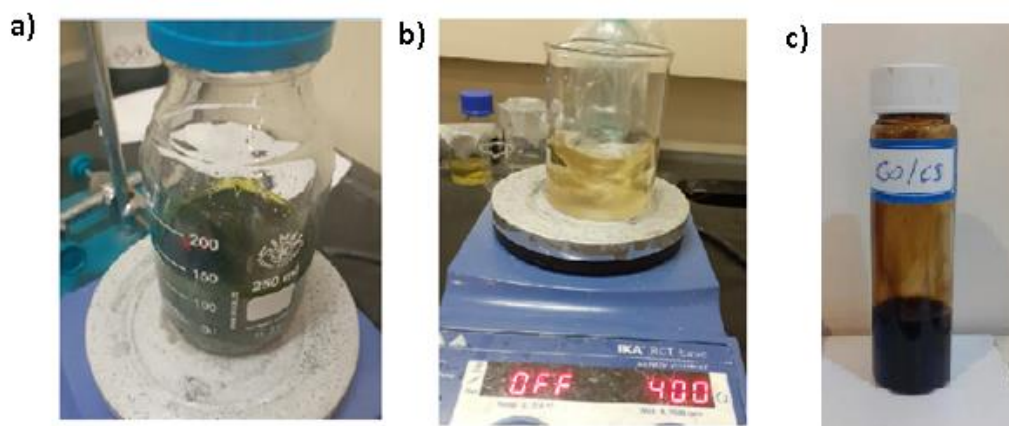

Image S3. Graphene oxide (GO) dispersion. a) The mixture of oxidized graphite, H_2SO_4, and $KMnO_4$ as a green color. b) The mixture after adding DI-water and H_2O_2 to the mixture prepared in -a-, showing a light brown or gold color. c) GO/CS dispersion in acetic acid.
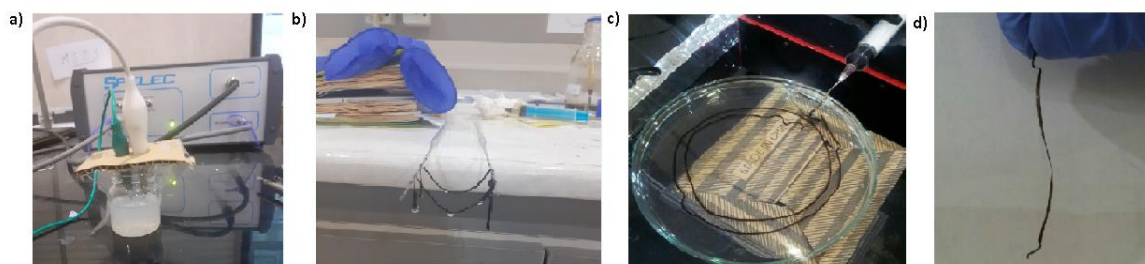
Image S4. a) The cell containing RGO/CS fibers in PVA/KCl gel polymer electrolyte for doing the electrochemical tests, b) The as-prepared GO/CS fibers, c) The wet-spinning preparation process of GO/CS fibers, d) RGO/CS fiber after hydrothermal reduction of GO at 120 °C.
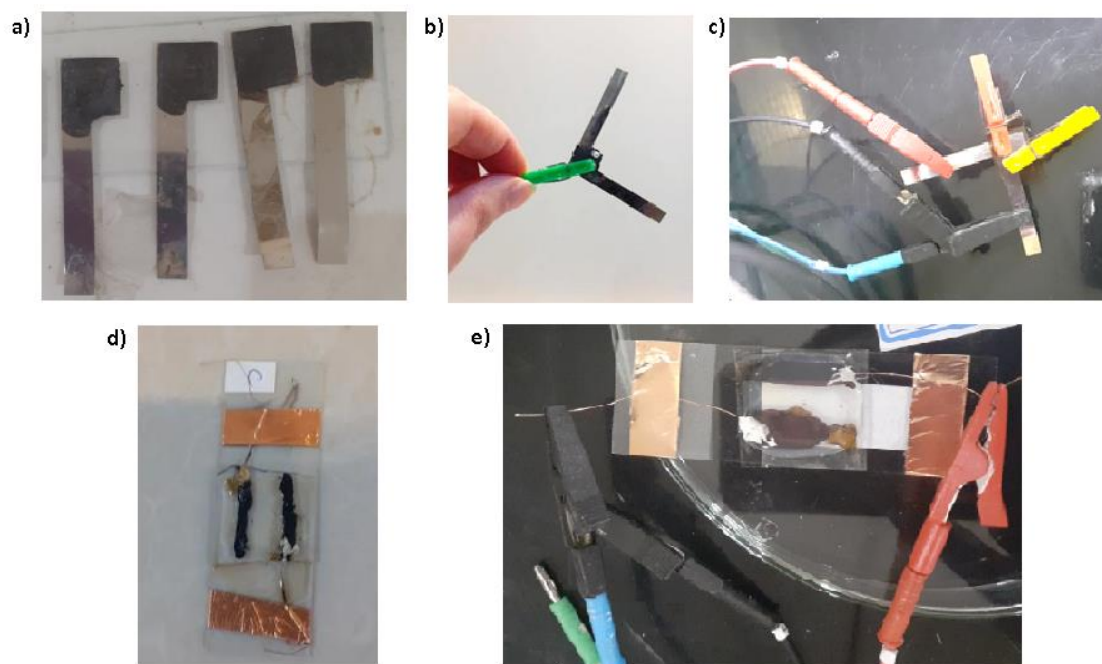

Image S5. a) RGO/CS composite film electrodes on stainless steel substrate. b) Solid-state supercapacitor based on RGO/CS film composite. c) The cell containing PVA/KCl gel polymer electrolyte sandwiched between RGO/CS films for doing the electrochemical tests. d) RGO/CS composite film electrodes on PET substrate as flexible solid-state supercapacitor. e) The cell containing RGO/CS film electrodes covered by PVA/KCl gel polymer electrolyte for doing the electrochemical tests.
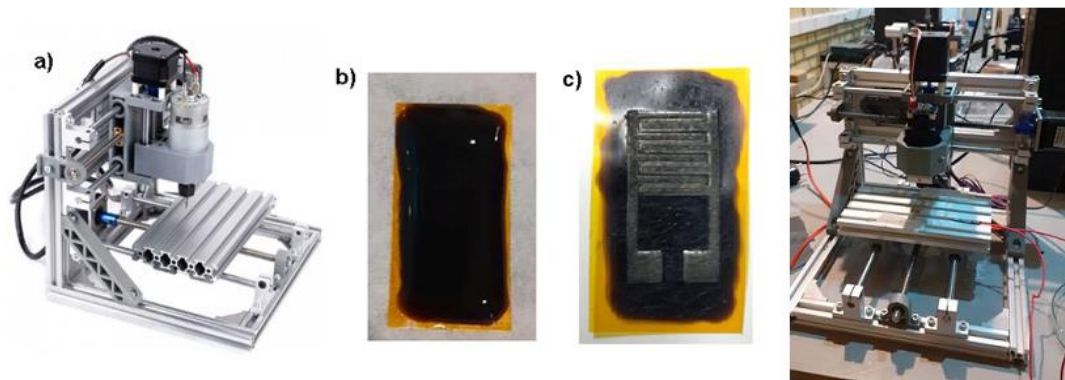
Image S6. a) Laser 3D-printing device. b) GO/CS film prepared on the polyimide (PI) substrate at room temperature. c) Flexible solid-state supercapacitor based on RGO/CS film composite using laser printing.
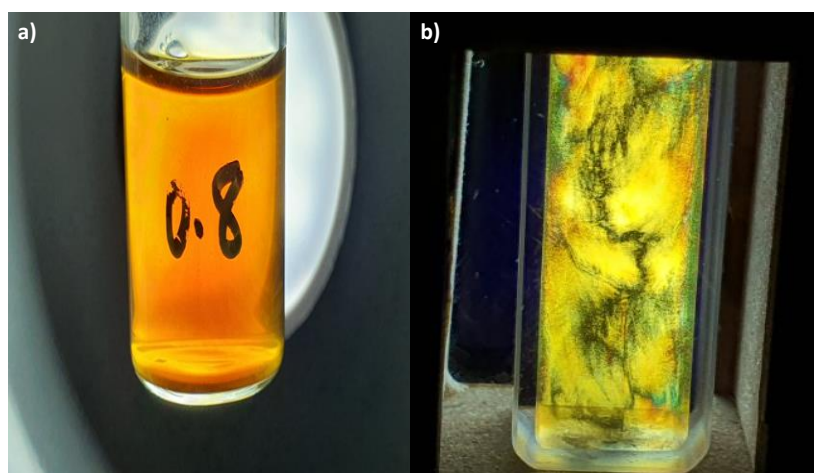

Image S7. a) Graphene oxide (GO) dispersion, b) Polarized Optical Microscopy (POM) image depicting the lyotropic nematic liquid crystalline phase of graphene oxide (GO).
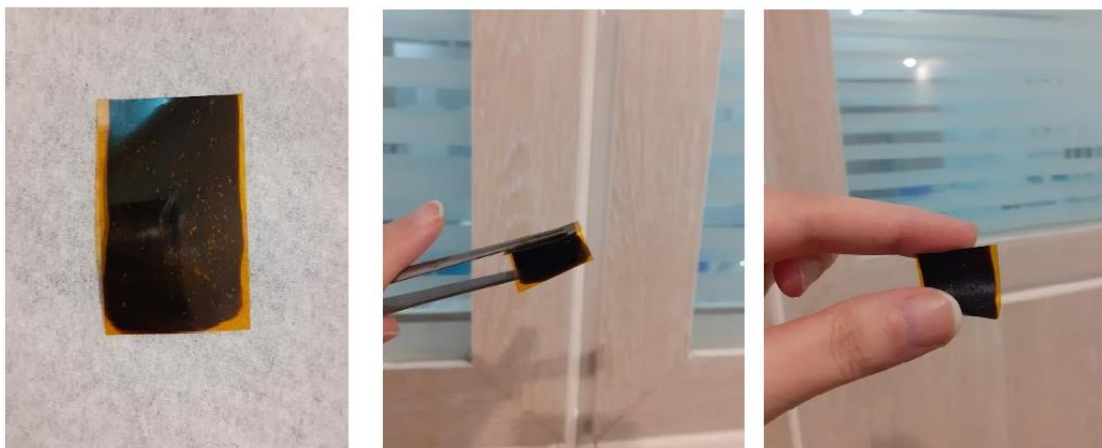
Image S8. Flexible film-type electrodes on the polyimide (PI) substrate based on RGO/CS for solid-state supercapacitors.

APPENDIX 3 - Publications Derived from the Thesis

1. Saeideh Alipoori, Seyed Hamed Aboutalebi, Murat Barsbay, Enhancing the Performance of Solid-State Supercapacitors: Optimizing the Molecular Interactions in Flexible Gel Polymer Electrolytes, Journal of Solid State Electrochemistry, 2024, https://doi.org/10.1007/s10008-024-05809-6

2. Saeideh Alipoori, Seyed Hamed Aboutalebi, Murat Barsbay, Additive-free electrode materials based on RGO and chitosan: Toward developing a high-performance solid-state supercapacitor for sustainable biomedical applications, (Submitted to the Journal of Energy and Environmental Science, RSC)